UNIVERSITAT POLITÈCNICA DE VALÈNCIA

DEPARTAMENT DE COMUNICACIONS

Photonic-assisted RF Signal Processing based on Slow and Fast Light Technological Platforms

Ph.D. THESIS

by

Juan Sancho

Valencia, June 2012

UNIVERSITAT POLITÈCNICA DE VALÈNCIA

DEPARTAMENT DE COMUNICACIONS

Photonic-assisted RF Signal Processing based on Slow and Fast Light Technological Platforms

Juan Sancho, M.Sc.
Optical and Quantum Communications Group (OQCG)
ITEAM Research Institute
Universidad Politécnica de Valencia (UPV)
Camino de Vera s/n, 46022 Valencia, SPAIN
juasandu@upvnet.upv.es

Ph.D. Supervisors:

Prof. Salvador Sales Maicas
Dr. Ivana Gasulla Mestre

Valencia, June 2012

To my parents
and grandfather Pepe

A person who never made a mistake never tried anything new.

Albert Einstein

Acknowledgements

I would like, at the outset, to thank my thesis supervisors Salvador Sales and Ivana Gasulla for the guidance, support and scientific contribution during these three and a half years of research. My sincerely gratitude also goes to Prof. José Capmany, leader of the *Optical and Quantum Communications Group*, whose broad knowledge and interest have helped bring about the achievements of this outcome.

All the people in the *Optical and Quantum Communications Group* are thanked for creating a pleasant and positive atmosphere. Indeed, I am very grateful to my partner and friend Juan Lloret, with whom I have had the gift to work with for the last years. He is mainly responsible for that I have become a better researcher and person.

My special thanks and sympathy also go to Prof. Luc Thévenaz for hosting me at EPFL University in Switzerland during my three months stay. I really spent a great time in such a beautiful country. Two excellent people, Nikolay Primerov and Sanghoon Chin, whom I had the privilege of meeting in Luc's laboratory, also deserves my truly gratefulness. Their technical assistance and discussions let me understand all the physics behind Brillouin systems. In particular, Nikolay Primerov not only was an excellent co-worker but also has become a good friend.

I owe many thanks to Perrine Berger, Jérôme Bourderionnet and Alfredo De Rossi from THALES in France, for the good and fruitful collaborations. My warm gratitude also goes to all the people whom I have interacted with through the GOSPEL project. They have been responsible for many interesting and pleasant meetings.

I wish to thank my family for their unconditional support. Particularly, I owe immeasurable gratitude to my parents for their help and affection, for believing in me during my whole life and basically for making it all possible. My grandfather Pepe also deserves my thankfulness for showing interest and encouraging me since the beginning of my studies.

Last but no least, I would like to thank Juncal for her forbearance, loving support, help and understanding even during difficult times. She is my guiding light, keeping me on a steady course and an even keel, despite myself.

Abstract

Slow and fast light (SFL) effects have shown outstanding capabilities across the dynamic control of the speed of light in different media. Indeed, one of the most exciting motivations lies in the SFL potential application to the framework of photonic-assisted radio-frequency (RF) signal processing.

This Ph.D. thesis points out the performance evaluation of current SFL device platforms so as to enable several tasks required in the microwave photonics (MWP) field with the added value of tunability and broadband operation. In this context, technologies such as stimulated Brillouin scattering (SBS) effects in standard and polarization maintaining fibers (PMF), fiber Bragg gratings (FBG), semiconductor optical amplifiers (SOA) and photonic crystal (PhC) waveguides have been under study. From km to mm-scale footprints, these SFL device platforms stand for the evolution towards the integration of MWP components and subsystems in photonic integrated circuits (PIC). Analytical and numerical models have been developed in order to understand the physical processes governing the SFL propagation on the different device platforms, as well as to describe the proposed MWP approaches. The performance analysis of two of the key functionalities required for MWP signal processing, i.e. tunable phase shifting and true time delay (TTD) operation, has been presented by means of the above proposed platforms. A TTD system, based on the so-called separate carrier tuning (SCT) technique, has been reported through SBS effects in standard fibers. In addition, the SBS interaction in PMFs has been evaluated aiming at performing dynamic Brillouin gratings (DBG), whose phase induced has been addressed. A distributed sensing system based on the continuous reflection of a short pulse along a weak FBG has also been demonstrated. A complete analysis of the nonlinear distortion introduced in the phase shifter has been addressed for cascaded structures comprising an SOA device under the coherent population oscillation (CPO) effect and an optical filtering stage. A novel fully-tunable 360° phase shifter implemented using only one SOA followed by a conveniently designed notch filter has also been reported. The suitability of exploiting the dispersive feature of a PhC waveguide to perform TTDs has been demonstrated. The phase shifting and true time delaying capabilities of the proposed approaches have been put to the test for implementing tunable and reconfigurable complex-valued multi-tap MWP filters. The performance of the reported technological platforms have been evaluated in terms of several figures of merit (FOM) so as to characterize their impact on the MWP link and also to identify the use of the most proper technology depending on the final processing task to be developed.

Resumen

Los efectos de luz lenta y luz rápida (SFL) han mostrado unas capacidades excepcionales sobre el control dinámico de la velocidad de la luz en diferentes medios. Una de las motivaciones más estimulantes radica en la potente aplicación de estos sistemas en el marco del procesado fotónico de señales de radio frecuencia (RF).

En esta tesis doctoral, se evalúan las prestaciones de las plataformas de SFL actuales para desarrollar múltiples tareas que se requieren en el campo de la fotónica de microondas (MWP) con el valor añadido de sintonizabilidad y operación en banda ancha. En este contexto, el *scattering* de Brillouin estimulado (SBS), tanto en fibra estándar como en fibra mantenedora de polarización (PMF), redes de Bragg (FBG), amplificadores ópticos de semiconductor (SOA) y cristales fotónicos (PhC) han sido las tecnologías bajo estudio. Desde escalas del orden de km hasta mm, estas plataformas de SFL representan la evolución hacia la consolidación de componentes y subsistemas de MWP en circuitos fotónicos integrados (PIC). Diversos modelos analíticos y numéricos se han desarrollado con el objetivo de entender los procesos físicos que gobiernan la propagación a través de las diferentes plataformas de SFL, así como para describir los enfoques de MWP propuestos. Además, a través de las plataformas presentadas se ha llevado a cabo el análisis de las prestaciones de dos de las funcionalides clave que se requieren para el procesado fotónico de señales de microondas, desfasadores sintonizables y retardos verdaderos (TTD). Se ha propuesto un sistema de TTD basado en la llamada técnica de sintonización separada de la portadora (SCT) a través de los efectos de SBS en fibras estándar. Se ha evaluado la interacción del SBS en PMF con el propósito de desarrollar redes de Brillouin dinámicas (DBG), cuya fase generada ha sido fruto de estudio. Por otro lado, también se ha demostrado un sistema de sensado distribuido basado en la reflexión continua de un pulso estrecho a lo largo de una FBG débil. Un análisis completo de la distorsión no lineal introducida en el desfasador ha sido descrita para estructuras en cascada formadas por un SOA bajo el efecto de las oscilaciones coherentes de la población (CPO) y una etapa de filtrado óptico. Se ha propuesto también un novedoso desfasador, completamente sintonizable e implementado utilizando únicamente un SOA seguido de un filtro *notch*, el cual ha sido convenientemente diseñado para incrementar el rango del desfasador. Se han explotado las características dispersivas de un PhC para desarrollar TTD. Se han puesto a prueba las capacidades de los sistemas presentados, en cuanto a generar desfases y retardos verdaderos, para la implementación de filtros de MWP con múltiples coeficientes complejos, sintonizables y reconfigurables. Se han evaluado las prestaciones de las plataformas tecnológicas propuestas en el contexto de

diversas figuras de merito (FOM) para caracterizar su impacto en el enlace de MWP y además identificar el uso de la tecnología más adecuada dependiendo de la tarea final de procesado a ser desarrollada.

Resum

Els efectes de la llum lenta i la llum ràpida (SFL) han manifestat unes capacitats excepcionals sobre el control dinàmic de la velocitat de la llum en diferents medis. Una de les motivacions més estimulants radica en la potent aplicació d'aquests sistemes en el marc del processament fotònic de senyals de ràdio freqüència (RF).

En aquesta tesi doctoral, s'avaluen les prestacions de les plataformes de SFL actuals per a desenvolupar múltiples tasques que son requerides en el camp de la fotònica de microones (MWP) amb el valor afegit de sintonitzabilitat i operació en banda ampla. En aquest context, el *scattering* de Brillouin estimulat (SBS), tant en fibra estàndard com en fibra mantenidora de polarització (PMF), xarxes de Bragg (FBG), amplificadors òptics de semiconductor (SOA) i cristalls fotònics (PhC) han sigut les tecnologies sota estudi. Des d'escales de l'ordre de km fins a mm, aquestes plataformes de SFL representen l'evolució cap a la consolidació de components i subsistemes de MWP en circuits fotònics integrats (PIC). S'han desenvolupat diversos models analítics i numèrics amb l'objecte de comprendre el processos físics que governen la propagació a través de les diferents plataformes de SFL, així com per a descriure els enfocaments proposats de MWP. A més a més, a través de les plataformes presentades s'ha dut a terme l'anàlisi de les prestacions de dos de les funcionalitats essencials que es requereixen per al processament fotònic de les senyals de microones, desfasadors sintonitzables i retards vertaders (TTD). Un sistema TTD basat en l'anomenada tècnica de sintonització separada de la portadora (SCT) ha sigut proposat a través dels efectes de SBS en fibres estàndard. La interacció del SBS en PMF ha sigut avaluada amb l'objecte de desenvolupar xarxes de Brillouin dinàmiques (DBG). Així, la fase generada ha sigut objecte d'estudi. Per altra banda,també s'ha demonstrat un sistema de sensat distribuït. Aquest està basat en la reflexió continua d'un pols estret al llarg d'una FBG feble. Un anàlisi complet de la distorsió no lineal introduït en el desfasador ha sigut descrita per a estructures en cascada formades per un SOA sota l'efecte de les oscil·lacions coherents de la població (CPO) i una etapa de filtrat òptic. S'ha proposat també un innovador desfasador, completament sintonitzable i implementat, utilitzant únicament un SOA seguit d'un filtre *notch*, el qual ha sigut convenientment dissenyat per a incrementar el rang del desfasador. S'han explotat les característiques dispersives d'un PhC per a desenvolupar TTD. S'han posat a prova les capacitats dels sistemes presentats, quant a generar desfases i retards vertaders, per a la implementació de filtres de MWP amb múltiples coeficients complexos, sintonitzables i reconfigurables. S'han evaluat les prestacions de les plataformes tecnològiques proposades en el context de diverses figures de mèrit

(FOM) per a caracteritzar el seu impacte amb l'enllaç de MWP i, a més a més, identificar l'ús de la tecnologia adequada dependent de la tasca final de processament a ser desenvolupada.

List of Acronyms

ASE	Amplified spontaneous emission
AWG	Arrayed waveguide grating
CPO	Coherent population oscillations
CW	Continuous-wave
DBG	Dynamic Brillouin grating
DC	Direct current
DD	Dual drive
DFB-LD	Distributed-feedback laser-diode
EDFA	Erbium doped fiber amplifier
EIT	Electromagnetically induced transparency
EMI	Electromagnetic interference
EOM	Electro-optic modulator
ER	Extinction rate
FBG	Fiber Bragg grating
FIR	Finite impulse response
FOM	Figure of merit
FP	Fabry-Perot
FSR	Free spectral range
FWHM	Full width at half maximum
FWM	Four wave mixing
HD	Harmonic distortion

ICP Inductively coupled plasma

IMD Intermodulation distortion

LSA Lightwave spectrum analyzer

MOCVD Metal-organic chemical vapour deposition

MSSL Main to secondary side-lobe

MWP Microwave photonics

MZ Mach-Zehnder

MZM Mach-Zehnder modulator

NF Noise figure

ODSB Optical double sideband

OEO Opto-electronic oscillator

OFDR Optical frequency domain reflectometry

OLCR Optical low-coherence reflectometry

ONF Optical notch filter

OSA Optical spectrum analyzer

OSSB Optical single sideband

OTDR Optical time-domain reflectometry

PAA Phased array antenna

PBG Photonic bandgap

PBS Polarization beam splitter

PhC Photonic crystal

PIC Photonic integrated circuit

PM Phase modulator

PMF Polarization maintaining fiber

PMMA Poly-methyl-meta-acrylate

PRBS Pseudo-random bit sequence

PSS Phase shifter stage

RF Radio-frequency

RS Regenerator stage

RIN	Relative intensity noise
SBS	Stimulated Brillouin scattering
SCT	Separate carrier tuning
SFDR	Spurious-free dynamic range
SFL	Slow and fast light
SNR	Signal-to-noise ratio
SOA	Semiconductor optical amplifier
SOCF	Synthesis of optical coherence function
SPM	Self-phase modulation
SRS	Stimulated Raman scattering
TE	Transverse electric
TM	Transverse magnetic
TTD	True time delay
VNA	Vectorial network analyser
VOA	Variable optical attenuator
XGM	Cross gain modulation
XPM	Cross phase modulation

Contents

List of Figures

Index of tables

Chapter 1
Introduction

The possibility of using nonlinear optical methods to exercise unprecedented control over the propagation velocity of light through different media has been widely attracting increasing attention over the past years [1]. This research field, well-known by the name of slow and fast light (SFL), is currently being deeply stimulated by the outstanding progress in optical communications and all-optical signal processing.

Next-generation access networks will require solutions capable to perform optical tasks with not only high data rate and high throughput, but also low power consumption. Optical buffers and tunable delay lines are expected to become key devices for temporal storage as well as timing adjustment of optical packets [2]. However, the capabilities demanded by these envisioned practical tasks cannot be yet supported by the current SFL approaches. Nevertheless, the SFL impact awaits to be furnished in applications where its characteristics can unleash its entire potential.

In this context, one of the most exciting motivations lays in the SFL potential application to the framework of microwave photonics (MWP) [3, 4]. MWP accomplishes the generation, processing and transport functionalities of radio-frequency (RF), microwave and millimeter-wave signals directly in the optical domain. Thus, MWP brings a series of inherent advantages compared with the electronic signal processing in terms of reconfigurability, low loss, electromagnetic immunity (EMI), low weight and high degree of physical flexibility. Furthermore, several SFL device platforms can perform the integration of microwave photonic components and subsystems in photonic integrated circuits (PIC), which results in additional advantages related to low-cost, reliability and power consumption [5].

The generation of continuously tunable optical delays and phase shifts becomes a key element in a wide range of targeted MWP applications, among which one can quote the filtering of microwave signals, the synchronization of optoelectronic oscillators, the control of optically-fed phased array antennas, and future reconfigurable radio frequency front-ends, among others [6]. With these applications in view, large efforts are currently being accomplished so as to develop these basic MWP functionalities through different SFL effects [7].

1.1 Slow and fast light propagation

1.1.1 SFL physical principles

SFL effects lead to a control of the speed of a light signal in a particular dispersive device or medium. In this sub-section, two different ways to describe the light wave propagation, i.e. phase and group velocities, will be introduced.

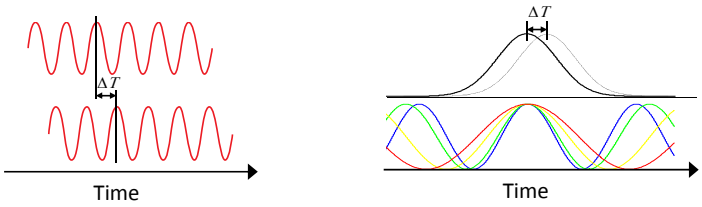

(a) (b)

Figure 1.1: (a) A monochromatic wave and (b) a pulse of light being delayed as they propagate through an optical dispersive medium.

Figure 1.1(a) shows a pure travelling sinusoidal wave comprised only by one angular frequency ω and propagated through a medium with refractive index n. Hence, the propagation velocity results described by the phase velocity v_p. In fact, this term is usually defined as the velocity at which particular points of constant phase travel through the medium for a plane wave, which is given as

$$v_p = \frac{\omega}{k} \equiv \frac{c}{n}, \tag{1.1}$$

being k the wave vector of the monochromatic signal and c the speed of light in vacuum. It must be noticed that the phase velocity indicates only how the phase of the monochromatic signal is delayed in the medium.

However, an optical pulse of light exhibits totally different properties when compared to a monochromatic signal. As Fig. 1.1(b) illustrates, a pulse can be thought of as resulting from constructive and destructive interference among various frequency components. At the peak of the pulse, the components tend to add up in phase and to interfere destructively in the temporal wings of the pulse. Actually, in a material with refractive index that is frequency-dependent, each of their frequencies propagates with different phase velocity, resulting in a temporally shift of the pulse with respect to the same pulse travelling through the vacuum. This shift is inversely proportional to the group index of the material n_g, which depends on the dispersion of the refractive index $dn/d\omega$. The fact that the pulse is temporally shifted implies that it is travelling at different velocity, known as the group velocity v_g, which is defined as

$$v_g = \frac{d\omega}{dk} = \frac{c}{n + \omega \frac{dn}{d\omega}} \equiv \frac{c}{n_g}. \tag{1.2}$$

Therefore, control of the group velocity relies on the dispersion of the refractive index. When the medium shows so-called normal dispersion ($dn/d\omega > 0$), the term slow light propagation is employed. In contrast, when the medium shows anomalous dispersion ($dn/d\omega < 0$), the case is referred to as fast light propagation.

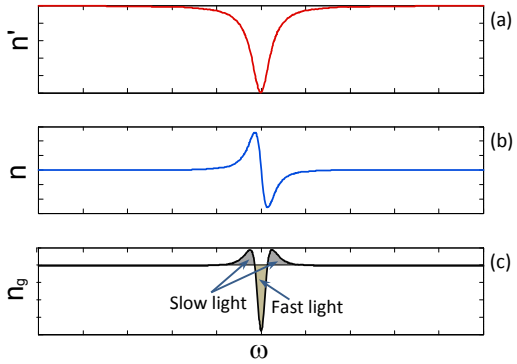

Figure 1.2: Relationship between a loss narrow-band resonance and the refractive index, governed by the Kramers-Kronig relations. (a) The imaginary part, (b) the real part and (c) the group refractive index as a function of the resonance angular frequency.

Through the Kramers–Kroenig relations, which link the real n and imaginary n' parts of the effective index by means of the Hilbert transforms [8], it is possible to understand the SFL effects produced in a medium which is traversed by an optical signal. These refractive index relations are illustrated in Fig. 1.2. As it is clearly observed, any gain/loss resonance induced in the imaginary part of the refractive index leads to a rapid variation of the real part in the vicinity of the resonance. An increase of the group refractive index will be understood as slow light propagation, while a decrease will be referred as fast light.

The n_g modifications nature can be very different depending on whether the SFL mechanism is based on the intrinsic optical properties of a material system (material dispersion) or based on structured optical materials (structural dispersion) [9]. Indeed, modifications of the material dispersion are achieved by means of an artificial manipulation of the absorption or amplification in the medium. The tunability flexibility of the v_g through a control parameter, for instance, the electrical current or the optical power, is the main advantage of the SFL platforms under this dispersion. [10]. In contrast, the structural dispersion is modified by a proper design of the structural properties of the optical waveguides. The main advantage relies on the fact that the energy velocity coincides with the group velocity, resulting in an enhancement of the nonlinear effects [10].

1.1.2 SFL device platforms

One of the pioneering examples of the use of material dispersion was accomplished in the late nineties through the effect of electromagnetically induced transparency

(EIT) in atomic gasses [11]. In this case, the light velocity was spectacularly slowed down to 17 m/s, equivalent to the speed of a bike, in the vicinity of the narrow-band ($\sim$ MHz) EIT resonance. However, the extreme environmental conditions (cryogenic temperatures) required to carry out this nonlinear effect, as well as its inherent narrow bandwidth spectral characteristic severely limited the range of applications within the telecommunication field. Since then, SFL research has flourished with a quest for enlarging the range of effects and media that can be exploited to the purpose.

An interesting physical mechanism for light speed control based on material dispersion at room temperature is that of coherent population oscillations (CPO) using solid crystals [12]. In that case, wave mixing between different spectral components of a signal leads to a change in the relative amplitude and phase of the spectral components and thereby the group velocity. Although this technique results in remarkable reduction of the group velocity, it seems still far from being acceptable for real application systems since it only operates at a very well-defined wavelength and its achievable time delay is harshly limited to around 10% of the signal duration. Among this, semiconductor waveguides have demonstrated a large four-wave mixing efficiency making them very suitable for CPO-based light control [13]. These waveguides appear as a promising technology because they can provide both very fast ($\sim$ hundreds of ps) electrically and optically controlled tunability over a bandwidth of several tens of GHz in a compact device.

Nonlinear effects in optical fibers have become a favorable underlying mechanism in variable optical group delay demonstrations, including stimulated Brillouin scattering (SBS) [14] and stimulated Raman scattering (SRS) [15]. Indeed, SBS-based SFL systems [14] have proved to be an unmatched and unprecedented flexible timing tool as a result of their unique spectral tailoring capability. Some of its inherent advantages include room temperature operation, high potential for large signal bandwidths and seamless integration in fiber optic communication systems. Besides, dispersion-compensating fibers (DCF) [16] have been successfully proposed as a means to implement tunable delays.

On the other hand, the strong modification of the transmission mode dispersion (structural dispersion) in photonic crystal (PhC) waveguides has been also exploited for light slow-down [17]. A key aspect offered by PhC waveguides is that they offer a large bandwidth and wavelength flexibility, unlike slow light schemes that interact with a material resonance. In addition, they become a promising approach for passive chip integration of SFL devices.

Last, fiber Bragg gratings (FBG) [18] and coupled cavities implemented by cascading several ring-type resonators [19] have also demonstrated relevant capabilities to control the speed of light in structured optical materials.

1.2 Tunable phase shifts and true time delays for MWP applications

The inherent advantages reported by the SFL devices in terms of broadband spectral behavior, low losses and tunable dispersion, among others, can be applied to perform microwave signal processing, and most particularly, to achieve continuous control of the phase or delay of the microwave/RF signals propagating in a MWP link.

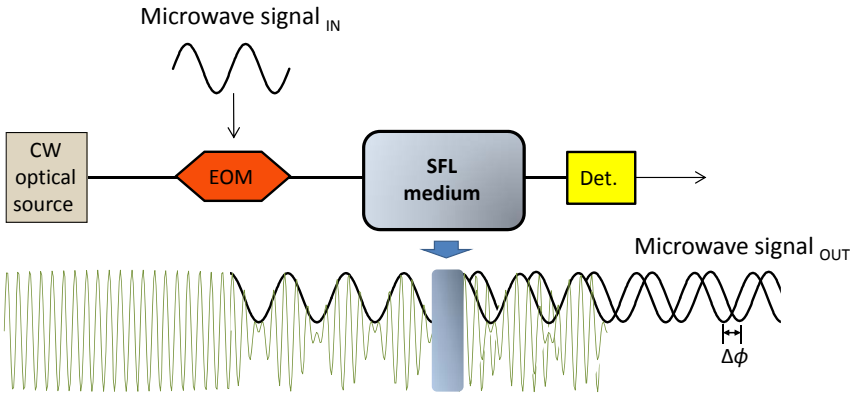

Figure 1.3: Basic implementation of a MWP link including a slow and fast light device.

Figure 1.3 sketches the basic architecture of a MWP link based on SFL effects. A continuous-wave (CW) optical source or laser is intensity modulated by a microwave signal. The SFL device processes the modulated carrier by changing the group velocity of the light propagating through the medium. Indeed, as occurs with pulses, each of the modulated signal frequency components will travel with a different phase velocity, resulting in an overall envelope time shift. After photodetection, this tunable time delay or advance is translated into a phase change $\Delta\phi$ in the monochromatic microwave signal.

The phase ϕ introduced by a given SFL medium can be expressed as

$$\phi = kL = \frac{\omega}{c} nL, \tag{1.3}$$

where L denotes the length of the SFL device. Thus, modification in the refractive index n of the medium are directly translated into phase changes. Through the dynamic control of this phase, SFL devices can perform two important MWP functionalities, tunable phase shifters and true time delays. The phase shifter approach is related to the possibility of achieving constant phase shifts with frequency, as Fig. 1.4(a) illustrates. However, in the case of true time delay (see Fig. 1.4(b)) the phase shift is linearly dependent to the modulating frequency.

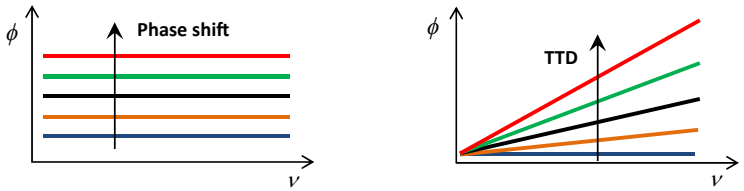

(a) (b)

Figure 1.4: Phase response of a tunable RF (a) phase shifter and (b) true time delay.

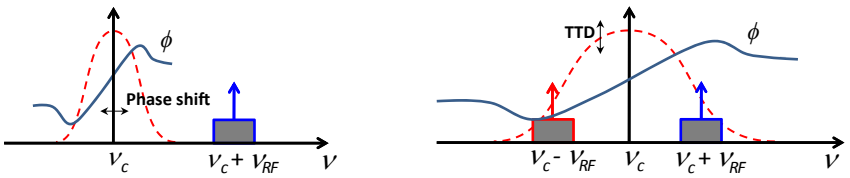

Figure 1.5: Implementation of a tunable (a) phase shifter and (b) true time delay in a SFL resonant medium.

In this context, the phase shifter approach is usually achieved by spectrally placing the optical carrier inside the resonance (see Fig. 1.5(a)) while the RF subcarrier stays outside. When beating occurs at the photodetector, the detected signal will experience a constant phase shift with frequency that is determined by the phase difference between the optical carrier and subcarrier. However, implementing TTD operation requires both the carrier and modulating sideband to be located inside the resonance, as illustrated in Fig. 1.5(b). Thus, all the spectral components will experience a linear phase change, proportional to a time delay. Either a variation in the spectral position of the optical carrier or a modification in the resonance provides the desired tunability of these MWP functionalities.

The previous concepts are now applied to exploit two major MWP applications, namely reconfigurable filters and optically-fed phased array antennas.

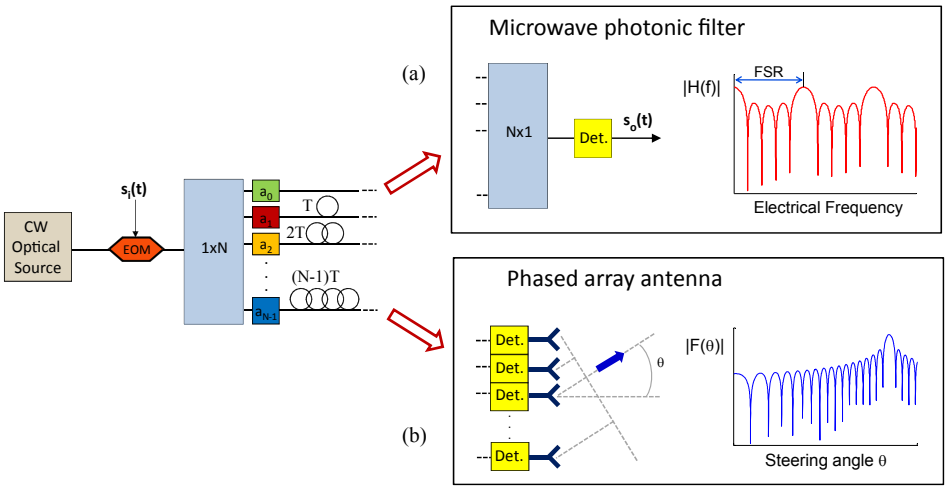

Figure 1.6: Layout and transfer function of a (a) generic microwave photonic filter and (b) optically-fed phased array antenna.

In particular, finite impulse response (FIR) filters [20] are based on combining at their output a finite set of delayed and weighted replicas or taps of the input optical intensity signal. The usual implementation of these filters in the context of MWP

follows the approach shown in Fig. 1.6(a). An input RF signal $S_i(t)$ is conveyed by the optical carrier and the composite signal is fed to a photonic circuit that first samples the signal in the time domain, using a $1xN$ optical coupler and an optical delay lines network, with the delay of the r_{th} tap being rxT, where T is referred to the incremental delay. The sampled signals are then weighted in phase and amplitude to provide the desired filter impulse response. Finally, the samples are recombined and RF converted by means of an optical detector producing the output RF signal $S_o(t)$. The electrical frequency response of such structure is given by

$$H(\nu) = \sum_{r=0}^{N} a_r e^{-i(2\pi r \nu T)}, \tag{1.4}$$

where a_r denotes the filter complex coefficients, which are implemented by optical components. Equation 1.4 identifies a transfer function with a periodic spectral characteristic whose frequency period is referred to as the filter free spectral range (FSR). The FSR is essentially inversely proportional to the time spacing between adjacent samples in the impulse response (FSR=$1/T$). So, dynamic control of T is basically required for the development of reconfigurable MWP filters, providing the FSR tunability. Nevertheless, in order to get resonance tunability while the FSR and spectral shape of the filter response keep unaltered, a phase shift ($\Delta\phi = 2\pi\nu T$) is preferable rather than a time delay T. These filters are usually performed in incoherent regime, in which the coherence length of the used optical source is shorter than T, since any possible optical interference caused by environmental condition such as temperature and mechanical variation can influence the filter impulse response.

However, in the case of optically-fed phased array antenna, the N delayed samples are RF converted by N photodiodes to feed N radiating elements, as illustrated in Fig. 1.6(b). The normalized angular far-field pattern of the radiated electric field, or antenna diagram $F(\theta)$, is given by the Fourier transform of the output electric field [21],

$$F(\theta) = \frac{1}{N} \sum_{r=0}^{N-1} a_r e^{-i2\pi r \nu \left(T - \frac{d}{c}\sin\theta\right)}, \tag{1.5}$$

where θ is the far field angular coordinate and d is the spacing between adjacent radiating elements. The complex coefficients a_r are in this case typically used for side-lobes reduction in the antenna far-field pattern. From Eq.1.5, the direction θ_0 of maximum radiated energy can be adjusted by tuning the incremental time delay T according to

$$T = \frac{d}{c}\sin\theta_0. \tag{1.6}$$

It is important to notice that the use of MWP phase shifters to perform the phased array tunability will inevitably induce beam squinting effects, where the main lobe of the radiation pattern will drift away from the desired angle with changes in operating frequency. This undesired effect limits the use of phased array antennas in broadband applications. On the contrary, true time delays can perform tunability and, at the same time, compensate for this beam squint effect [22].

1.3 Thesis objectives

This Ph.D. thesis has been fulfilled within the framework of the European Community's Seventh Framework Program (FP7/2007-2013) under the GOSPEL (GOverning the SPEed of Light) project. The research program proposed by GOSPEL focusses on the development and complete characterization of novel room temperature SFL technologies and their applications in the field of MWP. The different SFL mechanisms under consideration comprise linear and nonlinear semiconductor photonic crystal waveguides with position controlled embedded quantum dots, active semiconductor waveguides based on quantum dots, advanced engineered optical fibers and resonant-type devices based on silicon-on-insulator and III-V materials. In addition, some applications in which the project has been stimulated include true time delay antenna feed systems for radars, complex microwave filters and high spectral purity opto-electronic oscillators.

The main objective of this work has been related to the performance evaluation of current SFL device platforms to enable several tasks required in the MWP field with the added value of tunability and broadband operation. In particular, technologies such as SBS effects in fibers, FBGs, semiconductor and photonic crystal waveguides have been under study. From km to mm-scale, these device platforms represent the evolution towards PICs. Besides, the different approaches must be evaluated in terms of several figures of merit (FOM) so as to characterize their impact on the MWP link and also to find an optimal solution in order to implement basic MWP functionalities.

The described overall aim embraces different specific goals that should be properly accomplished:

1. Propose novel and more efficient SFL based approaches implemented by using the different technological platforms.

2. Develop analytical and numerical models to understand the physical processes governing SFL propagation on the different device platforms.

3. Implement photonic-based tunable phase shifts and true time delay functionalities in broad microwave and millimeter spectral bands by exploiting SFL effects in each technology.

4. Apply the proposed SFL-based approaches as key elements in the implementation of more complex signal processing tasks, such as, tunable and reconfigurable complex-valued multi-tap MWP filters.

5. Design new platforms to perform high effective distributed temperature and strain sensing systems.

6. Evaluate the performance of the developed microwave signal processors in the context of several FOMs, such as gain, noise degradation, nonlinear generation, loss, power consumption and size, among others.

1.4 Structure of the thesis

The content of this dissertation is addressed in four main chapters, being each of them adequately focused in one of the different SFL technological platforms embraced by the aforementioned overall objective.

Chapter 2 focuses on SBS effects in optical fibers for signal processing techniques in MWP links. A performance analysis of a tunable phase shifter and true time delay (TTD) line is presented for development of a two-tap reconfigurable MWP filter. The true time delay system is achieved by separately tuning the optical phase of the carrier. The SBS interaction in polarization maintaining fibers is evaluated to accomplish dynamic Brillouin gratings (DBG). In addition, an analytical model describing the phase induced by the DBGs is provided. In this way, four different schemes for the realization of MWP filters using these dynamic reflectors is experimentally addressed.

A distributed temperature and strain sensing system based on the continuous reflection of a short pulse along a weak FBG is addressed in chapter 3. The distributed capabilities of such a device are briefly discussed to perform basic MWP functionalities. Optical signal processing tasks including a tunable delay line and a photonic integrator are experimentally demonstrated.

In chapter 4, microwave phase shifting and true time delaying capabilities are evaluated using respectively CPO and cross gain modulating (XGM) effects in semiconductor optical amplifiers (SOA). An optical field model that contains the equations accounting for any general order of both harmonic and intermodulation distortions generated in a CPO-based phase shifter is provided. A complete analysis of the nonlinear distortion introduced in the phase shifter is addressed for cascaded structures comprising an SOA device under the CPO effect and an optical filtering stage. A novel fully-tunable 360° phase shifter implemented using only one SOA followed by a conveniently designed notch filter is also reported. A notch-type filter is demonstrated using this tunable MWP phase shifter. In addition, the performance of MWP phase shifters based on both the cascaded and single SOA approaches is theoretically and experimentally evaluated in terms of several FOMs. In particular, gain, noise and nonlinear distortion are characterized as a function of the phase tunability control mechanism.

The use of a highly dispersive PhC waveguide is demonstrated for implementing tunable TTD lines in chapter 5. A tunable multi-tap filter is provided by proper wavelength multiplexing of optical carriers. In addition, the PhC performance is evaluated in terms of several FOMs including issues concerning the power consumption, loss, tunability limitations, physical size and dispersion-related amplitude distortion.

The conclusions and future perspectives are presented in chapter 6. The most relevant features of the proposed SFL technologies in terms of several FOMs are discussed. A comparison attending the metric results is addressed so as to identify the most suitable medium for a given MWP task.

Chapter 2

SFL effects using stimulated Brillouin scattering for MWP applications

2.1 Introduction

The attractiveness underlying the use of the SBS effect in optical fibers for signal processing techniques in MWP links relies mainly on its inherent narrow-band nonlinear spectral characteristics [14]. As a consequence, SBS allows the transmitted electrical signal to be processed directly in the optical fiber used as the transmission medium. In addition, it must be kept in mind that, up to date, SBS has been a favorable signal processing mechanism thanks to its robustness, simplicity of implementation and moderate pump power in standard fibers at room temperature [23] compared with other nonlinear effects in silica optical fibers [16, 24].

Different MWP applications in which SBS has been widely proposed include the selective single sideband amplification of modulated waveforms [25], the photonic implementation of microwave phase shifters [26] and FIR filters having negative and complex weights [27], and the realization of advanced modulation formats [28]. SBS also serves as the gain mechanism in Brillouin fiber lasers [29], in sharp tunable optical filters [30], and even in all-optical data storage [31]. Last, among the wide diversity of optical delay line schemes that have been reported over the last years [13, 32–34], SBS has been devised as one potential approach to generate continuously tunable signal delays [35]. However, the apparent perfect true time delay generated by such slow light mechanisms suffers from two major obstacles: nearly finite delay time-signal bandwidth product and strictly limited operating frequency. This drawback implies that only modest maximal time delays can be expected at high RF frequencies. Besides, the operating frequency is essentially limited by the bandwidth of the induced optical resonance, which prevents its complete implementation for practical applications in microwave photonics.

To overcome these limitations, a theoretical solution has been proposed by separate carrier tuning the optical phase of the carrier [36]. The SCT technique predicts that significant improvement for the generation of TTDs can be achieved by separately performing a MWP phase shifter and slow light system. Numerical TTDs in the order of hundred of ps have been reported using microresonators [36]. However, this value can be improved up to few ns through the dispersion induced by the narrow-band SBS resonance. Thus, SBS effect becomes a good candidate for SCT technique when few ns of TTD are targeted.

On the other hand, a more flexible alternative has been proposed to create long variable optical delays of broadband signals [37, 38]. It makes use of SBS interaction between two pumps that are co-polarized along one principal axis of a polarization maintaining fiber (PMF) [39–41]. The interaction generates a so-called DBG, which in turn could reflect incoming signal waves that are polarized along the orthogonal principal axis. DBGs are essentially optical wave reflectors that can be created at any preset position along the entire PMF. The phase of the reflected waveform is inherently stable, since Brillouin reflections are phase conjugated [8]. Therefore, variable-position DBGs become an attractive platform for the construction of MWP filters. Other applications include time reversal of pulse trains and all-optical calculus such as differentiators and integrators [42–44].

In this chapter, a complete analysis of the performance of a tunable phase shifter and TTD will be presented for development of a two-tap dynamic microwave filter based on SBS effects in standard fibers. The photonic phase shifter, based on the combined use of SBS signal processing and optical single sideband (OSSB) modulation [26], will be used as a phase compensator for the TTD system. In addition, numerical calculations of the phase induced by the DBGs will be provided. In this way, an alternative approach will be proposed for generating broadband true time delays and phase shifts. Besides, four different schemes for the realization of MWP filters using these dynamic reflectors will be demonstrated. The location of the DBGs along a PMF will be controlled by proper temporal coding on the pump waves. The first configuration will be a simple notch-type Mach-Zehnder (MZ) approach, whereby the delay imbalance between the two arms is tuned using one movable grating along the PMF. A multi-tap performance will be demonstrated in the second configuration, where the filter is created through the combined reflections from multiple DBGs along a PMF. In the next configuration, double generation of DBGs will be deployed for improving the frequency limitations of previous implementations. Local gratings will be built up using pulsed pumps in the three first approaches. However, such gratings decay according to the finite acoustic lifetime [40] and must be periodically refreshed. To overcome this limitation, a novel technique for the generation of localized and stationary DBGs will be used in the third implementation of MWP filters. The method relies on phase modulation of the two pump waves by a common, high-rate pseudo-random bit sequence (PRBS) [45].

Different collaborations between several GOSPEL partners (the optical and quantum communications group (OQCG) at UPV in Spain, the group for fiber optics (GFO) at EPFL in Switzerland and THALES in France) have been fulfilled so as to obtain the achievements of this chapter. First, a week collaboration between UPV and EPFL in the OQCG laboratory. Next, another short collaboration between UPV, EPFL and THALES carried out in Switzerland. Finally, a collaboration between UPV and EPFL during a three month stay at GFO.

2.2 Principle of operation

The effect of SBS can be described as the interaction of two counter-propagating waves that are detuned in frequency, a strong pump wave and a typically weak Stokes wave. The process is schematically depicted in Fig. 2.1(a). The pump wave and the Stokes wave counter-propagate in the fiber creating a moving interference pattern that induces an acoustic wave via the electrostriction effect. The acoustic wave, in turn, is accompanied by a traveling grating of refractive index variations, due to the electrostriction effect [8]. The SBS interaction is efficient only when the difference between the optical frequencies of the pump and signal waves is near (below to 30 - 50 MHz) to a fiber-dependent parameter, the Brillouin shift ν_B, which is of the order of 10 - 11 GHz in silica fibers at room temperature [8]. An input signal whose frequency is ν_B lower than that of the pump wave (Stokes) experiences SBS amplification, as illustrated in Fig. 2.1(b). If the input signal frequency is ν_B above that of the pump wave (anti-Stokes), SBS-induced signal attenuation is obtained instead.

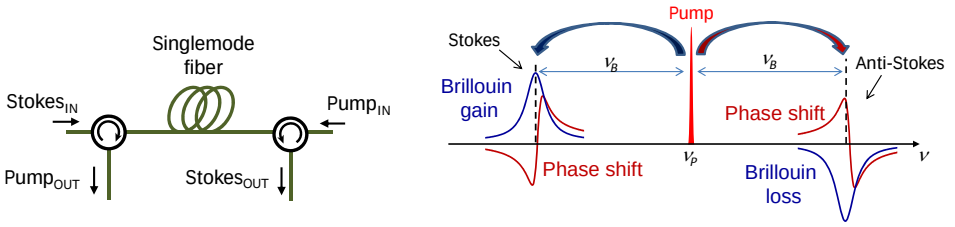

(a) (b)

Figure 2.1: (a) Schematic diagram of the SBS process. (b) Generation of Brillouin gain and loss spectra due to the nonlinear SBS interaction between a pump wave and a Stokes wave.

Assuming a frequency detuning $\Delta\nu$ of the Stokes wave from the SBS gain line center deviation from ν_B, the spatial evolution of the electric fields of the pump E_P and Stokes E_S waves under SBS is described by the following coupled equations [46],

$$\begin{aligned} \frac{\delta E_P}{\delta z} &= -\frac{g_B}{2A_{eff}} \frac{|E_S|^2}{1+2i\left(\frac{\Delta v}{\Delta v_B}\right)} E_P - \frac{\alpha}{2} E_P \\ \frac{\delta E_S}{\delta z} &= \frac{g_B}{2A_{eff}} \frac{|E_P|^2}{1-2i\left(\frac{\Delta v}{\Delta v_B}\right)} E_S + \frac{\alpha}{2} E_S, \end{aligned} \tag{2.1}$$

where A_{eff}, $\Delta\nu_B$, and α denote the mode effective area, Brillouin gain bandwidth and optical intensity attenuation coefficient, respectively. On the other hand, the Brillouin gain coefficient is given by

$$g_B = \frac{2\pi n^7 p_{12}^2}{c\lambda_p^2 \rho \Delta\nu_B v_A}, \tag{2.2}$$

being n the refractive index, λ_p the pump wavelength, p_{12} the longitudinal elasto-optic coefficient and v_A the acoustic velocity in the fiber. In silica fibers, the measurable value of g_B is approximately $2.5 \cdot 10^{-11}$ m/W.

The Stokes gain and loss versus the frequency detuning from ν_B are characterized in Fig. 2.2(a). These results have been represented for different pump powers and for a fixed Stokes optical power of 1 μW. The following typical parameters were assumed: $\Delta\nu_B = 30$ MHz, $\alpha = 0.2$ dB/km and $A_{eff} = 30 \cdot 10^{-12}$ m^2. It is clearly noticeable that by increasing the pump power the gain enters in saturation and its spectrum becomes broader than the Lorentzian profile corresponding to the Brillouin gain coefficient. This can be explained by the depletion suffered by the pump wave due to the transfer of power to the Stokes wave. On the other side, the SBS-induced loss resonance is mathematically described in the same manner as the Stokes scattering. The only difference is that the sign of Brillouin gain is negative and the frequencies of the two waves are swapped. It exhibits a similar behavior compared with the Brillouin gain spectrum, however the spectral shape of the Brillouin loss spectrum keeps the Lorentzian profile even for high pump powers. The phase shifts associated to the SBS gain and loss spectra are depicted in Fig. 2.2(b). These curves are characterized by a maximum and a minimum value of phase shift symmetrically located around the curve center. The gain flattening effect for saturation operation is translated to the nonlinear phase shift. For linear operation the maximum and minimum of the phase shift curve match the Brillouin linewidth $\Delta\nu_B$, but their frequency difference increases as the gain becomes more saturated.

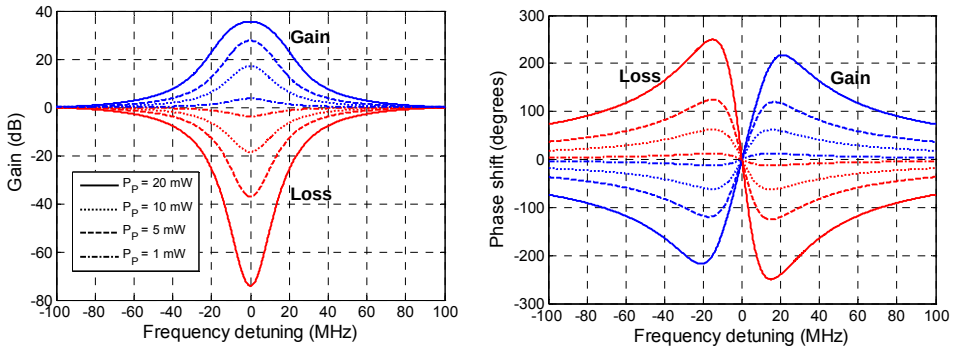

(a) (b)

Figure 2.2: (a) Brillouin gain (blue curves) and loss (red curves) spectrum and (b) their corresponding phase shift vs. the frequency detuning between Stokes and Brillouin frequency.

2.3 Phase shifter based on double SBS generation

Figure 2.3 sketches the principle behind the SBS-based MWP phase shifter [26]. It is based on counter-propagating an OSSB modulated optical carrier with two pump waves, Pump$_A$ and Pump$_B$, in an optical singlemode fiber to generate simultaneously Brillouin gain and loss spectra that modify the optical carrier [47]. The OSSB modulation is required since this modulation format provides a mapping between the optical and the electrical domains, i.e. the induced amplitude and phase changes in the optical spectrum are directly translated to the electrical domain [48]. By adjusting

the relative frequency difference among the three waves, the Brillouin gain and loss experienced by the carrier can be compensated, and also the phase shifts provided by both spectra can be doubled. The bandwidth of this phase shifter is just limited by the bandwidth of the optical transmitter and receiver deployed, and it can provide a phase shift that can be dynamically tuned in a range greater than 360°. It must be noticed that the modulation sideband is only altered as long as the modulation frequency matches the Brillouin gain / loss resonance. These resonances not only appear at few megahertz from the optical carrier but also at $\nu_C + 2\nu_B$ and $\nu_C - 2\nu_B$ since each pump wave generates gain and loss spectra.

Three coupled differential equations for the complex amplitudes of the Pump_A, Pump_B and carrier waves are used to describe this double interaction [46],

$$\begin{aligned} \frac{\delta E_{P_{A,B}}}{\delta z} &= \left[-\frac{g_B}{2A_{eff}} \frac{|E_C|^2}{1+2i\left(\frac{\Delta v}{\Delta v_B}\right)} - \frac{\alpha}{2} \right] E_{P_{A,B}} \\ \frac{\delta E_C}{\delta z} &= \left[\frac{g_B}{2A_{eff}} \frac{|E_{P_A}|^2}{1-2i\left(\frac{\Delta v}{\Delta v_B}\right)} - \frac{g_B}{2A_{eff}} \frac{|E_{P_B}|^2}{1+2i\left(\frac{\Delta v}{\Delta v_B}\right)} + \frac{\alpha}{2} \right] E_C. \end{aligned} \tag{2.3}$$

The solution of these coupled equations under small pump depletion conditions shows that the Brillouin gain and attenuation experienced by the carrier nearly compensates, while, at the same time, the phase shifts provided by both interactions are added. Besides, it is found that this phase shift can be tuned adjusting the frequency detuning among these optical waves.

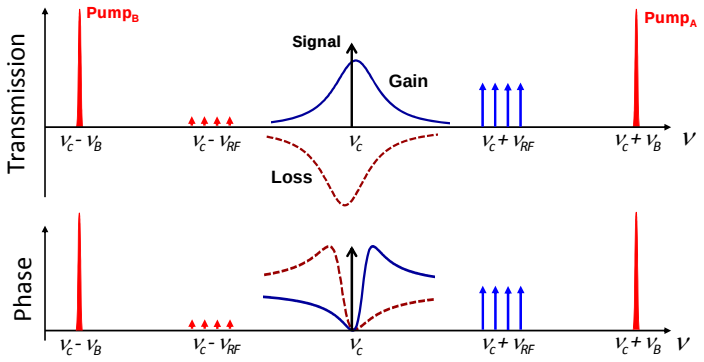

Figure 2.3: Principle of operation for implementing a full microwave phase shifter based on the SBS processing of the optical carrier and single sideband generation.

The aforementioned technique has been experimental validated employing the schematic layout depicted in Fig. 2.4. A 10-km-long dispersion shifted fiber (DSF) was used as a Brillouin gain medium and the Brillouin characteristics of this fiber were measured, showing a Brillouin shift ν_B of 10.71 GHz and an SBS gain bandwidth $\Delta\nu_B$ of $\sim$ 30 MHz. The output of a commercial distributed-feedback laser-diode (DFB-LD) operating at 1551 nm was employed as a light source to generate the microwave signal and two Brillouin pumps using two wideband electro-optic modulators (EOM). High frequency stability between the signal and the two Brillouin pumps is obtained in this way [49]. The laser source was then split in two arms. On the signal branch,

the light was externally modulated at the operating frequency ν_{RF} using the EOM_1 driven by the vectorial network analyzer (VNA) RF output. In order to operate at broadband frequencies and additionally accomplish single sideband generation, both the carrier and higher sideband were selected by using an arrayed waveguide grating (AWG) band-pass filter with more than 50 GHz bandwidth and $\sim$ 40 dB rejection band. Then this single sideband modulated signal was delivered into the DSF.

The light from the second branch was modulated through the EOM_2 at the RF frequency $\nu_B + \Delta\nu$. The EOM_2 was biased to suppress the optical carrier. The erbium-doped fiber amplifier (EDFA) and the tunable attenuator assured the optical power level of the pump waves, which in this technique was properly set at 10 dBm. The higher and lower frequency sidebands of the pump wave led to Brillouin gain and loss resonances, respectively, shifted by $+\Delta\nu$ and $-\Delta\nu$ with respect to the carrier frequency, with nearly identical depth and spectral shape. Therefore, the amplitude of the carrier must remain almost constant since the gain and loss for the carrier is mutually canceled out, while the associated optical phase shift imparted on the carrier is doubled, as illustrated in Fig. 2.3.

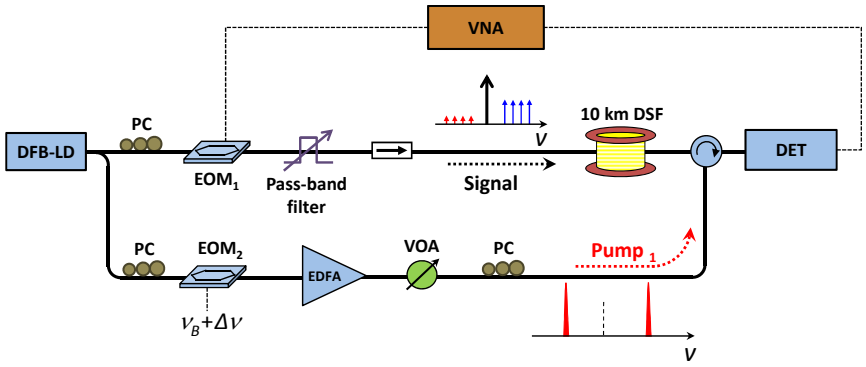

Figure 2.4: Schematic diagram for the generation of a broadband tunable phase shifter, based on SBS.

Figures 2.5(a) and 2.5(b) illustrate the experimental and calculated results for the RF phase shift and power variation, respectively, as a function of the modulation frequency that determines the spectral separation of the pump waves from the optical carrier. The RF tone modulating the EOM_1 was set at 20 GHz. The numerical results were accomplished by solving the differential coupled equations shown in Eq. 2.3 using the Runge-Kutta method. A very good agreement is observed. More than 360° phase shift was achieved simply by tuning the RF tone modulating the EOM_2, which actually was centered at 10.71 GHz, only 22 MHz. The OSSB modulation scheme assures that the carrier phase shift is directly derived from the RF phase shift. Only 2 dB of RF power variation is observed when the phase shift is tuned. Ideally, the gain and loss of the generated SBS spectra would perfectly compensate each other. However, this happens just for a perfectly Lorentzian Brillouin spectral shape and for a non-depleted gain spectrum (see Fig. 2.2(a)).

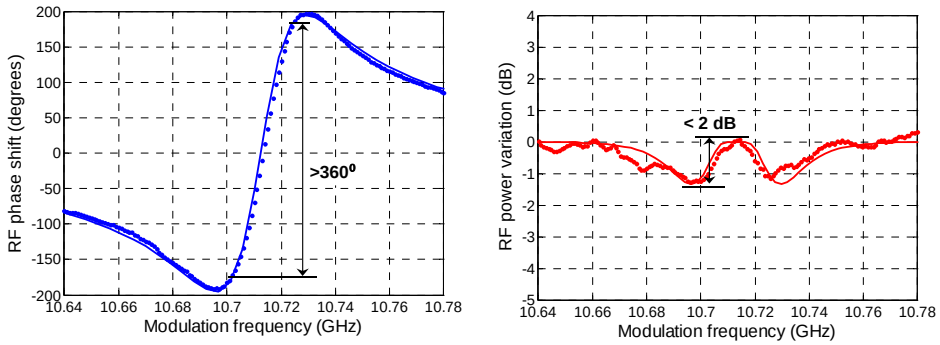

(a) (b)

Figure 2.5: Measured (markers) and calculated (solid curve) (a) phase shift and (b) power variation of the RF signal as a function of the modulation frequency in EOM_2.

On the other hand, Fig. 2.6 depicts the frequency response of the photonic phase shifter by tuning the modulation frequency, i.e. the Brillouin frequency shift, from 10.7 to 10.722 GHz. The frequency response of the phase shift is almost flat, but it displays a small ripple attributed to the frequency response of the band-pass filter deployed in the setup. Nevertheless, a sharp phase change is observed at ~ 21.4 GHz, which correspond to $\nu_C + 2\nu_B$ where the Brillouin loss resonance from the $Pump_1$ takes place. However, it is important to mention that the bandwidth of this resonance is only restricted to few tens of MHz. This technique has been previously confirmed from 1 to 18 GHz [26]. Here, an operational bandwidth up to 40 GHz is demonstrated, which in turn is just limited by the bandwidth of the modulator, detector and band-pass filter employed.

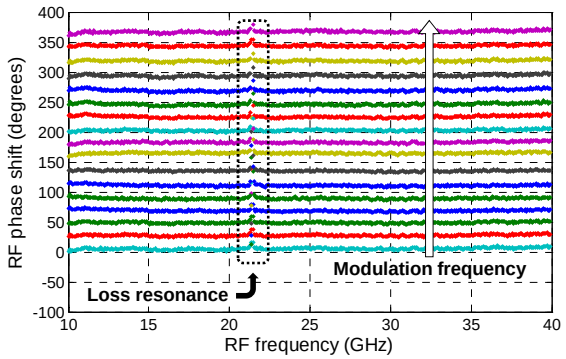

Figure 2.6: Measured RF phase shift as a function of the RF frequency for different modulation frequencies in EOM_2.

2.4 True time delay line based on SBS and separate carrier tuning

In general, TTD can be simply achieved through the dispersion induced by a single broadband resonance centered on ν_C, with full width at half maximum (FWHM) of $2\nu_{RF}$, as illustrated in Fig. 2.7(a). This way a constant group delay and linear phase shift with respect to the microwave frequency are obtained. However, in principle, this configuration shows a critical limitation since the true time delay generated by the resonance-induced dispersion only applies within the linear zone of the phase shift, which limits the microwave signal frequency to the resonance bandwidth.

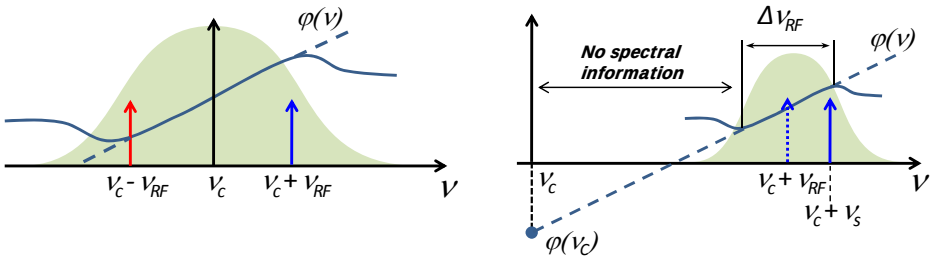

(a) (b)

Figure 2.7: (a) Classical true time delay approach in MWP. (b) Separate carrier tuning principe to correctly operate true time delay over the RF signal bandwidth simply by controlling dispersion properties, separately at carrier frequency and signal bandwidth.

One of the main drawbacks of the dispersion induced by the Brillouin resonance generation is its relative narrow bandwidth, which prevents its use in high frequency TTD devices. However, this bandwidth limitation can be overcome using the so-called separate carrier tuning (SCT) approach in a OSSB modulation system [36]. The concept is illustrated in Fig. 2.7(b) where an OSSB signal comprises an optical carrier at frequency ν_C and a modulation sideband at frequency $\nu_C + \nu_{RF}$. Here, a spectrally broadened Brillouin pump induces a broadband resonance centered at $\nu_C + \nu_{RF}$. Thus, the RF signal at ν_S experiences a phase shift $\varphi(\nu_S)$, which depends linearly on the RF signal frequency in a spectral bandwidth $\Delta\nu_{RF}$ centered on ν_{RF},

$$\phi(\nu_S) = 2\pi\,(\nu_S - \nu_{RF})\,\tau_S, \tag{2.4}$$

where the signal group delay τ_S is given by

$$\tau_S = \frac{1}{2\pi}\frac{\partial\phi}{\partial\nu_S}\bigg|_{\nu_S=\nu_{RF}}. \tag{2.5}$$

Typically, in high frequency systems, the RF signal has a finite bandwidth $\Delta\nu_{RF}$ of $\sim 10\%$ of the operating RF frequency ν_{RF}. TTD operation implies a constant group delay over the entire frequency range including the carrier and the modulation

sideband. Since no information is carried in the major part comprised in the large spectral range between the carrier frequency and the modulation sideband centered on the RF signal, the requirement of constant group delay across the entire bandwidth can potentially be relaxed across this region. The RF group delay can be expressed as

$$\tau_{RF} = \frac{\phi(\nu_C + \nu_{RF}) - \phi(\nu_C)}{2\pi\nu_{RF}}. \tag{2.6}$$

TTD operation is simply achieved by calculating the phase shift necessary to make signal and RF group delays match,

$$\tau_{TTD} = \tau_S = \tau_{RF}, \tag{2.7}$$

since the phase shift at the center of the Brillouin resonance $\varphi(\nu_{RF})$ is zero. This situation can be effectively realized by separately managing the dispersion properties at the carrier frequency and around the signal bandwidth, as shown in Fig. 2.7(b). Indeed, the required carrier phase offset $\varphi(\nu_C)$ so as to satisfy the TTD operation is not constant and varies with the generated delay according to

$$\phi_{offset} = -2\pi\nu_{RF}\tau_S. \tag{2.8}$$

It is important to mention that for the case of optically-fed phased array antenna systems [21], the consequences of this phase offset translates into the emission angle of maximum radiated energy,

$$\sin(\theta_0) = \frac{\nu_S - \nu_{RF}}{\nu_S} \times \sin(\theta_0)|_{TTD}, \tag{2.9}$$

where $\sin(\theta_0)|_{TTD}$ stands for the true time delay situation with a constant phase offset. In this case, the scanning angle θ_0 will depend on ν_S (beam squint). In addition, when compared to a true time delay system, typically hundred times larger delays will be required to provide the same steering angle θ_0.

This SCT architecture not only avoids these beam squint problems, but also it shows two crucial advantages: first, it is independent on the operating RF frequency since the optical resonance can be flexibly displaced at any desired RF frequency; second, it can produce a large TTD with a proper bandwidth at high frequency RF signals since the signal bandwidth of interest is substantially lower than the RF signal frequency.

The SCT concept has been experimentally demonstrated using the schematic diagram depicted in Fig. 2.8, in which two distinct Brillouin slow light systems are basically combined. A 20-km-long DSF was used as a Brillouin gain medium. The output of a commercial DFB-LD was used to feed the TTD system. The laser source was split in three arms. The first branch was used for generating the RF signal. The pump wave required to perform the SBS-based phase shifter (Pump_1) was generated in the second arm. Last, the third branch was deployed for inducing the signal group delay through Pump_2. Figure 2.9 illustrates the optical frequency spectra of these waves as well as the resonances induced by the pump waves.

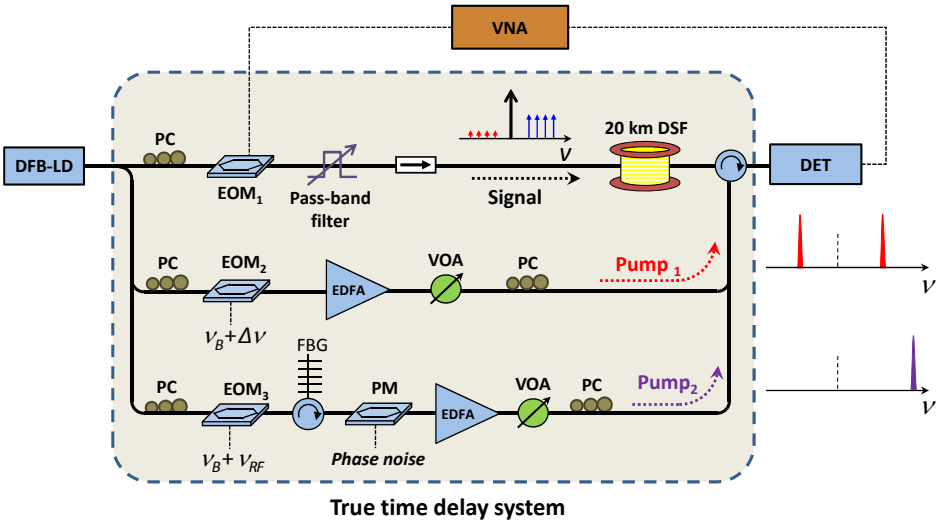

Figure 2.8: Schematic diagram for the generation of tunable true time delay based on SBS and the separate carrier tuning method.

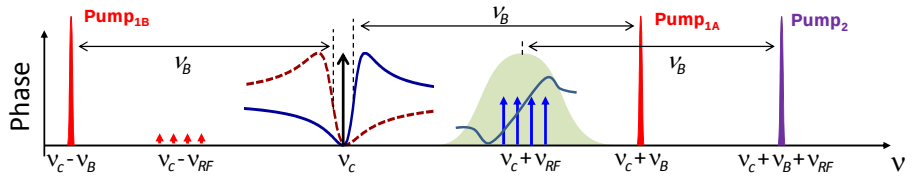

Figure 2.9: RF signal and pumps optical frequencies for implementing tunable true time delay, based on SBS generation and separate carrier tuning.

The lower branch was modulated at $\nu_B + \nu_{RF}$ using EOM_3 driven by an RF synthesizer, and the carrier was completely suppressed by applying an adequate bias to the EOM. Only the higher frequency sideband was selected using an FBG operating in reflection to be used as Pump_2. The pump wave was then strongly boosted using an EDFA to generate strong dispersion around RF signal, thus producing sufficient group delays for microwave signals. The optical power of Pump_1 was controlled using a variable optical attenuator to precisely adjust the amount of group delay. Moreover, its state of polarization was controlled to match the state of signal polarization before entering into the DSF, so as to maximize the Brillouin interaction. The optical phase of Pump_1 was externally modulated through an external electro-optic phase modulator (PM) so as to broaden its power spectrum. Actually, if the linewidth of the pump wave is not negligible with respect to the Brillouin linewidth ν_B, the effective Brillouin gain coefficient can be obtained by the convolution of the pump power spectrum $P(\nu)$ with the inherent Brillouin gain coefficient of the fiber $g_B(\nu)$ [50],

$$g\left(\nu_{eff}\right) = P\left(\nu\right) \otimes g_B\left(\nu\right). \tag{2.10}$$

So, the spectral width of Pump_1 in the output of the modulator was simply extended by increasing the amplitude of white noise applied to the PM.

The OSSB signal and Pump_1 waves generated in the upper and middle branch, respectively, follow the same principle to that described in Fig. 2.4 for the phase shifter approach. The carrier to the Pump_1 resonance frequency detuning $\Delta\nu$ was accurately adjusted so as to induce the proper phase shift to ensure Eq. 2.7. As a result, it makes possible to generate correct true time delay for the whole signal bandwidth while dispersion across the entire bandwidth is no longer required unlike typical slow light systems. As it has been previously shown in Fig. 2.6, since this optical phase shift is imparted on the carrier, the corresponding phase shift of the electrical signal is therefore constant with respect to the RF frequency. As a periodic wave, the adjustment of the optical carrier phase $\varphi\left(\nu_C\right)$ can be performed modulus 2π. A 360° tunability of the optical carrier is then sufficient to achieve TTD operation. After detection, the delayed RF signal was measured using a VNA.

As previously described, the SCT performance basically consists in two Brillouin systems: an SBS-based phase shifter [26], which is responsible for tuning the carrier phase shift, and a SBS-based delay line, which controls the microwave subcarrier delay by changing the SBS pump power. Then the electrical phase transfer function of the SCT system can be expressed as

$$H\left(\nu\right) = e^{-i\phi_{offset}} e^{-i2\pi(\nu-\nu_{RF})\tau_S}. \tag{2.11}$$

Figures 2.10(a) and 2.10(b) show respectively the gain and phase variations of the RF signal as a function of the signal frequency swept in the vicinity of the Brillouin resonance induced by Pump_2. These results were obtained for a fixed optical carrier phase shift while the pump power of the SBS delay line was varied from 5 to 110 mW. The SBS gain spectrum was centered at 6 GHz above the optical carrier frequency. It is clearly observed that, for each pump power, the RF phase shift exhibits a linear dependence on shift as a function of RF frequency, and also a moderate amplitude change within $\sim$ 100 MHz bandwidth. It was only limited due to instrumental issues in terms of available power and bandwidth of the white noise. Within this bandwidth, the delay as defined by Eq. 2.5 varies from 0.5 to 8 ns while the SBS pump power is increased.

Figure 2.11(a) depicts the phase offset as a function of the delays shown in Fig. 2.10(b). For true time delay operation, the optical carrier phase shift must be adjusted for each delay in order to finally obtain a constant phase offset with respect to the delay. Figure 2.11(b) illustrates the phase shift results versus the RF frequency when the phase offset is properly adjusted. The linear regions of the phase curves have been extrapolated down to the origin of frequencies. The figure inset shows a zoom of the phase measurement within the Brillouin spectral bandwidth for 4 ns delay.

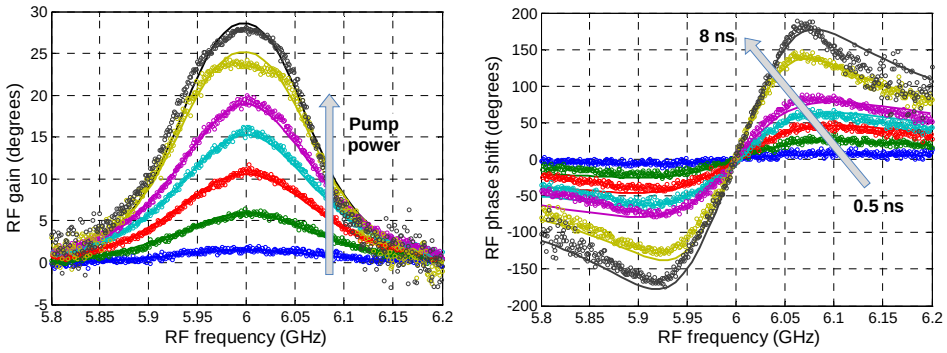

(a) (b)

Figure 2.10: Measured (markers) and calculated (solid curves) (a) gain and (b) phase shift of the RF signal as a function of RF frequency when increasing the Brillouin pump power from 5 to 110 mW.

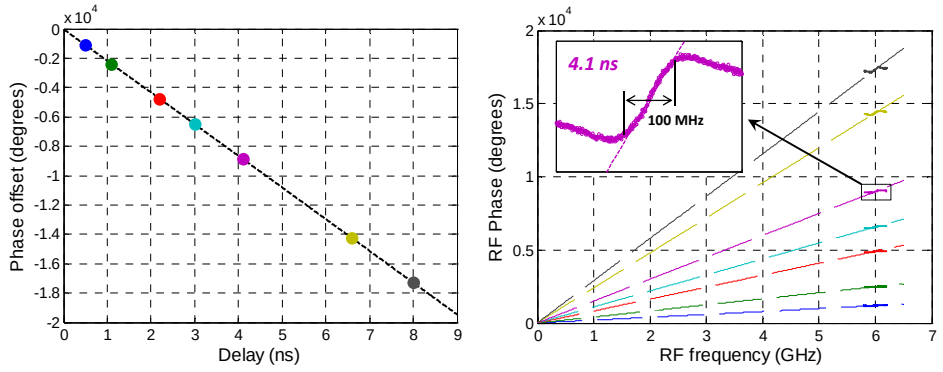

(a) (b)

Figure 2.11: (a) SBS-SCT based true time delay. For delays from 0.5 to 8 ns, the optical carrier phase shift is adjusted to ensure a constant extrapolated phase offset at the origin of RF frequencies. (b) Associated phase offset as a function of the delay.

On the other hand, Fig. 2.12(a) illustrates the modulus 2π function of the phase offset as a function of the applied delay corresponding to Fig. 2.10(b) data. Besides, Fig. 2.12(b) shows the phase of the detected RF signal as a function of the RF frequency while the optical carrier phase shift is tuned using the SBS-based phase shifter. The pump power of the SBS delay line (Pump_2) was fixed, corresponding to a 8 ns delay. 2π phase tunability was achieved, which is an essential requirement to compensate any value of mod (ϕ_{offset}). The SCT delay line therefore operates as a TTD element, providing a tunable TTD up to 8 ns, within an instantaneous RF bandwidth of 100 MHz. The operating frequency of 6 GHz was in this case limited by equipment availability, but the SBS-based SCT technique can be in principle applied at any operating frequency.

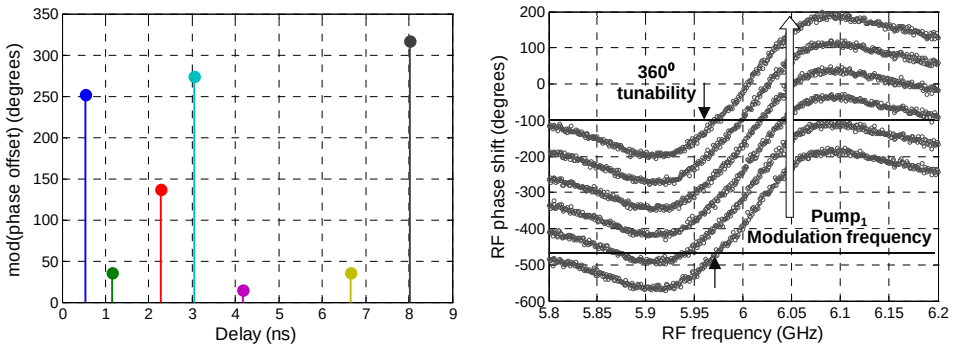

(a) (b)

Figure 2.12: (a) Modulus 2π of the phase offset as a function of the delay for the measured Brillouin time delays. (b) Tuning of the optical carrier phase shift when the Brillouin time delay is fixed at 8 ns.

2.5 MWP filter using SBS effects

The TTD concept described in section 2.4 is now applied for a major MWP application, FIR filters [20]. In a multi-tap complex coefficient filter, the separate carrier tuning technique not only enables to independently adjust the elementary delay T between adjacent filter taps, but also the phase of the complex coefficients a_r. On the one hand, the frequency detuning between Pump_{1A} and Pump_{1B} waves with respect to the optical carrier (see Fig. 2.9) allows for the phase shifter tunability (φ_{offset}), which means a change in the complex coefficients, $a_r \rightarrow a_r \times e^{ir\phi_{offset}}$. Then a homothetic transformation of the filter spectral response, described in section 1.2, is obtained,

$$H'(\nu) = \sum_{r=0}^{N-1} a_r e^{ir\phi_{offset}} e^{-2i\pi r\nu T} = \sum_{r=0}^{N-1} a_r e^{-2i\pi r\left(\nu - \frac{\phi_{offset}}{2\pi T}\right)T} = H\left(\nu - \frac{\phi_{offset}}{2\pi T}\right). \tag{2.12}$$

On the other hand, the influence of the Brillouin resonance centered at $\nu_C + \nu_{RF}$ induces a signal group delay τ_S, which yields a FSR change. Therefore, the filter response can be expressed as

$$H'(\nu) = \sum_{r=0}^{N-1} a_r e^{-i2\pi r(\nu T + (\nu - \nu_{RF})\tau_S)} = \sum_{r=0}^{N-1} a_r e^{-i2\pi r\left(\nu + \frac{(\nu-\nu_{RF})\tau_S}{T}\right)T} = H\left(\nu + \frac{(\nu-\nu_{RF})\tau_S}{T}\right). \tag{2.13}$$

This way the filter is fully reconfigurable: its central frequency can be adjusted by Eq. 2.12, while its FSR can be changed through Eq. 2.13.

The basic configuration of a notch-type incoherent MWP filter is performed by a two tap structure [4, 51, 52]. Figure 2.13 schematically depicts the experimental setup of a SBS-based tunable filter. Two distinct and mutually incoherent DFB-LD were deployed in order to do not limit the minimum time delay (T) of the filter. Hence, it made possible to obtain a higher FSR for the filter. Besides, the spectral difference between both lasers was properly adjusted so as to avoid any signal distortion caused by the beating frequency between the lasers. Light output from DFB-LD$_1$ was delivered to the tunable TTD system, based on SBS as described in the previously section. On the other side, the DFB-LD$_2$ output was fed to an EOM and propagated through a fixed optical path to provide the targeted FSR of the filter. The two branches of the MWP filter had a path imbalance of 7.5 m, corresponding to $T = 37.5$ ns. Both light outputs were modulated by the output port of a common VNA and recombined to mutually interfere. The amplitude and phase of the photodetected RF signal was monitored by the input port of the VNA to perform the filter transfer function.

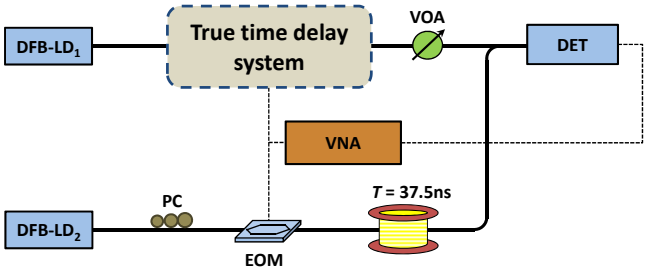

Figure 2.13: Experimental layout of dynamically reconfigurable microwave photonic filter based on SBS.

According to Eqs. 2.11 and 1.4, the frequency response of the two-tap notch filter is given by

$$H(\nu) = a_0 + a_1 e^{i(\phi_{offset} - 2\pi\nu T_0 - 2\pi(\nu - \nu_{RF})\tau_S)}, \tag{2.14}$$

where ν_{RF} corresponds to the RF central frequency (6 GHz in this case). In particular, a_0 and a_1 determine the extinction ratio (ER) of the notch filter, which is given by $ER = (1+\kappa)^2 \Big/ (1-\kappa)^2$, being κ the ratio between them.

As it is clearly observed from Fig. 2.10, the linear RF phase dependence as a function of RF frequency is accompanied by a amplitude change of few dBs within 100 MHz bandwidth. The largest delay for achieving a moderate amplitude change between the filter taps, and thus a good performance in terms of ER, was 7 ns.

First, in order to get the tunability of the FSR, the Brillouin time delay was tuned in the upper branch of the filter. Figure 2.14 illustrates the frequency response of a the two-tap MWP filter when the Pump$_2$ power is adjusted to generate 0.5 ns (blue), 4 ns (red) and 7 ns (black) time delays. This figure depicts the case in which the phase of the optical carrier is kept unaltered. The delays resulting from the Brillouin generation added to that fixed path delay yielding a total delay imbalance between the two filter taps of 38 ns, 41.5 ns and 44.5 ns, corresponding to a FSR

of 26.3 MHz, 24.1 MHz and 22.5 MHz, respectively. This means that the FSR can be decreased down to 16% of its initial value. Experimental measurements (markers) show a good agreement with theoretical calculations (dashed curves). The observed small deviations of the RF response from the ideal behavior are attributed to the amplitude variations and non-completely linear phase response generated by SBS system. It must be considered that a noise source is used to broaden the Brillouin gain, resulting in small deviations from the Gaussian gain shape and thus in phase fluctuations.

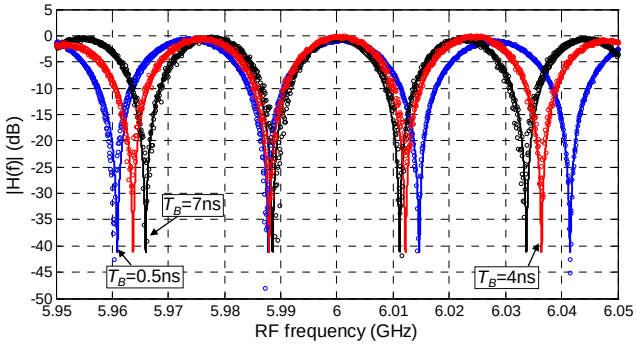

Figure 2.14: Measured (markers) and simulated (solid curves) frequency response of a twp-tap filter for 5 mW (blue), 60 mW (red) and 100 mW (black) $Pump_2$ power.

Second, the effect of a pure phase shift on the optical carrier has been measured by recording the filter spectral transfer function. Figure 2.15 displays the frequency response of the filter obtained with the SBS pump power ($Pump_2$) set at 100 mW and thus a fixed TTD, preserving its free spectral range. The 7 ns resulting from the Brillouin generation added to the fixed path delay (37.5 ns) corresponding to a FSR of 22.5 MHz. In this figure, continuous tunability was demonstrated as the phase of the higher-coefficient tap is modified by tuning the carrier phase shift using SBS-based phase shifter. In addition, it is important to notice that the central frequency of the notch filter is tuned while maintaining the shape of the transfer function unaltered, since the true time delay between the arms of the filter is fixed. The maximum achievable phase shift was greater than 360°, which leads to a continuously full tuning range of the filter response. In this case, the filter central frequency is only limited by the lab instrumentation.

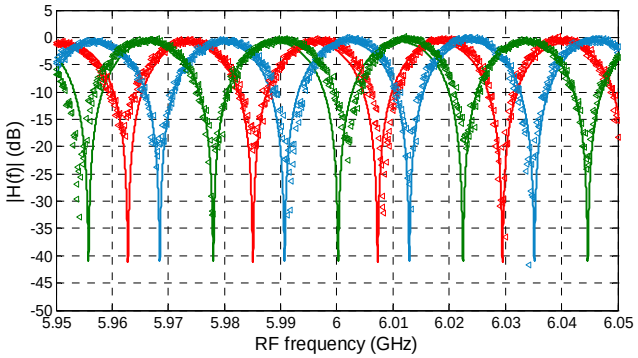

Figure 2.15: Measured (markers) and simulated (solid curves) filter frequency response by tuning the carrier phase shift for 110 mW Pump_2 power.

Finally, the combination of both effects, the phase shifter and Brillouin time delay, allow for the complete filter tunability in terms of FSR and central frequency. In Fig. 2.16 the SBS-based phase shifter is used to maintain a notch position at a given frequency. From Eq. 2.14 it is easy to infer that a notch can then be positioned at any arbitrary frequency ν_{notch} providing that the optical carrier phase shift φ_{offset} satisfies

$$\phi_{offset} = \text{mod}\left(\pi + 2\pi\nu_{notch}T + 2\pi\left(\nu_{notch} - \nu_{RF}\right)\tau_S\right), \tag{2.15}$$

where mod is the modulus 2π function. In the particular case illustrated in Fig. 2.16, 258.12° and 300.24° carrier phase compensation for the 7 ns and 4 ns curve, respectively, were required to fix a notch position at 5.961 GHz. This way a reconfigurable notch filter with more than 30 dB extinction ratio has been achieved, showing an excellent agreement with theoretical prediction from Eq.2.14.

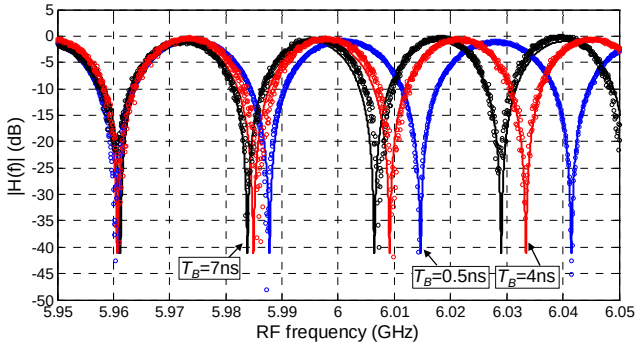

Figure 2.16: Measured (markers) and simulated (solid curves) frequency response of a twp-tap filter for 5 mW (blue), 60 mW (red) and 100 mW (black) Pump_2 power and for different carrier phase shifts to fix the frequency of the notch at 5.961 GHz.

2.6 Dynamic Brillouin gratings

The demonstrations and applications seen in previous sections make use of interactions between two optical waves along standard fibers. However, a more flexible alternative is based on the SBS interaction in PMFs [39–41]. This way yields the generation of DBGs, which act as a movable reflectors for incoming signals waves that are polarized along the orthogonal principal axis.

The DBG operation principle is schematically depicted in Fig. 2.17, where two Brillouin pumps, Pump_1 and Pump_2, are counter-propagated through the slow polarization axis (x-axis) of a PMF to generate the so-called dynamic grating of refractive index variations by stimulated Brillouin scattering [37, 39, 40, 53–56]. This acoustic mirror can be switched on and off and even moved along the fiber, depending on the profile of the pump waves. The frequency offset between the pump waves equal to the Brillouin frequency ν_B of the PMF. The generated DBG can reflect the orthogonally polarized (y-polarized) wave, the signal wave, at a different optical frequency $(\nu + \Delta\nu)$ propagating in the direction of Pump_1, provided that a phase-matching condition is satisfied [39],

$$\Delta\nu = \frac{\Delta n}{n} \cdot \nu, \tag{2.16}$$

where Δn is the birefringence ($\Delta n \equiv n_x - n_y$) of the PMF, and the frequency offset $\Delta\nu$ amounts to 40-80 GHz in most cases [39]. On a broader context, SBS dynamic gratings can be regarded as a three-wave process (one wave is acoustic) in an electrostictive medium [8].

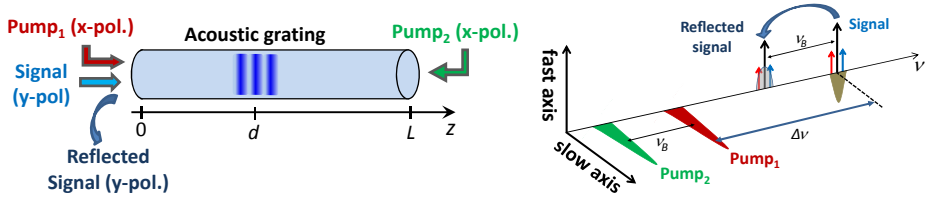

(a) (b)

Figure 2.17: (a) Principle to generate localized dynamic Brillouin gratings in PMF. (b) Spectra of pump and signal waves.

The DBG generation has been recently demonstrated through the interaction of pump pulse trains counter-propagating along the fiber [37], as illustrates Fig. 2.18(a). The acoustic wave builds up at the pulse crossing point as long as the pulses physically overlap, thus grating length and periodicity are determined by the pulse duration and repetition ratio, respectively. However, the grating generation is restricted by the acoustic lifetime τ_B ($\sim$ 10 ns in standard single mode fibers) [39]. It means that the gratings must be refreshed by periodic pump pulses at a repetition rate faster than the acoustic lifetime, thus the strength of reflection is temporally varying.

A new technique for the generation of SBS dynamic gratings that are both localized and stationary has been recently proposed [45] in order to overcome this

limitation. The principle, shown in Fig. 2.18(b), relies on the phase modulation of the two pump waves by a common PRBS, with a symbol duration that is much shorter than τ_B. In this case, the half of the word length used to generate the pseudo-random code determines the grating periodicity.

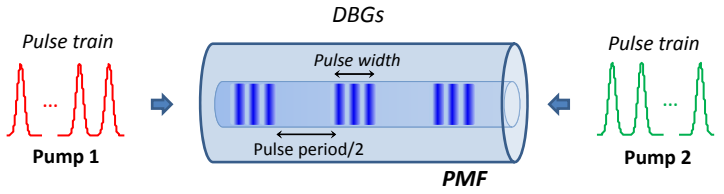

(a)

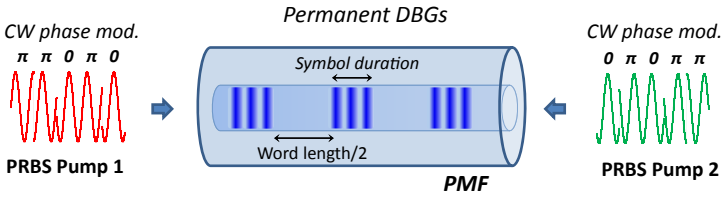

(b)

Figure 2.18: DBGs generation based on the interaction of (a) pulse train and (b) PRBS phase modulated pump waves.

Despite the spatial period, and therefore, the fact that the amplitude of the acoustic grating does not vary with time, DBG based PRBS generation normally exhibit substantially less reflectivity level than pulsed DBGs due to the continuous wave operation of the pumps. This disadvantage relies on the peak power of the pumps used to build up the gratings. It is well known that the lower the ratio between train period and FWHM is, the lower the peak power becomes. Therefore, since the PRBS signal is equivalent to a squared pulse train, that relation turns lower compared to a common pulsed DBG implementation.

DBGs have been so far proposed as a powerful tool in communication or sensor applications as a wide range tunable delay line [37, 54], or a distributed sensing mechanism with a high spatial resolution [55,56]. Simply by applying a relative delay between both pump waves, any crossing point of the two pumps can be addressed. As a consequence, signal pulses can be reflected at any preset position along the fiber, resulting in a large signal delay with low signal distortion. Figure 2.19(a) illustrates the normalized time waveforms of the reflected 500 ps width Gaussian pulses while shifting the grating position. As it is observed, a continuously induced time delay of $\sim$ 3.2 ns was obtained with negligible pulse distortion, which mostly relies on the fiber dispersion. It must be pointed out that the maximum achievable time delay is physically determined by the fiber length. On the other hand, dynamic grating reflections show opposite dependences on temperature and strain, which leads to the possibility of discriminative measurement of temperature and strain when analyzed together with Brillouin frequency distribution. This way DBGs add another dimension to ordinary distributed fiber sensors based on Brillouin scattering such as

BOTDA (Brillouin optical time-domain analysis) [57] and BOCDA (Brillouin optical correlation-domain analysis) [58]. Figure 2.19(b) shows the 3D map of the distributed Brillouin gain spectrum along 1 m-long PMF. The relative power of the reflected signal, as a function of the dynamic grating position and the detuning of the signal frequency is illustrated. A 10 mm-long section of metal piece was placed in contact with a high-current resistor, to generate a local hot-spot. It is clearly observed that the gain distribution near the 10 mm heated section is clearly separated from the rest of the fiber that remains under normal environmental condition, hence verifying the high spatial resolution of this system.

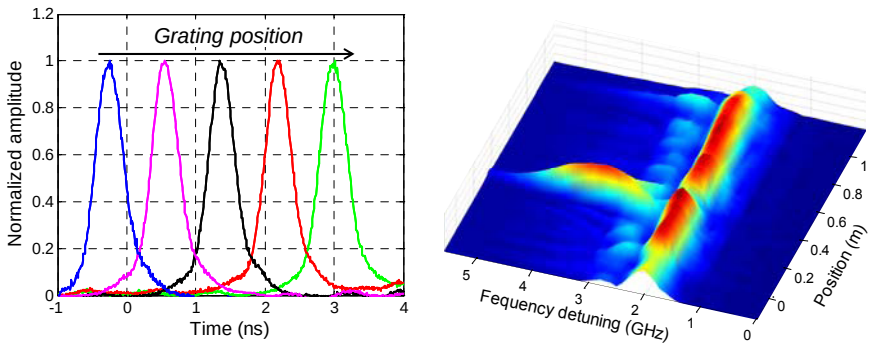

(a) (b)

Figure 2.19: DBG applications: (a) optically tunable time delays and (b) high performance distributed fiber sensor with discrimination of temperature and strain.

2.7 Basic MWP functionalities using DBGs

The grating capabilities in terms of delaying optical pulses have been successfully demonstrated in literature [37, 54]. However, the DBG interaction with microwave signals has not been yet demonstrated. Some numerical calculations are here shown so as to analyze the phase response of the modulated microwave signal through the DBG reflection. This way two different implementations have been studied to obtain basic MWP functionalities (i.e. TTD lines and phase shifters).

As it has been previously mentioned in 2.6, the DBG principle relies on the interaction of two optical pumps. Therefore, considering the beginning of the PMF as the origin of the optical phase for Pump_1 and Pump_2, the optical fields of both counter-propagating pumps, polarized along the x-axis n_x and meeting at the position d (see Fig. 2.17(a)), can be expressed as

$$\begin{aligned} E_{P_1}|_{z=d} &= a_{P_1} e^{i2\pi\left(\nu_{P_1} t - \frac{\nu_{P_1}}{c} n_x d\right)} \\ E_{P_2}|_{z=d} &= a_{P_2} e^{i2\pi\left(\nu_{P_2} t + \frac{\nu_{P_2}}{c} n_x (d-L)\right)}, \end{aligned} \tag{2.17}$$

where a_{P_1}, a_{P_1}, ν_{P_1}, and ν_{P_2} stand for the amplitude and frequencies of Pump_1 and Pump_2, respectively, while L denotes the length of the PMF.

The acoustic wave generated through the SBS interaction between these pump fields is given by

$$G = a_{DBG} E_{P_1} E_{P_2}^{*} = a_{DBG} a_{P_1} a_{P_2} e^{i2\pi\left(\nu_B t - \frac{\nu_{P_1}}{c} n_x d - \frac{\nu_{P_2}}{c} n_x (d-L)\right)}, \tag{2.18}$$

being a_{DBG} the grating reflectivity and $\nu_B = \nu_{P_1} - \nu_{P_2}$ the angular Brillouin frequency.

The generation of tunable TTDs through DBG interaction can be accomplished by reflecting both the carrier and two sidebands from the same grating, as illustrated in Fig. 2.17(b). The optical field of these waves after propagating a distance d is represented as

$$\begin{aligned} E_S|_{z=d} = a_C e^{i2\pi\left(\nu_C t - \frac{\nu_C}{c} n_y d\right)} + a_{RSB} e^{i2\pi\left((\nu_C + \nu_{RF}) t - \frac{(\nu_C + \nu_{RF})}{c} n_y d\right)} + \\ a_{LSB} e^{i2\pi\left((\nu_C - \nu_{RF}) t - \frac{(\nu_C - \nu_{RF})}{c} n_y d\right)}, \end{aligned} \tag{2.19}$$

where a_C, a_{RSD} and a_{LSD} are respectively the carrier, right and left sideband amplitudes. ν_C and ν_{RF} denote the angular frequency of the carrier and RF modulating signal, respectively. Taking into account that $\nu_C n_y = \nu_{P_1} n_x$ from [39], the signal reflection through the grating at the position $z = d$ can be written as

$$\begin{aligned} E_{SR}|_{z=d} = E_S|_{z=d} G^{*} = \\ a_{DBG} a_{P_1} a_{P_2} \left[\begin{array}{l} a_C e^{i2\pi\left((\nu_C - \nu_B) t + \frac{\nu_{P_2}}{c} n_x (d-L)\right)} + \\ a_{RSB} e^{i2\pi\left((\nu_C + \nu_{RF} - \nu_B) t - \frac{\nu_{RF}}{c} n_y d + \frac{\nu_{P_2}}{c} n_x (d-L)\right)} + \\ a_{LSB} e^{i2\pi\left((\nu_C - \nu_{RF} - \nu_B) t + \frac{\nu_{RF}}{c} n_y d + \frac{\nu_{P_2}}{c} n_x (d-L)\right)} \end{array} \right]. \end{aligned} \tag{2.20}$$

Now, the reflected signal propagates back to the detection point, which has been chosen to be $z = 0$. Thus, the reflected signal at the beginning of the PMF can be expressed as

$$\begin{aligned} E_{SR}|_{z=0} = \\ a_{DBG} a_{P_1} a_{P_2} \left[\begin{array}{l} a_C e^{i2\pi\left((\nu_C - \nu_B) t + \frac{\nu_{P_2}}{c} n_x (d-L) - \frac{\nu_{CR}}{c} n_y d\right)} + \\ a_{RSB} e^{i2\pi\left((\nu_C + \nu_{RF} - \nu_B) t - \frac{\nu_{RF}}{c} n_y d + \frac{\nu_{P_2}}{c} n_x (d-L) - \frac{\nu_{CR} + \nu_{RF}}{c} n_y d\right)} + \\ a_{LSB} e^{i2\pi\left((\nu_C - \nu_{RF} - \nu_B) t + \frac{\nu_{RF}}{c} n_y d + \frac{\nu_{P_2}}{c} n_x (d-L) - \frac{\nu_{CR} - \nu_{RF}}{c} n_y d\right)} \end{array} \right], \end{aligned} \tag{2.21}$$

where ν_{CR} defines the angular frequency of the reflected carrier, which can be written as $\nu_{CR} = \nu_{P_2} n_x / n_y$. Finally, the optical waves comprising the signal are beaten in the photodetector at $z = 0$. Therefore, the photocurrent generated at the modulation frequency ν_{RF} is proportional to

$$i\left(\nu_{RF}\right)\big|_{z=0} \propto \left|4a_{DBG}a_{P_1}a_{P_2}a_C\left(a_{RSB}+a_{LSB}\right)\right| e^{i\left(-2\frac{2\pi\nu_{RF}}{c}n_y d\right)}. \tag{2.22}$$

From Eq. 2.22, the phase of the photodetected signal can be expressed as $\phi = -2\nu_{RF}n_y d/c$, while the signal delay as $\tau = n_y 2d/c$.

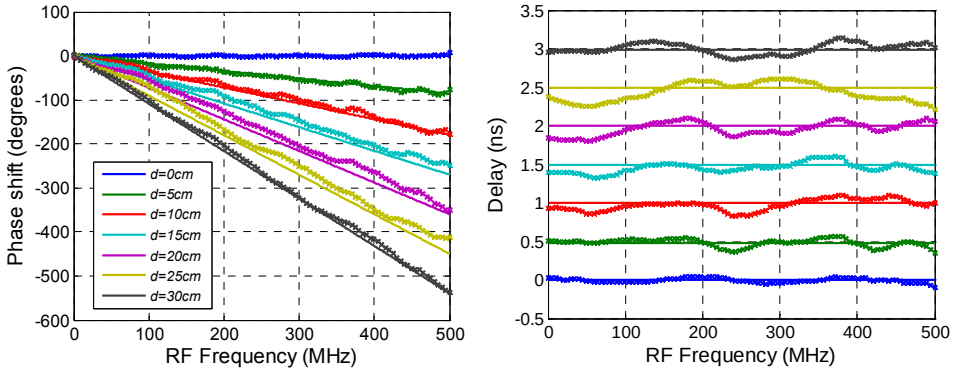

(a) (b)

Figure 2.20: Measured (markers) and calculated (solid curves) (a) phase shift as a function of the modulation frequency for different DBG positions along the fiber and (b) the corresponding true time delay.

Figures 2.20(a) and 2.20(b) illustrate the phase shift and corresponding time delay, respectively, as a function of the RF frequency for different grating positions along the PMF. The grating was build up through 400 ps pump pulses yielding $\sim$ 1GHz bandwidth. The same as occurred in Fig. 2.19(a), the position of the DBG was tuned by applying a relative delay between both pump waves. As it is clearly observed in Fig. 2.20(b), the perfectly proportional evolution of the phase of the RF signals with respect their operational frequency implies TTD operation. As expected from Eq. 2.22, the obtained TTD corresponds to twice the propagation length. In addition, larger delay values can be simply achieved by using longer PMF. It must be pointed out that the TTD bandwidth and operational frequency remain limited to half the grating bandwidth in this implementation.

On the other hand, the phase shifter approach relies on the independent reflection of the optical carrier and one sideband from two different gratings. In such a way, these two DBGs are generated by counter-propagating two double pump waves, as illustrates Fig. 2.21. Thus, the gratings are physically overlapped at the same fiber position but at different central frequency.

Two acoustic waves are generated through this double SBS interaction, the one whose will reflect the optical carrier and the other for reflecting one sideband,

$$\begin{aligned} G_C &= a_{DBG}a_{P_1}a_{P_2}e^{i2\pi\left(\nu_B t-\frac{\nu_{P_1}}{c}n_x d-\frac{\nu_{P_2}}{c}n_x(d-L)\right)}, \\ G_{SB} &= a_{DBG}a_{P_1}a_{P_2}e^{i2\pi\left(\Omega_B t-\frac{\nu_{P_1}-\nu_G}{c}n_x d-\frac{\nu_{P_2}-\nu_G}{c}n_x(d-L)\right)}. \end{aligned} \tag{2.23}$$

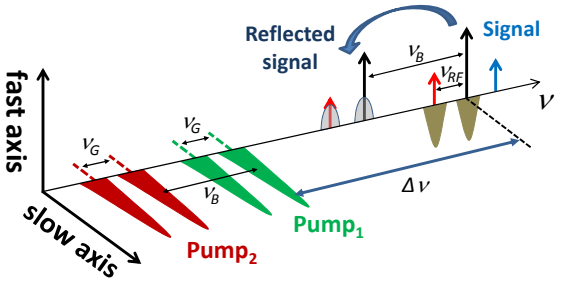

Figure 2.21: Optical frequencies of the pump and signal waves for the double grating generation.

The optical field of the signal is now composed only by two spectral lines, the carrier and the red sideband. The blue sideband can be neglected since it will not be reflected. After propagating a distance d, this optical field is represented as

$$E_S|_{z=d} = a_C e^{i2\pi\left(\nu_C t - \frac{\nu_C}{c} n_y d\right)} + a_{LSB} e^{i2\pi\left((\nu_C - \nu_{RF})t - \frac{(\nu_C - \nu_{RF})}{c} n_y d\right)}. \tag{2.24}$$

Then the carrier wave of the signal matches the resonance of one DBG, whereas the lower sideband is in resonance with the second DBG. At that time, the signal is back-reflected to the detection point, which again has been chosen to be $z = 0$. Thus, the reflected signal at the beginning of the PMF can be expressed as

$$E_{SR}|_{z=0} = a_{DBG} a_{P_1} a_{P_2} \left[\begin{array}{l} a_C e^{i2\pi\left((\nu_C - \nu_B)t - \frac{\nu_{CR}}{c} n_y L\right)} + \\ a_{LSB} e^{i2\pi\left((\nu_C - \nu_{RF} - \nu_B)t + 2\frac{\nu_{RF} - \nu_G}{c} n_y d - \frac{\nu_{CR} - \nu_G}{c} n_y L\right)} \end{array} \right]. \tag{2.25}$$

Finally, due to the beating between the optical waves in the photodetector, the photocurrent at the modulation frequency ν_{RF} is proportional to

$$i\left(\nu_{RF}\right)|_{z=0} \propto \left|4 a_{DBG} a_{P_1} a_{P_2} a_C a_{LSB}\right| e^{i2\pi\left(-2\frac{\nu_{RF} - \nu_G}{c} n_y d - \frac{\nu_G}{c} n_y L\right)}. \tag{2.26}$$

Hence, the phase shift depends not only on the ν_{RF} and d, but also on the spectral difference between both gratings ν_G and the fiber length L. This last dependence appears as a result of the two gratings relative phase shift since they are located at different frequencies.

Figures 2.22(a) and 2.22(b) show the calculated results of the phase shift as a function of the grating position d and the spectral difference between both gratings ν_G. The results have been simulated for $L = 1.2$ m, $\nu_G = 5$ GHz in Fig. 2.22(a) and $d = 20$ cm in Fig. 2.22(b). As occurred in Fig. 2.10(b), the phase changes illustrated in Fig. 2.22(a) are equivalent to a signal group delay, but not TTD since the phase origin is centered at 5 GHz, thus it will produce the well-known beam squint in

radar applications as explained in 2.4. However, the phase shifter implementation is numerically demonstrated in Fig. 2.22(b). As it is observed, 2π tunability is obtained with only 200 MHz frequency detuning. Thus, the TTD condition can be simple met by adjusting the spectral difference between the gratings as it has been demonstrated through the SCT technique in the section 2.4. In this case, the phase shifter / TTD bandwidth still limited by the grating resonance, while its central frequency is only restricted by the bandwidth of the modulators and driving equipment.

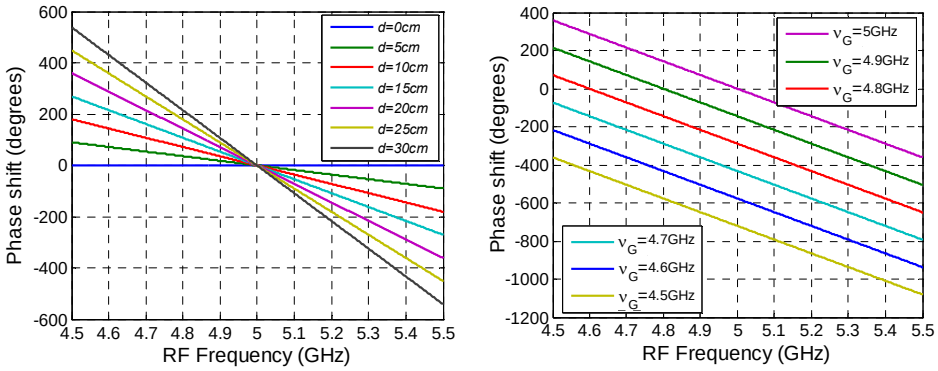

(a) (b)

Figure 2.22: Phase shift as a function of the modulation frequency when the signal is reflected from two DBGs (a) for different grating positions along the fiber and (b) for different spectral separations between the two gratings.

2.8 MWP filter implementations based on DBG reflections

As a potential application, four different MWP filter implementations based on DBG generation are here presented, where the location of the reflection gratings can be dynamically controlled within a PMF by tuning the time delay between the pump waves.

The generic experimental layout of the DBG-based MWP filter is illustrated in Fig. 2.23. The DFB-LD 1 was used to generate the two pump waves. The laser source was then split into distinct fiber channels. The power in the upper channel was boosted using an EDFA up to $\sim$ 200 mW, polarized along the slow axis of the PMF and launched into the PMF as Pump_1. The optical power in the other channel was modulated by using the EOM_1 driven by a microwave signal at the Brillouin shift frequency ν_B ($\sim$ 11 GHz). The EOM_1 was biased in order to suppress the optical carrier. The upper sideband was filtered using a narrow-band FBG and then amplified by a second EDFA to $\sim$ 200 mW to be used as Pump_2. This way the stability of the frequency difference between the two pumps was secured. The polarization of Pump_2 was also aligned along the slow axis before entering the opposite end of the fiber. The output signal of a second DFB laser (DFB-LD 2) was modulated by an

RF tone from the output port of a VNA using the EOM_2, amplified and polarized along the fast axis of the PMF. According to the high birefringence of the PMF, the dynamic grating resonance appeared at 73 GHz above the frequency of $Pump_2$, hence the optical frequency of the DFB-LD 2 was precisely placed at the center of the DBG using temperature and current controls. The reflected signal was finally detected and measured by the input port of the VNA.

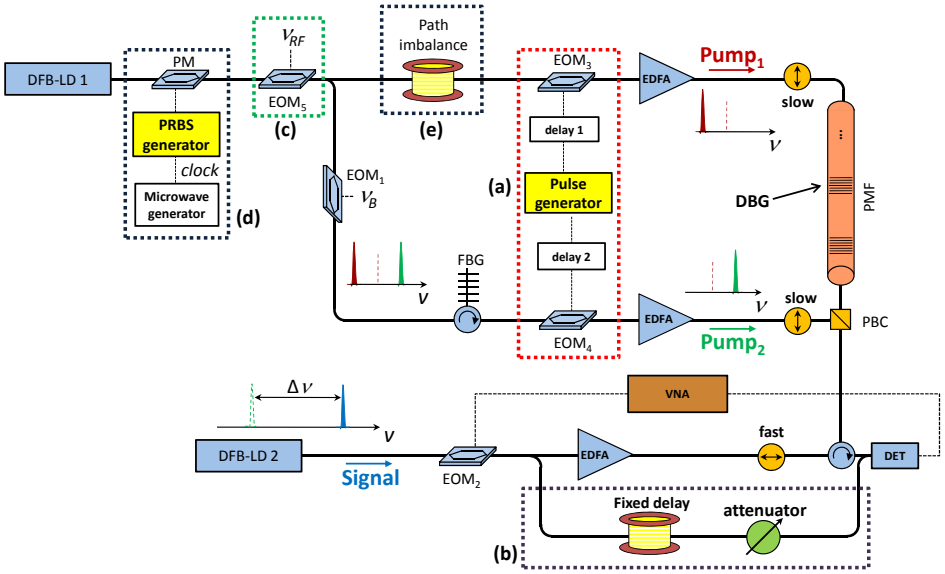

Figure 2.23: Experimental setup to realize MWP filters, using a single or multiple dynamic Brillouin grating reflectors.

Four distinct filter configurations have been accomplished by successively implementing different variations in the setup. In the first and second configurations, both Brillouin pump signals were pulse shaped using the EOM_3 and EOM_4, as shown in Fig. 2.23(a). The relative time delay between the two pumps was accurately set to place the DBG at any desired position along the PMF. In first configuration, a single grating is generated along the PMF, playing the role of a simple reflector delaying the signal. Thus, a fixed delaying arm in the signal channel was added to build up the filter in a MZ configuration, as shown in Fig. 2.23(b).

In the second and third configurations, multiple dynamic gratings are generated along the PMF and each grating reflection is equivalent to an individual tap. So, the fixed arm used as a second tap is no longer required. Besides, in third configuration the DFB-LD 1 is externally modulated by the EOM_5 (Fig. 2.23(c)) at the RF frequency of ν_{RF}, with its bias set to completely suppress the carrier. This way, double dynamic gratings can be generated at a same position in fibers, reflecting signal optical frequencies that are separated by $2\nu_{RF}$. This arrangement helps to increase the bandwidth of the filters, as will be discussed later.

In fourth configuration, the laser output is modulated through a PM driven by a common PRBS generator as shown in Fig. 2.23(d), and the building blocks of insets

2.23(a), 2.23(b) and 2.23(c) are removed for this implementation. DBGs are generated at periodic discrete locations, in which the modulated pumps are correlated. A path imbalance is added in Pump_1 arm (Fig. 2.23(e)), so that high-order correlation peaks are obtained along the PMF [45]. The correlation peaks are scanned by changing the clock rate of the PRBS generator [45].

2.8.1 MWP filter based on an hybrid configuration: DBG + delay line (1^{st} configuration)

The DBG was generated through interaction between two counter-propagating Brillouin pump pulses. When the acoustic wave builds up at the pump pulses crossing point, the dynamic grating gradually decays [39], thus it needs to be periodically regenerated. The repetition rate of both Brillouin pumps was adjusted at 5 ns, which is shorter than the acoustic lifetime ($\sim$ 10 ns) [39] to assert that the grating is refreshed before it vanishes.

According to this repetition rate, the gratings were periodically created along the fiber with a periodicity of 2.5 ns due to the crossing counter-propagative configuration. This periodicity was longer than the 2 ns transit time through the 40 cm PMF used in this configuration. It assured that only one dynamic grating was present along the fiber. The spectral bandwidth of the DBG was determined by its physical length, and hence by the pulse duration of the Brillouin pumps [38]. The pumps pulses were Gaussian shaped with a FWHM of 400 ps, corresponding to a DBG reflectivity bandwidth that was far broader than 1 GHz. This figure is of importance since the bandwidth of the grating acts as an actual limitation in terms of instantaneous bandwidth for signal processing.

This particular configuration yields to a two-tap FIR filter comprising real coefficients (see section 1.2), where the filter transfer function can be expressed as

$$H(\nu) = a_0 + a_1 e^{-i(2\pi\nu T_0 + 4\pi\nu\tau_{DBG})}, \tag{2.27}$$

being T_0 the time delay imbalance between the filter arms when the DBG is placed at the beginning of the fiber ($d = 0$), and τ_{DBG} the grating delay, which can be expressed as $\tau_{DBG} = n_y d/c$. As explained in section 1.2, the FSR tunability in a transversal filter implementation relies on dynamic control of the filter basic delay T ($T = T_0 + \tau_{DBG}$, which can be accomplished by changing the grating position d along de fiber. Besides, windowed samples can be performed by applying the proper weight to each tap.

Although T in this configuration is proportional to the coherence time τ_C, the filter worked under incoherent regime since the phase fluctuations of the dynamic grating were added to the reflected signal. In such a way, the signal coming from the lower branch of the MZ turned uncorrelated with the reflected signal from the grating.

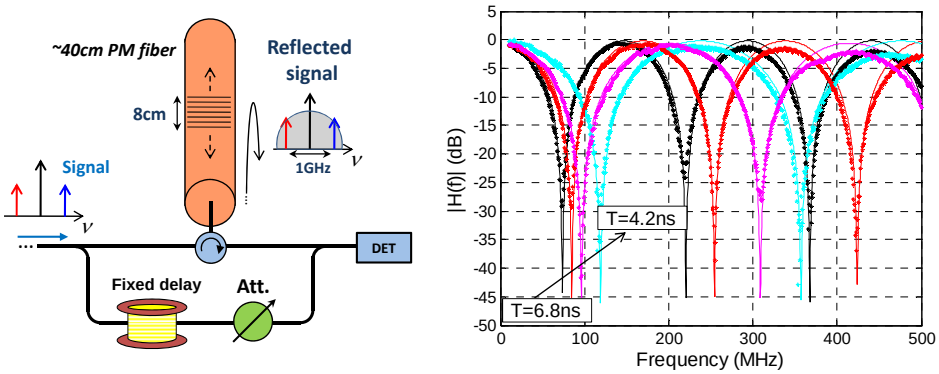

(a) (b)

Figure 2.24: (a) Basic filter layout and (b) frequency response of the two-tap filter implementation in first configuration.

Figure 2.24(a) depicts the basic layout of the filter in first configuration. The original RF-modulated signal from the fixed arm was combined with the reflected replica from the moveable dynamic grating to generate a two-tap filter response. Since the optical carrier and both sidebands were reflected by the same grating, the operating frequency of the filter was limited to the half of the grating bandwidth, on the order of 500 MHz in this case. A $\sim$ 80 m-long optical fiber was introduced as a fixed delay in lower branch of the layout to compensate the fiber length of several optical components in the upper branch, such as EFDA, circulator and couplers. The fixed path also provided a length imbalance of $\sim$ 1 m between the two taps.

Figure 2.24(b) shows the measured notch-type frequency response of the filter obtained for different grating position. The experimental filter responses (markers) are in good agreement with calculated estimations (solid curves). The small deviation observed at high frequencies are attributed to the finite bandwidth of the dynamic grating since the reference tap, i.e. the fixed path, exhibited a constant frequency response. The relative delay between the fixed and variable paths was tuned from 4.2 to 6.8 ns, corresponding to continuous FSR variation of up to 62%. The maximum delay variation is actually limited by the PMF length. The response can be reconfigured with additional parallel taps, however such scaling is rather complicated. In addition, both the bandwidth and central frequency of this filter configuration are restricted to the order of 500 MHz.

2.8.2 MWP filter based on multiple DBGs (2^{nd} configuration)

Second to fourth configurations are based on the generation of multiple dynamic gratings along the fiber. Thus, the spectral response of the filter results from the combination of multiple reflections with different time delays, which is ideally equivalent to a multi-tap filter configuration with identical and positive weights [59]. The number of taps comprising the filter is readily reconfigurable by simply changing the number of DBGs generated in the fiber. Due to the unique feature of phase conjuga-

tion in Brillouin scattering [8], all delayed RF signals from different gratings remains in phase, resulting in no coherence constraints.

In 2.25(a) is illustrated the basic layout of the two-tap filter in second configuration. The two signal reflections are combined in the fotodetector yielding a filter transfer function to that shown in Eq. 2.27. However, in this case, the basic filter delay T keeps determined by the pulse train repetition rate. On the other hand, the frequency response of such a filter generated from two dynamic grating reflections is illustrated in Fig. 2.24(b). The DBGs were created along 60 cm-long. By changing the repetition rate of both counter-propagating pump pulse trains, i.e. the filter basic delay, from 3.3 to 5.2 ns around 58% of FSR tunability was achieved. Since both the carrier and sidebands are reflected by the same grating, the bandwidth and central frequency of this filter configuration are again limited to half the grating bandwidth. In this case, the filter builds up from multiple grating reflections, thus to accomplish windowing by applying different weights of each tap turns difficult since all the pump pulses are usually generated with the same optical power. However, after the pump interaction for generating the gratings the power of the pulses decay, which means that the DBG created at the position where the two pumps waves first meet will exhibit higher reflectivity compared with neighboring gratings. This way an inherent rectangular window is created.

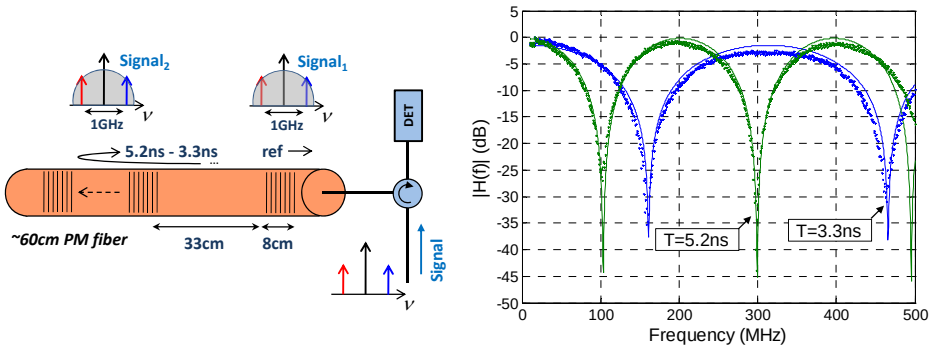

(a) (b)

Figure 2.25: (a) Basic filter layout and (b) frequency response of the two-tap filter implementation in second configuration.

2.8.3 MWP filter for high-frequency applications based on multiple spectrally detuned DBGs (3^{rd} configuration)

To enhance the RF baseband frequency response and thus demonstrate the high flexibility of the configuration, Brillouin Pump_1 and Pump_2 were modulated to eventually consist of two different optical frequencies separated by $2\nu_{RF}$ (see Fig. 2.21 and Fig. 2.23(c)) in third configuration. Using this arrangement, the carrier wave of the signal matches the resonance of one DBG, whereas one of its sidebands is in resonance with a second DBG which is overlapping in position. While the filter bandwidth remains on the order of 1 GHz, its central frequency is arbitrarily adjusted through ν_{RF}. The

central frequency is only restricted by the bandwidth of the modulators and driving equipment.

This configuration corresponds to a multi-tap FIR filter (see section 1.2), where its transfer function is expressed as

$$H(\nu) = \sum_{r=0}^{N-1} a_r e^{-i2\pi r \tau_{RR}(\nu-\nu_G)}, \tag{2.28}$$

being τ_{RR} the pulse train period or repletion rate, which can be defined as $\tau_{RR} = 2\left(\tau_{DBG_r} - \tau_{DBG_{r-1}}\right)$.

The simplified layout of the filter architecture is illustrated in Fig. 2.26. The frequency responses of different number of dynamic gratings (two, three and four) created along 110 cm-long PMF are demonstrated in Figs. 2.27(a), 2.27(b) and 2.27(c), respectively. The optical power reflectivity of the gratings was on the order of -35 dB. The filter thus works in low reflectance regime, and hence multiple interfering reflections are negligible. In this particular type of implementation, the Q factor depends only on the number of taps comprising the filter [59]. For the two-tap configuration, the repetition rate of pump pulses was tuned from 4 to 6.6 ns, corresponding to a 65% change of the FSR, while preserving the 1 GHz bandwidth. The length of the PMF restricted the FSR variations of the higher-order filters: 17% for three DBGs, and practically none for four. Figure 2.27(c) also represents the numerical results (dashed curves) of the filter response when the spectral difference between the two gratings ν_G is detuned 200 MHz, which corresponds to $\sim 187°$ phase shift. This way the filter will be able to accomplish complex coefficients.

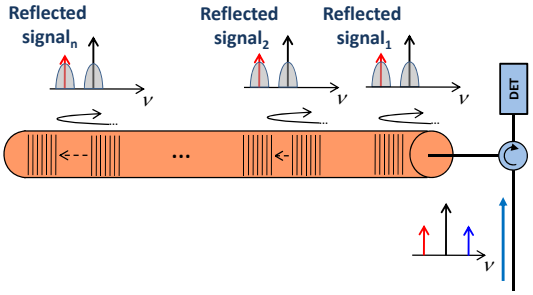

Figure 2.26: Basic filer layout based on multiple grating reflections.

Birefringence uniformity along the PMF is critical to achieve equal taps, since the signal frequency of maximum reflectivity varies with birefringence. The birefringence non-uniformity can explain the mismatch between experimental results and theoretical calculations, especially when the number of coefficients is increased.

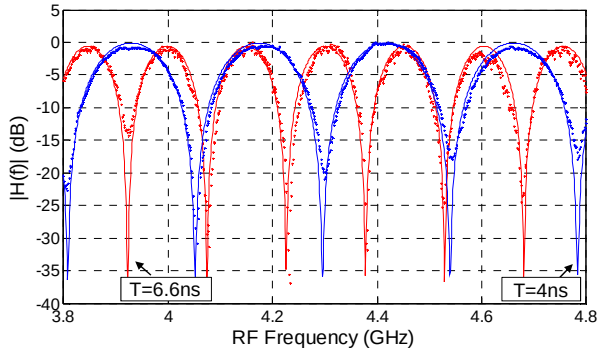

(a)

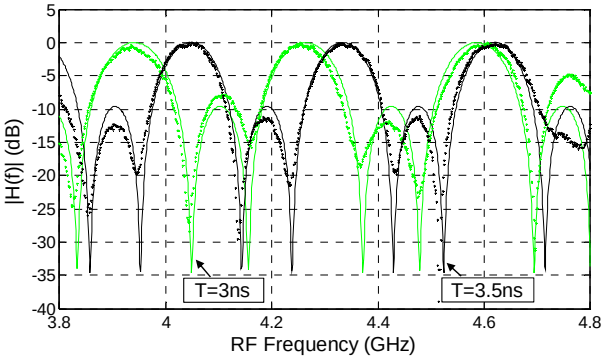

(b)

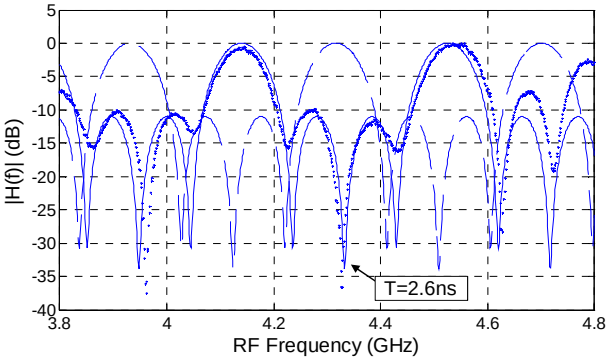

(c)

Figure 2.27: Frequency response of the (a) two-tap, (b) three-tap and (c) four-tap MWP filter in third configuration.

2.8.4 MWP filter based on DBGs generated by a pseudo-random sequence (4^{th} configuration)

Unlike the previous configurations, here the two Brillouin pumps were shaped to deliver constant power, but their optical phases were externally modulated through a PM driven by a PRBS generator. In this configuration, the stimulated Brillouin scattering interaction between the two pumps is efficiently restricted to narrow regions where their phases are steadily correlated. This way stationary DBGs are obtained, whose length matches the spatial extent of a single modulation bit [45]. However, stationary gratings appear with a periodicity that equals half the PRBS word length, hence multiple gratings can be implemented along a single PMF to realize multi-tap MWP filters, as shown in Fig. 2.28(a). Since the grating delay is proportional to twice the propagation length, the basic filter delay T corresponds to the PRBS word length.

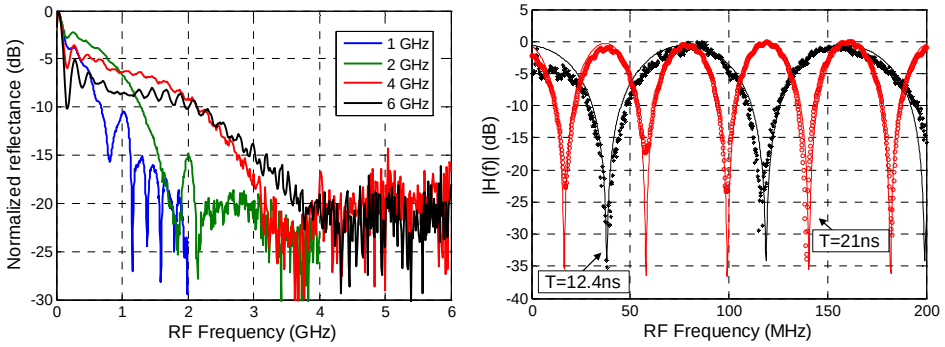

(a) (b)

Figure 2.28: (a) Generation of stationary dynamic gratings using PRBS phase modulation. (b) Spectral response of the two-tap MWP filter in fourth configuration.

In this experiment, a 2 m-long PMF was used as a delaying medium and the modulation frequency of PRBS was varied between 6 - 10 GHz with 127 bits word length, which was the lowest available in the PRBS generator. Two correlation peaks could be created along the PMF with a relative delay in the range of 12.7 – 21.1 ns. The FSR of the resulting MWP notch filter ranged between 47 and 78 MHz, which means a variation of 66%, as shown in Fig. 2.28(b).

The DBGs obtained using this method are stationary and do not require periodic refreshing every τ. Therefore, the restriction of the relative delay to the order of τ is removed. On the other hand, the continuous power of the pumps used in this technique is much lower than the peak power of the pump pulses that were used before. Since the strength of the DBG reflection scales quadratically with the pump power, the stationary DBGs tend to be considerably weaker than pulsed ones.

2.9 Conclusions

In this chapter, Brillouin slow light elements have been demonstrated to offer novel and outstanding capabilities in MWP systems. In particular, thanks to the achievement of broadband fully tunable phase shifters, true time delay lines and reconfigurable multi-tap filters.

SBS effects in standard optical fibers have been carried out for the development of an innovative all-optical tunable TTD line based on separate carrier tuning technique. Two SBS systems have been implemented to separately manage the dispersion characteristics at the optical carrier [26] and RF subcarrier frequencies. An optical pump power control was deployed for adjusting the time delay, while an electrical control mechanism was required for the phase shifter tunability. A TTD continuously tunable up to 8 ns was achieved, within 100 MHz instantaneous bandwidth. It must be pointed out that this technique has no physical limitation on operating RF frequency since the Brillouin resonance can be positioned at any desired RF frequency. In addition, these systems can provide a signal bandwidth up to 12 GHz with high flexibility [50]. The implementation of the SBS-based SCT technique has also been demonstrated in a reconfigurable MWP notch filter. The TTD induced led to a 20% tunability of the FSR of the filter, and the optical carrier phase shifting then enabled to control the origin of the FSR variation, matching the reference frequency.

The phase response of dynamic Brillouin grating reflectors in PMFs has been studied so as to accomplish an alternative approach for generating broadband RF true time delays and phase shifts. Besides, four different configurations to realize multi-tap MWP filters have been demonstrated. The spectral responses of the proposed filters were dynamically tuned and reconfigured by simply changing the characteristics of single or multiple DBG generations. A FSR variation larger than 60% in a two-tap filter was achieved, within up to 1 GHz instantaneous bandwidth. The first configuration allowed for any spectral range tunability, however the number of taps and the central frequency could not be scaled. MWP filters based on second to fourth configurations were based on multiple grating reflectors successively created along the same fiber, and the need of a reference tap with a fixed optical delay line could be eliminated. In these configurations the birefringence uniformity along the fiber was carefully inspected for a consistent frequency response. Second configuration improved the filter reconfigurability, yet its bandwidth and central frequency were also restricted to the grating spectral profile. In the third configuration, two distinct dynamic Brillouin gratings were localized at the same position, so that the resonance frequency of one grating could match the incident optical carrier and another could reflect one of the two modulation sidebands. This way the central operation frequency of the filter was extended beyond that of first and second configuration. Finally, the correlation technique based on the external PRBS optical phase modulation proposed in fourth configuration enabled the generation of stationary DBGs. This technique alleviates the need for periodic refreshing, help extend the range of attainable FSRs, and improve the tunability and the scalability of the filter response.

It must be mentioned that the delay range obtained through SBS interaction (0 - 8 ns) was demonstrated along $\sim$ 20 km standard fiber. However, the same results can be achieved through DBGs with less than 1-m-long PMF. This means a footprint reduction of more than five orders of magnitude. In addition, the signal bandwidth is improved from 100 MHz to 1 GHz when using dynamic reflectors.

The objectives of this chapter have been fulfilled and recognized by the community in the following international publications:

- Y. Antman, N. Primerov, **J. Sancho**, L. Thévenaz, and A. Zadok, "Localized and stationary dynamic gratings via stimulated Brillouin scattering with phase modulated pumps", Optics Express, vol. 20, no. 7, pp. 7807-7821, 2012.
- **J. Sancho**, N. Primerov, S. Chin, Y. Antman, A. Zadok, S. Sales, and L. Thévenaz, "Tunable and reconfigurable multi-tap microwave photonic filter based on dynamic Brillouin gratings in fibers", Optics Express, vol. 20, no. 6, pp. 6157-6162, 2012.
- **J. Sancho**, S. Chin, M. Sagues, A. Loayssa, J. Lloret, I. Gasulla, S. Sales, L. Thévenaz and J. Capmany, "Dynamic microwave photonic filter using separate carrier tuning based on stimulated Brillouin scattering in Fibers", IEEE Photonics Technology Letters, vol. 22, no. 23, pp. 1753-1755, 2010.
- S. Chin, L. Thévenaz, **J. Sancho**, S. Sales, J. Capmany, P. Berger, J. Bourderionnet, and D. Dolfi, "Broadband true time delay for microwave signal processing, using slow light based on stimulated Brillouin scattering in optical fibers", Optics Express, vol, 18, no. 21, pp. 22599-22613, 2010.
- **J. Sancho**, J. Lloret, N. Primerov, S. Sales, L. Thévenaz and J. Capmany, "Recent implementations of fiber and integrated tunable microwave photonics filters", submitted to Conference of the 14th International Transparent Optical Networks (ICTON), Coventry (England), 2012.
- Y. Antman, N. Primerov, **J. Sancho**, L. Thévenaz, and A. Zadok, "Variable delay using stationary and localized Brillouin dynamic gratings", in SPIE Photonics West, San Francisco (USA), invited paper 82730C, 2012.
- Y. Antman, N. Primerov, **J. Sancho**, L. Thévenaz, and A. Zadok, "Long variable delay and distributed sensing using stationary and localized Brillouin dynamic gratings", in National Fiber Optic Engineers Conference (NFOEC), Los Angeles (USA), paper JW2A.24, 2012.
- L. Thévenaz, S. Chin, P. Berger, J. Bourderionnet, S. Sales and **J. Sancho**, "Slow light fiber systems in microwave photonics", in SPIE Photonics West, San Francisco, (USA), invited paper 79490B, 2011.
- **J. Sancho**, S. Chin, M. Sagues, A. Loayssa, J. Lloret, I. Gasulla, S. Sales, L. Thévenaz and J. Capmany, "True time delay on tunable microwave photonic filter based on stimulated Brillouin scattering in fibers", in 36th European Conference of Optical Communication (ECOC), Turin (Italy), paper P.1.18, 2010.

Chapter 3

Long fiber Bragg gratings: spectral analysis and applications

3.1 Introduction

For several decades FBGs have been considered key devices in all-fiber based systems due to their simplicity, compatibility, polarization independence and low cost, among others. An FBG is a fiber-optic component characterized by a periodic perturbation of the refractive index which is permanently photo-induced along the length of a single-mode optical fiber [60, 61]. Indeed, a uniform FBG operated in the linear regime becomes a band-pass filter, reflecting only a narrow spectral band around its characteristic Bragg frequency.

Several methods have been proposed to measure Bragg-frequency distribution along an FBG [62–64] aiming at development temperature/strain sensors. In this context, the optical low-coherence reflectometry (OLCR) technique [62] has demonstrated a good performance in terms of spatial resolution. However, this method shows a limited measurement range and a slow response time. Another commonly resorted approach, the technique based on optical frequency domain reflectometry (OFDR) [63] requires post-signal processing and an auxiliary interferometer to compensate any non-linearity on the ramp signal, making the setup complex. The third distributed sensing mechanism is that based on the synthesis of optical coherence function (SOCF) [64]. This promising technique lets selectively address a particular position along the FBG and move the interrogating position by simply tuning the modulation frequency of the light source. However, this method demands a very complicated setup and expensive devices.

In the context of photonic-assisted RF signal processing, different promising solutions have been proposed in the literature featuring tailored grating designs [51, 65–67]. In particular, an optically-induced RF phase-shift by means of OSSB modulation and the FBG narrow-band optical filtering characteristic has been proposed in [51]. This way a four-tap tunable MWP filter has been experimentally

demonstrated to highlight the enhanced tuning performance provided by complex coefficients. On the other side, an interesting TTD system is that based on the cascade of two switched tunable chirped FBGs [65] including solenoid tuners. A three-tap filter has been implemented showing the viability of such cascaded technique. The filter tunability was carried out through the electrical current injected to the solenoids. An analysis of the performance of phased array antennas steered by a single 40-cm-long chirped fiber grating is demonstrated in [66]. Furthermore, in [67] a tunable optical delay line based on the use of a single chirped FBG through the differential group delay curve has been presented. One significant advantage relies on the fact that this configuration does not require any wavelength shift. Consequently, the full grating bandwidth can be used to delay optical pulses nearly as broad as the grating reflection band.

Finally, the design and realization of photonic equivalents to fundamental electronic devices becomes a primary step towards the practical realization of all-optical circuits. Two important and relevant examples of these fundamental devices are a photonic temporal differentiator [68, 69] and a photonic temporal integrator [70, 71]. These FBG-based signal processors have been identified as key elements to build up ultrafast all-optical circuits for real-time computing [72].

In this chapter, an alternative approach to characterize the distributed optical properties of a uniform long FBG with very low reflectivity will be demonstrated. It is important to notice that such a weak and uniform FBG can be considered as a permanent DBG, thus sensing and time delaying mechanisms so far reported in [37, 54–56] can be exploited using the passive nature of an FBG. In this way, a distributed FBG temperature/strain sensing system will be provided through time-resolved analysis of the grating spectral profile after launching an ultra-short pulse into a long weak FBG. The proposed technique will be also adapted to achieve all-fiber continuously tunable time delays for broadband optical pulses. In addition, the distributed characteristic of the FBG-based sensor will be exploited in order to perform MWP basic functionalities, such as phase shifters and true time delays. Finally, the experimental realization of a photonic integrator design will be addressed, reporting integration of arbitrary time-limited optical waveforms (pulses) with high bandwidth, which is required for future ultrafast all-optical signal processing.

This chapter is the result of a collaboration between UPV and EPFL during a three month stay at GFO in Switzerland.

3.2 Principle of operation

The operation principle to perform a distributed analysis of the spectral properties of a weak FBG relays on optical time-domain reflectometry (OTDR) [73], as illustrated in Fig. 3.1. An ultra-short optical pulse, which has duration much shorter than the transit time through the FBG, is launched into the long grating. Thus, if the grating reflectivity is weak enough (it can be controlled by the ultraviolet exposure time during the fabrication process), the incident pulse is continuously back-reflected while propagating through the entire grating length. Then the spectral property of the reflection spectrum is temporally analyzed and straightforwardly transposed into equivalent distance. The time-resolved power spectrum of the reflected light can be

measured as a function of position along the fiber, resulting in a 3D mapping of the localized FBG spectrum convolved with the pulse spectrum.

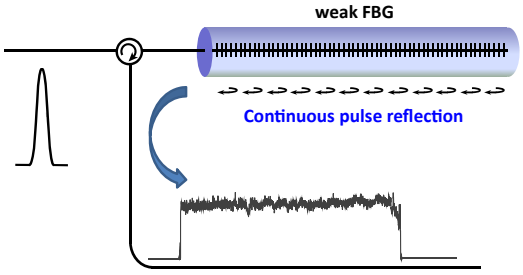

Figure 3.1: Principle to characterize time-resolved FBG spectrum using an ultra-short optical pulse.

Figure 3.2(a) shows the amplitude variation of the back-reflected light as a function of the frequency while the pulse is propagating through a long FBG. The time duration of the pulse reflection equals the round-trip propagation time through the grating, i.e. twice the grating length. Indeed, it represents the distributed central frequency of the FBG convolved with the pulse spectrum. It is important to notice that the spatial resolution of this technique is essentially determined by half the pulse duration, such as SOCF [64]. Consequently, ambient temperature and strain information along the grating can be deduced since the central frequency of the FBG reflection resonance exhibits a linear dependence on temperature and/or strain applied to the grating. Figure 3.2(b) shows theoretical simulations of ultra-short pulse propagation through the FBG for two different reflectivities, 40% and 95%, respectively [74]. It is clearly observed that in case of a strong grating the incident pulse is completely reflected in the initial section of the grating. However, a tiny fraction of the pulse can be continuously reflected up to the end of the grating in the case of a weak FBG. Thus, the spectral response of the grating can be interrogated along the entire length. As a direct consequence, the linear relationship between a shift of the central grating frequency and a change of ambient temperature or strain makes possible to measure the temperature/strain distribution along the grating with a high spatial resolution.

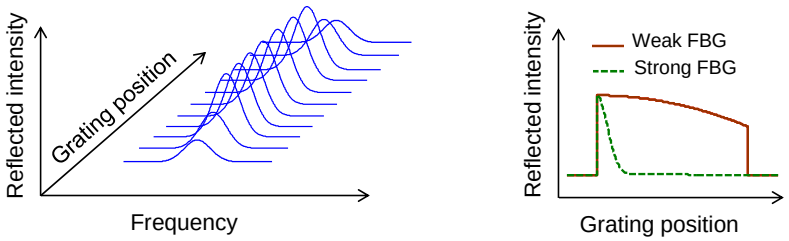

Figure 3.2: (a) Bragg frequency distribution measurement by OTDR technique. (b) Reflected pulse from a weak and strong FBG.

3.3 Distributed sensing system

As it has been previously mentioned, in order to implement an FBG-based distributed sensor, the coupling coefficient (defined as the optical power coupling between counter propagating modes per unit of length) has to be sufficiently low to ensure that the FBG reflection temporal impulse response keeps constant over the duration corresponding to the total grating length. In this case, a 10-cm long FBG with a 40% total reflectivity was employed as a distributed temperature sensor. Initially, the grating dependence with temperature was measured by inserting the FBG into a thermally-controlled oven. From Fig. 3.3 it is observed that the central frequency of the grating resonance presents a thermal coefficient of -1.233 GHz/°C.

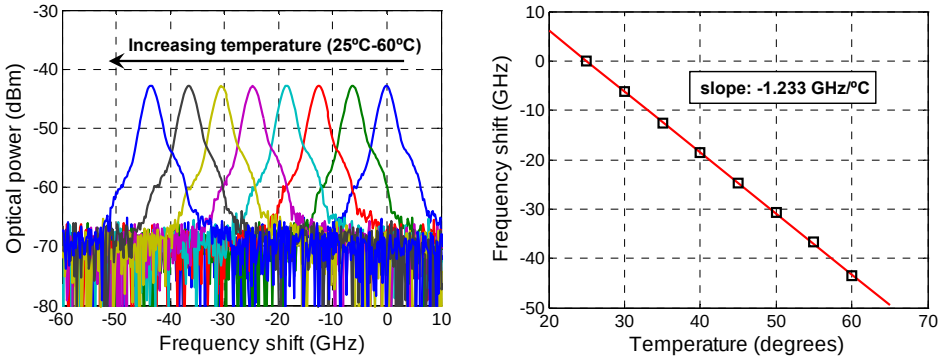

(a) (b)

Figure 3.3: (a) Spectra of the grating reflections by increasing temperature. (b) FBG resonance central frequency as a function of temperature.

The experimental layout to investigate the distribution of the FBG spectrum is depicted in Fig. 3.4. A DFB-LD operating at 1549 nm was used as a light source. The output light was externally modulated by means of an EOM through a 2 ns repetition rate pulse train, equivalent to 40 cm in distance that is twice round-trip propagation distance through the fiber sensor. Therefore, it was guaranteed that only one pulse travels along the entire length of the grating, leading no reflection overlapping between neighboring pulses. In addition, a nonlinear-optical loop mirror (NOLM) [75] was inserted at the output of the EOM in order to compress the optical pulse and eliminate any stray background DC component present on the optical pulse, thus to avoid any interference noise possibly caused by CW reflections. As a result, a Gaussian-shaped optical pulse with FWHM duration of 20 ps, corresponding to a spatial resolution of 4 mm, was generated, as shown in the inset of Fig. 3.4. To accurately measure the distribution of the grating spectral characteristics, the central frequency of the signal pulse was precisely controlled by the injection current applied to the DFB-LD. An isolator was placed at the FBG output so as to avoid any undesired reflection from the end facet of the fiber. Finally, the reflected pulse was captured and monitored by means of an OSA and a high-speed oscilloscope.

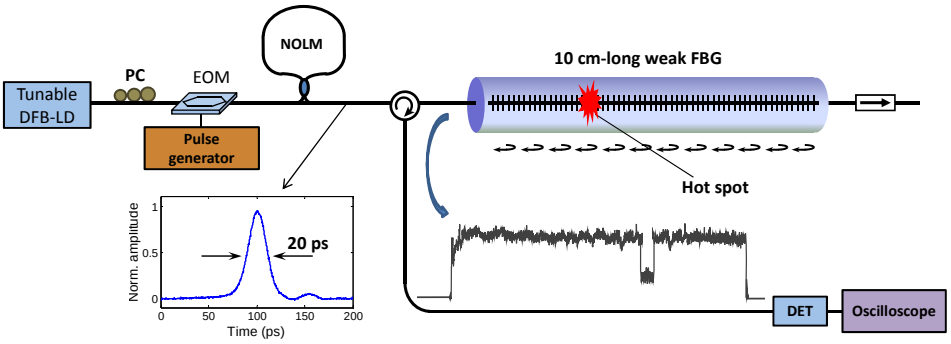

Figure 3.4: Experimental layout to interrogate temperature distribution with a 4 mm spatial resolution along the 10 cm-long FBG sensor.

Figures 3.5(a) and 3.5(b) illustrate, respectively, numerical results of the distributed FBG spectrum at room temperature and when inserting a hot spot at the center of the grating. The reflected pulse is simply the inverse Furier Transform of the product between the input pulse spectrum and the grating reflection response. On the other side, Fig. 3.6(a) shows an experimental measurement of the distributed FBG spectrum with 4 mm spatial resolution obtained by step-wise scanning the central frequency of the signal pulse. The central frequency of the FBG resonance was determined by the peak position of the reflection without any fitting process, as shown in Fig. 3.6(b). It is clearly observed that the FBG frequency exhibits around 2 GHz of variation along the grating when the ambient temperature along the whole length of the grating remains constant. This measured frequency deviation may be a result of a manufacturing non-uniformity. Nevertheless, it proves that the grating was nearly uniformly written along its 10 cm length. To validate the concept of the proposed distributed sensing system, an 8 mm-long hot spot was placed at the beginning of the grating, as shown in Fig. 3.7. A local Bragg frequency shift due to the temperature applied into the heated section is clearly observed. In addition, the frequency deviation of -31 GHz shown in Fig. 3.7(b) matches the temperature variation when the hot spot was set $\sim 25°C$ above the room temperature.

Figure 3.8 shows the normalized spectra for the FBG and reflected pulses at the beginning and at the end of the grating. The nominal FBG spectrum was measured under CW illumination giving a FWMH spectral width of 1.7 GHz. However, in the proposed configuration when an optical pulse was launched into the long grating, the FBG spectrum was measured to be 21.8 GHz, which roughly corresponds as expected to the optical pulse spectral width ($\sim$ 22 GHz). It means that in this type of distributed sensor the grating spectral response is automatically matching the pulse spectrum. In other words, the effective length of the grating is reduced to the pulse spatial width instead of the real physical grating length. In case of Gaussian transform-limited pulses, the spectral width of the pulse $\Delta v_{\mathrm{Pulse}}$ is given as $\Delta v_{\mathrm{Pulse}} \approx 0.441/\Delta T_{\mathrm{FWHM}}$ [61], where ΔT_{FWHM} denotes the pulse temporal width. It is important to notice the existence of a tradeoff between spatial resolution and temperature/strain accuracy in this type of sensing system. This means that when the signal pulse is significantly compressed to achieve a higher spatial resolution the

associated spectral broadening of the pulse and consequently of the FBG spectral response degrades the measurement accuracy. In addition, the results depicted in the figure show that the temporal width of the pulse reflection remains unaltered as it propagates along the grating. On the other hand, Fig. 3.9 illustrates the results to determine the measurement accuracy of the distributed sensing system. The FBG was stabilized in temperature and monitored along 2 hours. 20 time equispaced acquisitions of the grating central frequency distribution are depicted in Fig. 3.9(a). The standard deviation of these acquisitions is shown in Fig. 3.9(b), being its average value around 320 MHz. Thus, being $\sim$ 22 GHz the pulse spectral width and 0.32 GHz the spectral resolution, the resonance peak frequency can be measured with an accuracy of 1/70.

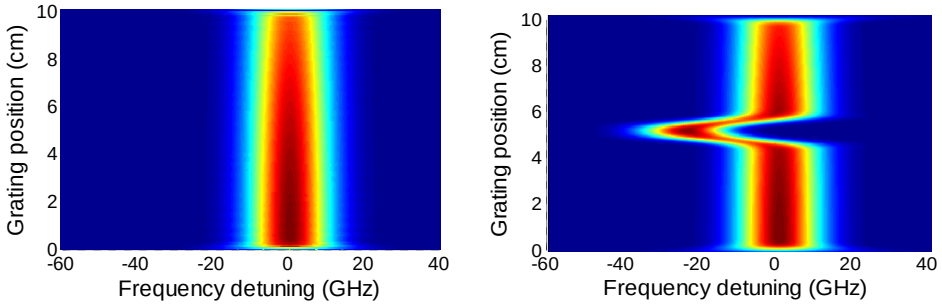

(a) (b)

Figure 3.5: Numerical results for the 3D mapping of the FBG spectrum (a) in normal condition and (b) when inserting a 5 mm hot spot at the center of the FBG.

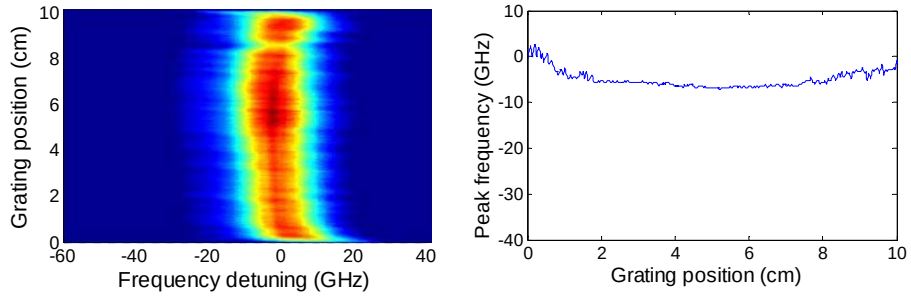

(a) (b)

Figure 3.6: (a) 3D mapping of the FBG spectrum and (b) grating central frequency distribution in normal condition.

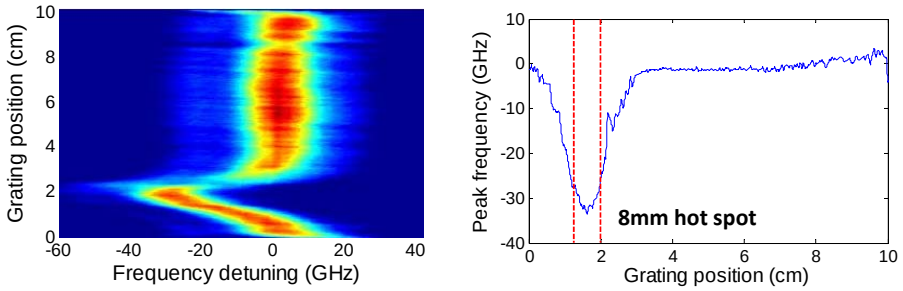

(a) (b)

Figure 3.7: (a) 3D mapping of the FBG spectrum and (b) FBG central frequency distribution when inserting an 8 mm hot piece of metal at the beginning of the FBG, heated $\sim 25°C$ above the room temperature.

Moreover, although the dispersion induced by such a weak grating can be considered negligible, the chromatic dispersion may act as a limitation in terms of the spatial resolution. For instance, if considering a 10 ps Gaussian transform-limited pulse (hence 1 mm spatial resolution) and the group velocity dispersion is 17 ps/km·nm, the pulse width broadening after propagating 1 km will be 1.0059. In this condition, no significant pulse broadening is observed, but this figure is important since it can estimate the maximum achievable sensing range without degrading the system performance for a desired spatial resolution.

This type of distributed sensor presents two crucial advantages when compared with any comparable distributed sensing systems based on stimulated scattering in fibers [76]: passive operation requiring no optical pumping, which is essentially required to create a fiber reflector and simpler configuration of the sensing setup.

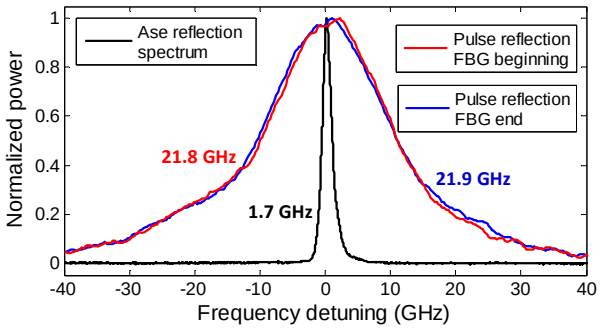

Figure 3.8: Measured spectral width for the FBG and reflected pulse.

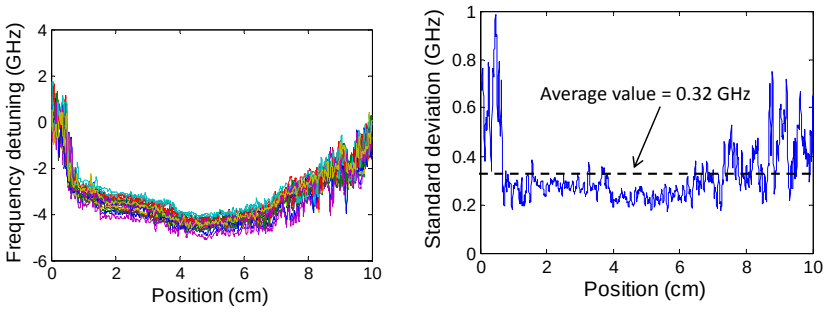

(a) (b)

Figure 3.9: (a) 20 acquisitions of the grating central frequency distribution at room temperature. (b) Standard deviation of the grating central frequency distribution at room temperature.

3.4 Tunable delay line

The proposed distributed sensor technique has been adapted to realize a simple all-fiber mechanically tunable delay line. By deploying the experimental setup illustrated in Fig. 3.4, the delay line performance can be easily accomplished just matching the central frequency of the optical pulse with that of the hot spot. The frequency-shifted grating can be repositioned by simply changing mechanically the temperature/strain position. Therefore, the round trip time of a signal spectrally positioned on the hot spot resonance can be tuned to achieve time delays as long as twice the grating single transit time.

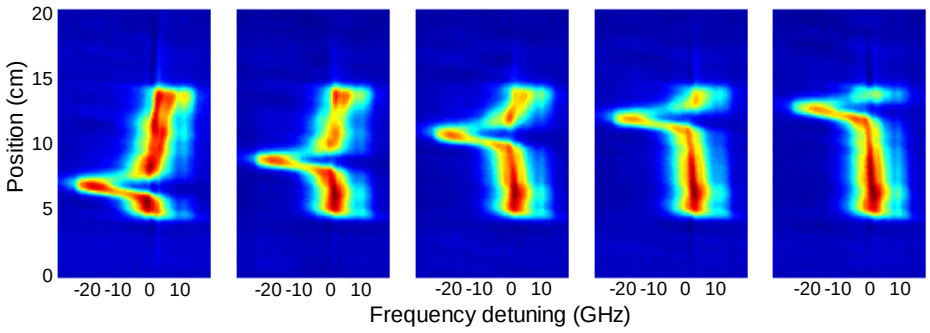

Figure 3.10: Spectrogram of the FBG distributed measurement while moving a 5 mm hot spot along the grating.

Figure 3.10 illustrates the 3-D maps of the measured FBG spectra while displacing a 5 mm hot spot along the grating. This also demonstrates the real capability to fully perform distributed measurements. 50 ps Gaussian pulses were used probe the FBG. Around 18 GHz of peak deviation is observed at the position, where the hot spot acts as a dynamic grating. This spectral separation assures that the whole pulse

spectrum ($\sim$ 10 GHz bandwidth in this particular case) will be selectively reflected by the spectral response of the hot spot. In this way, the pulse shape will remain unaltered. On the other side, Fig. 3.11 shows the normalized time waveforms of a delayed single pulse for different hot spot locations. By tuning the grating position, the optical pulse could be continuously delayed. Time delays of the back-reflected signal were clearly proportional to the grating position. The maximum achievable delay in this delay line approach is essentially determined by twice the grating length. The largest time delay achieved in this experiment was 585 ps with a minor signal distortion, but could be extended to 1 ns since the grating length is 10 cm. The optical power reflectivity is given by the convolution of signal pulse spectrum and grating spectrum, which in this case was on the order of -30 dB. In addition, the proposed tunable delay line must be suitable for real data stream.

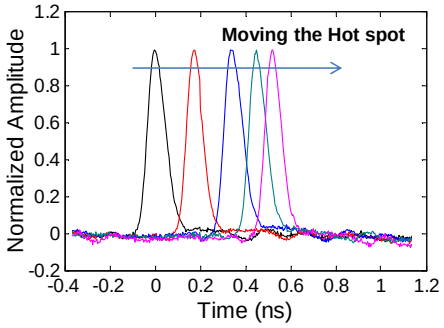

Figure 3.11: Time waveforms of the delayed signal pulses while moving the 5 mm hot spot along the grating.

3.5 MWP basic functionalities

The previously reported FBG-based distributed temperature/strain sensor brings the possibility of exploring MWP basic functionalities, i.e. phase shifters and TTDs. Besides, back-scattered reflections from different grating reflectors yields the combination of delayed replicas of the same signal in the photodetector, which means MWP filters.

In order to perform these MWP tasks through the distributed sensing system, hot spot tunability along the grating is required. Figure 3.12(a) illustrates the spectral location for the carrier, blue and red-shifted sidebands so as to carry out phase shifting and time delaying tasks, while Fig. 3.12(b) represents the phase response that would be obtained for each particular case after photodetection. For instance, TTD can be accomplished by placing both the carrier and sidebands at the same frequency resonance generated by the hot spot$_1$. Signal bandwidth and tunability result determined by the hot spot size and grating length, respectively. It must be noticed that the operational frequency of this TTD system is restricted with regards to the resonance bandwidth. Yet, several applications may not require true time delay operation and thus, frequency constraints can be relaxed. In such a way, simple

time delays can be achieved by placing the hot spot$_2$ at a fixed position within the grating. It is important to avoid the main grating reflection since a FP cavity is created, and thus multiple reflections could degrade the system performance. The red sideband is then reflected by the movable hot spot$_1$, while the optical carrier is back-scattered by the hot spot$_2$. This means an operational frequency only limited by the maximum temperature/strain change applied to the grating. For instance, these time delays can be used for tuning the spectral range of a MWP filter. Nevertheless, in a phased array antenna (PAA) system, changes in the operational frequency will introduce an uncontrolled beam squint in the radiating pattern. Hence, an additional phase shift for the optical carrier is required to perform TTD free from frequency constraints [36]. Finally, a tunable phase shifter can be implemented by placing the optical carrier in the central frequency of the movable resonance (hot spot$_1$) and the blue sideband at the hot spot$_2$ spectral position. It is important to notice that the frequency limitations reported for tunable delays are applied for this phase shifter approach.

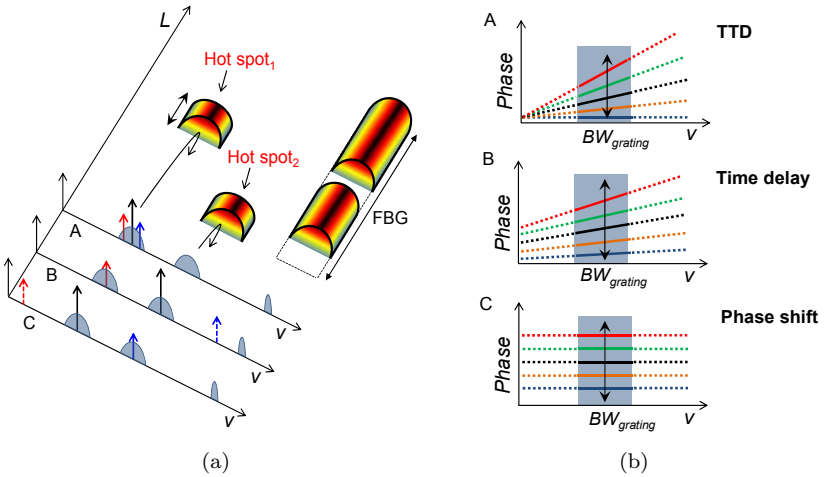

(a) (b)

Figure 3.12: (a) Hot spots physical positions within the grating and carrier, left and red-sideband spectral locations to accomplish MWP basic functionalities. (b) Illustration of TTD, time delay and phase shift over the grating bandwidth.

The suitability of implementing tunable phase shifting and time delaying tasks can be applied to perform reconfigurable MWP filters through multiple signal reflections along several hot spots. Figure 3.13(a) illustrates the different hot spots locations for the achievement of a three-tap MWP filter, while Fig. 3.13(b) depicts the filter frequency response that would be obtained. The same as occurred for the time delay implementation, the red sideband and the optical carrier are reflected by the hot spot$_1$ and hot spot$_2$, respectively. Nevertheless, two replicas of the hot spot$_1$ are introduced at different equispaced locations along the grating length so as to obtain different contributions of the same signal and thus, build up the filter after photodetection. It must be noticed that the equivalent length between hot spots in time corresponds to half the filter basic delay. The filter bandwidth and operational frequency of the filter remains determined, respectively, by the hot spot$_1$ length and position within the grating.

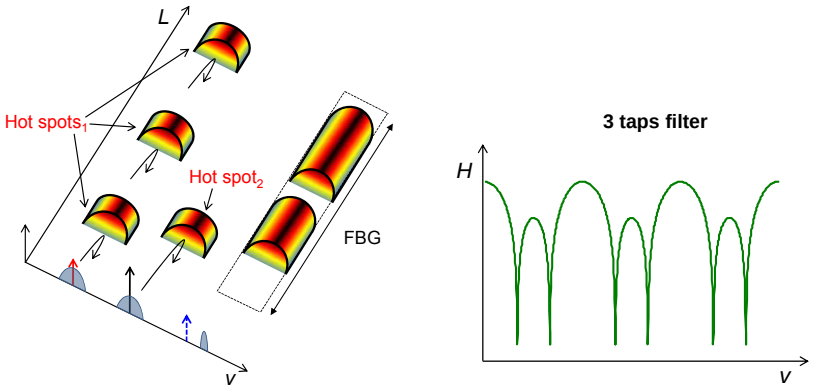

(a) (b)

Figure 3.13: (a) Hot spots physical positions within the grating and carrier, left and red-sideband spectral location to implement a MWP filter. (b) Simulated frequency response of a three-tap filter.

The main drawback of these MWP tasks rely on the thermal control of the grating. The FBG must be completely stabilized in temperature so as to avoid any frequency shift. In addition, the reconfiguration time reaches ms scales, which is larger compared with other SFL device platforms.

3.6 All-optical temporal integrator

The temporal integrator implementation is based on a previously proposed design [71, 77] using a simple uniform FBG. It has been shown that a weak-coupling uniform FBG operated in reflection provides the time integral of the electric field of an input arbitrary optical signal over a limited time window, which is fixed by the round-trip light propagation time along the total grating length. In contrast to previous experimental integrators based on resonant cavity filters [70], the FBG-based integrator design does not exhibit a fundamental limitation regarding the bandwidth of the optical signals to be processed. Thus, this approach is particularly appropriate for application in ultra-short optical pulse generation and processing.

The FBG-based integrator relies on the so-called time-domain design method, where the functionality of an ideal integrator is emulated over a finite time window using a linear optical filter [77]. Considering that the temporal impulse response of an ideal integrator is proportional to the unit step function, it has been demonstrated that a finite-time integrator can be implemented using a linear optical filter providing a constant temporal impulse response over a certain limited duration (operation time window of the integrator) [77,78]. As mentioned above, this required impulse response can be practically achieved from a weak-coupling uniform FBG working in reflection (see Fig. 3.14(a)). In this scheme, the optical signals to be processed must be spectrally centered at the Bragg frequency of the weak FBG. Thus, when a short pulse enters to the FBG, the reflected light becomes proportional to part of the pulse which

is inside the FBG. This way the reflected waveform represents the time integral of the input optical waveform. The theoretical input waveforms and the expected outputs from an ideal uniform FBG-based photonic integrator are shown in Fig. 3.14(b). The two different input pulse waveforms correspond to a transform-limited Gaussian optical pulse and a symmetric double-pulse waveform, consisting of two temporally separated in-phase replicas of the same Gaussian optical pulse. This integral extends over a finite time window, as determined by the grating length. It can be easily shown that the complex envelope of the output waveform after the integration time window is actually given by the time-inverted cumulative integral of the time-inverted version of the input temporal complex envelope [77].

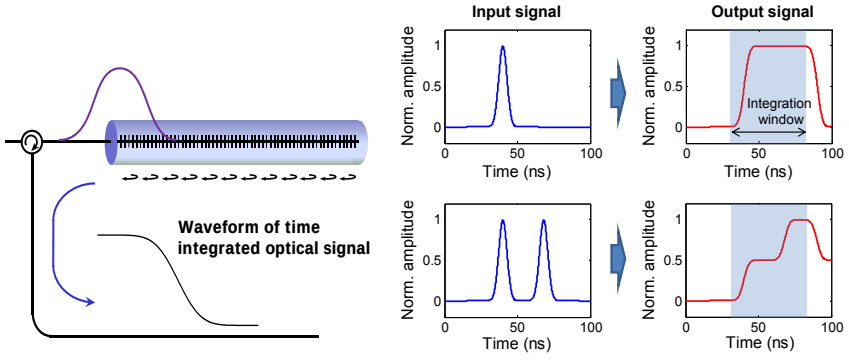

(a) (b)

Figure 3.14: (a) Schematic of a weak-coupling FBG-based integrator and its reflection temporal impulse response. (b) Theoretical input and output pulses from an ideal FBG-based temporal integrator for two different input waveforms: Gaussian pulse and symmetric double pulses.

A uniform FBG with length around 10 cm was used for the experimental demonstration, which corresponds to a maximum round-trip propagation time, i.e. integration time windows, around 1 ns. Operation in the weak-coupling regime was ensured by keeping the FBG peak reflectivity lower than 40%. A 50 ps FWHM Gaussian pulse, at a repetition rate of 500 MHz, was launched to probe the grating with its optical frequency centered at the FBG resonance. For the time-domain characterization of the pulse waveforms, a slow (6 GHz) and fast (20 GHz) oscilloscopes were employed.

Figure 3.15 shows the measured temporal complex envelopes for the input and output optical signals in the performed experiment. The results are only for the integration experiment of a Gaussian pulse. When a high-speed oscilloscope is used, the reconstructed temporal waveform at the FBG integrator output (red markers) shows an excellent agreement both with the numerical integration of the corresponding measured input pulse waveform (over the 250 ps integration time window) and with the theoretical predictions in Fig. 3.14(b). However, the pulse reflection measured with the 6 GHz oscilloscope (green markers), exhibits a temporal envelope which corresponds to a 170 ps integrated pulse, the faster pulse waveform that can be processed by this oscilloscope.

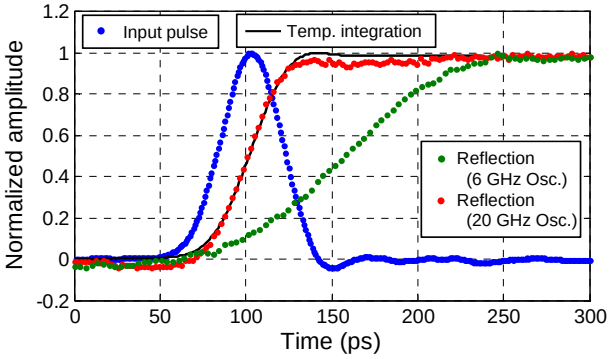

Figure 3.15: Measured (markers) and calculated (black solid curve) time traces of the transformed input signal for temporal integration when using a 6 GHz and a 20 GHz bandwidth oscilloscope.

3.7 Conclusions

In this chapter, a technique for complete analysis of the spectral characteristics of a long-length FBG and its potential application for fiber distributed sensing and signal processing of broadband optical signals has been demonstrated. A distributed temperature/strain sensing mechanism with 4 mm spatial resolution has been reported along a 10 cm length weak FBG. The spatial resolution is only determined by the time duration of the input pulse used to probe the grating. A method for achieving large signal delays with very low distortion in FBGs has also been ad-dressed. 50 ps Gaussian pulses have been continuously delayed up to 585 ps by relocating a hot piece of metal along the entire grating. The suitability of implementing tunable phase shifts and true time delays through the distributed FBG approach has been described by relocating several hot spots within the grating. In addition, it has been shown the time integral of the electric field of an input arbitrary optical signal over a 1 ns time window, which is equivalent to twice the propagation length of the FBG.

The capabilities of the FBG approach in terms of signal processing and distributed temperature/strain sensing have been performed in a device whose size is in the order of DBG's scale (cm-scale). However, the main advantages of this technological platform compared with DBGs rely on its passive operation requiring no optical pumping as well as the simpler experimental setup.

Some of the results of this chapter have been submitted to the following international publications:

- **J. Sancho**, S. Chin, D. Barrera, S. Sales and L. Thévenaz, "Time-resolved analysis of a long fiber Bragg grating: principle and its applications", submitted to Optics Express, 2012.
- S. Chin, **J. Sancho**, D. Barrera, S. Sales and L. Thévenaz, "Time-resolved analysis of a long fiber Bragg grating: principle and its applications", in SPIE Photonics Europe, Brussels (Belgium), paper 8439-06, 2012.

Chapter 4

SFL effects in semiconductor optical amplifiers for MWP applications

4.1 Introduction

During the last decades, SOAs have been widely researched and developed to accomplish many different signal processing tasks in optical communication systems through several nonlinear effects, including self-phase modulation (SPM), XGM, cross phase modulation (XPM) and four wave mixing (FWM) effects. Key applications have included wavelength conversion [79], optical gates [80], and optical regeneration [81]. Among them, MWP applications are targeting higher operation frequencies and functionalities that are demanding small devices with low weight. Semiconductor based structures provide these features and also allow on-chip integration with other devices while lowering the manufacturing costs [13, 34, 82].

CPO effects in SOAs [83] constitute one of the most promising approaches for the processing of optically carried microwave signals. CPO effects offer continuous tunability of the delay, or phase shift, through the injected current, as well as the optical pump, providing another degree of freedom for manipulating the optical signal [13, 34, 82]. One of the most relevant advances of CPO in SOAs relay on the implementation of fully tunable 360 phase shifters over bandwidths in excess of several GHz [84]. However, when used for TTD generation, CPO effects have an intrinsic limit in terms of operating frequency range and bandwidth, which cannot exceed few hundred of MHz [85]. Counter-propagation XGM effects in SOAs enables to get rid of this limitations, leading to the generation of modest time delays at high frequencies in a single SOA device [86].

The remainder of this chapter is organized as follows. First, the principle of operation of the CPO-based phase shifter will be shown involving the cascade of several phase shifting stages. Then, an optical field model that contains the equations accounting for any general order of both harmonic and intermodulation distortions will be provided. Next, an experimental and theoretical analysis of the nonlinear distortion introduced in the phase shifter will be addressed for structures comprising

an SOA device under the CPO effect and an optical filtering stage. Different filtering scenarios will discussed in order to optimize the nonlinear performance. In addition, the cascade of three phase shifting stages comprising an SOA + filter will be subject of the same nonlinear evaluation, which will be accomplished as a function of the SOA input optical power, injection current and modulation frequency. Furthermore, a fully-tunable 360° microwave phase shifter implemented using only one SOA followed by a conveniently designed notch filter will be reported. In this way, four SOAs and two optical filters are saved in comparison with the cascaded approach. Besides, the performance of MWP phase shifters based on both the cascaded and single SOA approaches will be theoretically and experimentally evaluated in terms of several FOMs. In particular, gain, noise and nonlinear distortion will be characterized as a function of the phase tunability control mechanism. Following, a fully tunable notch-type filter will be demonstrated using the more compact solution. The achievement of true time delays using XGM in a nonlinear SOA will be provided after that. The results will be yield in a counter-propagation configuration between two optical beams.

4.2 Principle of operation

In this section, the physics underlying of CPO effects in active semiconductor waveguides will be briefly explained. Following, the enhancement of slow-down by optical filtering will be discussed and finally, the most significant advances to reach 360°, achieved by cascading several photonic shifting stages, will be provided.

4.2.1 Coherent population oscillations in SOAs

The physical process governing the SFL operation regime in SOAs is coherent population oscillations, which leads to FWM and complex XGM [12,87–89]. Basically, the CPO effect relies on the interaction between light and the propagation medium. Considering the SOA as a two-level system, when two laser beams with slightly different optical frequencies, denoted as the strong pump and weak probe, propagate through the semiconductor waveguide, the carrier population in the active region will oscillate at the frequency difference between the pump and the probe. This carrier oscillation will alter the gain experienced by the weak probe, as illustrated by the spectral notch in Fig. 4.1(a). The bandwidth of the spectral notch is characterized by the inverse of the carrier lifetime and leads to a large change of the refractive index dispersion, which finally accounts for the SFL effects [13].

Figure 4.1(b) sketches a basic phase shifter implementation where a microwave signal at the angular frequency Ω is initially intensity modulated onto a continuous-wave laser. In the frequency domain this implies that the optical signal at the Mach-Zehnder modulator (MZM) output is composed of a strong carrier acting as the pump, and two weak sidebands comprising the probes. Due to the consequent intensity-modulation of the population oscillation when propagating through the semiconductor, the gain and the refractive index will be also modulated in time and these temporal gratings will scatter the strong pump [13].The components scattered to both sidebands will thus modify the susceptibilities seen by the probes. Furthermore, it must be noted that the magnitude of the mentioned modification can be

controlled either by the injection current or the input optical pump power. Therefore, after the propagation in the semiconductor waveguide, the signal envelope will experience a time delay / advance Δt. After the photodetection process, this time delay or advance will correspond to a microwave phase shift $\Delta\phi = \Delta t\Omega$.

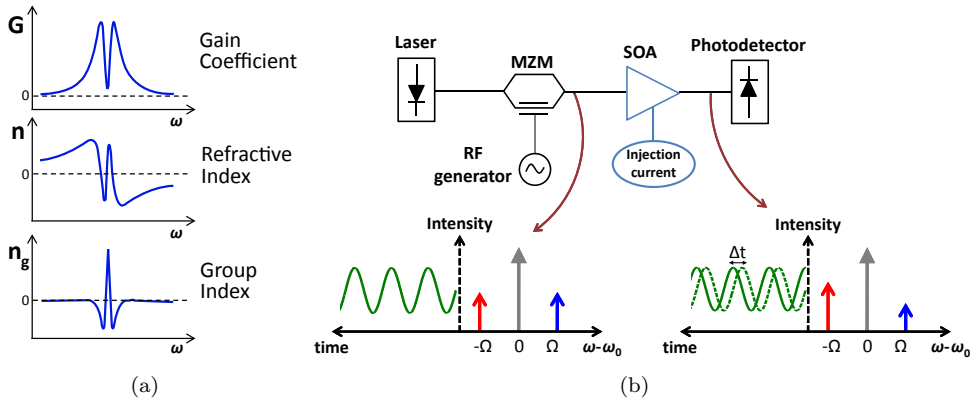

(a) (b)

Figure 4.1: (a) Gain, refractive index and group index resonance modification by coherent population oscillations. (b) Basic experimental scheme to realize SFL effects in semiconductor waveguides.

4.2.2 Enhancing the phase shifter performance by filtering

It has been confirmed in [34, 90, 91] that the use of CPO in standard SOAs presents a small time delay bandwidth product, what implies small microwave phase shifts ($\sim 30°$). Due to the detection of both microwave sidebands, the above mentioned refractive index dynamics cancel out and, hence, the phase change is governed solely by the gain dynamics. It has been suggested that the launching of a single sideband signal may enhance the degree of light-speed delay due to the effect of the refractive index dynamics [92]. However, the increase of the conjugate signal upon propagation will effectively counteract this effect. Instead, [93] and [94] demonstrated that the effects of the refractive index dynamics mediated wave mixing can be exploited to enhance the RF phase shift by the use of an optical filtering scheme prior to detection. Fig. 4.2(a) depicts the basic configuration. After propagation through the waveguide, the red-shifted sideband is blocked by an optical notch filter, which can be accomplished by an FBG. Figure 4.2(b) shows theoretical results comparing the cases of an unfiltered double sideband signal (green curve) and a single sideband signal with a blue (blue curve) and a red (red curve) frequency sideband, respectively. The results demonstrate that blocking the red-shifted sideband increases the range over which the phase shift can be tuned to approximate values of 150° for microwave frequencies up to 50 GHz.

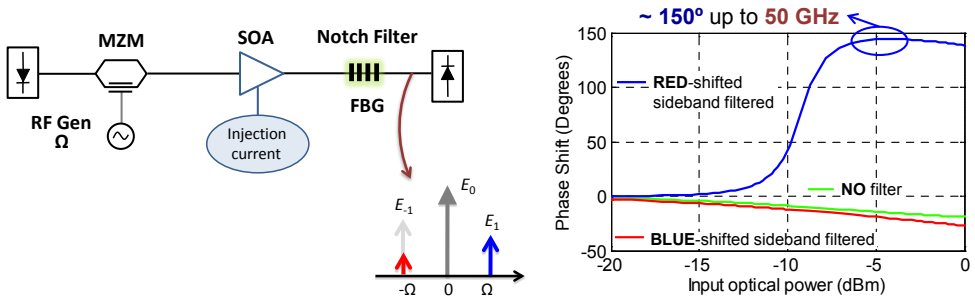

(a) (b)

Figure 4.2: (a) Basic scheme to enhance light slow-down by employing optical filtering to remove the red-shifted sideband before detection. (b) Microwave phase shift as a function of the optical power at the SOA input.

In order to describe qualitatively why large phase excursions can be obtained after the detection process, and only in the case of blocking the red sideband, a perturbation method has been studied in [93] and [94]. Considering a small propagation distance δL through the SOA, the spatial variation along the propagation coordinate of the gain and refractive index gratings can be neglected. Writing the input field as

$$E(t,z) = \left(E_0(z) + E_1(z)\, e^{j\Omega t} + E_{-1}(z)\, e^{-j\Omega t}\right) e^{j(\omega_0 t - \beta_0 z)}, \tag{4.1}$$

with carrier field amplitude E_0 and sidebands E_1 and E_{-1} detuned from the carrier by the microwave angular frequency Ω, the analytical expressions for the electrical field of the sidebands after amplification and interaction in the SOA can be expressed as

$$\begin{cases} E_1(\delta L) \cong \varepsilon\,(1 + \delta\gamma_1 + \alpha\delta\beta_1 + j\delta\beta_1 - j\alpha\delta\gamma_1) \\ E_{-1}(\delta L) \cong \varepsilon\,(1 + \delta\gamma_1 - \alpha\delta\beta_1 - j\delta\beta_1 - j\alpha\delta\gamma_1)\,. \end{cases} \tag{4.2}$$

Here, ε measures the strength of the sideband at the input, α is the linewidth enhancement factor and the quantities $\delta\gamma_1$ and $\delta\beta_1$ are given by

$$\begin{cases} \delta\gamma_1 = -g_{sat}\frac{(1+S)S}{(1+S)^2+(\Omega\tau_s)^2}\delta L \\ \delta\beta_1 = -g_{sat}\frac{\Omega\tau_s S}{(1+S)^2+(\Omega\tau_s)^2}\delta L \end{cases}, \tag{4.3}$$

where g_{sat} is the saturated modal gain, S is the power normalized to the saturation power and τ_s is the carrier lifetime. For an SOA with positive gain, both $\delta\gamma_1$ and $\delta\beta_1$ are always negative.

When both sidebands are detected after the SOA, the phase shift becomes $\delta\phi = arg\{1 + \delta\gamma_1 + j\delta\beta_1\}$. A phase advance which does not depend on the α factor. On the contrary, when the red-shifted sideband is blocked before detection, the phase change turns $\delta\phi_1 = arg\{1 + \delta\gamma_1 + \alpha\delta\beta_1 + j(\delta\beta_1 - \alpha\delta\gamma_1)\}$. This way a contribution term related to the α factor is included. It clearly demonstrates an additional large phase

delay introduced by a positive (increasing) $-\delta\gamma_1$ in the imaginary part and a negative (decreasing) term $\delta\beta_1$ in the real part. On the other hand, if the blue-shifted sideband is blocked, the phase shift becomes $\delta\phi_{-1} = arg\{1 + \delta\gamma_1 - \alpha\delta\beta_1 + j(\delta\beta_1 + \alpha\delta\gamma_1)\}$. In this case, the refractive index dynamics related to α factor will cancel out to a significant extent because the magnitudes of both real and imaginary parts are increased by two extra terms ($-\delta\beta_1$ and $j\delta\gamma_1$) and thus, the phase shift becomes similar to the conventional case, without optical filtering.

4.2.3 360° by cascading several SOA-based phase shifter stages

Optical filtering enhanced slow light in standalone SOAs allows to achieve a $\sim 150°$ continuously tunable microwave phase shift [93]. Nonetheless, saturation effects inside the SOA make not possible to increase that absolute phase shift value by increasing the length of the SOA [95]. Therefore, in order to further increase the total phase shift range beyond the values obtained for a single phase shifter stage (PSS), the possibility of cascading several such stages has been studied in [84]. However, due to the optical filtering process performed at the output of the SOA, the single-sideband characteristic of the optical signal at the input of the following PSS does not allow to obtain a significant microwave phase shift after propagation through this second slow light stage. In other words, simply cascading several optical filtering assisted slow light stages does not imply an increase of the expected microwave phase shift [95]. For the implementation of this full 360° functionality it is necessary to include another SOA, acting as a regenerator (RS), between two PSS (Fig. 4.3). By exploiting high-efficiency four-wave mixing effects, the double sideband characteristic will be restored. After the regeneration, the optical signal will regain the same optical spectrum as the initial input. Hence, by adding the second slow light stage, the modulated optical signal will experience a similar effect as in the first stage. It has been demonstrated that when a third stage is likewise incorporated, a phase shift of more than 360° can be achieved in the frequency range from a few GHz to 40 GHz [84].

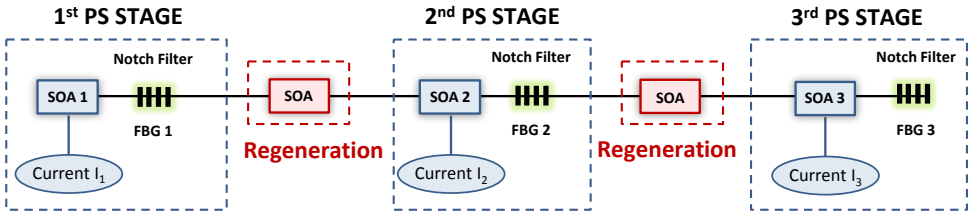

Figure 4.3: Simplified 360° microwave photonic phase shifter diagram showing the cascading of PSSs followed by regenerators.

However, since these phase shifters rely on signal propagation in active semiconductor waveguides, spontaneous emission adds noise to the signal, thus deteriorating the signal-to-noise ratio. Besides, it has been demonstrated [96] that filtering the signal after the SOA, apart from increasing the phase shift, further degrades the signal-to-noise ratio, predominantly due to the decrease of the RF amplitude. This degradation is noticeable when sequentially adding phase shifting stages [97]. In addi-

tion, the work reported in [98] addresses that the nonlinear distortion generated by the SOAs can further degrade the system performance.

4.3 Propagation model for the SOA-based phase shifter

As with any element in a microwave photonic link, the impact of the SOA-based phase shifter must be evaluated, especially in terms of the undesired nonlinear effects leading to harmonic and intermodulation distortions, which can degrade the systems performance [99]. A complete model based on this analysis for true time delay applications (SOA + detector configuration) has been recently published in the literature [98]. This model is based on the propagation of the optical intensities within the SOA devices. It has outlined the interplay that the contributions from direct amplification and the phase shifted components generated by CPO have on the evolution of third order nonlinear distortion terms.

However, for MWP phase shifters (SOA + optical filter + detector configuration), a full model on nonlinear distortion is missing. It must be stressed that a theory of multichannel amplification in SOAs has been developed in [100], which is based on the propagation of optical fields and takes into account intermodulation distortion for the particular case of M equispaced RF channels. However, the model does not consider the distortion induced at the amplifier input. The main purpose of the contribution that will be shown in this section is to develop a general model including every element required for microwave phase shifting operation.

Since many microwave photonic applications require operation at large modulation indices, it has been considered the undesirable, but potential, intermodulation and harmonic distortion (up to order D) introduced by a dual-drive electrooptic modulator (DD-EOM). Fig. 4.4 shows an electrical modulating signal composed of a general number M of tones of angular frequencies Ω_1, Ω_2, ... Ω_M.

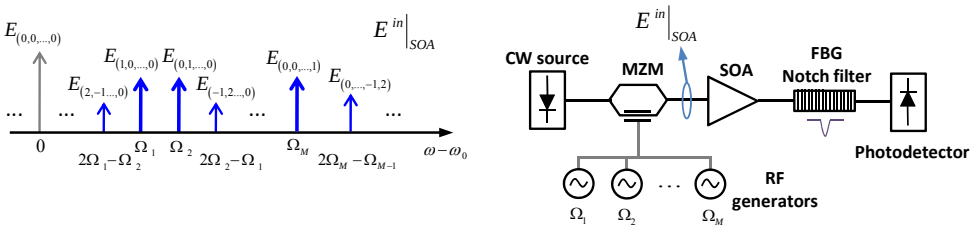

Figure 4.4: Schematic of the microwave photonic phase shifter and representative diagram of the spectral complex amplitude components at the SOA input.

For the determination of the output optical field of a DD-EOM, i.e. the initial conditions required at the input of the SOA device ($E^{in}\big|_{SOA}$), a general case applicable for any value of chirp in the EOM will be considered. This way the modulating signal is composed of two RF tones of angular frequencies Ω_1 and Ω_2. The voltage signals applied on both electrodes $V_a(t)$ and $V_b(t)$ can be defined as

$$\begin{aligned} V_a(t) &= V_{DC_a} + V_{RF_1}\cos(\Omega_1 t + \phi_{1a}) + V_{RF_2}\cos(\Omega_2 t + \phi_{2a}), \\ V_b(t) &= V_{DC_b} + V_{RF_1}\cos(\Omega_1 t + \phi_{1b}) + V_{RF_2}\cos(\Omega_2 t + \phi_{2b}), \end{aligned} \tag{4.4}$$

where each voltage is composed of a DC bias term, V_{DC_a} and V_{DC_b}. Besides, the RF tones are characterised by the same amplitude V_{RF_i} and different initial phases ϕ_{ia} and ϕ_{ib}, for $i = 1, 2$. Therefore, the general expression for the output optical field is given by

$$E_{out}(t)|_{EOM} = \frac{E_s}{2} e^{-j\frac{\pi}{V_\pi}\left[\frac{V_a(t)+V_b(t)}{2}\right]} \cos\left[\frac{\pi}{V_\pi}\left(\frac{V_a(t) - V_b(t)}{2}\right)\right], \tag{4.5}$$

where E_s comes from the input intensity provided by the laser and V_π is the quadrature voltage.

Reorganising terms in Eq. 4.5, the output optical field can be defined as

$$E_{out}(t)|_{EOM} = \frac{E_e}{4} e^{-j\phi_s} \left[\begin{array}{l} e^{j\varphi} e^{-j\frac{m_1}{2}\cos(\Omega_1 t + \phi_{1_b})} e^{-j\frac{m_2}{2}\cos(\Omega_2 t + \phi_{2b})} + \\ e^{-j\varphi} e^{-j\frac{m_1}{2}\cos(\Omega_1 t + \phi_{1_a})} e^{-j\frac{m_2}{2}\cos(\Omega_2 t + \phi_{2a})} \end{array} \right]. \tag{4.6}$$

where $\phi_s = (V_{DC_a} + V_{DC_a})\,\pi/(2V_\pi)$, φ represents the normalized bias voltage $\varphi = (V_{DC_a} - V_{DC_a})\,\pi/(2V_\pi)$ and the modulation indices are defined as $m_i = V_{RF_i}\pi/V_\pi$, for $i = 1, 2$.

After the expansion of the exponential terms in Eq. 4.6 in terms of Bessel functions of the first kind, the complex amplitude of the optical field, which will be injected at the SOA input port, can be expressed as

$$\begin{aligned} E_{out}(t)|_{EOM} = \tfrac{E_e}{2} e^{-j\phi_s} \sum_{k=-D}^{D} \sum_{l=-D}^{D} (-j)^{k+l} J_k(m_1) J_l(m_2) e^{j(k\Omega_1 + l\Omega_2)t} \\ \cdot \cos\left[\varphi + \tfrac{k(\phi_{1b} - \phi_{1a}) + l(\phi_{2b} - \phi_{2a})}{2}\right] e^{j\left[\frac{k(\phi_{1a} + \phi_{1b}) + l(\phi_{2a} + \phi_{2b})}{2}\right]}. \end{aligned} \tag{4.7}$$

Within the range of modulation frequencies and power level of interest, the carrier density is assumed to be linearly dependent on the optical intensity, and thus the main nonlinear mechanism that contributes to an oscillating gain is CPO [83]. Other mechanisms such as carrier heating, two-photon absorption, ultrafast nonlinear refraction, and spectral hole burning can be neglected since they have higher saturation powers [100]. Assuming the carrier density N to be spatially homogeneous, it can be stated that the interaction of light with carriers in the SOA is governed by the well-known carrier rate equation [83], defined as

$$\frac{dN}{dt} = \frac{I}{eV} - \frac{N}{\tau_s} - \Gamma a\,(N - N_{tr})\,|E|^2, \tag{4.8}$$

being I the injection current, e the unit electron charge, V the volume of the active region, τ_s the carrier lifetime, Γ the confinement factor, a the SOA differential gain and N_{tr} the transparency carrier density.

It has been considered an optical field which propagates along a traveling wave SOA given by

$$E(z,t) = \sum_{k_1=-D}^{D} \dots \sum_{\substack{k_M=-D \\ \left|\sum_{i=1}^{M} k_i\right| \leq D}}^{D} E_{(k_1,\dots k_M)} e^{-j\left[\left(\omega_o + \sum_{i=1}^{M} k_i\Omega_i\right)t - \sum_{i=1}^{M} \beta_{k_i\Omega_i} z\right]}, \tag{4.9}$$

where $E_{(k_1\dots,k_M)}$ defines the field complex amplitude and $\beta_{k_i\Omega_i}$ the propagation constant, both related to the angular frequency $\omega_0 + \sum_{i=1}^{M} k_i\Omega_i$, being ω_0 the angular frequency of the optical carrier while Ω_i the angular frequency of the i-th modulating tone. It is clear from Eq. 4.8 that the squared modulus (intensity) of the above field is required to solve the carrier rate equation.

Assuming perfect phase matching between the different RF terms and thus eliminating the z dependence in the exponential functions, the optical field from Eq. 4.9 can be expressed as

$$|E(t,z)|^2 = \sum_{k_1=-D}^{D} \dots \sum_{\substack{k_M=-D \\ \left|\sum_{i=1}^{M} k_i\right| \leq D}}^{D} \sum_{r_1=-D}^{D} \dots \sum_{\substack{r_M=-D \\ \left|\sum_{i=1}^{M} r_i\right| \leq D}}^{D} E_{(k_1,\dots k_M)} E^*_{(r_1,\dots r_M)} e^{-j\left[\sum_{i=1}^{M} (k_i - r_i)\Omega_i\right]t}, \tag{4.10}$$

which can be rewritten in terms of a Fourier series as

$$|E(t,z)|^2 = \sum_{m_1=-2D}^{2D} \dots \sum_{\substack{m_M=-2D \\ \left|\sum_{i=1}^{M} m_i\right| \leq 2D}}^{2D} S_{(m_1,\dots m_M)} e^{-j\left(\sum_{i=1}^{M} m_i\Omega_i\right)t}, \tag{4.11}$$

where $S_{(m_1,\dots m_M)}$ represents the component of the optical intensity at frequency $\sum_{i=1}^{M} m_i\Omega_i$ and can be defined as

$$S_{(m_1,\dots m_M)} = \sum_{k_1=-D+m_1}^{D} \dots \sum_{k_M=-D+m_N}^{D} E_{(k_1\dots,k_M)} E^*_{(k_1-m_1\dots,k_M-m_M)}, \tag{4.12}$$

being $\left|\sum_{i=1}^{M} k_i\right| \leq D$ and $\left|\sum_{i=1}^{M} k_i - m_i\right| \leq D$. Note that $S_{(-m_1,\dots -m_M)} = S^*_{(m_1,\dots m_M)}$, where * denotes the complex conjugate.

This optical beam interacts with carriers inside the semiconductor, through stimulated emission, and modulates the carrier density, introducing carrier population oscillations of RF frequencies $\sum_{i=1}^{M} m_i\Omega_i$. These oscillations generate, in turn, a temporal grating, causing dispersive gain and index modifications on the two sidebands of the travelling optical field while inducing wave mixing between them. It can be therefore assumed that the carrier density inside the SOA will oscillate following a similar variation, defined by

$$N(t) = \sum_{m_1=-2D}^{2D} \ldots \sum_{\substack{m_M=-2D \\ \left|\sum_{i=1}^{M} m_i\right| \leq 2D}}^{2D} N_{(m_1,\ldots m_M)} e^{-j\left(\sum_{i=1}^{M} m_i\Omega_i\right)t}. \tag{4.13}$$

From Eq. 4.13, the following coupled differential equation is determined as

$$\frac{dN(t)}{dt} = \sum_{m_1=-2D}^{2D} \ldots \sum_{\substack{m_M=-2D \\ \left|\sum_{i=1}^{M} m_i\right| \leq 2D}}^{2D} \left[-j\left(\sum_{i=1}^{M} m_i\Omega_i\right) N_{(m_1,\ldots m_M)} e^{-j\left(\sum_{i=1}^{M} m_i\Omega_i\right)t}\right]. \tag{4.14}$$

Substituting Eq. 4.11 - 4.14 into Eq. 4.8 and identifying the left and right handside terms for every frequency component in the carrier rate equation, yields the coefficients for the dynamic evolution of the gain, which can be expressed as

$$g(t) = \sum_{m_1=-2D}^{2D} \ldots \sum_{\substack{m_M=-2D \\ \left|\sum_{i=1}^{M} m_i\right| \leq 2D}}^{2D} g_{(m_1,\ldots m_M)} e^{-j\left(\sum_{i=1}^{M} m_i\Omega_i\right)t}. \tag{4.15}$$

It should be noted that for the last term in Eq. 4.8, a first order perturbation is taken since the small RF signal approximation is assumed, therefore

$$(N - N_{tr})\,|E|^2 \approx \left(N_{(0,\ldots 0)} - N_{tr}\right)|E|^2 + S_{(0,\ldots 0)}N - S_{(0,\ldots 0)}N_{(0,\ldots 0)}. \tag{4.16}$$

Defining the DC gain component as $g_{(0,\ldots 0)} = \Gamma a\left(N_{(0,\ldots 0)} - N_{tr}\right)$, it can be now expressed as

$$g_{(0,\ldots 0)} = \frac{\Gamma \bar{g}}{1 + S_{(0,\ldots 0)}/P_s}, \tag{4.17}$$

where $\bar{g}$ is the unsaturated modal gain given by

$$\bar{g} = a\left(\frac{I\tau_s}{eV} - N_{tr}\right), \tag{4.18}$$

while the saturation power is defined as $P_s = 1/(\Gamma a \tau_s)$.

For the rest of oscillating terms, the gain can be defined as

$$g_{(m_1,\dots m_M)} = \Gamma a N_{(m_1,\dots m_M)} = -\frac{g_{(0,\dots 0)}\frac{S_{(m_1,\dots m_M)}}{P_s}}{\left[1+\frac{S_{(0,\dots 0)}}{P_s} - j\left(\sum_{i=1}^{M} m_i\Omega_i\right)\tau_s\right]}. \tag{4.19}$$

Therefore, the dynamic evolution of the gain coefficient can be expressed as

$$g(t) = \sum_{m_1=-2D}^{2D} \dots \sum_{\substack{m_M=-2D \\ \left|\sum_{i=1}^{M} m_i\right| \le 2D}}^{2D} g_{(m_1,\dots m_M)} e^{-j\left(\sum_{i=1}^{M} m_i\Omega_i\right)t}. \tag{4.20}$$

The slowly varying envelope approximation of the propagation equation through the SOA device [100] is expressed as

$$\frac{dE}{dz} = \frac{1}{2}\left(-\gamma_{\text{int}} + g(1-j\alpha)\right)E, \tag{4.21}$$

where γ_{int} represents the internal waveguide losses and α the SOA linewidth enhancement factor.

Finally, substituting Eq. 4.9 and Eq. 4.20 in Eq. 4.21, the following coupled differential equation is derived as

$$\begin{aligned}&\frac{dE_{(k_1,\dots k_M)}}{dz} = \\ &-\frac{\gamma_{\text{int}}}{2}E_{(k_1,\dots k_M)} + \frac{(1-j\alpha)}{2}\sum_{m_1=-D+k_1}^{D+k_1} \dots \sum_{m_M=-D+k_M}^{D+k_M} g_{(m_1,\dots m_M)}E^{*}_{(k_1-m_1,\dots k_M-m_M)},\end{aligned} \tag{4.22}$$

being $\left|\sum_{i=1}^{M} k_i\right| \le D$ and $\left|\sum_{i=1}^{M} m_i\right| \le 2D$.

Eq. 4.22 can be solved using a fourth-order Runge–Kutta method, with the initial conditions for every complex field term being determined by the values of the field frequency components at the output of a DD-EOM.

Since the present contribution is based on an optical field model, the assessment of the optical filter at the output of the SOA can be evaluated as

$$E_{out}(z,t)|_{SOA+filter} = \sum_{k_1=-D}^{D} \cdots \sum_{\substack{k_M=-D \\ \left|\sum_{i=1}^{M} k_i\right| \leq D}}^{D} E_{(k_1,\ldots k_M)}\big|_{SOA} H_{(k_1,\ldots k_M)} e^{-j\left[\left(\omega_o + \sum_{i=1}^{M} k_i\Omega_i\right)t - \sum_{i=1}^{M} \beta_{k_i\Omega_i} z\right]}, \quad (4.23)$$

where $H_{(k_1,\ldots\ k_M)}$ represents the filter transfer function for each frequency component.

The microwave phase shift of interest for a given frequency component is that given by calculating the photocurrent i_d of a photodetector placed at the output of the SOA + filter for a detector responsivity $\Re$, as $i_{d(m_1,\ldots m_M)} = S_{(m_1,\ldots m_M)}\Re$, where the optical intensity $S_{(m_1,\ldots m_M)}$, comes through substituting the optical field obtained from Eq. 4.23 into Eq. 4.12.

The main contribution of this model relies on the consideration of M arbitrarily frequency-spaced modulating tones, in a way that every fundamental, harmonic and intermodulation distortion term falls at the same frequency locations within the channels band. In this context, another relevant aspect is the extension of the frequency components originated outside the initial electrical band. Besides, the model presented can be easily expanded to carry out the performance analysis of phase shifter cascaded structures.

4.4 Nonlinear distortion analysis in SOA-based phase shifters

The performance of the phase shifter device needs to be evaluated before its incorporation into a real MWP system, such as a filter [20] or phased array antenna [32]. Several FOMs provide the metrics capable for carrying out a MWP subsystem evaluation. Among the metrics, the spurious free dynamic range (SFDR) is one quality factor frequently employed in multi-channel systems or radar applications evaluating the time jitter influence. In this section, the harmonic (HD) and intermodulation distortions (IMD), which yields to the SFDR assessment, will be evaluated as a function of the phase shifter control mechanism.

The impact of the nonlinear distortion in the phase shifter performance has been accomplished through the photodetected RF power and phase shift evaluation at the system output. On one hand, the photodetected RF power can be defined as

$$P_{d(m_1,\ldots m_M)} = \left|S_{(m_1,\ldots m_M)}\Re\right|^2 Z_0, \quad (4.24)$$

being $S_{(m_1,\ldots m_M)}$ the Fourier component of the optical intensity specified in Eq. 4.12, and Z_0 the photodiode impedance. On the other hand, the photodetected phase shift is calculated as

$$\Delta\phi = \arg\left\{S_{(m_1,\ldots m_M)}\right\} - \phi_0, \tag{4.25}$$

where ϕ_0 is the microwave phase at some reference point, i.e. at fixed input power level and fixed bias condition for the SOA.

The general expression given by Eq. 4.7 to compute the optical field at the EOM output (initial conditions) has been applied. The particular case of a zero-chirp modulator, for which $V_a(t) = -V_b(t)$, has been considered since it is the kind of modulator used for the experimental validation. Under this assumption and particularizing for initial RF phases $\phi_{ia} = \phi_{ib} = 0$, the SOA initial condition for the complex field $E_{(k_1,k_2)}$ results in

$$E_{(k_1,k_2)}(t,0) = \frac{E_e}{2}\cos\left[\varphi/2 + (|k_1| + |k_2|)\,\pi/2\right] J_{k_1}(m_1) J_{k_2}(m_2) e^{j(k_1\Omega_1 + k_2\Omega_2)t}. \tag{4.26}$$

The remaining of this section is organized as follows. Sub-section 4.4.1 will be focused on the influence of the filtering scheme in the phase shifter performance, which will be based on a single stage (SOA + filter). The performance will be evaluated as a function of the SOA input optical power. First, the impact of the nonlinear distortion will be studied employing different optical filters at the input and output of the SOA device. Second, a more detailed distortion evaluation for two distinct spectral scenarios, with different filtering influence, will be provided. On the other hand, in sub-section 4.4.2 will be presented again the nonlinear assessment for cascaded structures (up to three phase shifter stages). The evaluation will be carried out as a function of the SOA injection current as well as the modulation frequency.

4.4.1 Nonlinear distortion influence on the filtering scheme

4.4.1.1 Harmonic distortion evaluation for different filtering scenarios

As it has been pointed out in section 4.2 of this chapter, when optical filtering is included to selectively suppress the red-shifted frequency sideband of the optical signal before photodetection, the refractive index dynamics leads to a considerable increase in the microwave phase shift. Yet, for those microwave photonic applications, where large signal operation is required, and consequently high level of nonlinear distortion is generated, two optical filtering schemes for suitable distortion reduction have been considered. An optical harmonic filtering stage prior to the SOA and a post optical filter implemented by an FBG operating in reflection has been considered, instead of considering a selective sideband notch filter as in previous literature [93, 94, 101]. Figure 4.5 shows the experimental setup assembled for evaluating the effect of harmonic distortion under the three aforementioned filtering schemes.

A DFB-LD operating at 1550nm was modulated by a 20 GHz microwave tone by means of a dual-drive zero-chirp EOM. The modulator was characterized by $V_\pi = 4$ V and was biased at $V_{DC} = 0.4975 \cdot V_\pi$. The bias was slightly different from the quadrature point $V_{DC} = 0.5 \cdot V_\pi$ in order to assure that a significat value of harmonic distortion was present at the SOA input. An electrical modulation index of $m = 14\%$

has been used to guarantee both small distortion and enough RF detected power to be above the floor of the RF spectral analyzer. The SOA injection current was set at 200 mA. An EDFA booster and a variable attenuator were used for controlling the optical input power in the measurements. On one hand, pre-filtering implementation (OF_1) was accomplish by a band-pass filter placed previous to the SOA. The band-pass filter was accomplished by an FBG operating in reflection, which requested the use of a circulator. This way the FBG attenuated more than 20 dB the high-order harmonics produced by the EOM. On the other hand, post-filtering scheme (OF_2) was carried out through two different FBGs, one operating in transmission (FBG TX) and the other one in reflection (FBG RX). FBG TX provided $\sim$ 40 dB attenuation level over the red-shifted fundamental frequency component, while $\sim$ 30 dB attenuation over both, the red-shifted sideband and the remaining higher order frequency components was given by the FBG RX. Finally, harmonic levels were measured using a lightwave spectrum analyzer (LSA), while the phase shift experienced by the fundamental tone was detected and measured by a VNA.

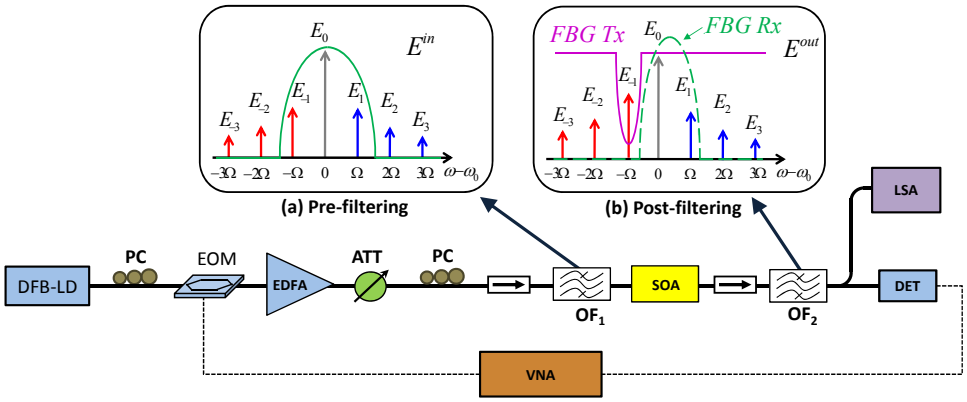

Figure 4.5: Experimental setup of a phase shifter based on different filtering schemes. (a) Optical filtering for harmonic distortion reduction before SOA propagation. (b) Both the FBG transmission and reflection schemes for optical post filtering.

The SOA device has been designed with a high output saturation power of 15 dBm. Some parameters that have been used in the previously described model are: linewidth enhancement factor $\alpha = 5$; cavity length $L = 1$ mm; unsaturable loss (1/m) $\gamma_{\text{int}} = 4/L$; unsaturated modal gain (1/m) $\Gamma\bar{g} = 5.5/L$. It must be stressed that the microwave phase shift, in this implementation, was optically controlled by means of the optical CW power at the SOA input.

Figure 4.6 depicts the computed and experimental values of the phase shifts as a function of the input optical power for different values of the modulation depth $q = |E_1(0)|^2/|E_0(0)|^2$. A significant dependence of the phase shift with the modulation index is observed in the post-filtering notch-type results. For higher modulation depths there is a large interaction between the fundamental tone and the harmonics within the SOA device, leading to phase fluctuations in the measured response. In order to overcome this dependence, the phase shifter results using the pre-filtering scheme are also represented in Fig. 4.6. As it is shown, the phase shift performance

is considerably more independent of the modulation depth. This means that harmonic distortion terms are significantly reduced since there is no substantial energy leak/phase change in the fundamental tone. Besides, less optical power is required to achieve a given phase shift value compared with the results shown for the post-filtering scheme.

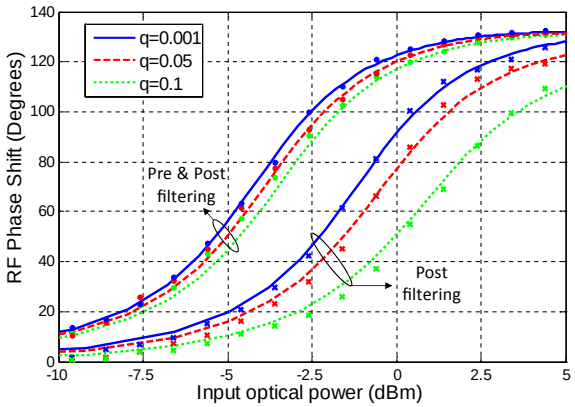

Figure 4.6: Theoretical (lines) and experimental (markers) RF phase shift for the case of post-filtering with an FBG operating in transmission and for simultaneous pre and post-filtering schemes.

However, the former scheme has the main drawback of requiring both pre and post-filtering stages. An efficient alternative to reduce harmonic distortion consists in using just a single band-pass post-filtering stage as shown at Fig. 4.5.

Figure 4.7 represents the theoretical and experimental photodetected RF power for the fundamental ($P(\Omega)$)and the second harmonic power ($P(2\Omega)$) versus the SOA input optical power. A low modulation depth ($q = 0.001$) was selected. Solid curves illustrate computed results while markers correspond to measurements. A relevant feature is the considerable increase of the second harmonic at the SOA output due to the semiconductor nonlinearities. Comparing with both post filtering configurations, it is noticeable how the inclusion of the optical notch filter (FBG Tx) results in a considerable increase of the nonlinear distortion level due to the CPO effect; which can be significantly decreased (by more than 10 dB) when resorting to the FBG operating in reflection. As expected [93], the photodetected RF power at the output $P(\Omega)_{out}$ shows, for both post filtering setups, a dip near to -2 dBm which is correlated with the sharp increase of the microwave phase shift.

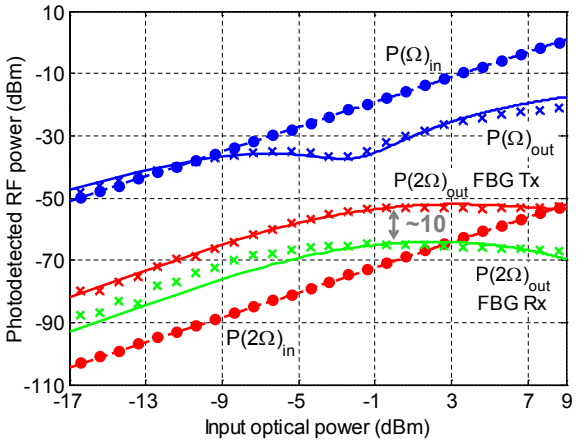

Figure 4.7: Theoretical (lines) and experimental (markers) results for the photodetected RF power from the fundamental tone, $P(\Omega)$, and the second harmonic, $P(2\Omega)$, versus the input optical power. The dashed curves are the calculated harmonics before the SOA and the solid curves are the calculated harmonics after the SOA+FBG, operating in transmission or in reflection.

4.4.1.2 Nonlinear distortion evaluation at different modulation frequencies

In multi-tone MWP systems where a phase shifter implementation based on CPO in SOA is required, the impact of nonlinear distortion leading to harmonic and intermodulation distortions needs to be evaluated. Two spectral separations have been considered in order to exhibit the spectral influence by the notch filter. The performance has been analyzed as a function of the SOA input optical power.

The detrimental nonlinear distortion generated by the microwave phase shifter has been studied assembling the experimental setup schematically depicted in Fig. 4.8. The DFB-LD output was modulated after passing through an external dual-drive zero-chirp EOM with two RF synthesizers. Both RF tones where generated at the same RF power while their spectral locations were selected in order to compare different optical filtering levels of the ref-shifted frequency components, that is, one case for $f_1 = 10.5$ GHz and $f_2 = 11$ GHz and another one for $f_1 = 9$ GHz and $f_2 = 12$ GHz. These frequency spacings ($\Delta f = f_2 - f_1$) of 0.5 and 3 GHz are representative of a broadband signal transmission scenario where different analogue or digital services can be located within the entire microwave or millimeter wave region, covering different MWP applications. The microwave phase shifter is formed by a commercial SOA and a filtering stage which has been implemented by an FBG operating in transmission. The SOA saturation power was 5 dBm at a bias current of 350 mA, characterized by a bandwidth over tens of GHz. The MZM output signal was amplified by a 20 dB-gain EDFA to assure the SOA operates under saturation conditions. The inset in Fig. 4.8 illustrates the FBG magnitude and phase responses. The magnitude notch presents a depth of -33 dB and a spectral -3 dB width of 11 GHz, while the maximum phase excursion of the spectral response has a value around 300 degrees. For better

understanding, the measured magnitude and phase shift responses of the FBG, as well as the spectral components affected by the grating, are shown in Fig. 4.9. Finally, the magnitude and the experienced phase shift of the fundamental, harmonic and intermodulation distortion terms were measured using a high-bandwidth VNA.

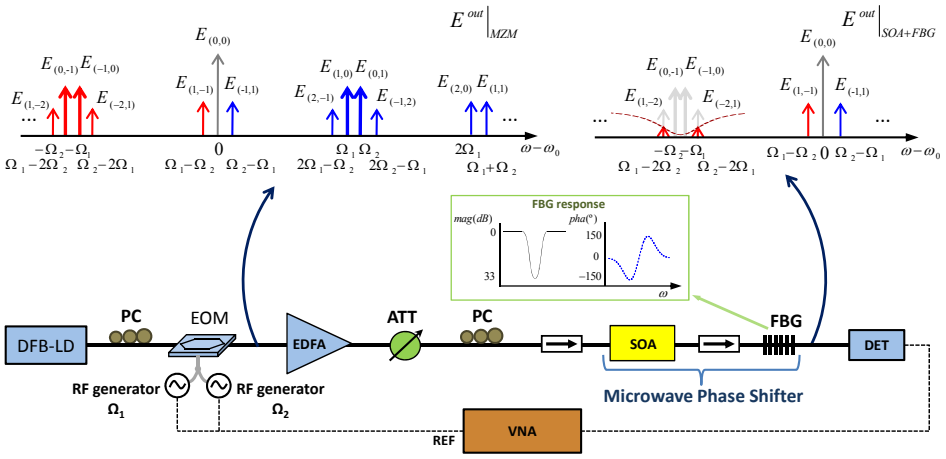

Figure 4.8: Schematic of the experimental setup to evaluate the nonlinear distortion at the output of a microwave phase shifter based on SOA + filtering scheme.

On one hand, harmonic and intermodulation product terms at the SOA input are illustrated in the left upper part of Fig. 4.8 ($E^{out}|_{MZM}$, which can be obtained from Eq. 4.7). The theoretical and experimental evaluation has been carried out for every fundamental, harmonic and intermodulation distortions tones up to 3^{rd} order, named as HD_3 and IMD_3. On the other hand, the diagram of the frequency components at the phase shifter output are depicted on the top right corner of Fig. 4.8 as ($E^{out}|_{SOA+FBG}$, which can be calculated from Eq. 4.23), where it can be appreciated how the notch filter blocks not only the fundamental tones at the red-shifted sideband (angular frequencies $-\Omega_1$ and $-\Omega_2$), yielding an attenuation level around 32 dB for $f_1 = 10.5$ GHz and $f_2 = 11$ GHz while 28 dB for 9 and 12 GHz, but also the 3rd order IMD terms placed at $\Omega_1 - 2\Omega_2$ and $\Omega_2 - 2\Omega_1$ providing an attenuation of around 32 dB and 5 dB, respectively, for each case.

Measured and computed results of both the photodetected RF power and experienced microwave phase shift, as a function of the optical power at the SOA input, for the case where the spectral separation between the modulating tones is 0.5 GHz (i.e. $f_1 = 10.5$ and $f_2 = 11$ GHz), are shown in Figs. 4.10 - 4.11. Fundamental tones and IMD3 terms placed at $2\Omega_1 - \Omega_2$ and $2\Omega_2 - \Omega_1$ are plotted in Fig. 4.10, while second order distortion elements (HD_2 and IMD_2) and IMD_3 contributions at $2\Omega_1 + \Omega_2$ and $2\Omega_2 + \Omega_1$ are illustrated in Fig. 4.11. On the other hand, the corresponding results for the case where $f_1 = 9$ GHz and $f_2 = 12$ GHz ($\Delta f = 3$ GHz) are illustrated in Figs. 4.12 - 4.13. The very good level of agreement between the theoretical (lines) results (from Eq. 4.24 and Eq. 4.25) and those rendered by the measurements (markers) confirms the validation of the aforementioned model.

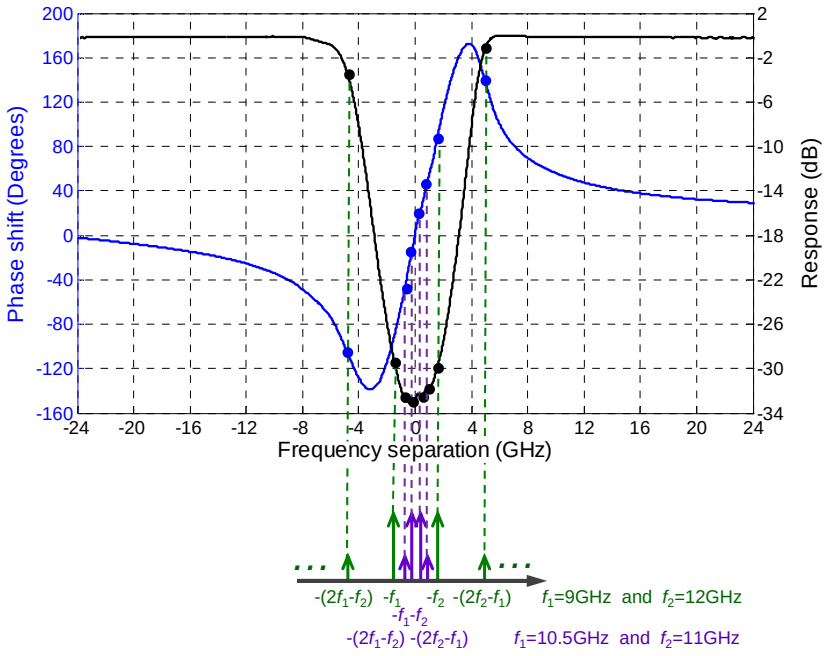

Figure 4.9: Measured FBG magnitude and phase shift reponses.

The following values for some of the parameters related to the SOA model described in the previous section (from Eq. 4.21) have been adopted in order to adjust computed and measured results: carrier lifetime τ_s = 110 psec, length L = 1 mm, unsaturable loss $\gamma_{\text{int}} = 4/L$, unsaturated modal gain $\Gamma\bar{g} = 5.5/L$, saturation power P_s = -6 dBm and a linewidth enhancement factor α = 7. The modeling of the optical filtering stage has been performed meticulously applying the pertinent measured values of attenuation and phase shift applied not only to the fundamental tones but also for all the DC, HD_2, IMD_2, HD_3 and IMD_3 terms. Note that in order to account for the effect of such filter, the optical field (and not the optical power) signal as obtained by solving Eq. 4.22 is requested.

The expected power dip / phase shift sharp transition of around 150° when filtering the red-shifted frequency sideband in the fundamental components is observed independently of the spectral separation between the evaluated electrical signals (see Figs. 4.10 and 4.12). However, smooth power / phase shift behavior is obtained for all the 2nd order terms (see Figs. 4.11 and 4.13), with a maximum phase advance of around 65°. Similar situation is established when no optical filtering stage is introduced after SOA propagation. It is interesting the behavior of the IMD_3 contributions placed at $2\Omega_1 + \Omega_2$ and $2\Omega_2 + \Omega_1$ (see Figs. 4.11 and 4.13), since their phase shift response tends to follow the sharp excursion characteristic of the fundamental signals, although no optical filtering has been implemented at their locations.

The effect of the FBG response on the IMD_3 terms placed at $2\Omega_1 - \Omega_2$ and $2\Omega_2 - \Omega_1$ is clearly appreciated when comparing between Δf = 0.5 and 3 GHz. On one hand, for Δf = 0.5 GHz, the high level of attenuation produced at these

frequencies (around 33 dB) results in a power notch similar to that occurred for the modulating signals connected to an even sharper phase shifter excursion. On the other hand, when $\Delta f = 3$ GHz, the photodetected power for these IMD_3 terms experiences a visible smoothed behavior correlated with a reduction, of the phase shift level from approximately 160° to 120°. Besides, the attenuation suffered from these is reduced to values of around 3 and 5 dB and, therefore, the large phase shift applied to these fields, due to the FBG, turns more significant after the photodetection beating. As it is observed in Fig. 4.13(b), both IMD_3 terms do not experience exactly the same behavior, since the FBG did not apply the same phase shift to them: 100° of negative phase shift for the $2\Omega_1 - \Omega_2$ term, while positive 150° for $2\Omega_2 - \Omega_1$. The above observations yield to state than not only the red sideband attenuation plays a significant role on the final photodected signal, but also the phase shift applied for the FBG to these fields.

In addition, when comparing both cases, more affected by noise phase shift data points have been measured for $\Delta f = 3$ GHz. This is a consequence of some thermal drifts experienced in the FBG response which lead to an appreciable fluctuation in the level of attenuation / phase shift applied by the filter. These fluctuations are more perceptible for the larger separation Δf, as in this case the fundamentals and, above all, both products at $2\Omega_1 - \Omega_2$ and $2\Omega_2 - \Omega_1$, are located in the slopes of the FBG notch response (see Fig. 4.9). Since at those frequencies the red shifted optical field components were only attenuated by 3 - 5 dB, the variations in the phase shift applied by the FBG become more sensible to possible optical wavelength drifts.

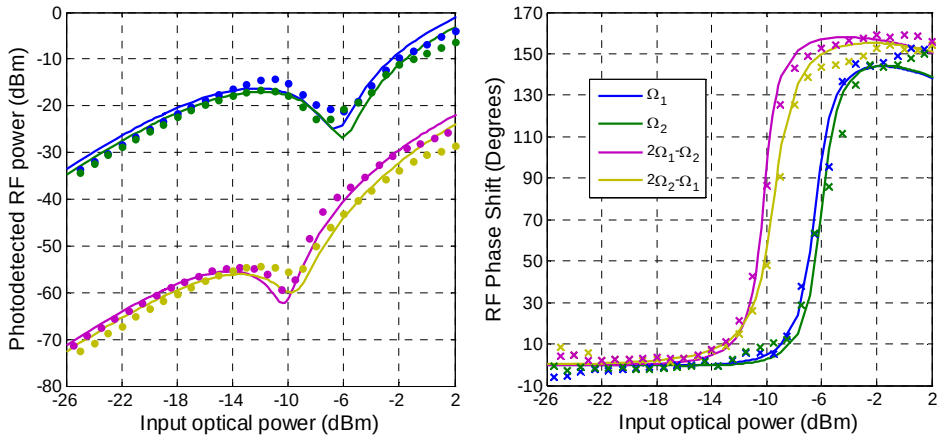

(a) (b)

Figure 4.10: Theoretical (lines) and experimental (markers) photodetected (a) RF power from fundamental [$P_{d(1,0)}$, $P_{d(0,1)}$] and IMD_3 [$P_{d(2,-1)}$, $P_{d(-1,2)}$] terms versus the SOA input optical power for $f_1 = 10.5$ GHz and $f_2 = 11$ GHz. (b) RF phase shift for [$\phi_{(1,0)}, \phi_{(0,1)}$] and [$\phi_{(2,-1)}, \phi_{(-1,2)}$].

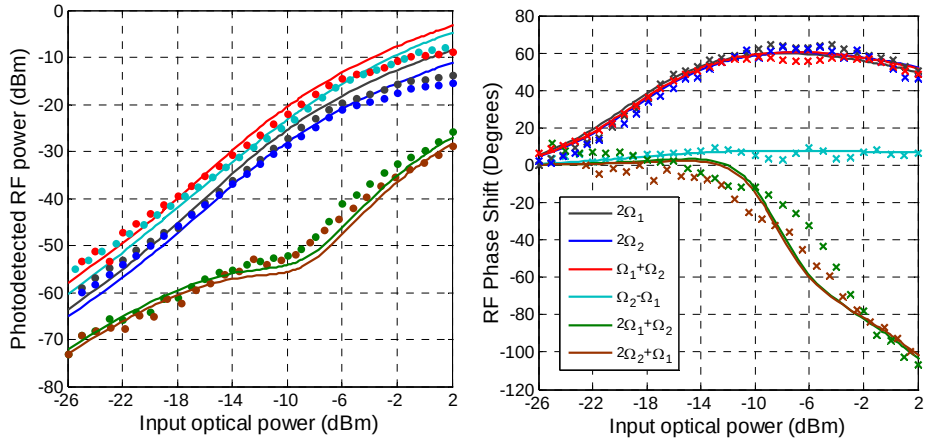

(a) (b)

Figure 4.11: Theoretical (lines) and experimental (markers) photodetected (a) RF power from HD_2 [$P_{d(2,0)}$, $P_{d(0,2)}$], IMD_2 [$P_{d(1,1)}$, $P_{d(-1,1)}$] and IMD_3 [$P_{d(2,1)}$, $P_{d(1,2)}$] terms versus the SOA input optical power for $f_1 = 10.5$ GHz and $f_2 = 11$ GHz. (b) RF phase shift for $[\phi_{(2,0)}, \phi_{(0,2)}]$, $[\phi_{(1,1)}, \phi_{(-1,1)}]$ and $[\phi_{(2,1)}, \phi_{(1,2)}]$.

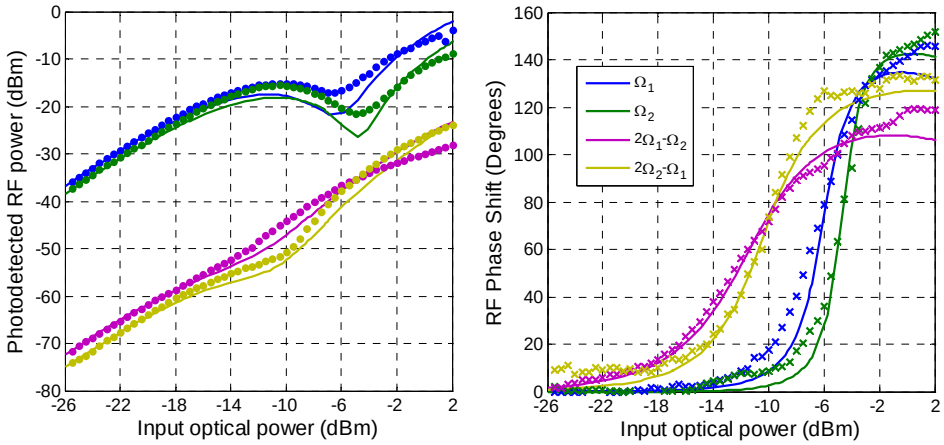

(a) (b)

Figure 4.12: Theoretical (lines) and experimental (markers) photodetected (a) RF power from fundamental [$P_{d(1,0)}$, $P_{d(0,1)}$] and IMD_3 [$P_{d(2,-1)}$, $P_{d(-1,2)}$] terms versus the SOA input optical power for $f_1 = 9$ GHz and $f_2 = 12$ GHz. (b) RF phase shift for $[\phi_{(1,0)}, \phi_{(0,1)}]$ and $[\phi_{(2,-1)}, \phi_{(-1,2)}]$.

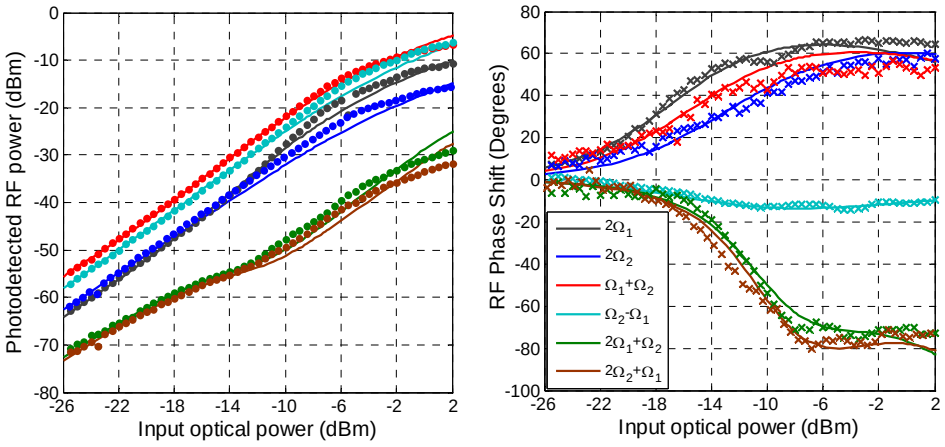

(a) (b)

Figure 4.13: Theoretical (lines) and experimental (markers) photodetected (a) RF power from HD_2 [$P_{d(2,0)}$, $P_{d(0,2)}$], IMD_2 [$P_{d(1,1)}$, $P_{d(-1,1)}$] and IMD_3 [$P_{d(2,1)}$, $P_{d(1,2)}$] terms versus the SOA input optical power for $f_1 = 9$ GHz and $f_2 = 12$ GHz. (b) RF phase shift for $[\phi_{(2,0)}, \phi_{(0,2)}]$, $[\phi_{(1,1)}, \phi_{(-1,1)}]$ and $[\phi_{(2,1)}, \phi_{(1,2)}]$.

The aforementioned theoretical model allows for exploring the possibility of designing potential applications in frequency and phase-tunable upconversion tasks. As it has been previously observed, the SOA increases the power of the second harmonic by a suitable post-filtering scheme. The idea is to take advantage of this functionality and, at the same time, by controlling the input CW power to the SOA to control the phase shift of the up-converted signal. The phase shift results for these upconverted signals ($2\Omega_1$ and $2\Omega_2$) are depicted in Figs. 4.11 and 4.13. As it can be clearly appreciated, a considerable phase excursion, which reaches more than 60 degrees, can be obtained for the upconverted tone which results in an extra degree of freedom.

4.4.2 Nonlinear distortion evaluation for cascading phase shifter stages

Once the HD and IMD, as well as the optical filtering influence, have been evaluated for a single phase shifter stage, the results for cascaded stages will be provided. The phase shifting control mechanism will be the SOA injection current into all the PSSs, instead of the input optical power employed in the previous subsection. This way the tunability speed becomes in the order of hundred of ps.

4.4.2.1 Evaluation of the phase shifter vs. the injection currents

As stated in section 4.2 of this chapter, an accumulated 360° phase shift functionality, by using the semiconductor technology, has traditionally required the cascade of up to three consecutive SOA + filter stages, [84]. However a complete evaluation of the

main figures of merit, including harmonic and intermodulation distortion, is missing for cascaded structures. From now on, the experimental and numerical evaluation for the nonlinear terms as a function of the involved SOA injection currents will be discussed at the output of each stage.

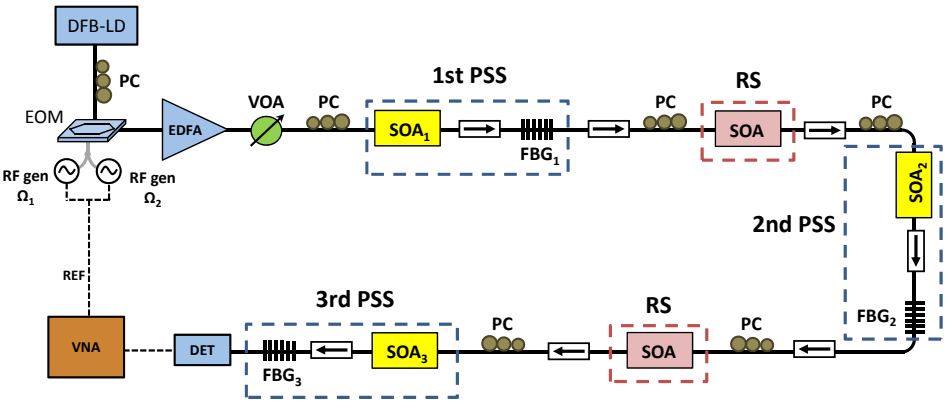

Figure 4.14: Experimental setup to evaluate the nonlinear distortion in three cascaded optical filtering enhanced slow light stages.

Figure 4.14 sketches the experimental setup involving a MWP phase shifter based on the cascade of three PSS, where a PSS is comprised of a SOA followed by an optical filter as described in sub-section 4.2.2 of the present chapter. The setup was made up by a DFB-LD operating in CW and placed at 1546.5 nm. Two RF signals with frequencies $f_1 = 20$ and $f_2 = 20.5$ GHz were imprinted on the optical carrier by means of a MZM. A low electrical modulation index was used. At the EDFA output, a variable optical attenuator (VOA) was used again to assure the proper optical power at the SOA input. Both the input and the output of the EDFA and SOA were appropriately isolated. Three identical FBGs were employed to block the lower frequency modulation sideband at the output of each stage, their transfer function is represented in Fig. 4.9. It must be taken into account that the semiconductor waveguides resorted for the implementation of the three PSSs, which were identically chosen, allow for a high wave interaction between the spectral terms along the structure, and also for high frequency CPO efficiency. The same currents were injected into both RSs (150 mA). A fixed input optical power level of 1 mW was adjusted at the first PSS input to assure that the SOA operates under saturation regime. The phase shift control mechanism consisted of progressively sweeping the injection current in the first, second and third PSSs, respectively. Particularly, the currents I_1, I_2 and I_3 were increased from 70 mA to 240 mA to achieve the desired total RF phase shift up to 360°. Both RF power variation and phase shift of the fundamental and nonlinear terms were measured using a high-frequency VNA. Theoretical results have been carried out by the aforementioned model through similar SOA parameters as used in previous sub-sections.

Figure 4.15 illustrates the measured and calculated photodetected RF power and phase shift for the fundamental and all the nonlinear distortion terms, as a function of the SOA injection current. Similar behavior for all the spectral terms

was obtained compared to distortion evaluation carried out as a function of the SOA optical input power and for the lowest spectral separation. At the system output, the total amount of $\sim 150^\circ$ RF phase shift is achieved at the fundamental frequencies, while $\sim 170^\circ$ is obtained for the IMD_3 terms. The corresponding microwave power changes are also shown in Fig. 4.15(a). A case without EOM distortion at the SOA input has also been considered in simulations. Only IMD_3 terms have been plotted since the rest of frequency terms shown a slightly deviation with respect to the normal distortion case. As it is observed, when there is no distortion prior the phase shifter, the SOA device generates the IMD_3 contributions with the power dip / phase shift transition located at similar injection currents than the fundamental terms.

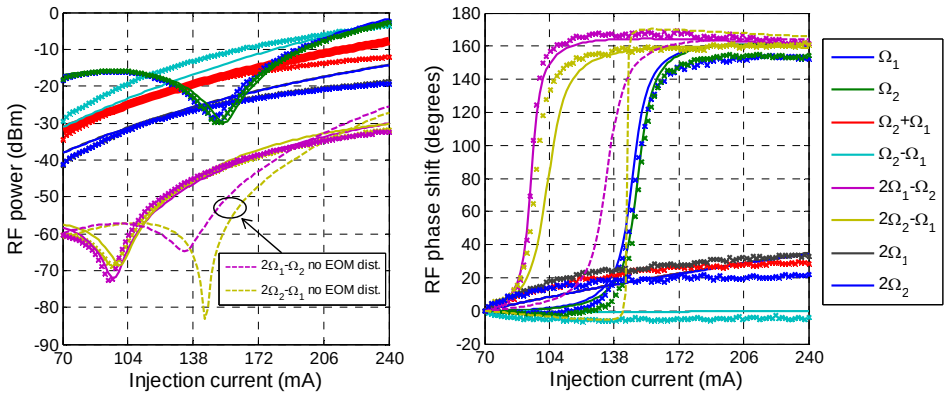

(a) (b)

Figure 4.15: Theoretical (lines) and experimental (markers) photodetected (a) RF power and (b) phase shift from fundamental, HD_2, IMD_2, HD_3 and IMD_3 terms versus the SOA injection current for $f_1 = 20$ GHz and $f_2 = 20.5$ GHz at the output of the first PSS.

Figure 4.16 shows the measured RF power changes and phase shifts for the fundamental and nonlinear terms at the output of the second PSS. It demonstrates the ability to double the microwave phase shift by cascading two optical filtering assisted SOAs. Initially, I_2 was fixed at 70 mA and then I_1 was continuously swept from 70 mA to 240 mA, obtaining in this way an accumulative phase shift of around 100° for the fundamental terms. However, it must be noted that no power dip / phase transition is observed for the IMD_3 terms. The current dependence of the RF phase shift is not as sharp as seen in [95]. This behavior can be attributed to the chirp of the optical signal propagation through SOA_1, first RS and SOA_2, since the magnitude of the phase shift depends strongly on the chirp when exploiting FWM effects in combination with optical filtering [95].

Following, I_2 was kept fixed at 240 mA. By increasing I_1 from 70 to 240 mA, the input optical signal into SOA_1 experiences a $\sim 150^\circ$ phase delay induced by SOA_2, which will be added to the phase shift imposed by SOA_1. The input optical signal into SOA_2 has a similar optical spectrum since the red-shifted sideband blocked by FBG_1 is restored after the regeneration. The final RF phase delay successfully reaches a phase shift of $\sim 270^\circ$ by cascading two PSSs, which is accompanied by more than

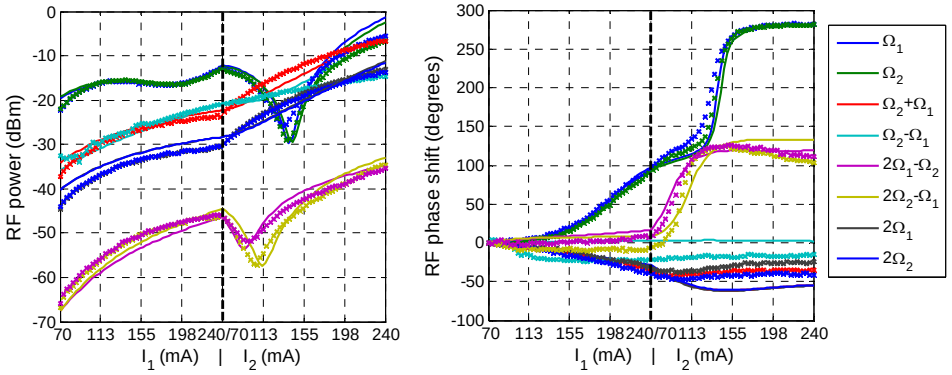

(a) (b)

Figure 4.16: Theoretical (lines) and experimental (markers) photodetected (a) RF power and (b) phase shift from fundamental, HD_2, IMD_2, HD_3 and IMD_3 terms versus the SOA injection current for $f_1 = 20$ GHz and $f_2 = 20.5$ GHz at the output of the second PSS.

20 dB of power variation for the fundamental tones. A sharp phase change of $\sim 130°$ is also shown for the IMD_3 frequencies. The power dips seen in the right part of Fig. 4.16(a) are correlated with the sharp phase change and is caused by SOA_2.

Figure 4.17 presents the measured and calculated photodetected RF power and phase shift for the fundamental and nonlinear distortion terms, as a function of the injection currents of SOA_1, SOA_2, and SOA_3. At the system output, $\sim 100°$, $\sim 105°$, and $\sim 190°$ phase delays are obtained by increasing I_1, I_2, and I_3, respectively. In this case, a total 395° phase shift at 20 GHz and 20.5 GHz is obtained. Since nonlinear phase shifts and large amplitude changes will be unacceptable for most MWP applications, these characteristics, as well as its frequency response, can be optimized by choosing different current combinations. Actually, by properly controlling all the three currents, less than 10 dB of RF power variation is possible to obtain. It is noticeable the high second order distortion increment at the third PSS output, while fundamental and IMD_3 terms experience a power level attenuation. It must be noted that the third stage misalignment, concerning the $\Omega_2 - \Omega_1$ term, is mainly due to the nonlinear behavior of the low-band frequency filter used by the VNA.

Among this, the good agreement observed between the theoretical and the experimental results verifies the scalability of the proposed scheme. Actually, not only the role of the five involved SOA devices have been taken into account for the theoretical simulations, but also the proper amplitude and phase change applied by every notch-filter to each optical field frequency component. Additionally, the frequency responses of the EOM, the EDFA and the photodetector have also been considered to obtain a proper validation of the experimental results.

Despite more than 360° have been achieved by cascading three PSS, the ASE noise could significantly reduce the carrier population, which in fact turns the regeneration efficiency weaker. To avoid this situation, three band-pass optical filters can be included after each PSS in the experimental setup shown in Fig. 4.14.

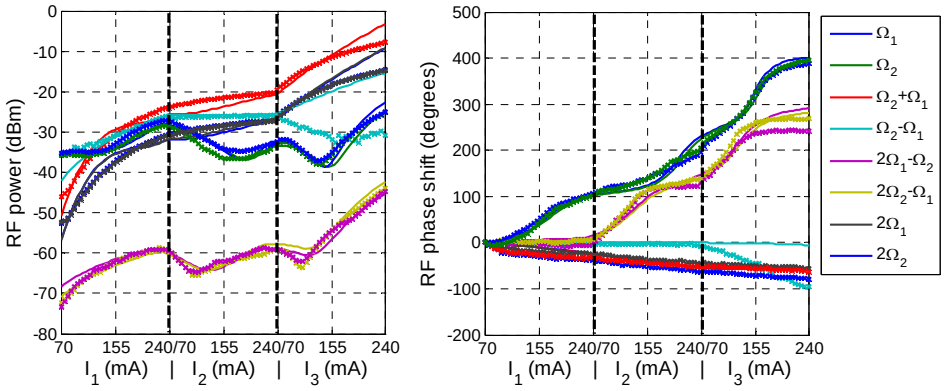

(a) (b)

Figure 4.17: Theoretical (lines) and experimental (markers) photodetected (a) RF power and (b) phase shift from fundamental, HD_2, IMD_2, HD_3 and IMD_3 terms versus the SOA injection current for $f_1 = 20$ GHz and $f_2 = 20.5$ GHz at the output of the third PSS.

4.4.2.2 Theoretical evaluation of the phase shifter vs. the modulating frequency

Targeting the evaluation of the nonlinear distortion influence on the frequency response, several simulations of the 360° phase shifter, comprising up to three PSSs, have been performed. Applications in MWP, such as filters, request broadband operation with a nearly constant RF power and phase shifts. The simulation results are capable of theoretically demonstrating the scalability of the phase shifting enhancement over a bandwidth of several tens of GHz. This feature becomes difficult to achieve in commercial microwave phase shifters or even in those based on other SFL approaches. Same values chosen for the proper adjustment of the theoretical and experimental results carried out in the previous section have been now applied for the analysis of the frequency response performance.

The frequency response of the photodetected RF power and phase shift from every fundamental tone, HD_2, IMD_2 and IMD_3 at the first PSS output and for a low modulation index is plotted in Fig. 4.18. It must be taken into account that every photodetected power and microwave phase shift curve has been plotted in terms of a common frequency. This is a generalized practice in the evaluation of the amplitudes and electrical powers of nonlinear RF terms. Both the RF power and phase shift have been calculated for the maximum ($I_{max} = 240$ mA) relative to the minimum current ($I_{min} = 70$ mA) used in the previous experiment.

A different spectral behavior is observed when comparing both fundamental signals with the rest of oscillating terms. When filtering the red-shifted frequency component, a maximum phase shift transition of around 160 degrees is obtained as expected for the tones at Ω_1 and Ω_2. This phase shift slope occurs at frequencies below a linear relation between the carrier lifetime τ_s and the linewidth enhancement factor α [93], while for higher frequencies the SOA pure amplification phenomenon

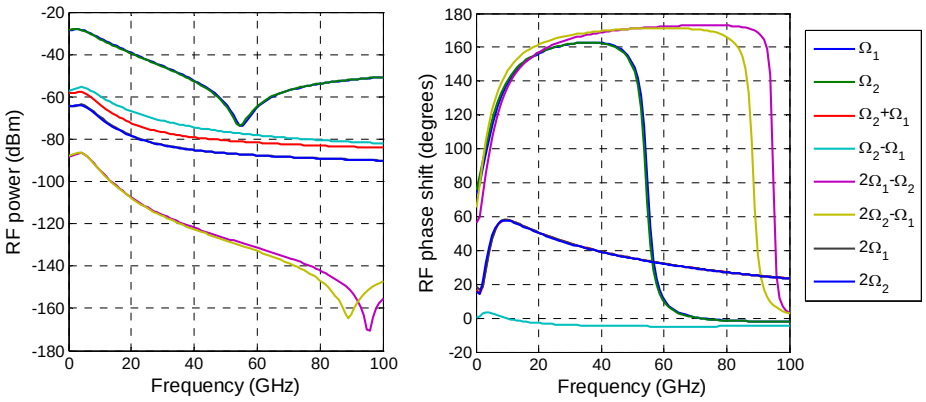

(a) (b)

Figure 4.18: Calculated (a) RF power and (b) phase shift as a function of the microwave frequency from fundamental, HD_2, IMD_2, HD_3 and IMD_3 terms at the output of the first PSS when $m = 0.01$.

dominates. For the fundamental tones, the power dip occurs where the signal is suffering a transition between these two regimes, being the one due to amplification in phase with the incident beat-note, while the CPO effect is in anti phase. However, in the case of HD and IMD_2 they mainly experience a low-pass frequency response, with no sharp transition in their respective phase shifts, in concordance with the results presented as a function of either the SOA injection current or input optical power. The IMD_3 frequency response is characterized by the same power dip / phase transition observed for the fundamental tones. The sharp phase shift transition, that characterizes the components at $2\Omega_1 - \Omega_2$ and $2\Omega_2 - \Omega_1$, reaches a remarkable maximum value of around 170°. Nonetheless, since lower injection currents are requested to perform the phase shift transition, as it is shown previously, the spectral bandwidth becomes higher than the fundamental frequencies.

The same results but for very high electrical modulation index are illustrated in Fig. 4.19. As expected, the RF phase shift performance is degraded since for very high m values there exists a non-negligible interaction between the fundamental and the different nonlinear contributions within the SOA, which consequently leads to important power and phase fluctuations. As it is shown, the nonlinear degradation turns higher at lower frequencies, since the higher the frequency, the lower the CPO efficiency becomes. It should be stressed that despite the above results correspond to large RF signal transmission, the application of the SOA device as a MWP linear phase shifting element must be considered under small signal regime.

Figure 4.20 illustrates the RF phase shift calculated values for different modulation indexes as a function of the microwave frequency. As it is observed, by increasing the electrical modulation index both the maximum achievable phase shift and linearity decay. For low modulation indexes, a quasi-linear behavior over almost 20 GHz is obtained; also more than 150° can be achieved up to 50 GHz, while less than 130° is obtained for higher modulation indexes. Better results can be accomplished by further increasing either the SOA injection current or the input optical power. Since

the phase shifter degradation can even, if required, be counteracted, an approach without EOM distortion has been considered in simulations. As it is shown, when distortion does not appear at the SOA input the phase shifter performance becomes improved. Actually, it turns difficult to get an EOM with no distortion generation, so in reality, it can be carried out by properly filtering the high-order harmonics and intermodulation products at the SOA input (band-pass filter). Furthermore, the same approach can be accomplished by filtering them after the SOA propagation simply modifying the selective notch filter that is required for assuring the MWP phase shifter functionality, as described in sub-section 4.4.1.1

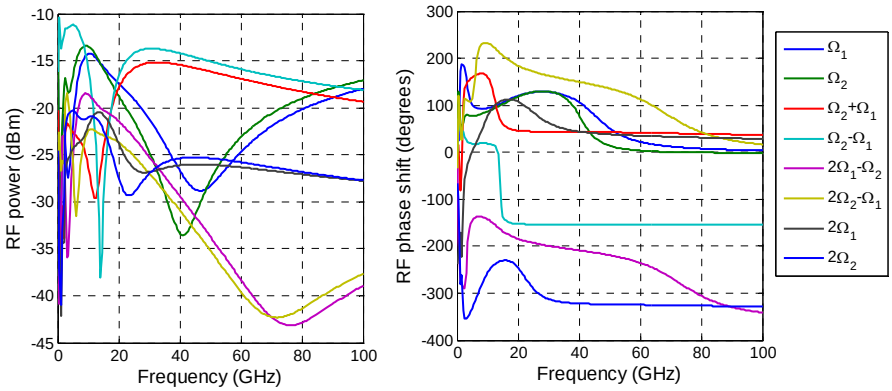

(a) (b)

Figure 4.19: Calculated (a) RF power and (b) phase shift as a function of the microwave frequency from fundamental, HD_2, IMD_2, HD_3 and IMD_3 terms at the output of the first PSS when $m = 0.5$.

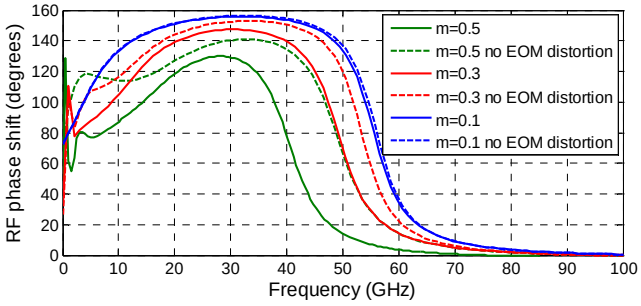

Figure 4.20: Calculated RF phase shift as a function of both the microwave frequency and electrical modulation index from the fundamental term at the output of the first PSS.

The frequency plots in Fig. 4.21 show the calculated RF power and phase shift from every fundamental tone, HD_2, IMD_2 and IMD_3 at the output of the second PSS. As expected, the two power notches are correlated with the two phase shift transitions for the fundamental frequencies. $\sim 290^\circ$ of maximum phase shift is obtained at the

neighboring frequencies of 20 GHz. Compared with one PSS, higher injection currents are requested to achieve the maximum phase value, which means less operational bandwidth. While IMD_3 terms address a similar behavior than the fundamental ones, less phase shift is obtained. In addition, the second notch is not observed at power curves since it occurs at further frequencies. It is important to mention that the spectral bandwidth of the notch-type filter used to block the red-shifted sideband, has not been taken into account in these simulations. Actually, the filter used for the experimental validation was characterized by a 10 GHz bandwidth. This means, not only a limited instantaneous bandwidth but also low frequency restrictions since the optical carrier must not be influenced by the filter.

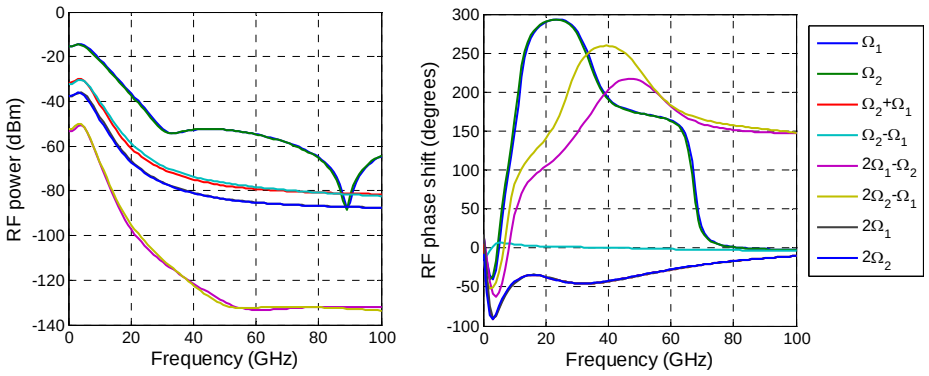

(a) (b)

Figure 4.21: Calculated (a) RF power and (b) phase shift as a function of the microwave frequency from fundamental, HD_2, IMD_2, HD_3 and IMD_3 terms at the output of the second PSS when $m = 0.01$.

Finally, the same frequency evaluation has been carried out when considering the whole three-PPS-based phase shifter. As it can be seen in in Fig. 4.22 a maximum phase shift value higher than 360° is achieved for the fundamental terms. As occurred for two PSSs, the higher the current needed to obtain the phase shift, the lower the operational frequency and bandwidth become. It is remarkable that only two notches are illustrated in the power plot although three were expected instead. Probably, a small third notch would appear at higher frequencies. Despite the harmonic and intermodulation distortions follow the same behavior that for previous stages, its noticeable in this case the higher power increasing of these terms compared with the fundamental tones.

For the SOA comprising each PSS and RS, as the microwave frequency increases, the phase shift generation and sideband regeneration efficiency will decrease. Dotted curves represent the calculated RF power and phase shift from the fundamental tones when the maximum injection current of all the three SOAs is further increased from 240 mA to 300 mA. As expected, not only the central frequency increases, but also the operational bandwidth where the maximum phase shift takes place. Compared with the 240 mA case, lower phase shifts are obtained at lower frequencies since once achieved maximum phase shift, increasing the injection currents turns detrimental due to saturation effects.

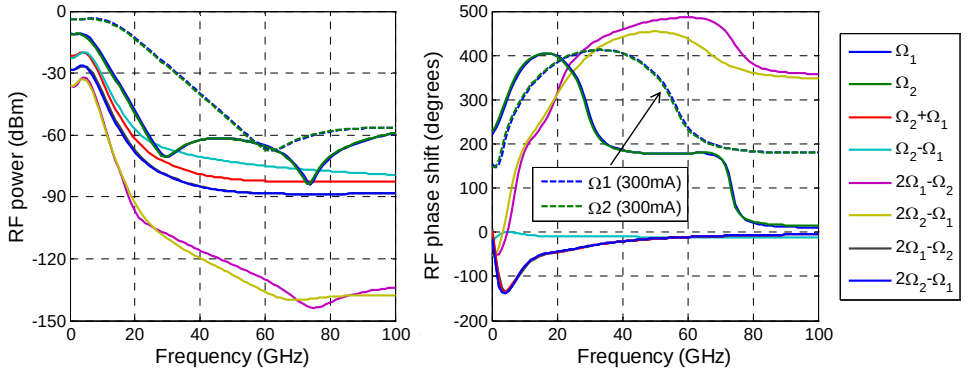

(a) (b)

Figure 4.22: Calculated (a) RF power and (b) phase shift as a function of the microwave frequency from fundamental, HD_2, IMD_2, HD_3 and IMD_3 terms at the output of the third PSS when $m = 0.01$.

4.5 Figures of merit for cascaded SOA-based phase shifter structures

With the objective of properly comparing the performance of MWP phase shifters implemented with different SFL technologies, a set of different Figures of Merit (FOM) must be analyzed. In this sense, the performance of the previously demonstrated cascaded-SOA-based full phase shifter will be evaluated in terms of the following well-known FOMs: the radiofrequency link gain (G_{RF}), the noise figure (NF) and the spurious free dynamic range (SFDR), [102]. Their characterization, which will require the built up of the experimental setup previously sketched in Fig. 4.14, will be accomplished in the phase shifter operation region governed by the combination of the three SOA injection currents.

The linear end-to-end RF gain (or loss) of a general MWP link is defined as the ratio of the RF power (at the modulating angular frequency Ω), delivered to a matched load at the photodetector output, to the available RF power at the input (at the same angular frequency Ω).

On the other hand, the degradation experienced by the microwave signal due to the existing noise sources will be accomplished by evaluating the noise figure parameter. In the present section, the laser noise contribution, the input and output thermal noises, the phase noise of the RF synthesizer, the shot noise as well as the amplified emission noise generated by the EDFA and all the five SOAs will be taken into account.

Finally, for the dynamic range evaluation, a common figure of merit will be resorted, the SFDR. It is widely employed to simultaneously characterize the linearity and noise characteristics of microwave devices, analogue-to-digital converters and optical devices such as laser diodes and external modulators [102–104]. It must be noted that the nonlinearity introduced by both the external electrooptic modulator and

optical processing stage can increase the nonlinear distortion affecting the SOA-based phase shifter, [98].

4.5.1 RF net gain evaluation

The RF net gain of a MWP link can be defined as the ratio between the RF power delivered at the detector output and the available RF power at the modulation device input,

$$G_{RF} \equiv 10 \log \left(\frac{P_{RF}|_{out}}{P_{RF}|_{in}} \right). \tag{4.27}$$

In addition, the input RF power can be expressed as a function of the modulation index (m), the quadrature voltage (V_π) and the RF generator impedance (Z_0) as

$$P_{RF}|_{in} = \frac{{V_{RF}}^2}{Z_o} = \frac{(mV_\pi/\pi)^2}{Z_o}. \tag{4.28}$$

Figure 4.23 reports the RF net gain as a function of the three PSS injection currents at the modulating frequency of 20 GHz (f_1). It is important to mention that the RF net gain keeps unaltered over a broad spectral bandwidth. Both measured (markers) and calculated (lines) results are illustrated showing good agreement. A common input power level of -15 dBm was obtained placing the photodetector at the input of the phase shifter. The results for the photodetected RF power, illustrated in the previous section, have been used to accomplish all the gain curves.

As it is clearly observed, the RF gain follows exactly the same behavior than the RF power at the output of each PSS, since the input RF power level does not depends on the injection current. The low RF gain values, especially for the third PSS, are mainly due to the saturation effects present in all the SOAs as well as the sideband suppression caused by the FBG. However, it can be improved by using amplification before photodetection.

On the other hand, the observed RF power variation within the phase shift tuning range represents a serious constraint to be considered. In particular, an RF power variation around 10 dB is obtained at the output of the third PSS. This fact could limit the assembling of this cascaded-SOA-based approach in real MWP applications.

The average RF net gain evolution as a function of the number of cascaded PSS is shown in Fig. 4.24. Average gain levels around 2 dB, -5 dB and -17 dB are obtained for the first, second and third PSS, respectively. It is important to notice that the large gain degradation, caused by further increasing from two to three PSSs, is due to the fact that the ASE noise accumulation at the input of the third PSS highly saturates the last stage.

Poor metrics performance can hamper the practical assembling in current applications. For this purpose, recommendations aiming at enhancing the performance of such an approach must be conveniently derived.

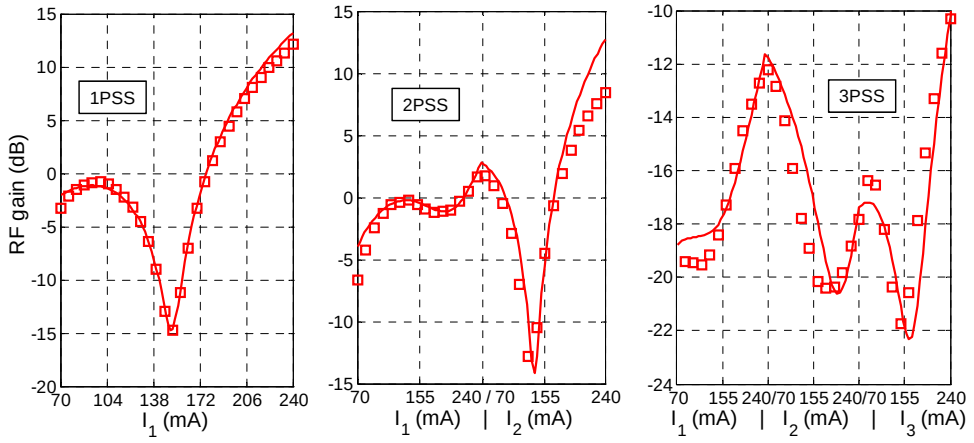

Figure 4.23: Theoretical (solid curves) and experimental (markers) RF net gain as a function of the SOA injection currents at the output of the (a) first, (b) second and (c) third PSS.

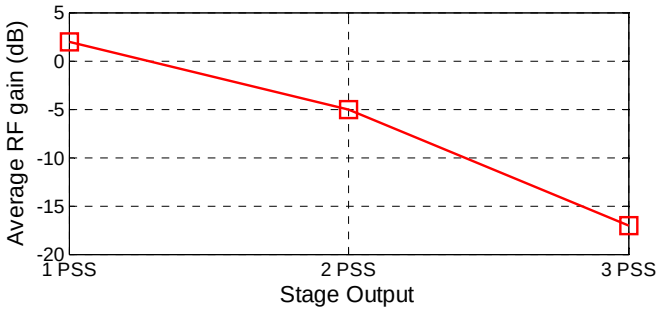

Figure 4.24: Average RF gain as a function of the stage output.

As already mentioned, the RF net gain can be improved by using amplification. Nonetheless, the RF output power variation is determined by the underlying physics of the CPO phenomenon accompanied by optical filtering. The phase shift slopes abruptness depends on the saturation status of all the SOAs and the degree of filtering of the lower frequency modulation sideband [94]. By adjusting the polarization state of the optical signal at each SOA input, the CPO efficiency can be controlled. This allows obtaining less deep RF power dips and consequently more relaxed linear behavior of the phase shift. As suspected, this fact would reduce the total RF power variation and therefore the NF peaks would also become lower.

4.5.2 Noise figure evaluation

As previously stated, the evaluation of the signal degradation in MWP links attending to the system added noise sources will require the analysis of the NF parameter [84]. NF is defined as the ratio of the signal-to-noise ratio at the input, SNR_{in}, to the signal-to-noise ratio at the output, SNR_{out}, while the SNR can be defined as the ratio between the RF power and the noise power level.

$$NF \equiv 10\log\left(\frac{SNR_{in}}{SNR_{out}}\right) = 10\log\left(\frac{P_{RF}|_{in}/P_{noise}|_{in}}{P_{RF}|_{out}/P_{noise}|_{out}}\right). \tag{4.29}$$

In such a cascaded structure (Fig. 4.14), several noise sources contribute to the total output noise level. In particular, the relative intensity noise of the laser (RIN), the phase noise of the RF synthesizer, the ASE noise generated by the amplifiers, the ASE and signal beat noise the thermal and shot noise.

$$P_{noise} = 10\log\left(\sigma^2_{RIN} + \sigma^2_{RF_{phase}} + \sigma^2_{ASE-ASE} + \sigma^2_{ASE-Signal} + \sigma^2_{Thermal} + \sigma^2_{Shot}\right). \tag{4.30}$$

Under typical real-application conditions, the term which mostly contributes to the total output noise is the ASE added by the SOAs [105].It is relevant to mention that the SOA gain has important implications on the ASE noise generation [106].

To characterize the dependence of the NF as a function of the injection current applied to each SOA, both the RF signal and noise levels must be obtained. These levels were measured at each PSS output to also characterize the impact of serially cascading stages on the noise performance.

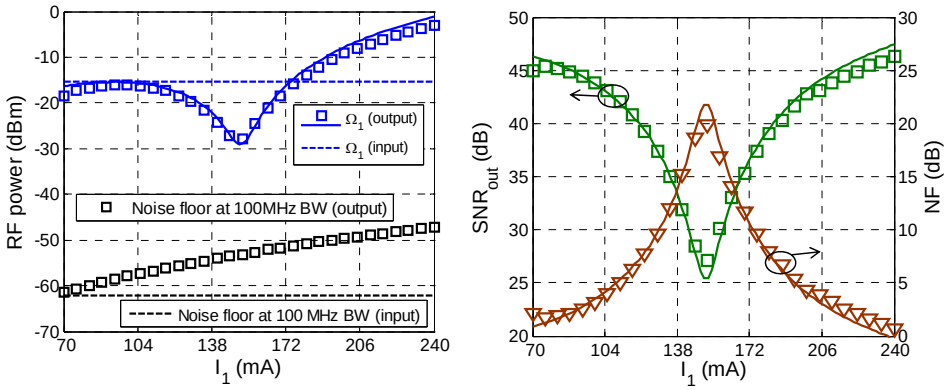

(a) (b)

Figure 4.25: Theoretical (solid curves) and experimental (markers) (a) RF power and noise level at the input (dashed curves) and output (markers), (b) SNR and NF as a function of the first PSS injection current.

Figure 4.25(a) illustrates the RF power and noise levels as a function of the SOA injection current at the input and output of the first PSS. An average RF power level of 13 dB is obtained. As it is observed, the noise increases according to the current I_1, specifically a noise degradation by more than 10 dB is obtained from 70 mA to 240 mA. The system bandwidth for noise integration purposes was 100 MHz. On the other hand, the evolution of the output SNR and final NF is shown on the right (Fig. 4.25(b)). The output SNR behavior mainly follows the RF output power showing a dip at the current where the maximum phase variation takes place. In average, an output SNR level of $\sim$ 40 dB is reached, while $\sim$ 48 dB of SNR has been obtained at the system input. It is important to remark that the SNR_{in} keeps unaltered as a function of the phase shifting control mechanism. As expected, the minimum in the SNR_{out} corresponds to the maximum level of NF. In general terms, the NF is characterized by the SNR_{out} complementary behavior. It must be noted that NF upper level of 20 dB is reached, while its average level turns around 8 dB.

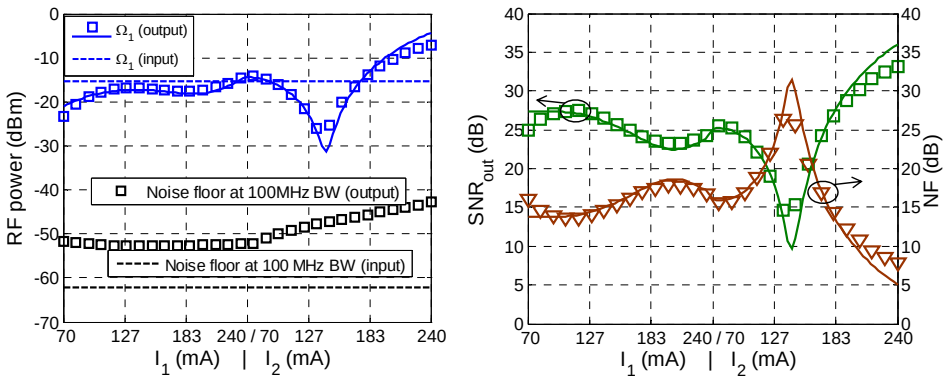

(a) (b)

Figure 4.26: Theoretical (solid curves) and experimental (markers) (a) RF power and noise level at the input (dashed curves) and output (markers), (b) SNR and NF as a function of the first and second PSS injection currents.

Figure 4.26(a) depicts the RF power and noise levels at the system input and second PSS output, while both the output SNR and NF are illustrated in Fig. 4.26(b). In this case, as expected, two SNR notches matching the maxima phase changes accomplished in both PSSs, respectively, can be observed. Since the saturation regime is different in both SOAs, different depth dips are obtained. In average, an output SNR level of around 32 dB is reached. This means an SNR degradation of 8 dB regarding the case in which a single PSS is implemented. The minimum value of the SNR is lowered until 21 dB. This value again corresponds to the upper limit of the NF, which in this case goes up to 26 dB. In average, a NF level of approximately 16 dB is obtained.

An interesting behavior can be observed in Fig. 4.27(a), since the noise power level remains constant for the two initial PSSs while, by increasing the third PSS injection current, the noise level increases accordingly. When taking into account three PSSs, an output SNR experiencing three smooth notches is obtained, as illustrated in Fig. 4.27(b). On average, the SNR level centers at 18 dB, which means a 14 dB

degradation regarding the two PSSs based implementation. The minimum SNR level is 9 dB, which corresponds to the maximum value of the NF. Now, this maximum level rises up to 37 dB, while getting an average value of about 30 dB.

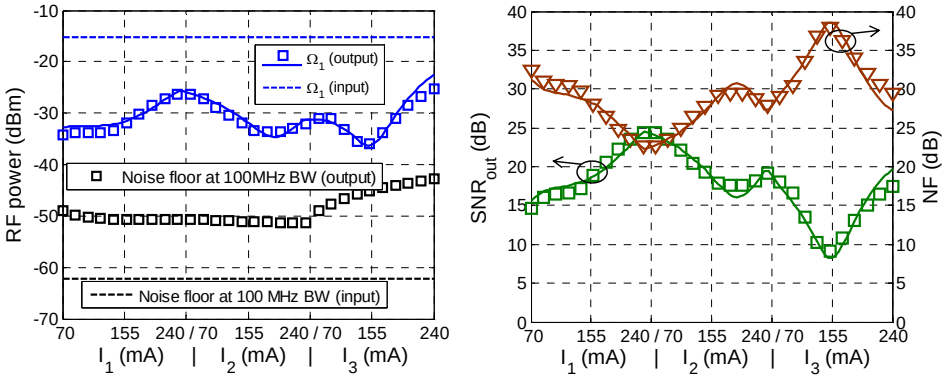

(a) (b)

Figure 4.27: Theoretical (solid curves) and experimental (markers) (a) RF power and noise level at the input (dashed curves) and output (markers), (b) SNR and NF as a function of the first, second and third PSS injection currents.

Figure 4.28 depicts the average level for the NF and the output SNR as a function of the number of PSSs taken in consideration. Results show a system degradation in terms of both the SNR and NF, proportional to the RF gain metric. The NF is directly dependent on the amount of phase shift that one wants to synthetize.

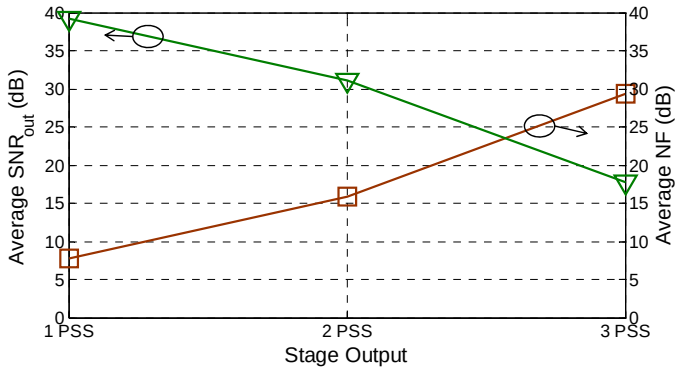

Figure 4.28: Average SNR at the output and NF of the RF signal as a function of the stage output.

The NF level can be further enhanced by a proper adjustment of each SOA bias point in terms of the injection current. It is well-known that the added noise in semiconductor waveguides is proportional to the power gain [97]. By increasing the input optical power and reducing the injection current, the power gain can be lowered without altering the CPO efficiency while operating the SOA in the saturation

regime [94]. As a consequence, the noise floor could be lowered and the SNR_{out} increased, giving as a result a NF reduction. Moreover, the total noise at the system output can be reduced by band-pass filtering the output of each PSS. In such a way, part of the added noise at the stage output will not be amplified by the following cascades stages. In addition, optical filtering prior to photodetection will also lower the noise level and, in consequence, the NF.

4.5.3 Spurious free dynamic range evaluation

Two-tone SFDR is defined as the carrier-to-noise ratio when the noise floor in the signal bandwidth equals to the power of a given order intermodulation product.

In this context, the SFDR of an RF link limited by 2^{nd} (SFDR_2) or 3^{rd} (SFDR_3) intermodulation distortion can be computed as

$$\begin{array}{l} SDFR_2 = 1/2\,(IP_2 - P_{noise})\ \left(dB \cdot Hz^{1/2}\right) \\ SDFR_3 = 2/3\,(IP_3 - P_{noise})\ \left(dB \cdot Hz^{2/3}\right), \end{array} \tag{4.31}$$

where IP_2 and IP_3 corresponds to the linearly extrapolated input powers in dBm at which respectively the fundamental and 2^{nd} or 3^{rd} intermodulation output powers would be equal. P_{noise} is the electrical noise power in dBm contained in 1-Hz bandwidth, which is derived from the previous subsection.

To obtain the values of the SFDR, the difference between the power intersection points with the noise curve relative to the fundamental (P_{Ω_1}) and the second ($P_{\Omega_2+\Omega_1}$ and $P_{\Omega_2-\Omega_1}$) or third order intermodulation products ($P_{2\Omega_1-\Omega_2}$ and $P_{2\Omega_2-\Omega_1}$) has been calculated. Actually, nonlinear distortion of 3^{rd} order is found to be the most harmful due to the nearby spectral placement of the fundamental frequencies. The SFDR referred to the fundamental term at the angular frequency Ω_1, can be thus expressed as

$$\begin{array}{l} SFDR_2 = \left\{P_{\Omega_2+\Omega_1}, P_{\Omega_2-\Omega_1}\right\} - P_{\Omega_1}\left(dB \cdot Hz^{1/2}\right) \\ SFDR_3 = \left\{P_{2\Omega_1-\Omega_2}, P_{2\Omega_2-\Omega_1}\right\} - P_{\Omega_1}\left(dB \cdot Hz^{2/3}\right), \end{array} \tag{4.32}$$

for every pair of IMD_2 and IMD_3 contributions. It is important to mention that SFDR values as high as possible are desired for enhancing the performance in terms of nonlinear distortion.

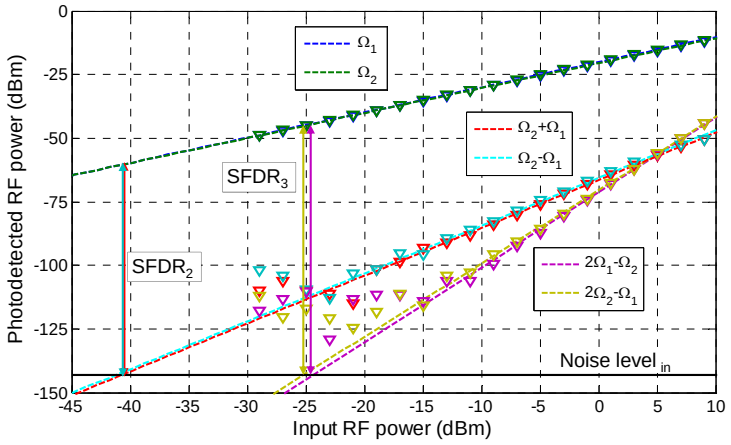

Figure 4.29: Theoretical (dashed curves) and experimental (markers) photodetected RF power from the fundamental [(Ω_1 and Ω_2)], IMD_2 [($\Omega_2 - \Omega_1$ and $\Omega_2 + \Omega_1$)] and IMD_3 [($2\Omega_1 - \Omega_2$ and $2\Omega_2 - \Omega_1$)] terms as function of the input RF power including 2^{nd} and 3^{rd} order SFDR determination at the first SOA input.

In order to study the impact of the nonlinear distortion in the phase shifter performance, the photodetected RF powers versus the RF input power to the EOM (which is related to the common electrical modulation index m) have been performed. These measured (markers) and computed (dashed curves) results are represented in Fig. 4.29 for every modulating frequency signal order and intermodulation product of interest; i.e. the fundamental and relevant IMD_2 and IMD_3 terms. They represent the equivalent detected RF power collected by the photodetector placed at the first SOA input. An input RF power level of 5 dBm is requested to accomplish the modulation index employed in the previous section ($m = 1\%$). The measured input noise level of around -142 dBm/Hz was used for computing the different intersection points. The values of SFDR from each pair of both 2^{nd} and 3^{rd} intermodulation products reach 83 dB·Hz$^{1/2}$ and 100 dB·Hz$^{2/3}$, respectively.

Figures 4.30(a) - 4.32(a) show the RF power for the fundamental signals (Ω_1 and Ω_2), IMD_2 ($\Omega_2 - \Omega_1$ and $\Omega_2 + \Omega_1$) and IMD_3 ($2\Omega_1 - \Omega_2$ and $2\Omega_2 - \Omega_1$) terms as a function of the input RF power when injecting the largest currents into all the three PSS. In order to get a common reference between the three representations, the results at the phase shifter input, shown in Fig. 4.29, are represented in Figs. 4.30(a) - 4.32(a) as dashed curves. It is easy to infer the RF gain/loss experienced by the different stages for the maximum SOA injection currents at the fundamental frequencies (20 and 20.5 GHz). As expected [102], the slope for the 2^{nd} and 3^{rd} order distortion terms is roughly twice and three times the slope for the fundamental signals, respectively. The noise floor reaches -127.5 dBm/Hz , -127.1 dBm/Hz and -122.7 dBm/Hz at the output of the first, second and third PSS, respectively. At the first PSS output, $SFDR_2$ and $SFDR_3$ values around 70 dB·Hz$^{1/2}$ and 97 dB·Hz$^{2/3}$ are achieved. While at the second PSS output, values around 65 dB·Hz$^{1/2}$ and 93 dB·Hz$^{2/3}$ for the second and third order SFDR are respectively obtained. Lastly, around 45 dB·Hz$^{1/2}$ and 62 dB·Hz$^{1/2}$ $SFDR_2$, and 75 dB·Hz$^{2/3}$ $SFDR_3$ values are achieved at the third PSS

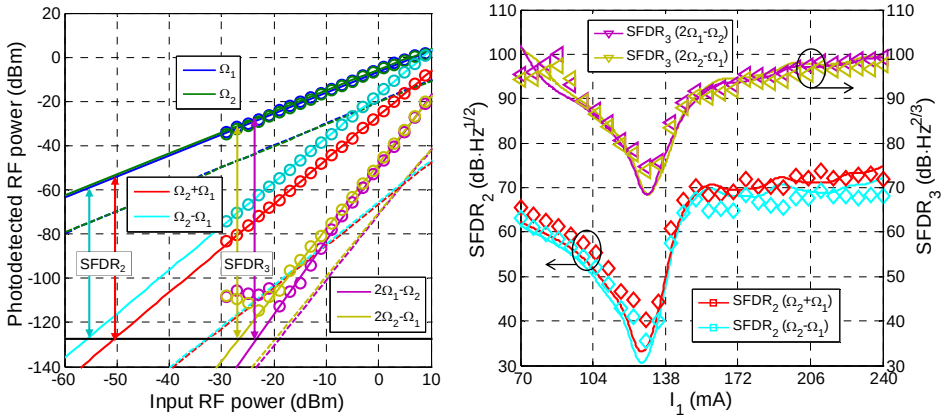

(a) (b)

Figure 4.30: (a) Fundamental, IMD_2 and IMD_3 terms at the first PSS output when $I_{PSS1} = 240$ mA. Dashed curves correspond to the RF power at the first SOA input. (b) $SFDR_2$ and $SFDR_3$ as a function of the injection current at the first PSS output.

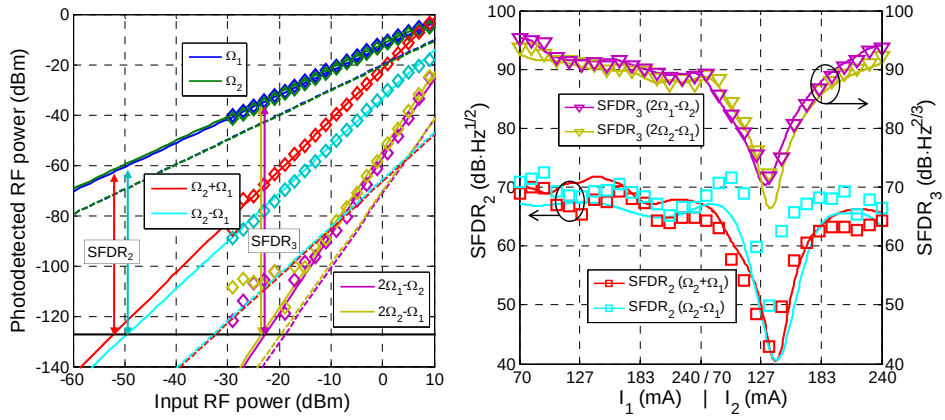

(a) (b)

Figure 4.31: (a) Fundamental, IMD_2 and IMD_3 terms at the second PSS output when $I_{PSS1} = I_{PSS2} = 240$ mA. Dashed curves correspond to the RF power at the first SOA input. (b) $SFDR_2$ and $SFDR_3$ as a function of the injection currents at the second PSS output.

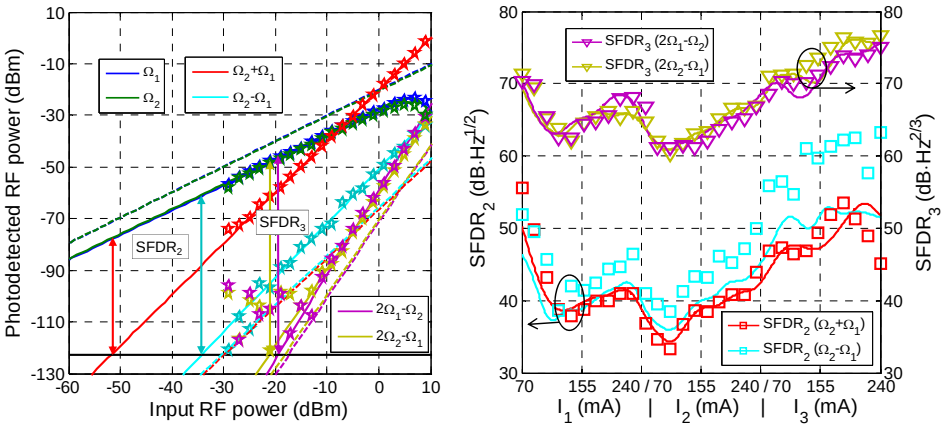

(a) (b)

Figure 4.32: (a) Fundamental, IMD_2 and IMD_3 terms at the third PSS output when $I_{PSS1} = I_{PSS2} = I_{PSS3}$ =240 mA. Dashed curves correspond to the RF power at the first SOA input. (b) $SFDR_2$ and $SFDR_3$ as a function of the injection currents at the third PSS output.

output. The low power behavior experienced by the $\Omega_2 - \Omega_1$ term at the third PSS output, is due to the nonlinear behavior of the low-band frequency filter used by the VNA. An interesting feature that can be observed in all the PSSs is related to the fact that the CPO effect produces mainly second order distortion as compared to third order contributions. This feature can be explained by analyzing Eq. 4.22, for the IMD_2 and HD_2 optical fields, where the dominant wave mixing terms in the double summation are due to the product of the fundamental component of the SOA dynamic gain (first-order CPO) and the fundamental signal contribution. For instance, in the case of the equation describing the evolution of $dE_{(1,1)}/dz$, the dominant terms are $g_{(0,1)}E_{(1,0)} + g_{(1,0)}E_{(0,1)}$, the magnitude of which is higher than those of the dominant wave mixing terms contained in the propagation equations for the IMD3 contributions, which are proportional to 2^{nd} order gain coefficients.

On the other hand, Figs. 4.30(b) - 4.32(b) illustrate the evolution for both the $SFDR_2$ and $SFDR_3$ as a function of the SOA injection currents comprising one, two and three PSS, respectively. The tendency is roughly the same for both $SFDR_3$ terms, since their spectral components are located relatively close to each other (0.5 GHz). However, slightly different behavior is observed for the $SFDR_2$ terms due to its large spectral separation (40 GHz). In principle, the SFDR is expected to experience similar performance that the output RF power (see Figs. 4.15 - 4.17). However, the current values in which the power dips appear do not correspond to those for which the SFDR drops. After observing the dynamics of the SFDR with the bias currents, one concludes that the distortion generation efficiency depends on the injected currents. This means that the slopes of the 2^{nd} and 3^{rd} order distortion RF powers are slightly altered as a function of the bias point. In particular, dips are due to slope relaxation. For both the 2^{nd} and 3^{rd} order distortions, the above-mentioned slope relaxation occurs at the same currents. This effect dominates over the SFDR

dips as a consequence of the phase shifting transitions. That is the reason why the SFDR presents such a behavior.

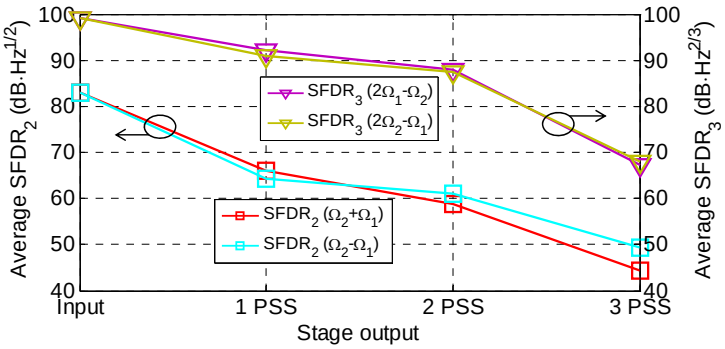

Figure 4.33: Average $SFDR_2$ and $SFDR_3$ as a function of the stage output.

Both the average $SFDR_2$ and $SFDR_3$ levels as a function of the stage output are represented in Fig. 4.33. SFDR values at the system input are also illustrated. It is clearly appreciable the large nonlinear degradation when cascading three PSSs. Similar degradation was obtained for the gain and noise evolution, since RF power and noise values are requested for obtaining the SFDR levels. It can be observed that a reasonably good margin of $SFDR_3$ up to the second PSS is achieved, high enough for the majority of applications where the phase shifter can be integrated. Note that while the 2^{nd} order intermodulation distortion can be significant, its effect can be neglected if the two subcarriers are placed within an octave in the RF spectrum.

In terms of the nonlinear distortion optimization, the limiting factor consists of the dependence of the generation efficiency of the 2^{nd} and 3^{rd} order products on the bias currents. The minimum values of SFDR could be further improved by engineering the SOAs in order to minimize the above-mentioned dependence.

4.6 Fully tunable MWP phase shifter based on a single SOA

As it has been conceptually described in section 4.2 of this chapter, and subsequently evaluated in terms of system performance and figures of merit in previous sections (4.4 and 4.5), a full 360° phase shift functionality based on semiconductor technology has been achieved, so far, using a cascade of three consecutive SOA based phase shifter stages, [84]. This technique allows obtaining cumulative phase shifts of more than 360° at microwave frequencies up to 40 GHz while providing, as previously demonstrated in this chapter, a nearly linear phase transition with less than 10 dB of power variation along the entire microwave bandwidth.

Nevertheless, achieving 2π phase shift by means of this approach requires the cascade of at least five SOA devices, being three of them followed by an optical filtering stage while the remaining two needed for regenerating the previously removed red-shifted sidebands. This complex configuration not only requests an independently

current control for each device but also implies a high RF deterioration in terms of noise level and nonlinear distortion, as reported in section 4.5.

On the other hand, one of the aspects that attracts most of the interest in the semiconductor based approach is related to the fact that previous work has experimentally demonstrated positive and negative phase shifts for different optimized modulation chirp values. In fact, $\sim 120^{\circ}$ phase delay and $\sim 170^{\circ}$ phase advance have been obtained at 19 GHz in a single phase shifter stage [95]. Although, at a first glance this particular behavior could open the possibility of reaching high microwave phase shift levels, the combination of both slow and fast light effects becomes actually not large enough to the get desired full 360° phase shift characteristic. This is highly desirable for many microwave photonics applications, such as microwave photonic filters and antenna beamsteering systems [20, 32].

It must be noted that previously reported work resorts to the use of optical notch filters solely directed to reject the red-shifted frequency sideband aiming at increasing the achievable microwave phase shift [84]. Nonetheless, the dispersion slope and the amplitude transfer function of the optical filter can play an important role in the phase shifter performance, as it has been demonstrated [107]. Actually, since the detected microwave signal depends on the coherent addition of two different beat components between the carrier and both sidebands, the delay or phase shift incurred to the signal by the filter placed at the SOA output sideband could be a decisive factor for the design of the required microwave phase shift.

As a consequence, this section deals with the particular proposal of an optical notch filter conveniently designed in order to obtain the proper phase shift and power attenuation combination required after the SOA propagation which, as a result, allows to implement a fully tunable microwave phase shifter by handling both slow and fast light effects. This means releasing four SOAs and two optical filters in comparison with the best approach previously reported [84]. It must be taken into account that the terms slow or fast light will be understood to refer to whether the phase shift of the modulation signal relative to a reference phase, is positive or negative, respectively.

4.6.1 Principle of operation

To overcome some of the main drawbacks of the cascaded structures and, at the same time, to reach the desired 360° phase shift, the basic phase shifter configuration based on CPO in SOAs described in subsection 4.2.2 of this chapter, which was actually firstly reported in [93], has been considered. Fig. 4.34 shows the phase shifter general schematic. The microwave signal modulated on the optical carrier suffers a phase shift as it propagates through the SOA [83]. A tailored optical filter is included as part of the optical signal processing to generate the maximum effect on the microwave phase shifts in combination with the SOA. The principle of operation of the novel approach proposed in this section focuses on exploiting not only the amplitude, but also the phase response of the optical filter to enhance the effect of the red signal sideband, resulting in either positive or negative microwave phase shifts, i.e. slow or fast light.

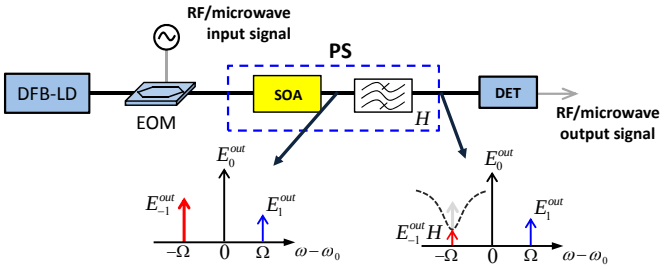

Figure 4.34: Schematic of a RF/microwave phase shifter based on SOA and optical filtering.

Based on the weak modulation assumption, the electric field at the phase shifter output can be approximated by

$$E^{out}(t,z) = \left(\left|E_0^{out}\right| e^{i\phi_0} + \left|E_1^{out}\right| e^{-i\Omega t + i\phi_1} + \left|E_{-1}^{out}\right| |H|\, e^{i\Omega t + i\phi_{-1} + i\phi_H}\right) e^{-i(\omega_0 t - k_0 z)}, \tag{4.33}$$

where ω_0 is the frequency of the optical carrier, k_0 is the propagation constant of the carrier, and Ω is the modulation frequency. E_0^{out}, E_1^{out} and E_{-1}^{out} are respectively the complex amplitudes of the carrier, blue and red-shifted sideband, while ϕ_0, ϕ_1 and ϕ_{-1} are the corresponding optical phase features. The modulus and phase components of the filter transfer function are represented by $|H|$ and ϕ_H, respectively.

Due to the beating between the optical waves in the photodetector, the photocurrent at the modulation frequency Ω is proportional to

$$i(\Omega) \propto \left|E_0^{out}\right| \left|E_1^{out}\right| e^{i(-\phi_0+\phi_1)} + \left|E_0^{out}\right| \left|E_{-1}^{out}\right| |H|\, e^{i(\phi_0-\phi_{-1}-\phi_H)}. \tag{4.34}$$

The phase shift of the microwave signal is determined by $\arg\{i(\Omega)\}$ minus a phase reference, normally corresponding to the phase obtained at the minimum input optical power or electrical injection current.

Figure 4.35 exhibits the evolution of the signal complex phasors in a polar representation by controlling the injection current of the SOA. Blue phasors represent the evolution of the first photocurrent term according to Eq. 4.34 (beating between the carrier and the blue-shifted sideband), red phasors correspond to the second term (the beat between the carrier and the filtered red-shifted sideband) and, finally, the total microwave photodetected signal is represented by black phasors. Moreover, dotted phasors designate the reference point. Fig. 4.35(a) illustrates the results reported in previous work [93], where the optical filter simply attenuates the red-shifted sideband and thus, a large positive phase shift is created. Nevertheless, as shown in Fig. 4.35(b), by inducing the proper phase change on the attenuated red sideband, an opposite phase slope behavior on the black phasor can be achieved, which means negative phase shift or fast light. Since the blue sideband at the SOA output has a depth power dip where the phase slope takes place, the attenuated red

sideband, with the proper applied phase change, can easily modify the behavior of the phase shifter performance.

Hence, the desired 360° phase shift range can be easily achieved by combining the SOA output with a tailored filter providing the desired phase and amplitude changes on the red-shifted sideband.

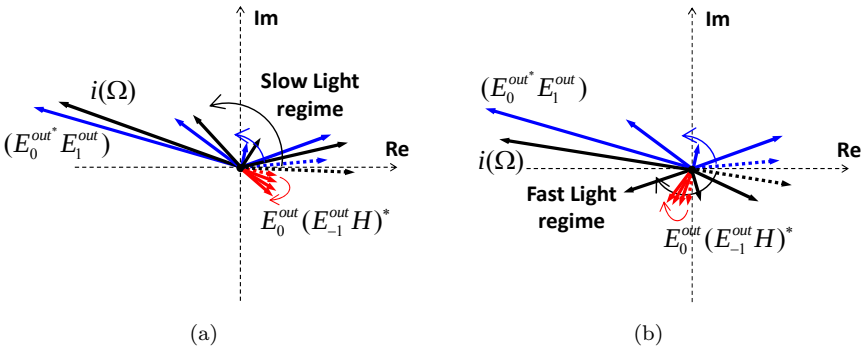

(a) (b)

Figure 4.35: Illustrations of the evolution of the complex phasors in a polar representation for two cases: (a) when the red-shifted sideband is only attenuated and (b) when it is attenuated and also phase shifted.

4.6.2 Computed results

Numerical calculations of the RF phase shift as a function of the attenuation and phase induced by the photonic notch filter are shown in Fig. 4.36. The following main parameters of the SOA have been used: P_{sat} = 4 dBm, τ_s = 140 ps, α = 6, Γ = 0.45, γ = 3000 m^{-1}, P_{in} = 0 dBm, Ω = 20 GHz, L = 1000 μm. All RF phase shifts are obtained upon increasing the injection current from 100 mA to 200 mA. On one hand, Fig. 4.36(a) depicts different RF phase shifts when the attenuation of the filter is fixed at -20 dB and the phase induced on the red-shifted sideband (ϕ_H) is tuned from -100° to 100°. It is easy to infer the existence of a high dependence on the phase parameter. When -100° $\leq \phi_H \leq$ 0°, slow light effect is observed inducing positive phase shifts. However, when 10° $\leq \phi_H \leq$ 100°, fast light behavior is achieved which induces a negative RF phase shift. Maximum phase delay and phase advance values of $\sim$ 175° and $\sim$ 185°, respectively, can be achieved. On the other hand, Fig. 4.36(b) depicts the total RF phase shift versus the filter-induced phase shift for different attenuation values. As it is clearly observed, an increase of the red sideband attenuation is accompanied by an increase in the RF phase shift. Thus, there are less filter phase constraints to obtain the full 360° phase shift. However, the higher the filter attenuation, the lower the signal-to-noise ratio becomes, since the photodetected RF power would be lower.

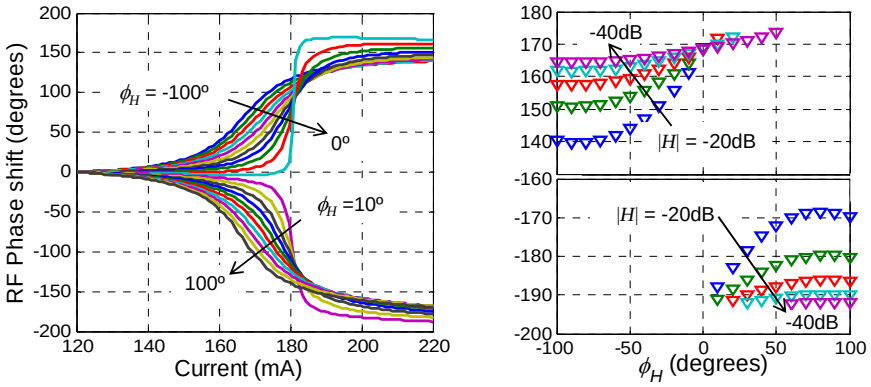

(a) (b)

Figure 4.36: (a) Calculated RF phase shifts as a function of the injection current as well as the ϕ_H. (b) Maximum values of phase shift induced by increasing the injection current as a function of ϕ_H and $|H|$.

The novel proposed phase shifter configuration exhibits a large flexibility in terms of the number of parameters that can be tuned in order to achieve the desired 360° phase excursion. For instance, the influence of the SOA input power is evaluated in Fig. 4.37, which shows the evolution of the RF phase shift for different optical power levels at the SOA input. The attenuation of the red-shifted sideband is kept to a constant value of 30 dB, while the induced phase remains at 20°. By tuning the SOA input optical power from -6 dBm to 8 dBm, the sign of the RF phase shift changes from negative to positive, since the attenuation and phase provided by the filter cannot satisfy the fast light condition for optical input powers greater than 1 dBm. When the SOA becomes more saturated, the efficiency of the CPO decays and therefore the phase slope is modified. As it is shown, by properly fixing the attenuation and phase values of the filter, moving from slow light to fast light regime is also possible by tuning the SOA input power.

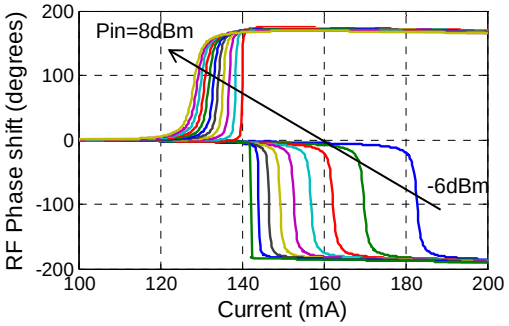

Figure 4.37: Calculated RF phase shifts induced by increasing the optical power at the SOA input as a function of the injection current.

4.6.3 Experimental results

In order to experimentally validate the aforementioned principle, some issues concerning the optical notch filter must be taken into account. A large FBG amplitude and phase dependence on the final RF phase shift has been previously shown, which requests high spectral stability to obtain the desired influence. Besides, it is well known that FBGs are very sensitive to strength and temperature modifications [108], hence the FBG employed was properly stabilized in order to minimize environmental fluctuations. Furthermore, the polarization of the signal which will be filtered by the grating can further modify the FBG spectral response. Fig. 4.38 shows the amplitude response of the FBG used in the experimental setup when two different and orthogonal polarizations were launched to probe the grating. As it can be observed, the amplitude depth is slightly different for the two polarizations. In addition, the left slope of the spectral shape response is detuned by approximately 500 MHz.

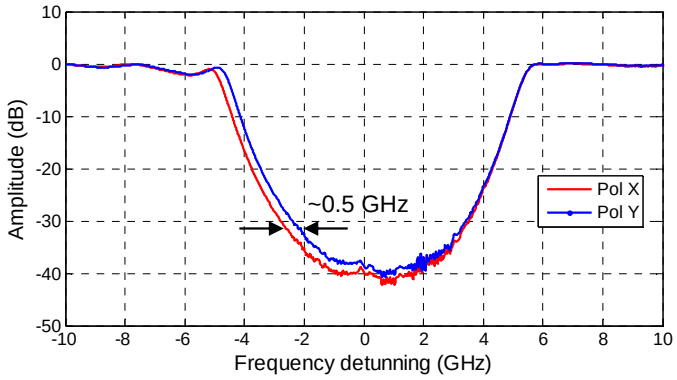

Figure 4.38: Measured FBG amplitude response as a function of the frequency detuning for two orthogonal polarizations at the grating input.

Since the FBG response depends slightly on the polarization state, the SOA influence on the polarization must be evaluated. This study has been carried out for two different and orthogonal polarization states at the SOA input (i.e. Pol X and Pol Y). A polarization beam splitter (PBS) was placed at the SOA output in order to characterize each polarization state as a function of the SOA injection current. Optical peak power of the carrier, red and blue sideband were measured by an optical spectrum analyzer (OSA) for Pol X, Pol Y and both combined at the SOA output. The main results are represented in Fig. 4.39. As it is observed, for the input polarization used in Fig. 4.39(a), all the spectral components experience a similar behavior as a function of the injection current. Yet, different optical power levels for each spectral line are obtained due to the beam splitter, since the polarization state was not maximized at the beam splitter input. On the other hand, by rotating the polarization to an orthogonal state at the SOA input (Fig. 4.39(b)), an interesting behavior is observed for the blue sideband. The optical power notch, where the maximum phase change takes place, occurs at different injection current values depending on the polarization state at the SOA output. The most important issue is related to the fact that the red-shifted sideband does not follow that specific behavior. This demonstrates that

whatever the polarization state feeds the SOA, the red sideband will not experience any polarization rotation at the SOA output, which means the same amplitude and phase level applied by the FBG to the red-shifter sideband along the SOA tunability.

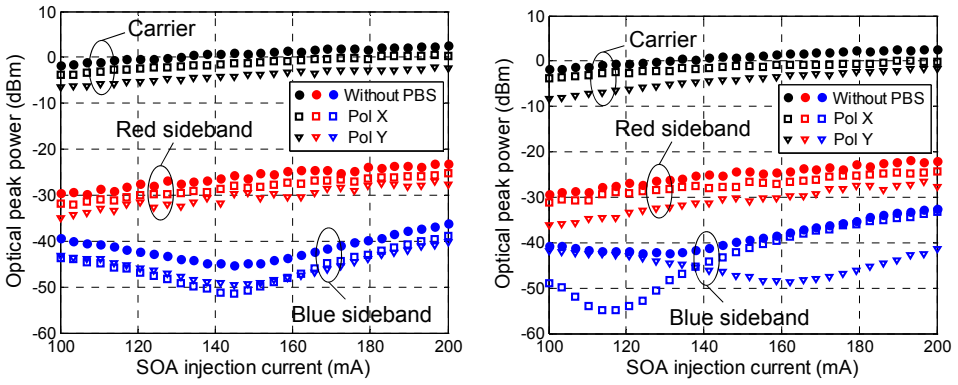

Figure 4.39: Optical peak power for the carrier, red and blue sidebands as a function of SOA injection current when applying (a) one polarization or (b) its orthogonal at the SOA input. Polarization X, its orthogonal (Pol Y) and both combined measured at the SOA output are also represented.

Once verified the notch filter stability, the suggested 2π phase shifter configuration has been experimentally investigated using the setup depicted in Fig. 4.34. It is based on the post-filtering scheme performed by a transmission FBG. A CW laser at 1556 nanometers was modulated using a microwave tone at 20 GHz by means of an external zero-chirp Mach-Zehnder modulator. The nonlinear SOA device, from CIP photonics, was designed with a low saturation output power of 4 dBm. As Fig. 4.38 illustrates, the grating can provide an attenuation greater than 40 dB at the frequency where the notch is centered and -3 dB bandwidth of approximately 10 GHz. The optical signal was photodetected and acquired by using a VNA.

3D and contour plots in Figs. 4.40 and 4.41 represent the experimental results for the microwave phase shift as a function of the SOA injection current, as well as the spectral position of the red-shifted sideband within the FBG. Different RF phase shift values were measured for different red-shifted sideband locations. The results were obtained for two optical powers at the SOA input of 0 dBm (Fig. 4.40) and 2dBm (Fig. 4.41). The targeted frequency areas are labelled as phase advance and delay. The measured spectral response of the FBG is shown in Fig. 4.42. Solid curves represent the measured amplitude and phase shift responses, while markers illustrate the spectral positions used to obtain the results illustrated in Figs. 4.40 and 4.41. The frequency area which allows generating positive and negative RF phase shifts is symbolized by the red inverted delta marker (∇). They correspond to an attenuation of $\sim$ 40 dB and a phase shift ranging from 20° to 80°, which means more than 1 GHz operational bandwidth.

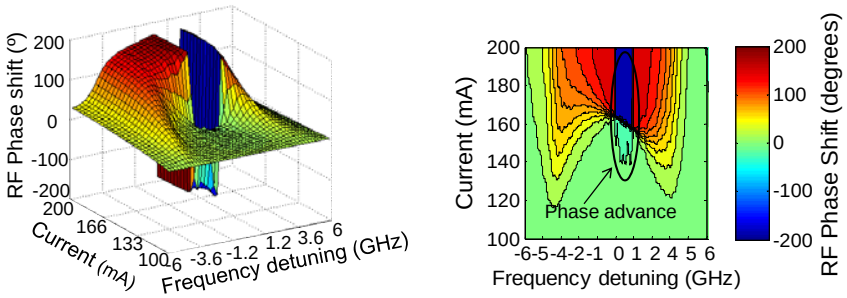

(a) (b)

Figure 4.40: (a) 3D and (b) contour representation of the measured RF phase shift as a function of both SOA input current and FBG frequency detuning when 0 dBm optical power is applied at the SOA input.

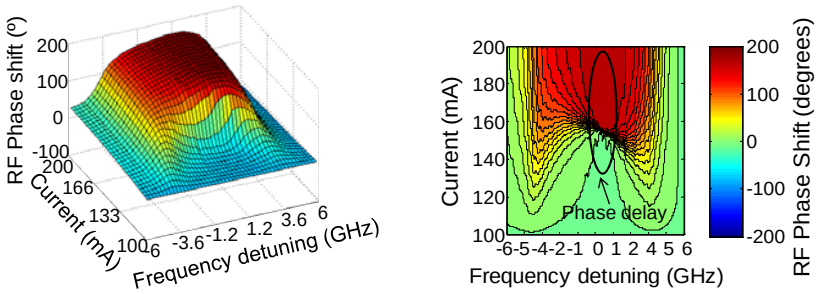

(a) (b)

Figure 4.41: (a) 3D and (b) contour representation of the measured RF phase shift as a function of both SOA input current and FBG frequency detuning when 2 dBm optical power is applied at the SOA input.

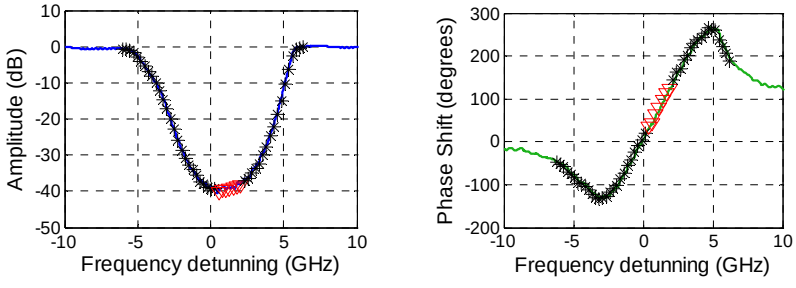

(a) (b)

Figure 4.42: Measured (solid curves) FBG (a) amplitude and (b) phase response. Markers represent the spectral locations used to obtain the 3D and contour results.

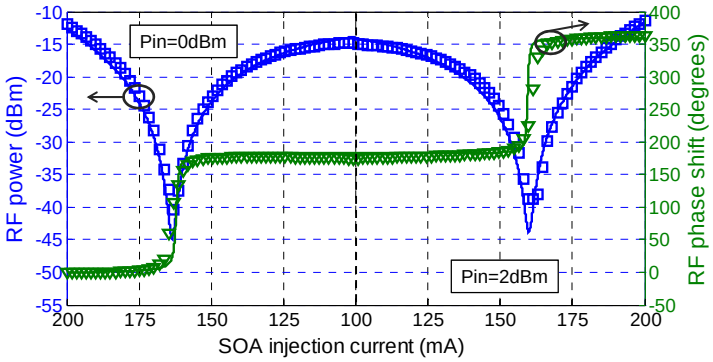

Figure 4.43: Theoretical (lines) and experimental (markers) photodetected RF power and phase shift as function of the SOA input current when the input power is fixed at 0 dBm and 2 dBm.

Figure 4.43 illustrates the experimental (markers) and theoretical (solid curves) results for the phase shift and power variation induced by slow and fast light effects through changing the injection current of the SOA for two different optical input powers, 0 and 2 dBm. For these two optical power levels, the reference phase is chosen at the injection current of 200 mA and for 0 dBm optical power. To reach these high values of RF phase shift, the FBG frequency detuning was fixed to provide 40 dB attenuation level and 60° phase shift over the red-shifted sideband. Being the SOA less saturated (0 dBm), $\sim$ 185° phase advance is achieved. On the other hand, the additional $\sim$ 175° phase delay, shown in the right part of Fig. 4.43, is induced by increasing 2 dB the optical input power. The phase shift reaches 360° by the combination of both slow and fast light effects. As expected, the sharp increase of the phase shift corresponds to a deep dip in the RF power. In addition, this configuration provides more degrees of tunability. Since the total phase shift depends on the filter detuning, the central frequency of the laser as well as the grating spectral position can be used for this purpose. Moreover, as with the optical power, the polarization state at the SOA input enables the modification of the CPO efficiency.

It has been shown that the optical filter enhances the available microwave frequency. Nonetheless, the instantaneous bandwidth of the microwave phase shifter depends highly on the filtering scheme. It has to ensure that at a certain frequency range the fast light condition is met. In this particular case, it can be achieved within a bandwidth greater than 1 GHz. Narrower filters would allow operating at lower central frequencies but at the cost of using less operational bandwidth.

4.6.4 FOMs evaluation

The proposed structure is now evaluated in terms of several FOMs in order to assure its implementation in real MWP systems. As it was evaluated for the SOA-cascade-based phase shifter, RF net gain, NF and SFDR concerning 2^{nd} and 3^{rd} order intermodulation products are the metrics employed for the cited assessment. The evaluation has been carried out at the same modulating frequencies used in section 4.5 (20 GHz

and 20.5 GHz) and for the SOA injection current values where the RF phase shifts take place. Furthermore, average metric levels for this phase shifter implementation, as well as the cascaded approach by using 3 PSSs, are represented in order to make a comparison between both solutions.

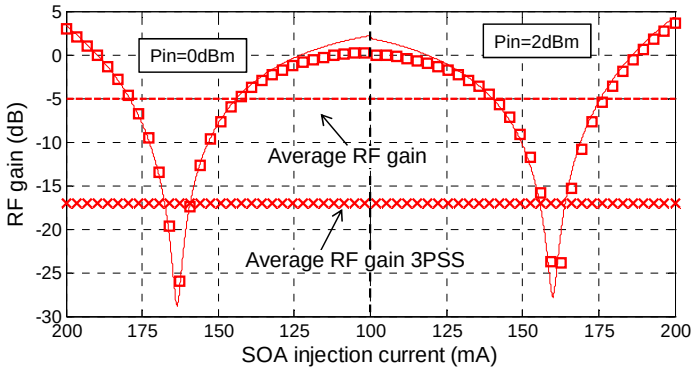

Figure 4.44: Theoretical (solid curve) and experimental (squared markers) RF net gain as a function of the SOA injection current when the input power is set either at 0 dBm or 2 dBm. Dashed curve represents the average level for the single SOA implementation while "x" markers show the average gain when cascading 3 PSSs.

Figure 4.44 reports the RF net gain as a function of the SOA injection current for two different optical input powers, 0 dBm and 2 dBm, at 20 GHz of modulation frequency. As expected, it obeys the same behavior than the photodetected RF power illustrated in Fig. 4.43. More than 25 dB of gain variation are achieved by tuning the injection current. Besides, by using an input RF power of -15 dBm, an average RF gain level of around -5 dBm is obtained. This means an improvement of the average gain level of about 12 dB compared with the cascaded case.

Figures 4.45(a) and 4.45(b) show respectively the evolution of the output SNR and NF as a function of the SOA injection current for two different optical powers at the SOA input. The inset in Fig. 4.45(a) represents the noise floor level integrated in a 100 MHz bandwidth by tuning the SOA injection current. A noise degradation of more than 10 dB is observed. On average, an output SNR level of around 33 dB is reached, while 48 dB of SNR is obtained at the system input. An SNR improvement of more than 15 dB compared with the case where 3 PSSs are implemented is illustrated. On the right, peaks in the NF response match the depth dips in the SNR_{out} plot. NF upper limit of 36 dB is reached, while its average levels turns around 15 dB. This means an increase of the NF level of $\sim$ 15 dB with respect to the case in which 3 PSSs are implemented.

On the other hand, Figs. 4.46(a) and 4.46(b) illustrate the evolution of both $SFDR_2$ and $SFDR_3$ terms, respectively, as a function of the SOA injection current comprising again 0 dBm and 2 dBm of optical power at the SOA input. It is clearly observed that the tendency is roughly the same for the $SFDR_2$ and $SFDR_3$ terms, despite the large spectral separation (40 GHz) between both $SFDR_2$ terms. At the SOA output, average $SFDR_2$ and $SFDR_3$ values around 63 dB·$Hz^{1/2}$ and 88 dB·$Hz^{2/3}$ are achieved. The values of SFDR from each pair of both 2nd and 3rd intermodulation

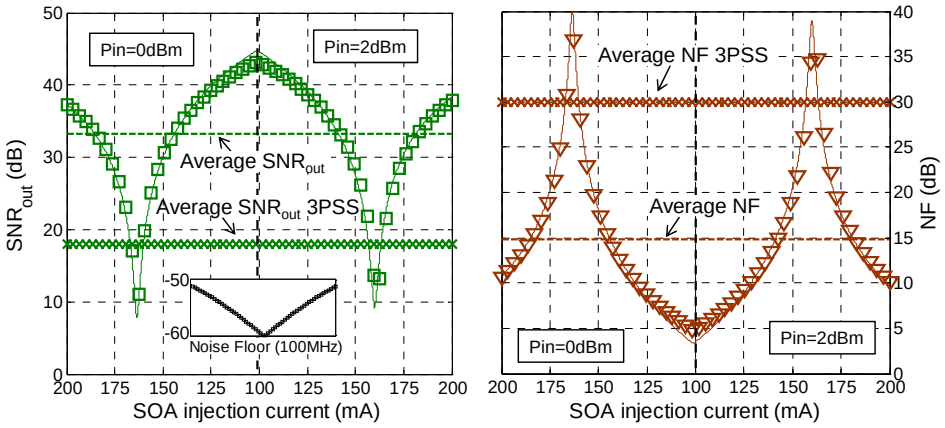

(a) (b)

Figure 4.45: Theoretical (solid curves) and experimental (markers) output (a) SNR and (b) NF as a function of the SOA injection current when the input power is set either at 0 dBm or 2 dBm. Dashed curves represent the average level for the single SOA implementation while "x" markers show the average gain when cascading 3 PSSs.

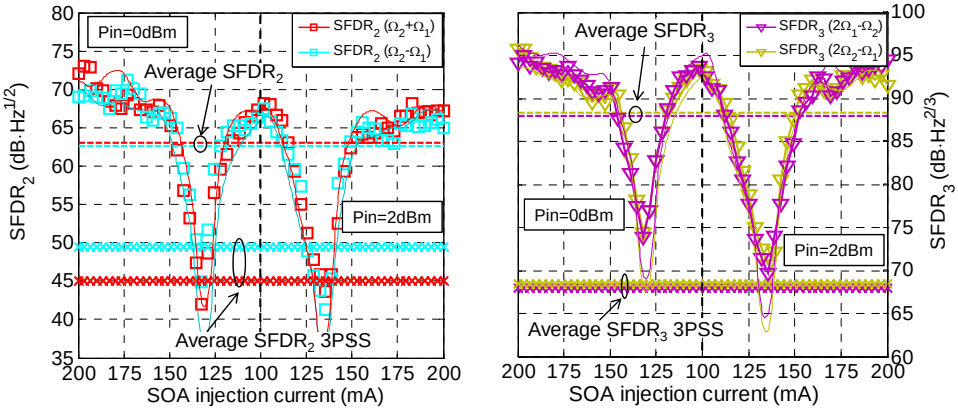

(a) (b)

Figure 4.46: Theoretical (solid curves) and experimental (markers) (a) $SFDR_2$ and (a) $SFDR_3$ as a function of the SOA injection current when the input power is set either at 0 dBm or 2 dBm. Dashed curves represent the average level for the single SOA implementation while "x" markers show the average gain when cascading 3 PSSs.

products at the SOA input are 83 dB·Hz$^{1/2}$ and 100 dB·Hz$^{2/3}$, respectively. Higher 2nd order nonlinear distortion degradation (20 dB) is obtained compared with third order distortion (12 dB). However, an SFDR increase of $\sim$ 14 dB and $\sim$ 20 dB, respectively, for the second and third order intermodulation, is obtained compared to the case in which the cascaded structure is assembled. The depth dips deviation in their responses indicates that the SFDR dynamics do not follow the same behavior as a function of the injection current compared to that seen either in Fig 4.44 or 4.45(a). This can be understood in terms of 2^{nd} and 3^{rd} order distortion, since their RF powers are slightly deviated as a function of the bias point.

Once observed the obtained metrics, it is possible to conclude that the main drawback of this technique is the inverse relation between total phase shift and low RF power level. Sharp phase slopes, and therefore depth power dips, are required to reach the desired 360°. This way the system performance turns diminished in terms of gain, noise and SFDR due to its straight dependence. For smaller phase shift requirements, i.e. less than 2π, different filtering scenarios can be considered in order to reduce the depth of the dip. The SNR performance can be also enhanced equalizing the detected power over the entire phase shifting tunability range. However, this implementation can be efficiently employed to obtain discrete phase shifts, either π or 2π, featuring high operational bandwidth and very fast tunability speed (hundred of ps) without power penalties.

4.7 Fully tunable MWP filter using the single SOA based phase shifter implementation

Based on the results exposed in last section, it can be concluded that a tailored filtering scheme after the SOA can provide a way to achieve a 360° microwave phase shift by combination of both slow and fast light effects. Therefore, this single-SOA basic configuration appears as one promising alternative for developing fully tunable MWP filters. In such a way, a tunable notch-type incoherent MWP filter has been accomplished by means of the phase shifter implementation described in section 4.5.

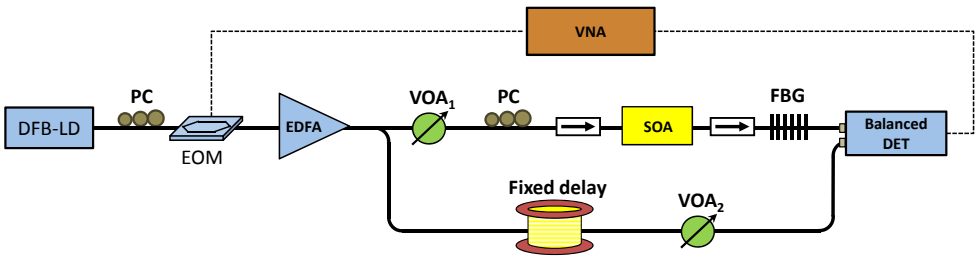

Figure 4.47: Experimental setup of a fully tunable two-tap MWP notch filter based on the single SOA phase shifter performance.

Figure 4.47 shows the experimental setup. The microwave notch filter comprised a simple Mach-Zehnder interferometer composed of two arms, one of which incorporates the microwave phase shifter, shown in the upper path, which was made up of an SOA followed by a tailored FBG. The EDFA and VOA_1 were used to adjust the SOA input optical power in order to switch from slow to fast light regime. A fixed delay was introduced in the lower branch of the filter layout to provide the desired spectral response. In addition, a balanced photodetector was employed to avoid coherence constraints, since the optical path length imbalance between the two branches was not large enough to accomplish the condition of incoherent regime. A second tunable attenuator (VOA_2) provided microwave power balance between the two arms to compensate the power variations at the phase shifter output. Tuning the central frequency of the filter was accomplished by two different control mechanisms: changing the SOA injection current or varying the optical input power. The RF input and output signal were, respectively, generated and collected by using a high-bandwidth VNA.

It has been previously reported that microwave phase shifts up to 360° were obtained at 20 GHz by combination of slow and fast light effects in SOAs. Further achievements are presented in Fig. 4.48, where the measured RF power and phase shifter responses within 1 GHz bandwidth centered at 40 GHz are illustrated. As it can clearly seen, different SOA injection currents and optical input power combinations yield nearly constant phase shifts over 1 GHz bandwidth. Full 2π tunability is demonstrated at 40 GHz. However, a low-pass filtering behavior is observed in the power response, due to the SOA dynamics. A maximum RF power variation of $\sim$ 2 dB is obtained. It should be noted that at certain combinations of current and optical power, the power response is highly degraded (more than 20 dB) as it has been shown in Fig. 4.43. Nevertheless, normalized power results have been plotted since this degradation can be compensated by a tunable attenuator.

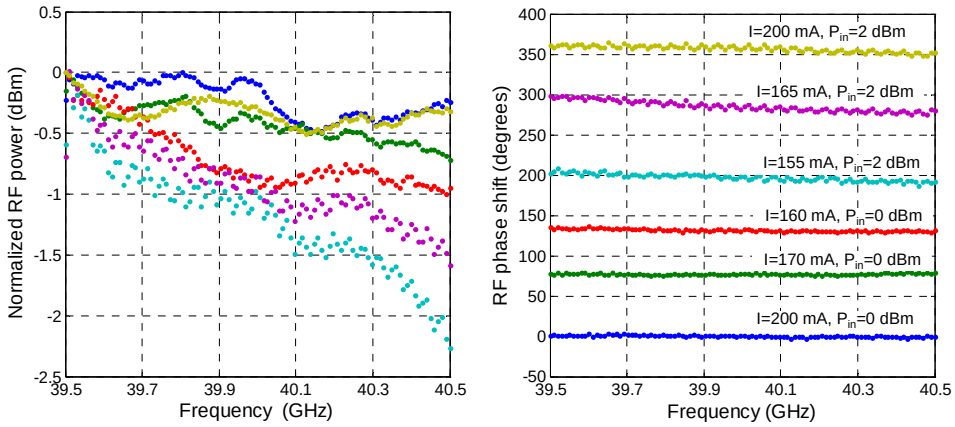

(a) (b)

Figure 4.48: Normalized (a) RF power and (b) phase shift responses as a function of the modulation frequency for different SOA injection currents and input optical powers.

Figure 4.49 shows the measured filter response for different SOA injection currents and optical input powers. The SOA injection currents and optical input power combinations for each curve correspond to those illustrated in Fig. 4.48(b). Experimental measurements (solid curve) are compared to theoretical calculations (markers) showing excellent agreement. The spectral response at the SOA injection current of 200 mA and optical input power of 0 dBm is chosen as the reference. The FSR obtained corresponds to 340 MHz, which means $\sim$ 60 cm optical fiber length imbalance between the two optical paths. A continuously 100% fractional tuning is obtained, while high notch rejection is achieved over the entire tuning range.

It is noticeable that the shape of the filter transfer function remains unaltered since there is no need to change the filter's basic delay in order to tune the transfer function. A stable filter response was obtained using the balanced photodetector, demonstrating that the tunable notch filter is free of coherence interference. The main drawback of the proposed scheme is derived from the fact that tuning the phase shifter performance not only affects its phase shift, but also alters its power level. However, this can be compensated by a tunable attenuator (VOA_2).

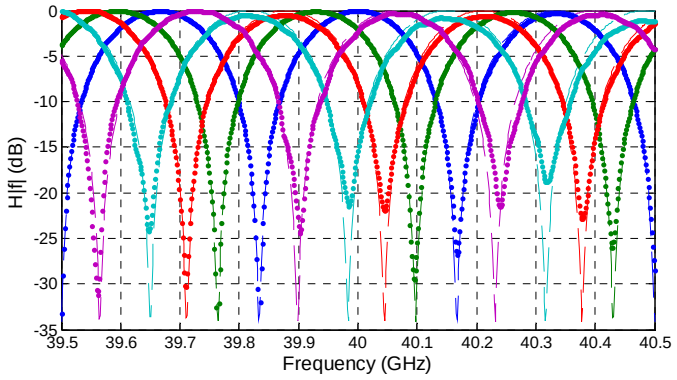

Figure 4.49: Frequency response of the two-tap complex-valued filter showing tunability.

4.8 True time delay line based on cross gain modulation in SOAs

The reported results shown in previous sections have been obtained through CPO effects in SOAs. This way a 360° phase shifter with broadband operation has been successfully obtained. In addition, a fully tunable notch-type MWP filter over its entire FSR has been demonstrated. Nevertheless, the achievement of TTD by using CPO effects cannot be accomplished over a broad bandwidth, i.e. tens of GHz, due to fundamental limitations [13, 109]. Up-converted CPO, in combination with XGM effects in SOAs [79, 110], enables to get rid of extend the operating frequency, leading to the generation of time delays at any high frequencies in a single SOA device [111].

However, in this co-propagating configuration, the XGM response exhibits a narrow-band TTD response (< 1 GHz) [85].

Nevertheless, XGM effects in SOAs can perform the achievement of broadband TTDs among two counter-propagating optical signals [86]. When these two optical beams propagate in opposite directions along the semiconductor waveguide the XGM response drops off significantly faster with the modulation frequency compared with the co-propagation case [111]. Altering the slope of the fall-off edge of the XGM response will lead to group velocity changes of the converted probe beam after the SOA propagation. In this way, tunable true time delays $\sim$ 10 ps have been demonstrated over a microwave frequency band from few GHZ to 35 GHz [86].

Here, the possibility to improve the reported TTD value is investigated by a tailored engineered nonlinear SOA. Relevant features are its small cross section, 1 mm-long waveguide and a low saturation power P_{sat} of 1 mW.

Figure 4.50 depicts the experimental setup to measure the time delay induced by XGM effects when two optical beams are counter-propagating through the SOA. The DFB-LD 1 light output at 1556.53 nm was modulated by the VNA RF output port. Its optical power at the input of the SOA was controlled by both the EDFA and VOA. The wavelength of the DFB-LD 2 was set at 1545 nm, and its optical power was fixed at -5 dBm. Four-wave mixing effects between both lasers can be neglected due to the large detuning. The SOA was electrically biased at 300 mA. PCs were used to maximize the XGM effect. After the SOA propagation, the light coming from the DBF-LD 2 was selected by an optical circulator, detected and measured by the VNA RF input port.

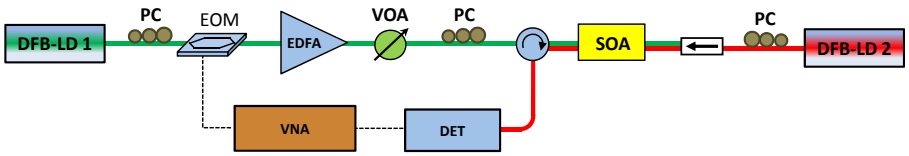

Figure 4.50: Experimental setup of a tunable true time delay line based on XGM effects in an SOA.

Figures 4.51(a) and 4.51(b) show the experimental RF power and phase shift responses of the XGM effect, respectively, as a function of the RF frequency when the optical power of the DFB-LD 1 is changed from -9 to 6 dBm. These results have been normalized to their minimum value in order to clearly compare the slopes. The power variation of the XGM response seen in 4.51(a) is caused by the transit time effect between both counter-propagating signals [112]. These slope changes thus imply large variations in the phase response of the RF signal carried by the DFB-LD 2, as illustrated in Fig. 4.51(b). As it is clearly observed, the phase shift exhibits a nearly linear behavior over a frequency range from few MHz to 40 GHz.

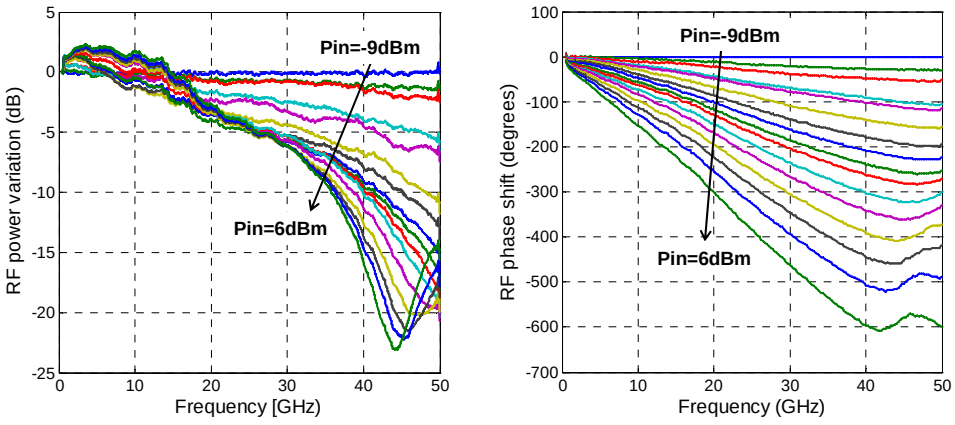

(a) (b)

Figure 4.51: Normalized (a) RF power and (b) phase shift of the XGM response as a function of the modulation frequency for different optical powers at the SOA input

On the other hand, the measured time delay is illustrated in Fig. 4.52. Around 40 ps tunable true time delay can be obtained up to 35 GHz by tuning 15 dB the SOA input optical power.

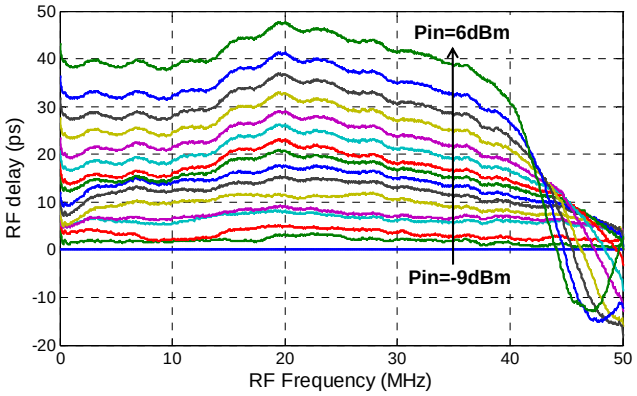

Figure 4.52: RF delay of the XGM response as a function of the modulation frequency for different SOA input optical powers.

4.9 Conclusions

In this chapter, a theoretical and experimental evaluation of the propagation, generation and amplification of signal, harmonic and intermodulation distortion terms in a MWP phase shifter, comprehending one or several stages of SOA under CPO regime

followed by an optical filter have been presented. A general optical field based model applicable to any number of arbitrarily spaced modulating tones that accounts for nonlinear distortion up to order D has been described.

For MWP applications where large signal operation is required, two different optical filtering implementations for the proper design of distortion-free phase shifters have been proposed. The performance of the phase shifter has been evaluated considering up to 3^{rd} order distortion when the modulating signal is composed of two RF tones, distinguishing two different spectral separations between them, namely 0.5 and 3 GHz, with the purpose of covering different MWP applications. The nonlinear evaluation has been carried out as a function of the SOA input optical power, injection current and modulation frequency. It has been confirmed that CPO based phase shifters are mainly limited by second order nonlinear distortion which can, nevertheless be overcome by pacing all the relevant input signals within an octave in the RF spectrum. This nonlinear distortion increases beyond the signal level after cascading three phase shifter structures, mainly due to the ASE accumulation.

In addition, the SFL effects induced by the optical filtering stage placed at the SOA output have been investigated. This way up to 360° phase shift has been demonstrated in a single SOA followed by a tailored FBG. The proposed scheme saves four SOAs and two optical filters compared with the best scheme previously reported [84]. In order to obtain an increase of the total phase shift by adding slow and fast effects, a very deep notch is induced in the phase shifter performance, which diminishes the SNR in the range of injected currents where the abrupt phase change takes place. It has been demonstrated that the phase shifter bandwidth, as well as the operating frequency, are strongly dependent on the filtering scheme. It has to be ensured that at a certain frequency range the fast light condition is met. In this case, an instantaneous bandwidth greater than 1 GHz has been successfully achieved.

The performance of the cascaded and single SOA MWP phase shifter configurations has been evaluated and compared in terms of several figures of merit. Indeed, the evaluation has focused on the assessment of the RF net gain, NF and SFDR as a function of the bias currents injected into the phase shifter stages. The behavior shown by the net gain and NF has been determined by the RF output power. However, the SFDR results have been mainly imposed by slightly changes in the slope of the generated distortion as a function of the bias currents. Maximum RF net gain variation of 27 dB, upper NF limit of 36 dB and minimum $SFDR_3$ of 70 dB·$Hz^{2/3}$ have been obtained for a single PSS, while the cascaded structure has reached $\sim$ 10 dB gain variation, 37 dB maximum NF and 60 dB·$Hz^{2/3}$ minimum $SFDR_3$. On the other hand, the average levels at the output of the cascaded structure turned in a system degradation of 12 dB, 15 dB and 20 dB for the RF net gain, NF and SFDR respectively compared with the single PSS based approach. Optimized performance can be accomplished, especially for the cascaded structure, by proper adjustment of the optical input power and the bias currents injected into all the SOAs.

The implementation of the fully tunable MWP phase shifter based on the single SOA approach has been deployed for the development of a reconfigurable MWP notch filter. The phase shifter, which was placed in one branch of the MZ structure, led to the 100% tunability of the filter central frequency without any spectral and shape alteration.

Finally, a MWP true time delay line realized by XGM effects in SOAs has been addressed in a counter-propagation configuration [86]. Around 40 ps continuously tunable true time delay up to 35 GHz has been demonstrated.

The reported phase shifter based on CPO effects requires the use of an optical filter after the SOA propagation. Despite an FBG has been deployed in this chapter, the combination of SOA followed by a more compact structure, such as a ring resonator, can perform the same results. In this way, the basic MWP functionalities, i.e. phase shifters and true time delays, can be achieved through a mm-scale SOA device based on CPO and XGM effects. This means a footprint reduction of six orders of magnitude compared with SBS effects in standard fibers and one order of magnitude compared with DBGs and FBGs.

The quality of the work has been recognized by the following international publications:

- **J. Sancho**, J. Lloret, I. Gasulla, S. Sales and J. Capmany, "Figures of merit for microwave photonic phase shifters based on semiconductor optical amplifiers", Optics Express, vol. 20, no. 10, pp. 10519-10525, 2012.
- **J. Sancho**, J. Lloret, I. Gasulla, S. Sales, and J. Capmany, "Fully tunable 360° microwave photonic phase shifter based on a single semiconductor optical amplifier", Optics Express, vol. 19, no. 18, pp. 17421-17426, 2011.
- I. Gasulla, **J. Sancho**, J. Capmany, J. Lloret, and S. Sales, "Intermodulation and harmonic distortion in slow light microwave photonic phase shifters based on coherent population oscillations in SOAs", Optics Express, vol. 18, no. 25, pp. 25677-25692, 2010.
- J. Lloret, **J. Sancho**, I. Gasulla, S. Sales and J. Capmany, "Governing the speed of light and its application to the microwave photonics field", Waves, no. 2, pp. 30-38, 2010.
- I. Gasulla, **J. Sancho**, J. Lloret, S. Sales and J. Capmany, "Harmonic distortion in microwave photonic phase shifters based on coherent population oscillations in SOAs", IEEE Photonics Technology Letters, vol. 22, no. 12, pp. 899-901, 2010.
- **J. Sancho**, J. Lloret, I. Gasulla, S. Sales, and J. Capmany, "2pi microwave photonic phase shifter based on single semiconductor optical amplifier", in IEEE Topical Meeting Microwave Photonics (MWP), Singapore (Singapore),paper 2181, 2011.
- J. Lloret, **J. Sancho**, I. Gasulla, S. Sales, and J. Capmany, "Performance metrics evaluation of cascaded SOA based slow light microwave photonic phase shifters", in IEEE Topical Meeting Microwave Photonics (MWP), Singapore (Singapore),paper 2175, 2011.
- **J. Sancho**, I. Gasulla, J. Lloret, S. Sales, and J. Capmany, "Third order intermodulation distortion in a 360 microwave photonic phase shifter based on slow light cascaded SOAs", in International Conference on Information Photonics (IP), Ottawa (Canada), paper 5953771, 2011.

- I. Gasulla, **J. Sancho**, J. Capmany, J. Lloret, and S. Sales, "Intermodulation and harmonic distortion in slow light SOA based microwave photonic phase shifters", in Optical Fiber Communication Conference (OFC), Los Angeles (USA), paper JWA051, 2011.
- I. Gasulla, **J. Sancho**, J. Lloret, S. Sales and J. Capmany, "Figures of merit for microwave photonic phase shifters based on coherent population oscillation slow and fast light effects", in the Conference of the 12th International Transparent Optical Networks (ICTON), Munich (Germany), invited paper We.B3.2, 2010.
- I. Gasulla, **J. Sancho**, J. Lloret, S. Sales, and J. Capmany, "Harmonic distortion in slow light SOA based microwave photonic phase shifters", in Optical Fiber Communication Conference (OFC), San Diego (USA), paper JWA52, 2010.
- I. Gasulla, **J. Sancho**, J. Lloret, L. Yaron, S. Sales and J. Capmany, "Harmonic distortion in SOA based slow/fast light microwave photonic phase shifters", in IEEE Topical Meeting Microwave Photonics (MWP), Valencia (Spain), paper Th3.6, 2009.

Chapter 5

SFL effects in photonic crystals for MWP applications

5.1 Introduction

MWP signal processing based on the previously described techniques (SBS effects in chapter 2, FBGs in chapter 3 and SOAs in chapter 4), along with additional reported approaches in the literature [113–115], rely on discrete optoelectronic devices, optical fibers and components leading to bulky, expensive and power-consuming architectures.

It must be taken into account that typical delay line footprints range from several tens of cm when using FBGs or DBGs to a few km when resorting to nonlinear effects in standard optical fibers. This characteristic will thus not be compatible with cost-effective solutions as it does not allow the integration of MWP devices on-chip. A different limitation will also imply that semiconductor-based approaches will not be capable of outperforming state-of-the-art electronic functionalities. Although SOA-based TTD (see section 4.8) reduce the footprint to mm-scale, the nonlinear distortion generation and tunability losses limit its performance in real MWP applications.

Indeed, the miniaturization of MWP processors, such as MWP filters, has been already reported on resonant delay lines provided by ring cavities and coupled resonant optical waveguides [116,117].Nevertheless, the delay line functionalities achieved with all these approaches rely on resonant operation, which means that tunable delay lines are obtained only at selected regions of the optical spectrum and with a limited operation bandwidth per delay product. Thus, non-resonant tunable dispersive optical delay lines will overcome this limitation, provided that they bring the required strong dispersion values in order to reduce the waveguide length.

In this context, PhC waveguides with tailored dispersion engineering are thus a natural choice towards achieving the goal of integrated MWP processors with unprecedented performance in terms of bandwidth and delay-length ratio [118].

In this chapter, the use of a GaInP/GaAs highly dispersive PhC waveguides will be demonstrated for implementing a tunable TTD line onto a mm-sized chip. By proper wavelength multiplexing of optical carriers, a tunable MWP filter, continuously tunable up to 50 GHz, will be implemented. In addition, the PhC performance will be evaluated in terms of several FOMs. These FOMs will address issues concerning the power consumption, loss penalty derived from the operating frequency and the delay, tunability limitations, physical size and dispersion-related amplitude distortion when employing the PhC waveguide as a tunable delay line.

This chapter is the outcome of a week collaboration between UPV and THALES carried out in the OQCG laboratory.

5.2 Principle and fabrication

PhC membrane technology combines patterning of a regular lattice of holes on a semiconductor with removal of a sacrificial layer, resulting in an extremely thin ($\sim$ 200 nm) layer suspended in air. This nanostructured material has unique optical properties, which can be tailored to a very broad extent through a proper design [119]. Local breaking of the periodicity (defects) results into photon transport (waveguide) [120, 121] or localization (resonant cavity) [122, 123].

A specific feature of membrane PhCs is the existence of a photonic bandgap (PBG), which appears under appropriate conditions and when the maximum index contrast is sufficiently large [124]. The PBG can be defined as a range of frequencies in which light cannot propagate in the structure. In the particular case of planar PhC waveguides, guided-mode bands propagate through their line defect, confined by total internal reflection in the vertical direction and Bragg reflection, due to the PBG, in this lateral direction. These bands can, in principle, be made as flat as desired by the appropriate design.

The origin of slow light in PhC waveguides arises from the coherent Bragg reflections, leading to a flat dispersion on the transverse electric (TE) field [125, 126]. At these so-called slow light frequencies, the light effectively travels slowly through the lattice via multiple Bragg reflections, leading to an enhanced local field density. This enhancement scales inversely with the group velocity, thus decreasing the threshold of intensity-dependent nonlinear effects such as Kerr, multi-photon absorption, or Raman scattering [127, 128]. The combination of the engineered group velocity enhancement, along with the small modal effective area of PhC waveguides ($\sim 2{\cdot}10^{-13}$ m^2), yields outstanding control over the optical modes [129].

The PhC waveguide employed in this chapter was fabricated using a planar process. First, a 200-nm-thick mask of silica was deposited on a semiconductor structure containing a 180-nm-thick layer of InGaP grown by metal-organic chemical vapour deposition (MOCVD) on GaAr. Then, a poly-methyl-meta-acrylate (PMMA) resist was spin on it and exposed using an e-beam writer. After etching of the silica mask, the III-V material was processed via inductively coupled plasma (ICP) etching and finally a self-standing membrane was obtained by wet etching of the underlying layer of GaAs.

It is important to notice that in these particular waveguides the propagation loss systematically increases when the group velocity is reduced, because of the enhanced impact of the fabrication imperfections, mainly roughness at the etched interfaces [130]. Besides, in long PhC waveguides (> 1 mm, as needed for optical delay lines) the impact of disorder eventually turns into multiple coherent scattering [131], which is detrimental for real MWP applications. That backscattering depends not only on the group velocity, but also on the field distribution of the transmission modes [132].

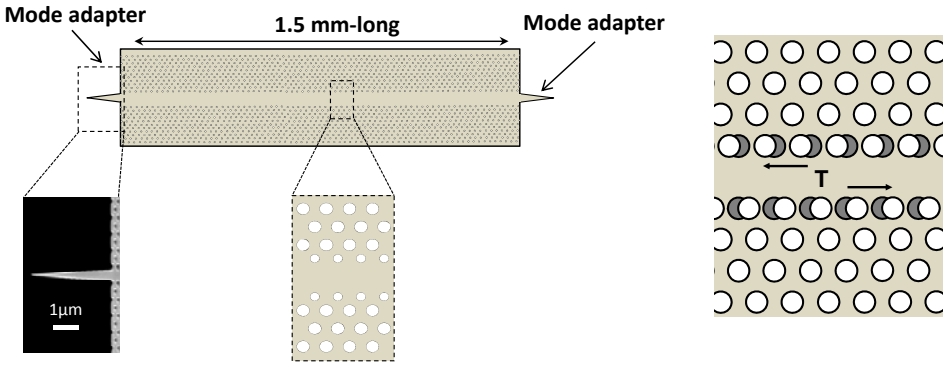

Figure 5.1: (a) PhC design including SEM image of the tapered coupler at the beginning of the waveguide. (b) Design of the PhC waveguide with the anti-symmetric shift of the first row of holes.

The waveguide design is shown in Fig. 5.1(a). The total length of the structure is 1.5 mm. The design consists of a triangular lattice of air holes with a period a of $\sim$ 482 nm, and hole radius of $\sim 0.26a$. The first row of holes performances a slightly smaller radius ($\sim 0.25a$), as it can be shown in the figure inset. The waveguide exhibits reduced loss in the slow light regime as a result of both design and fabrication optimization. The main idea is to apply an anti-symmetric shift of the first row of holes along the waveguide axis by $\sim 0.15a$, as illustrated in Fig. 5.1(b). This modification of the waveguide symmetry induces a coupling between the even and odd modes resulting in a "hump" shaped dependence of the group index on the wavelength, as illustrates the TE mode in Fig. 5.2 [133]. The transverse magnetic (TM) mode is also illustrated in Fig. 5.2.

The aforementioned design shows a substantial reduction of backscattering and an improvement of the transmission of modes. The estimated minimal propagation loss in the waveguide (around 1dB) [133] is added to the attenuation due to slow light. Considering that the best operating point for this waveguide in terms of large delay and moderate loss is at $n_g = 18$ (low impact of disorder), the propagation loss only increases by about 3 dB [133], so that the total propagation loss must be around 4 dB. In addition, the fabricated device contains mode adapters [134], shown in 5.1(a), reducing the total insertion loss to about 8 dB (from fiber to fiber).

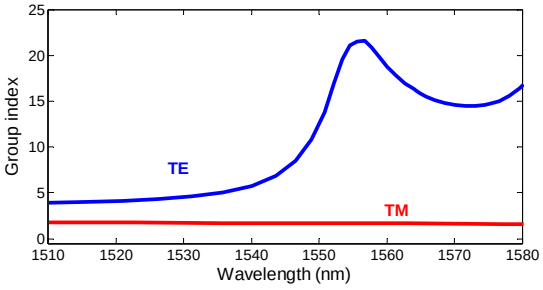

Figure 5.2: Calculated [133] dispersion (group index vs. wavelength) for the TE and TM modes.

5.3 True time delay characterization

The performance of the PhC acting as a RF signal delay line was characterized by measuring both the RF power and phase shift in the RF domain when inserting the device into a MWP link, as illustrates the schematic diagram in Fig. 5.3.

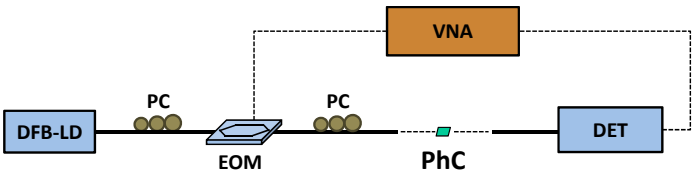

Figure 5.3: Schematic diagram for the characterization of the PhC-based delay line.

The DFB-LD output was used as the optical carrier of the MWP link. The RF signal was fed into the link through an EOM, which modulates the optical carrier intensity. PCs were deployed to adjust the polarization state at the input of the EOM and PhC waveguide. Lensed fibers were used for input and output optical coupling. A high-speed photodetector was followed by an RF amplifier in order to compensate for the loss introduced by the EOM and the PhC device. The power and phase variations of the waveguide from 10 MHz to 50 GHz were characterized by means of a two-port VNA whose output and input ports were respectively connected to the EOM RF input and the RF amplifier output.

Figure 5.4(a) depicts the measured phase shift of the PhC waveguide over the full RF frequency range and for optical carrier wavelength ranging from 1532 to 1555 nm. A linear variation of the phase shift with respect to the RF frequency is observed, which is the signature of TTD. The equivalent group delay varies according to the tuning of the optical wavelength, resulting in 100 ps delay tunability for a 33 nm optical bandwidth. On the other side, Fig. 5.4(a) shows the measured amplitude transfer function. A power variation of 7 dB, corresponding to a 3.5 dB change of the optical transmission, was experienced by the RF signal while tuning the delay up to 70 ps. This delay was accomplished by sweeping the carrier wavelength from 1532 nm to 1552 nm. As it is clearly observed, further delays turn in a detrimental RF

power response. This can be explained as follows: the impact of disorder results in a fast modulation of the optical transmission spectra, which in principle translates into a distorted transfer function of the microwave link. However, this effect is only noticeable when the delay is increased above 80 ps.

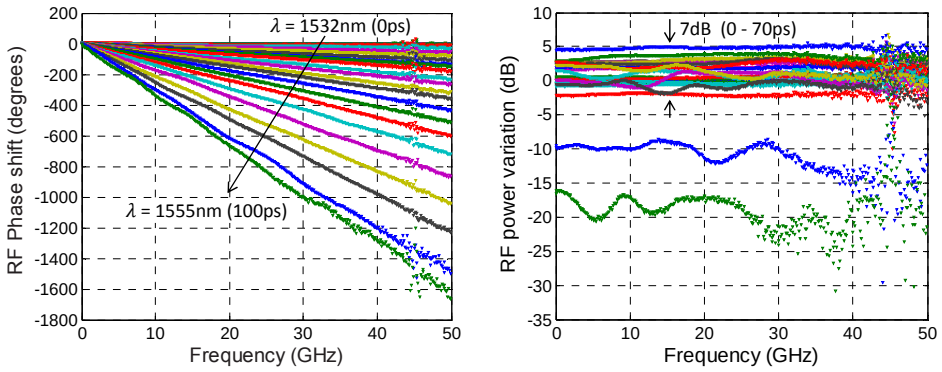

(a) (b)

Figure 5.4: (a) RF phase shift and (b) power variation as a function of the RF frequency when the carrier wavelength is swept from 1532 to 1555 nm.

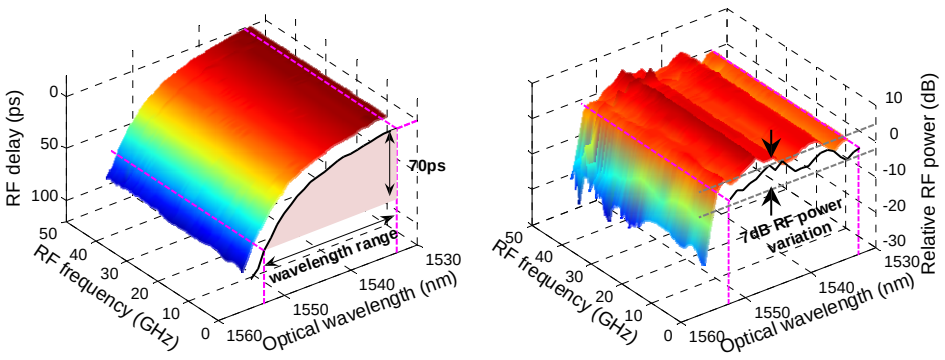

(a) (b)

Figure 5.5: 3D representation of the measured RF relative (a) delay and (b) power variation as a function of the wavelength and the RF frequency.

A 3D representation of the RF delay is plotted in Fig. 5.5(a), which is obtained according to $\Delta\tau = -\Delta\phi/2\pi\nu$. It involves the measurement of the RF phase shift along the wavelength range from 1532 to 1555 nm. A flat response over the entire RF frequency band of the microwave link is obtained, whatever the delay. The overall bandwidth of the device was limited by the modulator, detector and VNA bandwidths.

The RF power variations are also shown in Fig. 5.5(b). The inset illustrates the 7 dB variation along 20 nm optical bandwidth, corresponding to a TTD tunability up to 70 ps. The large bandwidth handling capability is a clear advantage, since narrow

band condition can be assumed. This assumption relies on the fact that the optical wavelength has to be swept over 20 nm to span over the full delay range, which is very large compared with the RF operating bandwidth ($\sim$ 0.4 nm).

5.4 MWP filter

The common implementation of a MWP FIR filter follows the approach shown in Fig. 1.6(a) within chapter 1. However, this scheme does not allow for an easy tuning, as this requires changing the value of T in each tap of the filter. An alternative approach (see Fig. 5.6) is based on the combination of a dispersive delay line and different optical carriers where the value of the basic delay T is changed by tuning the wavelength separation among the carriers, thereby allowing tunability [135]. While in the first case (see Fig. 1.6(a)) the intensity or weight of the r_{th} tap, represented by a_r, can be changed by inserting loss/gain devices in the different branches, with the second approach a_r is readily adjusted by changing the optical power emitted by the optical sources [135]. This sub-section focuses on the approach of Fig. 5.6 since it becomes more flexible.

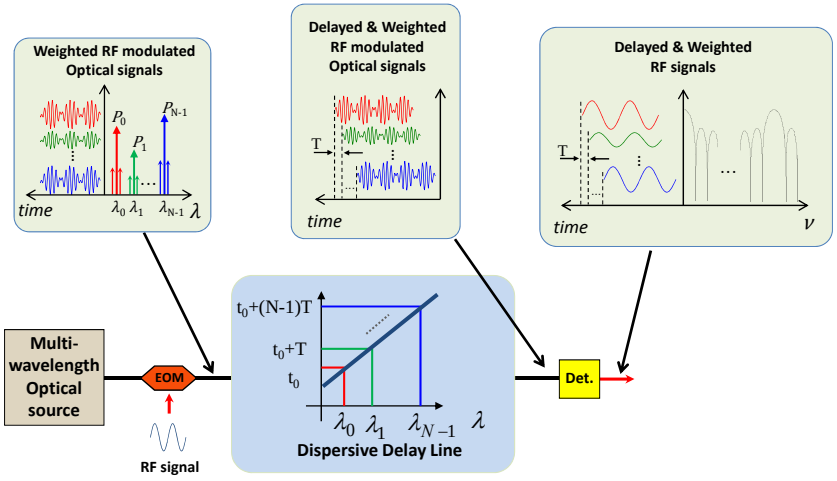

Figure 5.6: Schematic diagram of the compact approach of a MWP multi-tap filter based on a multi-wavelength optical source together with a single dispersive element.

First, a two-tap MWP notch filter scheme exploiting the group index disparity between the TE and TM modes into the PhC waveguide is considered. The principle of this simple implementation is illustrated in Fig. 5.7(a). The key point is that the dispersion of the TM is negligible compared with that of the TE mode. Therefore, when the optical carrier is coupled to the two polarization modes, the modulation envelope will experience a relative delay which is controlled by the carrier wavelength. In addition, by properly adjusting the polarization state of the input optical signal, their relative weight can be controlled.

The results for this polarization multiplexing PhC-based MWP filter were measured by deploying the same experimental setup used for the MWP link characterization (see Fig. 5.3). The input RF signal was imprinted on the optical carrier, properly polarized and launched into the PhC waveguide. The output electrical signal, after propagating through the waveguide and photodetection, is composed of the sum of two orthogonal intensity modes. By tuning the wavelength of the input laser, the optical modulation carried by the TM mode will experience a constant group delay close to the effective index of the PhC slab, $\tau_{TM} = L \times n_{g,T}/c$, being L the PhC waveguide length and $n_{g,TM} = n_{g,bulk} \sim 2$. Conversely, due to the slow TE mode propagation in the PhC structure, the signal carried by the TE mode will be delayed by $\tau_{TE} = L \times n_{g,TE}(\lambda)/c$, with λ the optical wavelength, and $n_{g,TE}$ ranging from 5 to 20, according to Fig. 5.2.

The filtered electrical signal at the output of the photodiode results then in a combination of both orthogonal delays. Thus, the filter transfer function, which is derived from Eq. 1.4, corresponds to

$$H(\nu) = 1 + e^{-i2\pi\nu\left(\frac{L}{c}[n_{g,TE}(\lambda) - n_{g,TM}]\right)}, \tag{5.1}$$

where the FSR of the filter equals to $c/(L(n_{g,TE}(\lambda) - n_{g,TM}))$.

Figure 5.7(b) illustrates the calculated and measured responses of the two-tap MWP filter. A good level of agreement between the experimental and theoretical results is observed. It must to be pointed out that, whatever the target frequency of the filter, a notch depth of $\sim$ 50 dB is obtained in this case. However, for the largest group delay (blue curve), notch depth deviations from the theoretical calculation are observed with a 50 dB depth for the first notch, decreasing to almost 30 dB for the higher order notches. When the tap weights are properly adjusted to optimize the first notch depth, the slight power fluctuations for a given delay, that can be observed in Fig. 5.5(b) along the RF frequency axis, lead to a tap weights misbalance at the other notch positions.

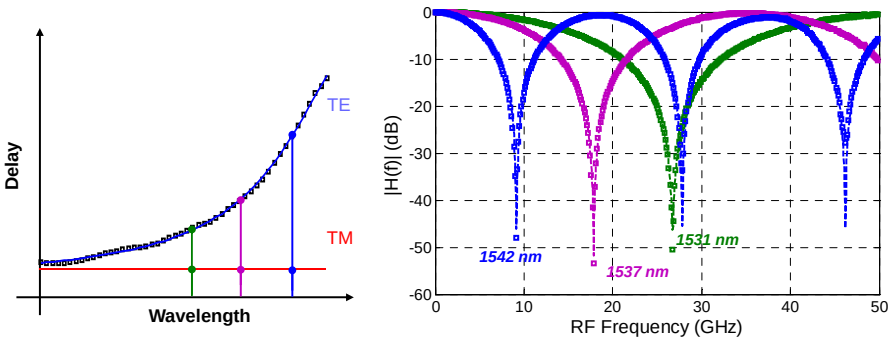

(a) (b)

Figure 5.7: Polarization-multiplexed-based two-tap MWP filter. (a) Delay profile for the modes TE and TM as a function of the wavelength. (b) Calculated (dashed curves) and measured (makers) results for the filter response as a function of the wavelength.

The practical interest of a notch-type filter is however limited to very specific applications, where a narrow-band rejection is required. The functionality and the attractiveness of MWP filters in terms of Q-factor and design flexibility improve as the number of taps (filter order) is increased, thus enabling band-pass filtering. A convenient approach for implementing a potentially large number of channels is based, as explained before, on a single dispersive optical element in combination with a multi-carrier optical source (i.e. implemented by means of a frequency comb or by wavelength division multiplexing), where each carrier is modulated by the same microwave signal. The delay experienced by each channel is readily controlled through the fine tuning of the corresponding optical carrier wavelength.

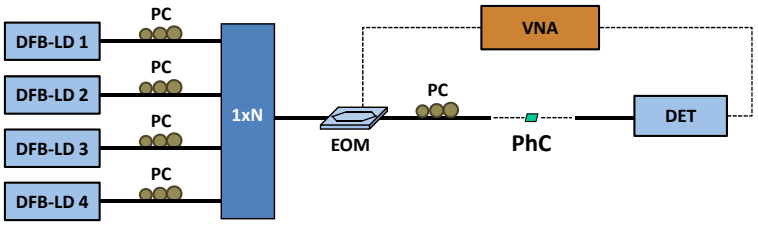

Figure 5.8: Experimental layout of four-tap PhC-based MWP filter.

In Fig. 5.8 is illustrated the generic layout of the four-tap PhC-based MWP filter assembled by combining four tunable lasers prior to modulation with the RF signal. Four replicas of the microwave signal, polarized along the slow axis (TE mode), will effectively propagate through the PhC with different delays, which are set to be equally time-spaced (with time shift T) by suitably setting the wavelengths of the four carriers. This principle is illustrated in Fig. 5.9(a). The uncorrelated nature of the four lasers guarantees the incoherent operation regime of the MWP filter. Thus, the electrical signal generated by the photodiode at the output of the PhC waveguide will result into the incoherent sum of the optical intensities of the four taps. The corresponding transfer function reads as

$$H(\nu) = \sum_{r=0}^{3} a_r e^{-jr\left(\frac{2\pi\nu}{FSR}\right)}, \tag{5.2}$$

where the FSR is equal to $1/T$. The tap weighting coefficients a_r are adjusted by controlling the relative intensities of the tunable lasers. In the experimental demonstration reported in this section, all the a_r were set at the same power level (uniformly apodized filter) although filter windowing can be easily performed. Using a single tunable delay line with a maximum delay τ_{max} of 80 ps and N taps enables the FSR to be tuned from $(N-1)/\tau_{\max}$ to infinity. Figure 5.9(b) presents a comparison between the expected spectral response of a four-tap MWP filter and the experimental results showing good agreement. The spectral range of the filter can be adjusted from 40 GHz to 70 GHz by tuning the wavelength of the four lasers within the PhC dispersion curve. The maximum extinction of the signal due to the notch cancellation reaches 50 dB. Around 10 dB of main to secondary side-lobe (MSSL) ratio is obtained, which can be further enhanced by windowing the filter taps. In addition, very low distortion of the RF signal is observer over the broad spectral range (0-50 GHz).

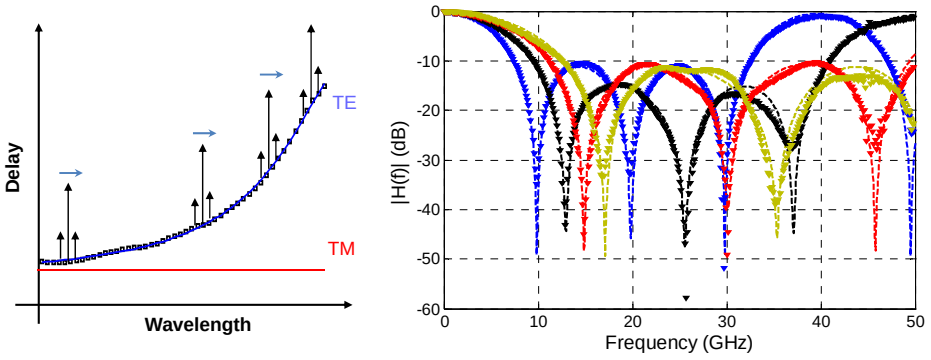

(a) (b)

Figure 5.9: PhC-multi-wavelength-based four-tap MWP filter. (a) Delay profile for the modes TE and TM as a function of the wavelength. Detail of the spectral placement for all the four taps within the TE delay profile. (b) Calculated (dashed curves) and measured (makers) results for the filter response with different spectral scenarios of the emission wavelengths.

5.5 Figures of merit for PhC-based delay lines

Once the suitability of using dispersion-engineered PhCs as tunable delay lines has been demonstrated for broadband RF signals, their performance metrics, given by several FOMs, need to be evaluated. The proposed FOMs address issues related to the power consumption, loss penalty derived from the operating frequency and the delay, tunability limitations, physical size and dispersion-related amplitude distortion when employing the PhC as a building block in filtering schemes. A brief description of each one will be provided.

5.5.1 Numerical fitting

In order to quantify the delay line limitations in terms of the most relevant FOMs, the measured PhC dispersive response is approximated by parabolic and Lorentzian functions as shown in Figs. 5.10(a) and 5.10(b), respectively. The parabolic assessment is representative of the typical fiber-based delay line implementation. The Lorentzian approximation brings a more accurate fitting, at the expense of using an expression with higher complexity compared with the parabolic case. Both figure insets illustrate the equations requested for obtaining the aforementioned approximations. In addition, the fitting values for each case are represented in Table 5.1.

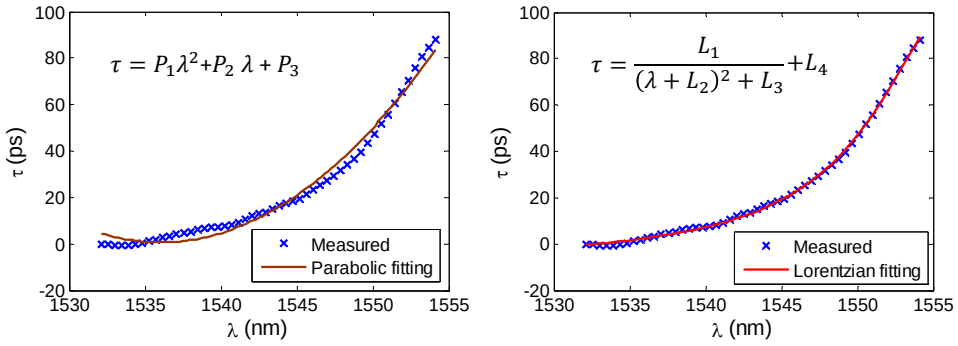

(a) (b)

Figure 5.10: PhC dispersion and fitting curves using (a) parabolic and (b) Lorentzian approximation.

Parabolic	
P_1	0.25
P_2	-775.33
P_3	595465.31

Lorentzian	
L_1	5152.66
L_2	1556.98
L_3	44.77
L_4	-8.15

Table 5.1: Fitting values for the parabolic and Lorentzian approximation.

5.5.2 FOM: Modulation scheme

Optical double and single sideband modulations (ODSB and OSSB) are the most common modulation schemes in MWP. ODSB implies less cost and complexity than OSSB modulation. However, chromatic dispersion effects severely limit the frequency-length product of the fiber links, mainly due to the well-known electrical carrier suppression effect when the ODSB modulation scheme is implemented [136]. To quantify this upper frequency restriction, the induced time delay over both frequency sidebands is evaluated.

In Fig. 5.11(a), λ_0, $\lambda_0-\Lambda$ and $\lambda_0+\Lambda$ represent, respectively, the wavelengths of the optical carrier, lower and higher RF subcarriers corresponding to the maximum dispersion profile within the usable PhC delay line spectrum. Both the lower and higher sideband delays are symbolized by τ_a and τ_b respectively.

As Fig. 5.11(b) illustrates, the carrier suppression effect attenuates the power of the detected microwave signal periodically with the length of the fiber l, the optical frequency and the chromatic dispersion D following

$$\nu = \nu_0\sqrt{\frac{N}{2Dlc}},\ N = 1, 3, 5, \ldots, \tag{5.3}$$

being ν_0 the optical carrier frequency and c the speed of light in vacuum.

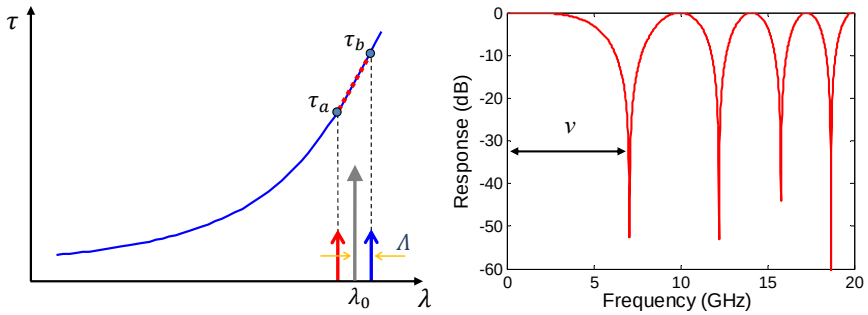

(a) (b)

Figure 5.11: (a) Carrier and sidebands location in the PhC dispersion curve to obtain (b) the carrier suppression effect response.

Within the current bandwidths for MWP applications (less than 50 GHz), the dispersion per length product can be approximated as the curve slope centered at the wavelength of the optical carrier by

$$Dl = \frac{\tau_b - \tau_a}{2\Lambda}. \tag{5.4}$$

The sideband delays ($\tau_a = \tau(\lambda_0 - \Lambda)$ and $\tau_b = \tau(\lambda_0 + \Lambda)$) can be calculated through both parabolic and Lorentzian functions. However, only the parabolic approach yields a compact expression for the dispersion per length product, which can be written as $Dl = P_2 + 2P_1\lambda_0$. Substituting in Eq. 5.3, the first frequency notch is obtained using the quadratic terms as

$$\nu \leqslant \nu_0 \sqrt{\frac{1}{2c(P_2 + 2P_1\lambda_0)}}. \tag{5.5}$$

At $\lambda_0 = 1553$ nm, the parabolic approximation shows an operational frequency limit of around 85 GHz in ODSB modulation, while by proceeding identically but using a more accurate approximation, such as the Lorentzian function, the frequency limits decays to 75 GHz.

5.5.3 FOM: Non-uniform delay tunability

Since PhC waveguides act as dispersive delay lines, the filter transfer function accomplished using these structures will experience an error related to an ideal or reference linear case, as illustrates Fig. 5.12(a). Two OSSB modulation signals have been considered in Fig. 5.12(b) so as to characterize the response error without taking into account the carrier suppression effect. λ_0 and $\lambda_0 + \Lambda$ represent the wavelengths of the optical carrier and RF subcarrier corresponding to the lowest channel, while $\lambda_0 + \Delta\lambda$ and $\lambda_0 + \Delta\lambda + \Lambda$ play a similar role for the highest channel.

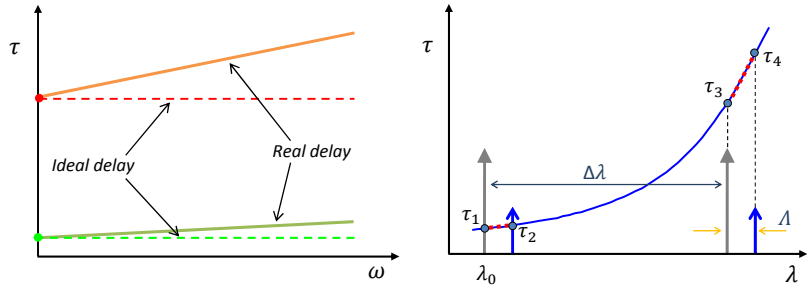

(a) (b)

Figure 5.12: (a) Ideal and real delays for implementing MWP filters. (b) Spectral locations and delays to obtain the error.

For an ideal delay line, the time delay difference between the optical carriers ($\Delta\tau_{carrier}$) should be equal to that experienced by the subcarriers ($\Delta\tau_{subcarrier}$). In practice, however, this last quantity depends on the subcarrier spacing (Λ). The response error will be carried out through the parabolic approximation, since the Lorentzian results cannot be simplified. Thus, these time delay differences are

$$\begin{aligned}\Delta\tau_{carrier} &= \tau_3 - \tau_1 = \Delta\lambda\left[P_2 + P_1\left(\Delta\lambda + 2\lambda_0\right)\right] \\ \Delta\tau_{subcarrier} &= \tau_4 - \tau_2 = \Delta\lambda\left[P_2 + P_1(\Delta\lambda + 2(\lambda_0 + \Lambda))\right]\end{aligned} \tag{5.6}$$

The error measure parameter can be defined as

$$\varepsilon\left(\Lambda\right)\% = 100x\left(\frac{\Delta\tau_{subcarrier} - \Delta\tau_{carrier}}{\Delta\tau_{carrier}}\right) = 100x\left(\frac{2P_1\Lambda}{P_2 + P_1(\Delta\lambda + 2\lambda_0)}\right). \tag{5.7}$$

From 5.7 the maximum operational frequency (in wavelength units) providing this maximum error value can be obtained as

$$\Lambda \leq \frac{\varepsilon\left[P + P_1(\Delta\lambda + 2\lambda_0)\right]}{2P_1}. \tag{5.8}$$

In applications where more than two coefficients are required, as for instance band-pass filtering and optical beamforming networks, a suitable response error can be obtained by averaging over all the relative errors. It can be calculated between any pair of optical carriers and their respective subcarriers as

$$\varepsilon\left(\%\right) = 100x\left[\frac{1}{N-1}\sum_{i=1}^{N-1}\left(\frac{2P_1\Lambda}{P_2 + P_1(\Delta\lambda_i + 2\lambda_{0\_i})}\right)\right]. \tag{5.9}$$

In case of filters, the impact of this error is in the form of a frequency deviation between the designed and the implemented RF transfer function. For a given microwave angular frequency Ω this deviation is given by

$$\Delta\Omega_{error} = \Omega - \frac{\Omega}{(1+\varepsilon)}. \tag{5.10}$$

In the measured PhC dispersion profile and having selected four coefficients (the most spaced ones), the response error obtained is 2.64 % for the parabolic approximation, giving a frequency deviation of 640 MHz at 25 GHz in case of the filter, as illustrates Fig. 5.13. Nonetheless, 3.22 % is the error obtained for the Lorentzian approximation, which yields a frequency deviation of 780 MHz at 25 GHz.

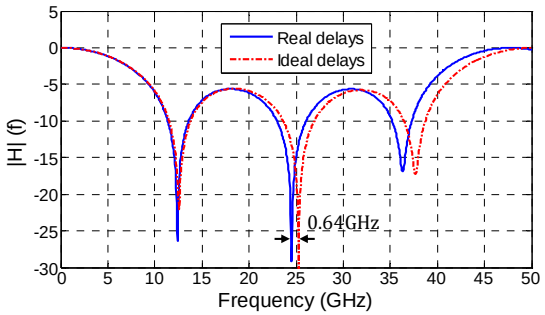

Figure 5.13: Frequency response of the four-tap filter built up using real and ideal delays approximated by a parabolic function.

5.5.4 FOM: Tunability resolution

The resolution expressed in number of bits is a frequently used metric to evaluate the minimum tuning step of a certain device. In the case of linear dispersive delay lines there is a direct relationship between the minimum time and wavelength steps. For nonlinear dispersive devices, such as the PhC, the resolution values must be obtained by making successive linear approximations each one valid within a given region of the usable spectrum. As an example, Fig. 5.14(a) shows a linear fitting of one of these regions within the PhC group delay curve.

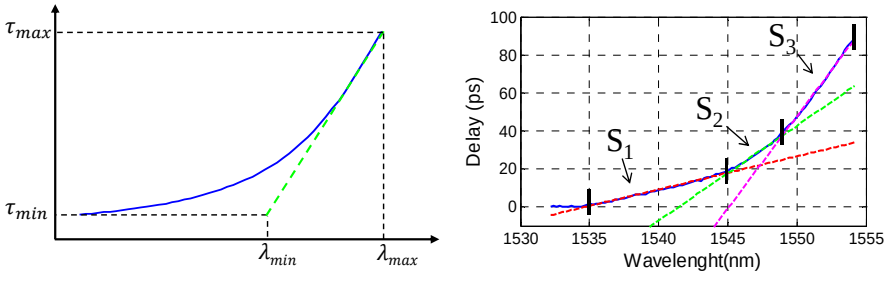

(a) (b)

Figure 5.14: (a) PhC dispersion curve and 1^{st} order fitting. (b) Different slopes to obtain the resolution.

The resolution in number of bits is given by the slope and step tunability as

$$num_{bits} = log_2\left(\frac{\lambda_{max} - \lambda_{min}}{\lambda_{step}}\right). \tag{5.11}$$

Figure 5.14(b) illustrates three possible linear fittings and thus three different slopes for this case, where 16, 15 and 14 bits of tunability resolution were obtained for the first, second and third slope, respectively.

5.5.5 FOM: Loss per unit delay

The ratio between the maximum optical loss penalty L_{max} and the total delay range $\Delta\tau$ is one of the most commonly used performance metric when referring to delay lines,

$$L_\tau = \frac{L_{max}}{\Delta\tau}. \tag{5.12}$$

As it has been explained in section 5.2, in order to obtain moderate propagation loss, the group index for the TE mode goes from $n_g = 4$ to $n_g = 18$. As the waveguide length is 1.5 mm, the relative propagation delay turns 70 ps, with 3.5 dB total optical propagation loss (see Fig. 5.5). Thus, the propagation loss, in units of loss per unit time, reach 50 dB/ns. This value is close although slightly larger than that reported in [137].

5.5.6 FOM: Power uniformity per unit bandwidth

Under ideal operation, a delay line should provide a tunable delay with negligible output power variation. In practice however, the modulus of the transfer function of a delay line is not uniform within its usable spectrum but rather suffers from power excursions or ripples around an average value. If ΔP_{max}(dB) denotes the maximum value of the power excursion within the usable spectrum BW of a delay line, a figure of merit describing the power uniformity over the available bandwidth can be defined as

$$P_{BW} = \frac{\Delta P_{max}\,(dB)}{BW}. \tag{5.13}$$

In the particular case of the PhC-based delay line, a P_{BW} value of 0.07 dB/GHz was obtained. It is important to notice that this low value is important for the MWP filter performance, since the uniformity of all taps is crucial for achieving deep notches.

5.5.7 FOM: Size

The total waveguide length is determined by the trade-off between the maximum achievable delay, integration-scale and propagation losses. The larger the length, the larger the maximum delay will become, at the cost of less compact devices and larger propagation losses. The transversal section is fixed by both the coupling efficiency and the modal propagation properties. The total size of the PhC-based waveguide is 1.5 mm-long.

5.5.8 FOM: Power consumption

In recent years, the so-called green engineering is attracting increasing interest. In this sense, low losses and bias-free-based approaches are preferred attending to energy efficiency. Due to the passive nature of the PhC waveguides, together with the relatively low propagation losses and good coupling efficiency, high performance solutions in the context of efficient energy use can be achieved in comparison with active approaches, such as SBS effects or SOAs.

5.6 Conclusions

In this chapter, the use of a 1.5 mm-long GaInP/GaAs highly dispersive PhC waveguide has been demonstrated for implementing a tunable TTD line. A properly designed structure has provided a substantial reduction of backscattering and an improvement of the transmission of slow modes. The design principle was based on the anti-symmetric shift of the first row of holes, which were performed with a slightly smaller radius. This way optical propagation loss of only 3.5 dB was achieved while tuning the delay up to 70 ps. An optical range of 20 nm was required to get full tunability.

The implementation of tunable and reconfigurable MWP filters has been successfully demonstrated through the PhC-based delay line. The filter tunability has been accomplished by wavelength multiplexing of optical carriers. Notch and bandpass operation have been performed by employing polarization multiplexing of the TE and TM modes and a multi-wavelength source, respectively. Relevant features include notch depth of 50 dB for the notch-type filter, broadband operation up to 50 GHz and tunable free spectral ranges over 70 GHz. Indeed, the operational bandwidth is only limited by the performances of the modulator and photodetector deployed.

Several FOMs for evaluating the PhC-based dispersive delay line have been provided involving the power consumption, loss penalty derived from the operating frequency and the delay, tunability limitations, physical size and dispersion-related amplitude distortion. Relevant features include the passive nature of the technology, low loss, high tunability resolution, low impact on the modulation scheme, relevant influence of the dispersion profile in the filter transfer function, high power uniformity per unit bandwidth, which is crucial for the MWP filter performance, and mm-scale size. In this way, a footprint reduction from two to five orders of magnitude compared to FBGs or DBGs and SBS effects in standard fibers approaches, respectively, has been reported.

The content of this chapter has been summarized and submitted for publication to the following international publications:

- **J. Sancho**, J. Bourderionnet, J. Lloret, G. Lehoucqa, P. Colmana, S. Xaviera, S. Sales, J. Capmany, S. Combrie and A. De Rossi, "Integrated microwave photonic crystal signal processor", submitted to Nature Photonics, 2012.
- **J. Sancho**, J. Lloret, J. Bourderionnet, G. Lehoucqa, P. Colmana, S. Xaviera, A. De Rossi, D. Dolfi, S. Sales and J. Capmany, "Microwave photonic signal processor based on an integrated dispersive delay line", submitted to IEEE Topical Meeting Microwave Photonics (MWP), Noordwijk (Netherlands), 2012.

Chapter 6

Conclusions and future perspectives

6.1 Summary and general conclusions

This Ph.D. thesis has been focused on the design, proposal and performance evaluation of current SFL technological platforms to the aim of realizing phase shifting and true time delaying functionalities in the field of MWP. The large tunability ranges and broadband operation enabled by these photonic-assisted approaches have been put to the test for implementing reconfigurable complex-valued multi-tap MWP filters. In particular, the aforementioned signal processing tasks have been implemented by means of the following device platforms: SBS effects in optical fibers, FBGs, nonlinear effects in SOAs and PhC waveguides. The most relevant metrics concerning the SFL technological platforms dealt with in this thesis have been summarized in Tabs. 6.1 and 6.2 aiming at identifying the most proper device for a given MWP application, i.e. phase shifting, time delaying and filtering. It must be noticed that *tuning time scale* in Tab. 6.2 is provided in the column entitled *tunab. control mechanism*.

In chapter 2, SBS effects have shown an unprecedented flexibility to offer all-optically controlled microwave signal processing functionalities. Two Brillouin-based mechanisms have been described targeting MWP applications: the conventional SBS amplification in standard fibers and the pulsed and pseudo-random signals interaction in PMFs, which yields the generation of DBGs. SBS in standard fibers has led to the development of a 40 GHz bandwidth fully tunable phase shifter, previously demonstrated up to 18 GHz [26]. In addition, a narrow-band limitation where the Brillouin loss resonance takes place (centered at $\sim$ 21 GHz) has been highlighted. SBS seems a promising technology to perform tunable phase shifts in terms of bandwidth (only limited by the photodetector (PD)), insertion loss and power variation (see Tab. 6.1). However, the km-scale footprint represents a serious obstacle for the PIC approach. Moreover, TTD operation has been demonstrated through the SCT principle [36], i.e. the combined dispersion induced by the SBS resonance in the vicinity of the RF signal and the phase characteristic of the optical carrier. Continuously tunable TTDs up to 8 ns within 100 MHz instantaneous bandwidth have been accomplished. Despite the ns-scale delay achieved through SBS effects in standard fibers, the large

power consumption, size and insertion loss, shown in Tab. 6.2, become important constraints to be considered. Furthermore, the SBS-based TTD approach has yield the implementation of a reconfigurable MWP notch filter, whose FSR has shown to be tunable for the 20% of its value. The main drawbacks of this technological platform for implementing MWP filters rely on the high complexity required for scalability, i.e. for increasing the number of filter taps, and the narrow-band operation (only 100 MHz). On the other hand, the previously reported pulse delaying capabilities of DBGs [37, 54] have been exploited in this thesis to accomplish MWP tasks. In contrast to SBS effects in standard fibers, DBGs have performed fully tunable phase shifts and large true time delays in a cm-scale fiber device, which means a footprint reduction of five orders of magnitude. However, the high insertion loss, power consumption and still limited bandwidth make DBGs not the most suitable technological platform for implementing these MWP functionalities. Additionally, the performance of multi-tap reconfigurable MWP filters has been demonstrated in four different configurations through the DBG mechanism. The spectral responses of the proposed variety of filters have been dynamically tuned and reconfigured, by simply changing the characteristics of single or multiple DBG generations, showing a fractional tuning over the FSR greater than 60% when implementing a two-tap filter. Indeed, the first configuration could perform any spectral range tunability, however the number of taps and the central frequency were not easily scaled. Following configurations were based on multiple grating reflectors successively created along the same fiber, and thus the need of a reference tap with a fixed optical delay line was eliminated. The FSR of the filter was governed by the number of taps and the fiber length. In these configurations the consistency of the frequency response was strongly dependent on the birefringence uniformity along the fiber. The operating frequency limitation seen in the two first configurations was successfully overcome by generating two distinct dynamic Brillouin gratings localized at the same position. Finally, the correlation technique based on the external PRBS optical phase modulation was proposed to alleviate the need for periodic grating refreshing and improve the tunability and the scalability of the filter response. It is important to notice that by simply changing the repetition rate of the pump pulses used to build up the DBGs it is possible to modify the number of filter taps, which means ease scalability. Thus, DBGs appears as a flexible tool to perform reconfigurable multi-tap MWP filters.

The DBG potential application so far reported in literature for implementing fiber distributed sensing systems [55, 56] and time delaying mechanisms [37, 54] has been applied in chapter 3 by exploiting the passive and permanent nature of an FBG. In this way, a complete analysis of the spectral characteristics of a 10 cm-length weak-coupling uniform FBG has been demonstrated. By launching an ultra-short optical pulse into the weak grating, the distributed spectral profile of the FBG convolved with the pulse spectrum has been obtained. In addition, a distributed temperature/strain sensing mechanism with 4 mm spatial resolution has been reported through such a weak FBG. The spatial resolution is only determined by the time duration of the input pulse used to probe the grating. A method for achieving large signal delays with very low distortion in FBGs has also been addressed. 50 ps Gaussian pulses were continuously delayed up to 585 ps by relocating a hot piece of metal along the entire grating. It must be pointed out that the achievable maximum delay can be simply expanded by using a longer grating. The suitability of implementing tunable phase shifts and TTDs through the distributed FBG approach has been described by relocating several hot spots within the grating. The time integral of the electric field

of a Gaussian optical pulse, such as the previously reported in [78], has also been addressed. The integration operation time window has been extended from 50 ps to 1 ns, which is equivalent to twice the propagation length of the FBG. The main advantages of this technological platform compared with DBGs rely on its passive operation requiring no optical pumping and also the simpler experimental setup. However, the high insertion loss, the large reconfiguration time and the impossibility of on-chip integration (see Tabs. 6.1 and 6.2) are important constraints for the implementation of the FBG approach in the MWP framework.

In chapter 4, CPO and XGM nonlinear effects in SOAs have shown remarkable capabilities in terms of phase shifting and true time delaying microwave signals, respectively. A theoretical and experimental evaluation of the propagation, generation and amplification of signal, harmonic and intermodulation distortion terms in a MWP phase shifter has been demonstrated. The phase shifter comprised one or several stages of SOA in the CPO regime followed by an optical filter [84, 93]. The study has been carried out as a function of the phase shifting control mechanism, i.e. the SOA input optical power and injection current, as well as the modulation frequency. In this context, a general optical field model has been provided, which is applicable to any number of arbitrarily spaced modulating tones and accounts for all order of both harmonic and intermodulation distortions at the phase shifter output. Two different optical filtering implementations and spectral separations between the RF tones, namely 0.5 and 3 GHz, have been reported, respectively, for the proper distortion-free design and for covering different MWP applications. It has been found that the second order nonlinear distortion is the term which mostly contributes to the system degradation in CPO based phase shifters. In addition, this nonlinear distortion reaches the RF signal level after cascading three phase shifter structures, mainly due to the ASE accumulation. A fully tunable phase shifter has been proposed and demonstrated in a single CPO-based SOA device followed by a tailored designed FBG. It saves four SOAs and two optical filters compared with the best scheme previously reported [84]. An instantaneous bandwidth greater than 1 GHz, limited by the filtering stage, has been successfully demonstrated. In fact, if the optical filter is broad enough, the phase shifter bandwidth is only restricted by the CPO dynamics in the semiconductor waveguide, which is in the scale of tens of GHz. It is important to mention that the size scales of the aforementioned fiber platforms represent a serious obstacle for the PIC approach. In contrast, SOA based on CPO effects appears as a feasible solution to implement MWP phase shifters since it can provide both electrical and optical control tunability over a broad bandwidth with moderate power consumption. Indeed, CPO-induced phase shifts in SOAs have been proposed followed by an FBG in this thesis work. Nevertheless, micro-ring resonators can play that role and thus, allow on-chip integration with other devices while lowering manufacturing costs. The novel phase shifter approach has been used as a key block in the implementation of a two-tap MWP filter, whose central frequency has shown fully tunability without any spectral and shape alteration. The spectral response of this filter can be reconfigured with additional parallel taps, however such scaling is rather complicated. Besides, the performance of MWP phase shifters based on both the cascaded [84] and single (novel) SOA approach has been evaluated in terms of several FOMs, i.e. gain, noise and nonlinear distortion, as a function of the phase tunability control mechanism. Maximum RF net gain variation of 27 dB, upper NF limit of 36 dB and minimum $SFDR_3$ of 70 $dB{\cdot}Hz^{2/3}$ have been obtained for a single phase shifting stage, while the cascaded structure has reached $\sim$ 10 dB gain variation,

37 dB maximum NF and 60 dB·Hz$^{2/3}$ minimum SFDR$_3$. Moreover, average levels at the output of the cascaded structure turned in a system degradation of 12 dB, 15 dB and 20 dB for the RF net gain, NF and SFDR, respectively, compared with the single phase shifter approach. Finally, TTD operation has been addressed through counter-propagation XGM effects in SOAs. The TTD range has been improved from the previously reported 10 ps [86] to 40 ps by means of a more nonlinear SOA design. SOA-based TTD operates at large bandwidths and provides on-a-chip integration, however the power consumption and tunability mechanism represent an important concern for its applicability in real MWP system (see Tab. 6.2).

Finally, in chapter 5, the suitability of exploiting the dispersive feature of a chip-sized delay line has been addressed aiming at performing MWP processing tasks. The underlying technology under study has been a GaInP/GaAs 1.5 mm long PhC waveguide capable of generating a controllable delay exceeding 70 ps, still with limited RF signal attenuation and degradation. The dispersive design of the PhC waveguide has yield the implementation of tunable and reconfigurable MWP filters. Notch and band-pass operation have been performed by employing, respectively, polarization multiplexing of the TE and TM modes and a multi-wavelength source. Relevant features include maximum notch depth of 50 dB, broadband operation up to 50 GHz and tunable FSRs over 70 GHz. Nevertheless, its scalability relies on the number of lasers at the system input, which implies increasing costs. The PhC-based TTD performance has also been evaluated through several FOMs including issues concerning the power consumption, loss penalty derived from the operating frequency and the delay, tunability limitations, physical size and dispersion-related amplitude distortion. Relevant features include the passive nature of the technology, low loss, high tunability resolution, low impact on the modulation scheme, relevant influence of the dispersion profile in the filter transfer function, high power uniformity per unit bandwidth, which is crucial for the MWP filter performance, and mm-scale size. In this sense, PhC waveguides appear as a promising technology for the TTD operation since they offer small footprint and enable very large operating bandwidth, mainly limited by the bandwidth of the PDs and group velocity dispersion (GVD).

SFL medium	**Bandwidth (Ghz)**	**Tunab. control mechanism**	**Tuning time scale**	**Optical insertion loss (dB)**	**RF power variation (dB)**	**Size scale**	**Power consumption**
SBS	PD limited	RF frequency detuning	us	~ 0	2	$\sim$ km	10 mW
DBG	~ 1 GHz	RF frequency detuning	us	~ 35	~ 3	$\sim$ cm - m	> 100 mW
FBG	~ 10 GHz	Thermal	ms	~ 30	~ 0	$\sim$ cm	Passive
SOA	Few GHz - 40 GHz	Injection current/optical	ns	2.5 - 8	10 - 20	$\sim$ mm - cm	1- 10 mW

Table 6.1: Comparison of the phase shifter approaches against several FOMs.

SFL medium	TTD max	Bandwidth (Ghz)	Tunab. control mechanism	Optical insertion loss (dB)	RF power variation (dB)	Size scale	Power consumption
SBS	8 ns	100 MHz	Optical power (us)	gain	4	$\sim$ km	5 - 110 mW
DBG	Fiber length limited	$\sim$ 1 GHz	Electrical delay (ms)	$\sim$ 35	$\sim$ 3	$\sim$ cm - m	$>$ 100 mW
FBG	FBG length limited	$\sim$ 10 GHz	Thermal (ms)	$\sim$ 30	$\sim$ 0	$\sim$ cm	Passive
SOA	40 ps	35 GHz	Optical power (us)	gain	10	$\sim$ mm	0.1 - 4 mW
PhC	70 ps	PD and GVD limited	Laser wavelength detuning (us)	8	7	$\sim$ mm	Passive

Table 6.2: Comparison of the TTD approaches against several FOMs.

6.2 Directions for future research

Although the SFL technological platforms reported in this thesis have shown unprecedented capabilities for the photonic-assisted RF signal processing, the optimization of their performance and demonstration of further applications in the MWP field will require additional research.

In particular, the open research lines include:

- Evaluate the propagation of finite-bandwidth RF signals through the SFL media instead of simply using sinusoidal microwave carriers.
- Study alternative MWP applications where the phase shifter and TTD functionalities can be applied, including phased array antennas or optoelectronic oscillators.
- Propose novel technological platforms for the realization of MWP phase shifter, TTD and filters, such as quantum-dots semiconductor waveguides, multi-core fibers and micro-ring cavities.
- Perform a deep analysis of the noise generated by SBS effects.
- Obtain experimental results for the DBG-based phase shifter and extend the operational bandwidth of the grating reflections deprived of further reflectivity constraints.
- Evaluate the SOA-based phase shifter using microring resonators instead of FBGs for filtering the red-shifted sideband after the SOA propagation.
- Find a proper mechanism for the RF power variation reduction at the output of the novel single SOA-based phase shifter. Another SOA in saturation regime could perform an equalized response.

- Exploit the polarization rotation of the blue sideband at the output of the SOA so as to find alternative ways to achieve compact phase shifters.
- Increase the resolution and length of the FBG distributed temperature/strain sensor and achieve experimental results for the MWP functionalities.
- Improve the PhC waveguide design in order to increase the TTD range and decrease the propagation loss.

Appendix A
Publications

A.1 Journal

J. Sancho, J. Bourderionnet, J. Lloret, G. Lehoucqa, P. Colman, S. Xaviera, S. Sales, J. Capmany, S. Combrie and A. De Rossi, "Integrated microwave photonic crystal signal processor", submitted to Nature Photonics, 2012.

J. Sancho, S. Chin, D. Barrera, S. Sales and L. Thévenaz, "Time-resolved analysis of a long fiber Bragg grating: principle and its applications", submitted to Optics Express, 2012.

J. Sancho, J. Lloret, I. Gasulla, S. Sales and J. Capmany, "Figures of merit for microwave photonic phase shifters based on semiconductor optical amplifiers", Optics Express, vol. 20, no. 10, pp. 10519-10525, 2012.

Y. Antman, N. Primerov, **J. Sancho**, L. Thévenaz, and A. Zadok, "Localized and stationary dynamic gratings via stimulated Brillouin scattering with phase modulated pumps", Optics Express, vol. 20, no. 7, pp. 7807-7821, 2012.

J. Sancho, N. Primerov, S. Chin, Y. Antman, A. Zadok, S. Sales, and L. Thévenaz, "Tunable and reconfigurable multi-tap microwave photonic filter based on dynamic Brillouin gratings in fibers", Optics Express, vol. 20, no. 6, pp. 6157-6162, 2012.

I. Gasulla, J. Capmany,**J. Sancho**, J. Lloret, S. Sales, "Application of slow and fast light effects to microwave photonics", Optica Pura y Aplicada, vol. 44, no.3, pp. 405-415, 2011.

J. Sancho, J. Lloret, I. Gasulla, S. Sales, and J. Capmany, "Fully tunable 360° microwave photonic phase shifter based on a single semiconductor optical amplifier", Optics Express, vol. 19, no. 18, pp. 17421-17426, 2011.

J. Lloret, F. Ramos, W. Xue, **J. Sancho**, I. Gasulla, S. Sales, J. Mørk and J. Capmany, "The influence of optical filtering on the noise performance of microwave photonic phase shifters based on SOAs", IEEE Journal of Lightwave Technology, vol. 29, no. 12, pp. 1746-1752, 2011.

J. Lloret, **J. Sancho**, M. Pu, I. Gasulla, K. Yvind, S. Sales, and J. Capmany, "Tunable complex-valued multi-tap microwave photonic filter based on single silicon-on-insulator microring resonator", Optics Express, vol. 19, no. 13, pp. 12402-12407, 2011.

I. Gasulla, J. Lloret, **J. Sancho**, S. Sales and J. Capmany, "Recent breakthroughs in microwave photonics", IEEE Photonics Journal, vol. 3, no. 2, pp. 311-315, 2011.

J. Sancho, S. Chin, M. Sagues, A. Loayssa, J. Lloret, I. Gasulla, S. Sales, L. Thévenaz and J. Capmany, "Dynamic microwave photonic filter using separate carrier tuning based on stimulated Brillouin scattering in Fibers", IEEE Photonics Technology Letters, vol. 22, no. 23, pp. 1753-1755, 2010.

I. Gasulla, **J. Sancho**, J. Capmany, J. Lloret, and S. Sales, "Intermodulation and harmonic distortion in slow light microwave photonic phase shifters based on coherent population oscillations in SOAs", Optics Express, vol. 18, no. 25, pp. 25677-25692, 2010.

J. Lloret, **J. Sancho**, I. Gasulla, S. Sales and J. Capmany, "Governing the speed of light and its application to the microwave photonics field", Waves, no. 2, pp. 30-38, 2010.

S. Chin, L. Thévenaz, **J. Sancho**, S. Sales, J. Capmany, P. Berger, J. Bourderionnet, and D. Dolfi, "Broadband true time delay for microwave signal processing, using slow light based on stimulated Brillouin scattering in optical fibers", Optics Express, vol, 18, no. 21, pp. 22599-22613, 2010.

J. Lloret, F. Ramos, **J. Sancho**, I. Gasulla, S. Sales and J. Capmany, "Noise spectrum characterization of slow light SOA-based microwave photonic phase shifters", IEEE Photonics Technology Letters, vol. 22, no. 13, pp. 1005-1007, 2010.

I. Gasulla, **J. Sancho**, J. Lloret, S. Sales and J. Capmany, "Harmonic distortion in microwave photonic phase shifters based on coherent population oscillations in SOAs", IEEE Photonics Technology Letters, vol. 22, no. 12, pp. 899-901, 2010.

A.2 Conference

J. Sancho, J. Lloret, J. Bourderionnet, G. Lehoucqa, P. Colman, S. Xaviera, A. De Rossi, D. Dolfi, S. Sales and J. Capmany, "Microwave photonic signal processor based on an integrated dispersive delay line", submitted to IEEE Topical Meeting Microwave Photonics (MWP), Noordwijk (Netherlands), 11 Sep 2012.

J. Sancho, J. Lloret, N. Primerov, S. Sales, L. Thévenaz and J. Capmany, "Recent implementations of fiber and integrated tunable microwave photonics filters", submitted to Conference of the 14th International Transparent Optical Networks (ICTON), Coventry (England), 2 July 2012.

S. Chin, **J. Sancho**, D. Barrera, S. Sales and L. Thévenaz, "Time-resolved analysis of a long fiber Bragg grating: principle and its applications", in SPIE Photonics Europe, Brussels (Belgium), paper 8439-06, 16 Apr 2012.

Y. Antman, N. Primerov, **J. Sancho**, L. Thévenaz, and A. Zadok, "Long variable delay and distributed sensing using stationary and localized Brillouin dynamic gratings", in National Fiber Optic Engineers Conference (NFOEC), Los Angeles (USA), paper JW2A.24, 3 Mar 2012.

Y. Antman, N. Primerov, **J. Sancho**, L. Thévenaz, and A. Zadok, "Variable delay using stationary and localized Brillouin dynamic gratings", in SPIE Photonics West, San Francisco (USA), invited paper 82730C, 2 Feb 2012.

J. Sancho, J. Lloret, I. Gasulla, S. Sales, and J. Capmany, "2pi microwave photonic phase shifter based on single semiconductor optical amplifier", in IEEE Topical Meeting Microwave Photonics (MWP), Singapore (Singapore),paper 2181, 18 Oct 2011.

J. Lloret, **J. Sancho**, I. Gasulla, S. Sales, and J. Capmany, "Performance metrics evaluation of cascaded SOA based slow light microwave photonic phase shifters", in IEEE Topical Meeting Microwave Photonics (MWP), Singapore (Singapore), paper 2175, 18 Oct 2011.

J. Lloret, **J. Sancho**, I. Gasulla, S. Sales, and J. Capmany, "Complex-coefficient microwave photonic tunable filter using slow light silicon-on-insulator-based microring resonator", in IEEE Topical Meeting Microwave Photonics (MWP), Singapore (Singapore),paper 2167, 18 Oct 2011.

J. Lloret, **J. Sancho**, I. Gasulla, S. Sales and J. Capmany, "True time delays and phase shifters based on slow light technologies for microwave photonics applications", in the Conference of the 13th International Transparent Optical Networks (ICTON), Stockholm (Sweden), invited paper 5971119, 26 June 2011.

J. Sancho, J. Lloret, I. Gasulla, S. Sales, and J. Capmany, "Microwave photonics applications using slow and fast light effects", in Slow and Fast Light conference (SL), Toronto (Canada), invited paper SLMA5, 12 June 2011.

J. Lloret, **J. Sancho**, I. Gasulla, F. Ramos, S. Sales, and J. Capmany, "Noise figure of slow light cascaded SOA based microwave photonic phase shifters", in Slow and Fast Light conference (SL), Toronto (Canada), paper SLWB5, 12 June 2011.

J. Sancho, I. Gasulla, J. Lloret, S. Sales, and J. Capmany, "Third order intermodulation distortion in a 360 microwave photonic phase shifter based on slow light cascaded SOAs", in International Conference on Information Photonics (IP), Ottawa (Canada), paper 5953771, 18 May 2011.

I. Gasulla, **J. Sancho**, J. Capmany, J. Lloret, and S. Sales, "Intermodulation and harmonic distortion in slow light SOA based microwave photonic phase shifters", in Optical Fiber Communication Conference (OFC), Los Angeles (USA), paper JWA051, 6 Mar 2011.

L. Thévenaz, S. Chin, P. Berger, J. Bourderionnet, S. Sales and **J. Sancho**, "Slow light fiber systems in microwave photonics", in SPIE Photonics West, San Francisco, (USA), invited paper 79490B, 22 Jan 2011.

I. Gasulla, **J. Sancho**, J. Lloret, S. Sales, and J. Capmany, "On the use of slow light effects for tunable and reconfigurable microwave photonic filters", in 2nd Mediterranean Photonics Conference, Eilat (Israel), invited paper, 29 Nov 2010.

J. Lloret, F. Ramos, **J. Sancho**, I. Gasulla, S. Sales and J. Capmany, "On the noise performance of slow light SOA-based microwave photonic phase shifters", in IEEE Topical Meeting Microwave Photonics (MWP), Montreal (Canada), paper TH4-28, 5 Oct 2010.

J. Sancho, S. Chin, M. Sagues, A. Loayssa, J. Lloret, I. Gasulla, S. Sales, L. Thévenaz and J. Capmany, "True time delay on tunable microwave photonic filter based on stimulated Brillouin scattering in fibers", in 36th European Conference of Optical Communication (ECOC), Turin (Italy), paper P.1.18, 19 Sep 2010.

I. Gasulla, **J. Sancho**, J. Lloret, S. Sales and J. Capmany, "Figures of merit for microwave photonic phase shifters based on coherent population oscillation slow and fast light effects", in the Conference of the 12th International Transparent Optical Networks (ICTON), Munich (Germany), invited paper We.B3.2, 27 June 2010.

P. Muñoz, R. Garcia-Olcina, J.D. Doménech, M. Rius, **J. Sancho**, J. Capmany, L.R. Chen, C. Habib, X.J.M. Leijtens, T. de Vries, M.J.R. Heck, L. Augustin, R. Notzel and D. Robbins, "InP monolithically integrated label swapper device for spectral

amplitude coded optical packet networks", in European Conference on Optical Integration (ECIO) Cambridge (UK), postdeadline paper FrPD1, 7 Apr 2010.

I. Gasulla, **J. Sancho**, J. Lloret, S. Sales, and J. Capmany, "Harmonic distortion in slow light SOA based microwave photonic phase shifters", in Optical Fiber Communication Conference (OFC), San Diego (USA), paper JWA52, 21 Mar 2010.

I. Gasulla, **J. Sancho**, J. Lloret, L. Yaron, S. Sales and J. Capmany, "Harmonic distortion in SOA based slow/fast light microwave photonic phase shifters", in IEEE Topical Meeting Microwave Photonics (MWP), Valencia (Spain), paper Th3.6, 14 Oct 2009.

Bibliography

[1] R. W. Boyd and D. J. Gauthier, "Controlling the velocity of light pulses," *Science*, vol. 326, pp. 1074–1077, Nov 2009.

[2] A. Willner, B. Zhang, L. Zhang, L. Yan, and I. Fazal, "Optical signal processing using tunable delay elements based on slow light," *IEEE Journal of Selected Topics in Quantum Electronics*, vol. 14, pp. 691–705, June 2008.

[3] A. J. Seeds and K. J. Williams, "Microwave photonics," *J. Lightwave Technol.*, vol. 24, pp. 4628–4641, Dec 2006.

[4] J. Capmany and D. Novak, "Microwave photonics combines two worlds," *Nature Photonics*, vol. 1, pp. 319–330, June 2007.

[5] J. Capmany, I. Gasulla, and S. Sales, "Microwave photonics: Harnessing slow light," *Nature Photonics*, vol. 5, pp. 731–733, Nov 2011.

[6] R. Jakoby, P. Scheele, S. Mller, and C. Weil, "Nonlinear dielectrics for tunable microwave components," *15th International Conference on Microwaves, Radar and Wireless Communications*, pp. 2–10, 2004.

[7] M. Santagiustina, G. Eisenstein, L. Thévenaz, J. Capmany, J. M. andJ.P. Reithmaier, A. D. Rossi, S. Sales, K. Yvind, S. Combrié, and J. Bourderionnet, "Slow light devices and their applications to microwaves and photonics," *IEEE Photonics Society Newsletter*, vol. 26, pp. 5–12, Feb 2012.

[8] R. W. Boyd, *Nonlinear Optics, 3er ed.* Academic Press, 2008.

[9] R. W. Boyd, "Material slow light and structural slow light: similarities and differences for nonlinear optics," *J. Opt. Soc. Am. B*, vol. 28, pp. A38–A44, Dec 2011.

[10] M. Santagiustina, "Electromagnetic energy velocity in slow light," in *Slow and Fast Light*, p. SLTuB5, Optical Society of America, 2011.

[11] L. V. Hau, S. E. Harris, Z. Dutton, and C. H. Behroozi, "Light speed reduction to 17 metres per second in an ultracold atomic gas," *Nature*, vol. 397, pp. 594–598, Feb 1999.

[12] M. S. Bigelow, N. N. Lepeshkin, and R. W. Boyd, "Superluminal and slow light propagation in a room-temperature solid," *Science*, vol. 301, pp. 200–202, July 2003.

[13] J. Mørk, R. Kjær, M. van der Poel, and K. Yvind, "Slow light in a semiconductor waveguide at gigahertz frequencies," *Opt. Express*, vol. 13, pp. 8136–8145, Oct 2005.

[14] K. Y. Song, M. Herráez, and L. Thévenaz, "Observation of pulse delaying and advancement in optical fibers using stimulated Brillouin scattering," *Opt. Express*, vol. 13, pp. 82–88, Jan 2005.

[15] D. Dahan and G. Eisenstein, "Tunable all optical delay via slow and fast light propagation in a raman assisted fiber optical parametric amplifier: a route to all optical buffering," *Opt. Express*, vol. 13, pp. 6234–6249, Aug 2005.

[16] J. Sharping, Y. Okawachi, and A. Gaeta, "Wide bandwidth slow light using a Raman fiber amplifier," *Opt. Express*, vol. 13, pp. 6092–6098, Aug 2005.

[17] T. F. Krauss, "Slow light in photonic crystal waveguides," *Journal of Physics D: Applied Physics*, vol. 40, p. 2666, Apr 2007.

[18] S. Longhi, "Group delay tuning in active fiber Bragg gratings: From superluminal to subluminal pulse reflection," *Phys. Rev. E*, vol. 72, p. 1, 2005.

[19] F. Morichetti, A. Melloni, A. Breda, A. Canciamilla, C. Ferrari, and M. Martinelli, "A reconfigurable architecture for continuously variable optical slow-wave delay lines," *Opt. Express*, vol. 15, pp. 17273–17282, Dec 2007.

[20] J. Capmany, B. Ortega, and D. Pastor, "A tutorial on microwave photonic filters," *J. Lightwave Technol.*, vol. 24, p. 201, Jan 2006.

[21] R. J. Mailloux, *Phased Array Antenna Handbook*. Artech House, 1995.

[22] I. Frigyes and A. Seeds, "Optically generated true-time delay in phased-array antennas," *Microwave Theory and Techniques, IEEE Transactions on*, vol. 43, pp. 2378–2386, Sep 1995.

[23] M. G. Herráez, K. Y. Song, and L. Thévenaz, "Arbitrary-bandwidth Brillouin slow light in optical fibers," *Opt. Express*, vol. 14, pp. 1395–1400, Feb 2006.

[24] Y. Okawachi, J. Sharping, A. Gaeta, M. Bigelow, A. Schweinsberg, R. Boyd, Z. Zhu, and D. Gauthier, "Tunable all-optical delays via Brillouin slow light in an optical fiber," in *Lasers and Electro-Optics, 2005. (CLEO). Conference on*, vol. 1, pp. 511–513, May 2005.

[25] X. Yao, "Brillouin selective sideband amplification of microwave photonic signals," *Photonics Technology Letters, IEEE*, vol. 10, pp. 138–140, Jan 1998.

[26] A. Loayssa and F. Lahoz, "Broad-band rf photonic phase shifter based on stimulated Brillouin scattering and single-sideband modulation," *Photonics Technology Letters, IEEE*, vol. 18, pp. 208–210, Jan 2006.

[27] A. Loayssa, J. Capmany, M. Sagues, and J. Mora, "Demonstration of incoherent microwave photonic filters with all-optical complex coefficients," *Photonics Technology Letters, IEEE*, vol. 18, pp. 1744–1746, Aug 2006.

[28] M. Sagues and A. Loayssa, "Orthogonally polarized optical modulation for microwave photonics processing using stimulated Brillouin scattering," in *Microwave Photonics (MWP), 2010 IEEE Topical Meeting on*, pp. 369–372, Oct 2010.

[29] J. Geng, S. Staines, Z. Wang, J. Zong, M. Blake, and S. Jiang, "Highly stable low-noise Brillouin fiber laser with ultranarrow spectral linewidth," *Photonics Technology Letters, IEEE*, vol. 18, pp. 1813–1815, Sep 2006.

[30] A. Zadok, A. Eyal, and M. Tur, "Gigahertz-wide optically reconfigurable filters using stimulated Brillouin scattering," *J. Lightwave Technology*, vol. 25, pp. 2168–2174, Aug 2007.

[31] Z. Zhu, D. J. Gauthier, and R. W. Boyd, "Stored light in an optical fiber via stimulated Brillouin scattering," *Science*, vol. 318, pp. 1748–1750, Dec 2007.

[32] D. Dolfi, P. Joffre, J. Antoine, J. P. Huignard, D. Philippet, and P. Granger, "Experimental demonstration of a phased-array antenna optically controlled with phase and time delays," *Appl. Opt.*, vol. 35, pp. 5293–5300, Sep 1996.

[33] Y. Liu, J. Yang, and J. Yao, "Continuous true-time-delay beamforming for phased array antenna using a tunable chirped fiber grating delay line," *Photonics Technology Letters, IEEE*, vol. 14, pp. 1172–1174, Aug 2002.

[34] H. Su, P. Kondratko, and S. L. Chuang, "Variable optical delay using population oscillation and four-wave-mixing in semiconductor optical amplifiers," *Opt. Express*, vol. 14, pp. 4800–4807, May 2006.

[35] A. Zadok, A. Eyal, and M. Tur, "Stimulated Brillouin scattering slow light in optical fibers," *Appl. Opt.*, vol. 50, pp. E38–E49, Sep 2011.

[36] P. Morton and J. Khurgin, "Microwave photonic delay line with separate tuning of the optical carrier," *Photonics Technology Letters, IEEE*, vol. 21, pp. 1686–1688, Nov 2009.

[37] S. Chin, N. Primerov, and L. Thévenaz, "Photonic delay line for broadband optical signals, based on dynamic grating reflectors in fibers," in *Optical Communication (ECOC), 2010 36th European Conference and Exhibition on*, pp. 1–3, Sep 2010.

[38] N. Primerov, S. Chin, K. Y. Song, and L. Thévenaz, "Ultra wide range tunable delay line using dynamic grating reflectors in optical fibers," in *Optical Fiber Communication (OFC), collocated National Fiber Optic Engineers Conference, 2010 Conference on (OFC/NFOEC)*, pp. 1–3, Mar 2010.

[39] K. Y. Song, W. Zou, Z. He, and K. Hotate, "All-optical dynamic grating generation based on Brillouin scattering in polarization-maintaining fiber," *Opt. Lett.*, vol. 33, pp. 926–928, May 2008.

[40] K. Y. Song, S. Chin, N. Primerov, and L. Thévenaz, "Time-domain distributed fiber sensor with 1 cm spatial resolution based on Brillouin dynamic grating," *J. Lightwave Technology*, vol. 28, pp. 2062–2067, July 2010.

[41] K. Y. Song and H. J. Yoon, "Observation of narrowband intrinsic spectra of Brillouin dynamic gratings," *Opt. Lett.*, vol. 35, pp. 2958–2960, Sep 2010.

[42] L. Thévenaz, N. Primerov, S. Chin, and M. Santagiustina, "Dynamic brillouin gratings: A new tool in fibers for all-optical signal processing," in *Photonics Conference (PHO), 2011 IEEE*, pp. 63 –64, oct. 2011.

[43] S. Chin, N. Primerov, K. Y. Song, L. Thévenaz, M. Santagiustina, and L. Ursini, "True time reversal via dynamic brillouin gratings in polarization maintaining fibers," in *Nonlinear Photonics*, p. NThA6, Optical Society of America, 2010.

[44] N. Primerov, S. Chin, L. Thévenaz, L. Ursini, and M. Santagiustina, "All-optical calculus based on dynamic brillouin grating reflectors in optical fibers," in *Slow and Fast Light*, p. SLMA3, Optical Society of America, 2011.

[45] Y. Antman, N. Primerov, J. Sancho, L. Thévenaz, and A. Zadok, "Localized and stationary dynamic gratings via stimulated Brillouin scattering with phase modulated pumps," *Opt. Express*, vol. 20, pp. 7807–7821, Mar 2012.

[46] G. P. Agrawal, *Nonlinear Fiber Optics, 3er ed.* Academic Press, 2001.

[47] A. Loayssa, D. Benito, and M. J. Garde, "Optical carrier brillouin processing of microwave photonic signals," *Opt. Lett.*, vol. 25, pp. 1234–1236, Sep 2000.

[48] J. E. Román, M. Y. Frankel, and R. D. Esman, "Spectral characterization of fiber gratings with high resolution," *Opt. Lett.*, vol. 23, pp. 939–941, June 1998.

[49] M. Nikles, L. Thévenaz, and P. Robert, "Brillouin gain spectrum characterization in single-mode optical fibers," *J. Lightwave Technology*, vol. 15, pp. 1842–1851, Oct 1997.

[50] Z. Zhu, A. M. C. Dawes, D. J. Gauthier, L. Zhang, and A. E. Willner, "Broadband SBS slow light in an optical fiber," *J. Lightwave Technol.*, vol. 25, pp. 201–206, Jan 2007.

[51] M. Sagues, R. G. Olcina, A. Loayssa, S. Sales, and J. Capmany, "Multi-tap complex-coefficient incoherent microwave photonic filters based on optical single-sideband modulation and narrow band optical filtering," *Opt. Express*, vol. 16, pp. 295–303, Jan 2008.

[52] W. Xue, S. Sales, J. Mørk, and J. Capmany, "Widely tunable microwave photonic notch filter based on slow and fast light effects," *Photonics Technology Letters, IEEE*, vol. 21, pp. 167–169, Feb 2009.

[53] Y. Dong, X. Bao, and L. Chen, "Distributed temperature sensing based on birefringence effect on transient Brillouin grating in a polarization-maintaining photonic crystal fiber," *Opt. Lett.*, vol. 34, pp. 2590–2592, Sep 2009.

[54] K. Y. Song, K. Lee, and S. B. Lee, "Tunable optical delays based on Brillouin dynamic grating in optical fibers," *Opt. Express*, vol. 17, pp. 10344–10349, June 2009.

[55] Y. Dong, L. Chen, and X. Bao, "High-spatial-resolution time-domain simultaneous strain and temperature sensor using Brillouin scattering and birefringence in a polarization-maintaining fiber," *Photonics Technology Letters, IEEE*, vol. 22, pp. 1364–1366, Sep 2010.

[56] S. Chin, N. Primerov, and L. Thévenaz, "Sub-centimeter spatial resolution in distributed fiber sensing based on dynamic Brillouin grating in optical fibers," *Sensors Journal, IEEE*, vol. 12, pp. 189–194, Jan 2012.

[57] T. Horiguchi and M. Tateda, "Optical-fiber-attenuation investigation using stimulated Brillouin scattering between a pulse and a continuous wave," *Opt. Lett.*, vol. 14, pp. 408–410, Apr 1989.

[58] K. Hotate and T. Hasegawa, "Optical fiber sensors. measurement of Brillouin gain spectrum distribution along an optical fiber using a correlation-based technique - proposal, experiment and simulation," *IEICE Trans Electron*, vol. 83, pp. 405–412, Mar 2000.

[59] J. Capmany, B. Ortega, D. Pastor, and S. Sales, "Discrete-time optical processing of microwave signals," *J. Lightwave Technol.*, vol. 23, p. 702, Feb 2005.

[60] K. Hill and G. Meltz, "Fiber bragg grating technology fundamentals and overview," *J. Lightwave Technology*, vol. 15, pp. 1263–1276, Aug 1997.

[61] T. Erdogan, "Fiber grating spectra," *J. Lightwave Technology*, vol. 15, pp. 1277–1294, Aug 1997.

[62] M. Volanthen, H. Geiger, and J. Dakin, "Distributed grating sensors using low-coherence reflectometry," *J. Lightwave Technology*, vol. 15, pp. 2076–2082, Nov 1997.

[63] H. Murayama, H. Igawa, K. Kageyama, K. Ohta, I. Ohsawa, K. Uzawa, M. Kanai, T. Kasai, and I. Yamaguchi, "Distributed strain measurement with high spatial resolution using fiber Bragg gratings and optical frequency domain reflectometry," in *Optical Fiber Sensors*, p. ThE40, Optical Society of America, 2006.

[64] K. Hotate and K. Kajiwara, "Proposal and experimental verification of Bragg wavelength distribution measurement within a long-length FBG by synthesis of optical coherence function," *Opt. Express*, vol. 16, pp. 7881–7887, May 2008.

[65] J. Mora, B. Ortega, A. Diez, M. Andres, J. Capmany, J. Cruz, and D. Pastor, "Highly tunable optically switched time delay line for transversal filtering," *Electronics Letters*, vol. 39, pp. 1799–1800, Dec 2003.

[66] B. Ortega, J. Cruz, J. Capmany, M. Andres, and D. Pastor, "Variable delay line for phased-array antenna based on a chirped fiber grating," *Microwave Theory and Techniques, IEEE Transactions on*, vol. 48, pp. 1352–1360, Aug 2000.

[67] C. Caucheteur, A. Mussot, S. Bette, A. Kudlinski, M. Douay, E. Louvergneaux, P. Mégret, M. Taki, and M. G. Herráez, "All-fiber tunable optical delay line," *Opt. Express*, vol. 18, pp. 3093–3100, Feb 2010.

[68] R. Slavík, Y. Park, M. Kulishov, R. Morandotti, and J. Azaña, "Ultrafast all-optical differentiators," *Opt. Express*, vol. 14, pp. 10699–10707, Oct 2006.

[69] M. A. Preciado and M. A. Muriel, "Design of an ultrafast all-optical differentiator based on a fiber Bragg grating in transmission," *Opt. Lett.*, vol. 33, pp. 2458–2460, Nov 2008.

[70] N. Q. Ngo, "Design of an optical temporal integrator based on a phase-shifted fiber Bragg grating in transmission," *Opt. Lett.*, vol. 32, pp. 3020–3022, Oct 2007.

[71] M. A. Preciado and M. A. Muriel, "Ultrafast all-optical integrator based on a fiber Bragg grating: proposal and design," *Opt. Lett.*, vol. 33, pp. 1348–1350, June 2008.

[72] M. A. Muriel, J. Azaña, and A. Carballar, "Real-time fourier transformer based on fiber gratings," *Opt. Lett.*, vol. 24, pp. 1–3, Jan 1999.

[73] M. K. Barnoski, M. D. Rourke, S. M. Jensen, and R. T. Melville, "Optical time domain reflectometer," *Appl. Opt.*, vol. 16, pp. 2375–2379, Sep 1977.

[74] L. Chen, S. Benjamin, P. Smith, and J. Sipe, "Ultrashort pulse reflection from fiber gratings: a numerical investigation," *J. Lightwave Technology*, vol. 15, pp. 1503–1512, Aug 1997.

[75] N. J. Doran and D. Wood, "Nonlinear-optical loop mirror," *Opt. Lett.*, vol. 13, pp. 56–58, Jan 1988.

[76] K. Y. Song, Z. He, and K. Hotate, "Distributed strain measurement with millimeter-order spatial resolution based on Brillouin optical correlation domain analysis," *Opt. Lett.*, vol. 31, pp. 2526–2528, Sep 2006.

[77] J. Azaña, "Proposal of a uniform fiber Bragg grating as an ultrafast all-optical integrator," *Opt. Lett.*, vol. 33, pp. 4–6, Jan 2008.

[78] Y. Park, T. J. Ahn, Y. Dai, J. Yao, and J. Azaña, "All-optical temporal integration of ultrafast pulse waveforms," *Opt. Express*, vol. 16, pp. 17817–17825, Oct 2008.

[79] T. Durhuus, B. Mikkelsen, C. Joergensen, S. Lykke Danielsen, and K. Stubkjaer, "All-optical wavelength conversion by semiconductor optical amplifiers," *J. Lightwave Technology*, vol. 14, pp. 942–954, June 1996.

[80] K. Stubkjaer, "Semiconductor optical amplifier-based all-optical gates for high-speed optical processing," *IEEE Journal of Selected Topics in Quantum Electronics*, vol. 6, pp. 1428–1435, Dec 2000.

[81] O. Leclerc, B. Lavigne, E. Balmefrezol, P. Brindel, L. Pierre, D. Rouvillain, and F. Seguineau, "Optical regeneration at 40 Gb/s and beyond," *J. Lightwave Technology*, vol. 21, pp. 2779–2790, Nov 2003.

[82] F. Öhman, K. Yvind, and J. Mørk, "Voltage-controlled slow light in an integrated semiconductor structure with net gain," *Opt. Express*, vol. 14, pp. 9955–9962, Oct 2006.

[83] G. P. Agrawal, "Population pulsations and nondegenerate four-wave mixing in semiconductor lasers and amplifiers," *J. Opt. Soc. Am. B*, vol. 5, pp. 147–159, Jan 1988.

[84] W. Xue, S. Sales, J. Capmany, and J. Mørk, "Wideband 360° microwave photonic phase shifter based on slow light in semiconductor optical amplifiers," *Opt. Express*, vol. 18, pp. 6156–6163, Mar 2010.

[85] P. Berger, M. Alouini, J. Bourderionnet, F. Bretenaker, and D. Dolfi, "Dynamic saturation in semiconductoroptical amplifiers: accurate model, roleof carrier density, and slow light," *Opt. Express*, vol. 18, pp. 685–693, Jan 2010.

[86] W. Xue and J. Mørk, "Tunable true-time delay of a microwave photonic signal realized by cross gain modulation in a semiconductor waveguide," *Applied Physics Letters*, vol. 99, p. 231102, Dec 2011.

[87] C. J. Chang-Hasnain and S. L. Chuang, "Slow and fast light in semiconductor quantum-well and quantum-dot devices," *J. Lightwave Technol.*, vol. 24, pp. 4642–4654, Dec 2006.

[88] J. Mørk, F. Öhman, M. Van Der Poel, Y. Chen, P. Lunnemann, and K. Yvind, "Slow and fast light: Controlling the speed of light using semiconductor waveguides," *Laser Photonics Review*, vol. 3, pp. 30–44, Aug 2009.

[89] J. Mørk, P. Lunnemann, W. Xue, Y. Chen, P. Kaer, and T. R. Nielsen, "Slow and fast light in semiconductor waveguide," *Semicond. Sci.Technol.*, vol. 25, p. 083002, July 2010.

[90] R. S. Tucker, P.-C. Ku, and C. J. Chang-Hasnain, "Slow-light optical buffers: Capabilities and fundamental limitations," *J. Lightwave Technol.*, vol. 23, p. 4046, Dec 2005.

[91] F. Öhman, K. Yvind, and J. Mørk, "Slow light in a semiconductor waveguide for true-time delay applications in microwave photonics," *Photonics Technology Letters, IEEE*, vol. 19, pp. 1145–1147, Aug 2007.

[92] A. Uskov and C. Chang-Hasnain, "Slow and superluminal light in semiconductor optical amplifiers," *Electronics Letters*, vol. 41, pp. 55–56, Aug 2005.

[93] W. Xue, Y. Chen, F. Öhman, S. Sales, and J. Mørk, "Enhancing light slowdown in semiconductor optical amplifiers by optical filtering," *Opt. Lett.*, vol. 33, pp. 1084–1086, May 2008.

[94] Y. Chen, W. Xue, F. Öhman, and J. Mørk, "Theory of optical-filtering enhanced slow and fast light effects in semiconductor optical waveguides," *J. Lightwave Technology*, vol. 26, pp. 3734–3743, Dec 2008.

[95] W. Xue, Y. Chen, F. Öhman, and J. Mørk, "The role of input chirp on phase shifters based on slow and fast light effects in semiconductor optical amplifiers," *Opt. Express*, vol. 17, pp. 1404–1413, Feb 2009.

[96] E. Shumakher, S. O. Dúill, and G. Eisenstein, "Signal-to-noise ratio of a semiconductor optical-amplifier-based optical phase shifter," *Opt. Lett.*, vol. 34, pp. 1940–1942, July 2009.

[97] J. Lloret, F. Ramos, W. Xue, J. Sancho, I. Gasulla, S. Sales, J. Mørk, and J. Capmany, "The influence of optical filtering on the noise performance of microwave photonic phase shifters based on SOAs," *J. Lightwave Technology*, vol. 29, pp. 1746–1752, June 2011.

[98] P. Berger, J. Bourderionnet, M. Alouini, F. Bretenaker, and D. Dolfi, "Theoretical study of the spurious-free dynamic range of a tunable delay line based on slow light in SOA," *Opt. Express*, vol. 17, pp. 20584–20597, Oct 2009.

[99] C. Cox and W. S. C. Chang, *Figures of merit and performance analysis of photonic microwave links*, vol. RF-Photonic Technology in Optical Fiber Links. Cambridge University Press, 2002.

[100] G. Agrawal and I. Habbab, "Effect of a four-wave mixing on multichannel amplification in semiconductor laser amplifiers," *IEEE Journal of Quantum Electronics*, vol. 26, pp. 501–505, Mar 1990.

[101] S. Duill, R. O'Dowd, and G. Eisenstein, "On the role of high-order coherent population oscillations in slow and fast light propagation using semiconductor optical amplifiers," *IEEE Journal of Selected Topics in Quantum Electronics*, vol. 15, pp. 578–584, June 2009.

[102] C. Cox, *Analog Photonic Links: Theory and Practice*, vol. RF-Photonic Technology in Optical Fiber Links. Cambridge University Press, 2004.

[103] V. Urick, M. Rogge, F. Bucholtz, and K. Williams, "The performance of analog photonic links employing highly compressed erbium-doped fiber amplifiers," *Microwave Theory and Techniques, IEEE Transactions on*, vol. 54, pp. 3141–3145, July 2006.

[104] V. Urick, F. Bucholtz, P. Devgan, J. McKinney, and K. Williams, "Phase modulation with interferometric detection as an alternative to intensity modulation with direct detection for analog-photonic links," *Microwave Theory and Techniques, IEEE Transactions on*, vol. 55, pp. 1978–1985, Sep 2007.

[105] S. Duill, E. Shumakher, and G. Eisenstein, "Noise properties of microwave phase shifters based on semiconductor optical amplifiers," *J. Lightwave Technology*, vol. 28, pp. 791–797, Mar 2010.

[106] M. Shtaif and G. Eisenstein, "Noise properties of nonlinear semiconductor optical amplifiers," *Opt. Lett.*, vol. 21, pp. 1851–1853, Nov 1996.

[107] S. O. Dúill, E. Shumakher, and G. Eisenstein, "The role of optical filtering in microwave phase shifting," *Opt. Lett.*, vol. 35, pp. 2278–2280, July 2010.

[108] S. James, M. Dockney, and R. Tatam, "Simultaneous independent temperature and strain measurement using in-fibre Bragg grating sensors," *Electronics Letters*, vol. 32, pp. 1133–1134, June 1996.

[109] A. Uskov, F. Sedgwick, and C. Chang-Hasnain, "Delay limit of slow light in semiconductor optical amplifiers," *Photonics Technology Letters, IEEE*, vol. 18, pp. 731–733, Mar 2006.

[110] H. Dorren, M. Hill, Y. Liu, N. Calabretta, A. Srivatsa, F. Huijskens, H. de Waardt, and G. Khoe, "Optical packet switching and buffering by using all-optical signal processing methods," *J. Lightwave Technology*, vol. 21, pp. 2–12, Jan 2003.

[111] P. Berger, J. Bourderionnet, F. Bretenaker, D. Dolfi, and M. Alouini, "Time delay generation at high frequency using SOA based slow and fast light," *Opt. Express*, vol. 19, pp. 21180–21188, Oct 2011.

[112] M. Nielsen, D. Blumenthal, and J. Mørk, "A transfer function approach to the small-signal response of saturated semiconductor optical amplifiers," *J. Lightwave Technology*, vol. 18, pp. 2151–2157, Dec 2000.

[113] R. Minasian, "Photonic signal processing of microwave signals," *Microwave Theory and Techniques, IEEE Transactions on*, vol. 54, pp. 832–846, Feb 2006.

[114] Y. Dai and J. Yao, "Nonuniformly-spaced photonic microwave delayline filter," *Opt. Express*, vol. 16, pp. 4713–4718, Mar 2008.

[115] E. Hamidi, D. Leaird, and A. Weiner, "Tunable programmable microwave photonic filters based on an optical frequency comb," *Microwave Theory and Techniques, IEEE Transactions on*, vol. 58, pp. 3269–3278, Nov 2010.

[116] E. Norberg, R. Guzzon, J. Parker, L. Johansson, and L. Coldren, "Programmable photonic microwave filters monolithically integrated in InPInGaAsP," *J. Lightwave Technology*, vol. 29, pp. 1611–1619, June 2011.

[117] P. Dong, N.-N. Feng, D. Feng, W. Qian, H. Liang, D. C. Lee, B. J. Luff, T. Banwell, A. Agarwal, P. Toliver, R. Menendez, T. K. Woodward, and M. Asghari, "Ghz-bandwidth optical filters based on high-order silicon ring resonators," *Opt. Express*, vol. 18, pp. 23784–23789, Nov 2010.

[118] M. Santagiustina, "Governing the speed of light: Recent advances and future perspectives of slow and fast light in microwave-photonics," in *Microwave Photonics, 2009. MWP '09. International Topical Meeting on*, pp. 1–4, Oct 2009.

[119] Y. Akahane, T. Asano, B.-S. Song, and S. Noda, "High-Q photonic nanocavity in a two-dimensional photonic crystal," *Nature*, vol. 425, pp. 944–947, Oct 2003.

[120] T. Baba, N. Fukaya, and J. Yonekura, "Observation of light propagation in photonic crystal optical waveguides with bends," *Electronics Letters*, vol. 35, pp. 654–655, Apr 1999.

[121] M. Loncar, D. Nedeljkovic, T. Doll, J. Vuckovic, A. Scherer, and T. P. Pearsall, "Waveguiding in planar photonic crystals," *Applied Physics Letters*, vol. 77, pp. 1937–1939, Sep 2000.

[122] J. Vuckovic, M. Loncar, H. Mabuchi, and A. Scherer, "Optimization of the Q factor in photonic crystal microcavities," *IEEE Journal of Quantum Electronics*, vol. 38, pp. 850–856, July 2002.

[123] T. Asano, B.-S. Song, Y. Akahane, and S. Noda, "Ultrahigh-q nanocavities in two-dimensional photonic crystal slabs," *IEEE Journal of Selected Topics in Quantum Electronics*, vol. 12, pp. 1123–1134, Dec 2006.

[124] K. Ohtaka, "Energy band of photons and low-energy photon diffraction," *Phys. Rev. B*, vol. 19, pp. 5057–5067, May 1979.

[125] M. Notomi, K. Yamada, A. Shinya, J. Takahashi, C. Takahashi, and I. Yokohama, "Extremely large group-velocity dispersion of line-defect waveguides in photonic crystal slabs," *Phys. Rev. Lett.*, vol. 87, p. 253902, Nov 2001.

[126] K. Inoue, N. Kawai, Y. Sugimoto, N. Carlsson, N. Ikeda, and K. Asakawa, "Observation of small group velocity in two-dimensional AlGaAs-based photonic crystal slabs," *Phys. Rev. B*, vol. 65, p. 121308, Mar 2002.

[127] M. Soljacic and J. D. Joannopoulos, "Enhancement of nonlinear effects using photonic crystals," *Nature Materials*, vol. 3, pp. 211–219, Apr 2004.

[128] T. Baba, "Slow light in photonic crystals," *Nature Photonics*, vol. 2, pp. 465–473, Aug 2008.

[129] C. Monat, B. Corcoran, M. Ebnali-Heidari, C. Grillet, B. J. Eggleton, T. P. White, L. O'Faolain, and T. F. Krauss, "Slow light enhancement of nonlinear effects in silicon engineered photonic crystal waveguides," *Opt. Express*, vol. 17, pp. 2944–2953, Feb 2009.

[130] E. Kuramochi, M. Notomi, S. Hughes, A. Shinya, T. Watanabe, and L. Ramunno, "Disorder-induced scattering loss of line-defect waveguides in photonic crystal slabs," *Phys. Rev. B*, vol. 72, p. 161318, Oct 2005.

[131] M. Patterson, S. Hughes, S. Combrié, N.-V.-Q. Tran, A. De Rossi, R. Gabet, and Y. Jaouën, "Disorder-induced coherent scattering in slow-light photonic crystal waveguides," *Phys. Rev. Lett.*, vol. 102, p. 253903, June 2009.

[132] S. Hughes, L. Ramunno, J. F. Young, and J. E. Sipe, "Extrinsic optical scattering loss in photonic crystal waveguides: Role of fabrication disorder and photon group velocity," *Phys. Rev. Lett.*, vol. 94, p. 033903, Jan 2005.

[133] S. Roy, M. Santagiustina, P. Colman, S. Combrie, and A. De Rossi, "Modeling the dispersion of the nonlinearity in slow mode photonic crystal waveguides," *Photonics Journal, IEEE*, vol. 4, pp. 224–233, Feb 2012.

[134] Q. V. Tran, S. Combrie, P. Colman, and A. De Rossi, "Photonic crystal membrane waveguides with low insertion losses," *Applied Physics Letters*, vol. 95, pp. 061105–061105–3, Aug 2009.

[135] D. Hunter and R. Minasian, "Tunable microwave fiber-optic bandpass filters," *Photonics Technology Letters, IEEE*, vol. 11, pp. 874–876, July 1999.

[136] H. Schmuck, "Comparison of optical millimetre-wave system concepts with regard to chromatic dispersion," *Electronics Letters*, vol. 31, pp. 1848–1849, Oct 1995.

[137] L. O'Faolain, S. A. Schulz, D. M. Beggs, T. P. White, M. Spasenović, L. Kuipers, F. Morichetti, A. Melloni, S. Mazoyer, J. P. Hugonin, P. Lalanne, and T. F. Krauss, "Loss engineered slow light waveguides," *Opt. Express*, vol. 18, pp. 27627–27638, Dec 2010.